# NTNU

Norwegian University of
Science and Technology

# Strongly Coupled Spin, Heat and Charge Currents in Superconducting Hybrids

## Marianne Etzelmüller Bathen

Nanotechnology
Submission date: June 2016
Supervisor: Jacob Rune Wüsthoff Linder, IFY

Norwegian University of Science and Technology
Department of Physics

## Abstract

We study the large thermoelectric effects arising as a result of strongly coupled spin, heat and charge currents in superconducting hybrids theoretically. Two new frameworks for calculating thermoelectric coefficients are presented, one including the possibility of spin-dependent bias application to homogeneously magnetized materials, and the other utilizing the quasiclassical framework allowing for spin-splitting polarizations along more than one axis. The thermoelectric coefficient $\alpha$ governing pure thermal spin currents, the Seebeck coefficient $S$ and the thermoelectric figure of merit $ZT$ are all maximized when tunneling is considered to be across an insulating barrier between two Zeeman-split superconducting reservoirs. The disadvantage of such a configuration is the large external magnetic fields which need be applied for the thermoelectric effects to arise. Therefore, we here present results indicating large thermoelectric effects of similar orders of magnitude arising in superconducting hybrids wherein the particle-hole symmetry is broken without the use of large external magnetic fields. Within the low-field material systems studied, all tunneling occurs from the middle of the central layer in a Josephson junction into a normal-metal electrode. The central nanowire in the Josephson junction (i) contains spatially varying magnetization, (ii) is coupled to spin-active interfaces (such as magnetic insulators) or (iii) has intrinsic spin-orbit interaction of Rashba type.

## Sammendrag

I denne masteroppgaven granskes de store termoelektriske effektene som oppstår som et resultat av sterkt koblede strømmer av spinn, ladning og varme i superledende hybridstrukturer teoretisk. To nye rammeverk for beregning av termoelektriske koeffisienter presenteres. Det ene tar høyde for muligheten for spinn-avhengige spenninger og temperaturgradienter i materialer med homogen magnetisering, og det andre utnytter det kvasiklassiske rammeverket for å studere brutte spinn-avhengige partikkel-hull symmetrier langs mer enn en akse. Den termoelektriske koeffisienten $\alpha$ som styrer termiske spinnstrømmer, Seebeck-koeffisienten $S$ og den termoelektriske graderingsfaktoren $ZT$ er alle maksimert når tunneleringstrømmer betraktes over en isolerende barriere mellom to Zeeman-splittede superledende reservoarer. Ulempen ved et slikt oppsett er de sterke magnetiske feltene som må påføres de superledende materialene for å oppmå store termoelektriske effekter. Derfor presenterer vi her i tillegg resultater som indikerer tilsvarende store termoelektriske effekter i superledende hybrider der partikkel-hull symmetrien kan brytes uten at sterke magnetiske felt behøves. I disse materialsystemene forekommer tunnelering mellom den sentrale delen av en Josephson junction og en elektrode av et normalt metall. Den sentrale nanotråden (i) innehar romlig varierende magnetisering, (ii) er koblet til spinn-aktive grensesjikter (som magnetiske isolatorer) eller (iii) innehar spinn-bane kobling.

## Preface

This thesis has been submitted as the end result of the 10 semester master programme in Nanotechnology at the Norwegian University of Science and Technology (NTNU), under the supervision of Professor Jacob Linder. The work was performed during the spring of 2016, and amounts to the equivalent of 30 ECTS-credits.The work performed during this time is a continuation of the 15 ECTS-credit specialization project conducted during the ninth semester of the programme. The work presented in this thesis has resulted in an article published in *Physical Review B* **93**, 224509 (2016). The paper is enclosed at the end of this thesis, and can be found in Appendix D.

I am primarily grateful to my supervisor, Professor Jacob Linder, for suggesting such an exiting project, and for always encouraging and challenging me. Secondly, I would like to thank Jabir Ali Ouassou for being so kind as to help me with porting my code to the Kongull cluster computer system. I also wish to thank the Nanotechnology class of 2016 for the last five years, which have been amazing. Finally, thank you so much to my parents and my brother, for your patience and for always supporting and believing in me.

This thesis was typeset in Latex, using the *Report* document class. The figures were created using *ipe*, or generated by MATLAB. The numerical work was performed in MATLAB, and the algorithm *bvp4c* used to solve boundary value problems. The MATLAB functions *plot* and *surf* were used to plot the resulting data.

*Marianne Etzelmüller Bathen*
Trondheim, June 2016

# List of abbreviations

**MRI** Magnetic Resonance Imaging

**SQUID** Superconducting Quantum Interference Device

**(MOS)FET** (Metal Oxide Semiconductor) Field Effect Transistor

**GMR** Giant Magnetoresistance

**S, SC** Superconductor

**F, FM** Ferromagnet

**(F)I** (Ferromagnetic) insulator

**MI** Magnetic insulator

**N, NM** Normal metal

**ZS** Zeeman-split superconductor

**DOS** Density of states

**SO(C)** Spin-orbit (coupling)

**L** Left

**R** Right or Retarded (Green function)

**A** Advanced (Green function)

**K** Keldysh (Green function)

**KL** Kuprianov-Lukichev

**EBL** Electron Beam Lithography

**EUVL** Extreme Ultraviolet Lithography

# List of symbols

$T_c$  Superconducting critical temperature

$T_{c,0}$  Superconducting critical temperature at zero magnetic field

$S$  Seebeck coefficient

$ZT$  Thermoelectric figure of merit

$\Delta$  Superconducting energy gap

$\Delta_0$  Superconducting energy gap at zero temperature and magnetic field

$\Gamma$  Dynes parameter for inelastic scattering

$D(E)$  Density of states

$\psi_\sigma(\boldsymbol{r}, t)$  Annihilation operator

$\psi_\sigma^\dagger(\boldsymbol{r}, t)$  Creation operator

$\varepsilon$, $E$  Quasiparticle energy in relation to the Fermi energy

$\sigma$  Spin state $\sigma = \pm$

$f^\sigma(E)$  Fermi-Dirac distribution function

$\boldsymbol{h}$  Ferromagnetic exchange field vector

$\sigma_x$, $\sigma_y$, $\sigma_z$  Pauli matrices in $2 \times 2$ spin space

$\boldsymbol{\sigma}$  Pauli vector

$\beta$  Rashba spin orbit coupling strength

$\boldsymbol{A}$  Spin-orbit field vector

$I_q$  Charge current

$I_s^\nu$  Spin current polarized along direction $\nu$

$\nu$  Direction $\{x, y, z\}$

$\dot{Q}$ Heat current

$\dot{Q}_s$ Spin heat current

$L$ Length [nm]

$\zeta$ Interface transparency

$\tau$ Interface transparency

$\xi$ Superconducting coherence length

$\Delta\theta$ Superconducting phase difference

$\psi$ Wave function

$h$ Exchange field strength

$\hat{\boldsymbol{g}}^{R,A,K}$ Retarded, advanced, Keldysh Green function matrix in Nambu space

$D$ Diffusion coefficient

$G_{MR}$ Spin-dependent tunneling probability coefficient

$G_\phi$ Parameter governing spin-dependent phase shifts due to scattering at interfaces

$P$ Polarization

$N_0(E)$ Normal-state density of states

$G_q$ Conductance quantum

$G_\sigma$ Spin-dependent conductance

$G$ Conductance coefficient

$\alpha$ Thermoelectric coefficient

$G_Q$ Thermal conductance coefficient

$\lambda$ Ferromagnetic domain wall length

$\mu$ Chemical potential

$\beta_j$ $1/(k_B T)$, $j = \{L, R\}$

$\Theta$ $\tanh^{-1}(\Delta/\varepsilon)$

$g$ Lande g-factor

$\phi$ Magnetization angle in the **yz**-plane for S/N/S Josephson junctions with spin-active interfaces

$\varphi$ Alignment angle of the SO-field in the **yz**-plane

# Color charts

The color charts shown below are standard MATLAB colormaps. The figures presenting the results throughout this thesis are color coded depending on which superconducting hybrids structures are being considered. The color coding will persist as follows:

Density of states in superconducting hybrids

Thermoelectric effects in Zeeman-split superconducting bilayers

Thermoelectric effects in superconductor/ferromagnetic domain wall/superconductor Josephson junctions

Thermoelectric effects in superconductor/spin-orbit coupled semiconductor/superconductor Josephson junctions

Thermoelectric effects in Zeeman-split superconductor/normal metal/superconductor Josephson junction hybrids

Thermoelectric effects in superconductor/ normal metal/ superconductor Josephson junctions with spin-active interfaces

Thermoelectric effects in superconductor/ conical ferromagnet/ superconductor Josephson junctions

# Contents

# Chapter 1

# Introduction

## 1.1 Background

Since the first observation of superconductivity by Kamerlingh Onnes in 1911 [1], it has been the subject of extensive research. The possible application areas for materials with zero DC electrical resistivity seem endless, and have fascinated scientists and laymen alike for more than a century. The celebrated BCS theory [2] greatly simplified calculations and predictions, as it provided a comprehensive explanation for the underlying physics of conventional superconductors. Discoveries such as the Meissner effect, where magnetic flux lines are expelled from superconducting materials [3], and the proximity effect allowing for leakage of superconducting currents into adjacent materials [4], only contributed to enhancing the interest. When so-called high-temperature superconductivity was discovered in 1986 [5], the expected radical breakthrough seemed imminent. However, as the critical temperatures of the high-$T_C$ superconductors are still fairly low compared to room-temperature, they can not be found in all everyday applications as of yet. Even though superconductors are today used for several different purposes, such as magnetic resonance imaging (MRI) [6], floating trains [7], superconducting quantum interference devices (SQUIDs) [8] and are proposed for use as qubits in quantum computing [9], one may argue that there is still a way to go for the major application areas to be found. The highest critical superconducting temperature reported as of yet was found in $H_2S$ just last year [10], and reported at 203 K at high pressures. Even though this is most certainly a step in the right direction, room-temperature superconductivity will probably not be readily available anytime soon. Nonetheless, there are some application areas which seem so promising that they may call for even low-temperature superconductivity.

For years, the continued increase in computational power has been predicted by what has become known as Moore's law concerning reduction of transistor size [11]. As the silicon-based metal oxide semiconductor field effect transistors (MOSFETs) [12] ap-

proach the limit of what is possible to achieve, the field of spintronics has emerged to attempt to solve the problem. Charge currents traveling through semiconductor materials meet with resistance generating heat dissipation, causing a decrease in efficiency. Utilizing the electron spin degree of freedom instead of or in addition to the charge poses a possible solution, as it could minimize heat dissipation effects and increase computational power. This comprises the ultimate goal of the field of spintronics [13]. Logic devices based on the spin degree of freedom instead of the charge, such as spin field effect transistors [14][15], magnon wave transistors [16] and devices based on the spin transfer torque [17][18][19] have been proposed and show much promise. A major result of spintronics research in use today is the giant magnetoresistance (GMR) effect, which has seen great use in the reading and storing of information [20]. In order to further brighten the prospects of spintronics as the gateway to increasing computational power, superconductors have been proposed as a key element in several devices [21]. Major reasons include spin lifetimes being long in superconductors due to a significant increase in spin flip relaxation time compared to the normal state [22][23], the size of the magnetoresistance induced by internal exchange fields in superconductors can approach infinity [24], and spin-transfer torques in superconductor/ferromagnet structures can become very large [25]. Superconducting hybrids have also been suggested for use as bipolar spin filters [26].

The superconducting proximity effect may present an elegant solution for generating and exploiting spin-polarized supercurrents. The superconducting entities known as Cooper pairs [27] can exit a superconductor and enter an adjacent material if they are grown in good contact. If the sizes of the superconductor and adjacent material are similar, and there is large interface transparency, this can be considered as a depletion of Cooper pairs from the superconducting side and is accompanied by a reduction in superconducting critical temperature, the temperature below which a material may become superconducting. This is known as the inverse proximity effect. When the superconductors are large compared to the adjacent material and interface transparencies are sufficiently low, this effect can be disregarded. The inverse proximity effect will therefore be neglected throughout this thesis. If a superconductor is coupled to some magnetic material, the field emanating from this material may alter the spin-polarization of the Cooper pairs through a process known as spin-mixing. When considering conventional BCS superconductors, as will be done herein, the Cooper pairs exiting a superconductor will be spin neutral. Such entities are known as spin-singlet Cooper pairs and are not spin-polarized. If they are made to interact with a magnetic material upon leaving the superconductor they may undergo a phase shift and become triplet Cooper pairs [28][29]. Following this process the Cooper pairs will still not be uniquely spin-polarized along a specific axis. If they enter a ferromagnetic material they will be readily ripped apart and destroyed by the magnetic exchange field. In order for Cooper pairs to survive over large length scales in ferromagnets they must reside in the so-called long range triplet state. In long-range triplet Cooper pairs, both electrons reside in the same spin state, which must be aligned with the magnetization. Such spin-polarized supercur-

rents have been seen to survive over relatively long distances in half metals, where all spins are aligned along the same axis [30][31][32]. In order to obtain such spin-polarized supercurrents one can utilize spin-active barrier elements at the interface between superconductors and other materials [33][34], couple superconductors to inhomogeneous ferromagnets with spatially varying magnetization such as conical ferromagnets [35] or ferromagnet/half metal bilayers [36], or grow superconducting materials adjacently to materials containing spin-orbit coupling [37][38][39][40]. Generating spin-polarized currents from spin-orbit coupled materials is a feat which also falls under the scope of the field known as spin orbitronics [41].

In addition to being hosts to the tantalizing possibility that is spin-polarized supercurrents, superconducting hybrids containing spin-active interfaces, magnetic inhomogeneities and spin orbit coupling may exhibit sizable electron-hole asymmetries. This effect is key to generating what is known as thermoelectric effects, where temperature gradients can result in electric currents and vice versa. Thermoelectric materials currently undergo extensive research as their ability to generate usable electric currents from waste heat is a desirable property in order to obtain more efficient energy usage [42]. As semiconductors contain the desired asymmetry and are readily available they probably constitute the main focus of thermoelectric research [43]. Moreover, superconductors were up to recently believed to be poor hosts for thermoelectric effects [44]. However, within the field of spin caloritronics [45], it has now been shown that superconductors offer vast possibilities. Spin caloritronics focuses on the interplay between currents of spin and heat. Superconductors are known to enhance central spintronics effect as well as enable spin-polarized supercurrents. When the proximity effect between superconducting and magnetically active materials is exploited to break the perfect particle-hole symmetry of superconducting materials, giant thermoelectric effects may arise. This has been shown for the case of a ferromagnet coupled to a superconductor via a tunneling interface, both theoretically [46][47] and recently also experimentally [48]. Here, the desired asymmetry was induces by applying an external Zeeman-field. Thermoelectric figures of merit $ZT$ and Seebeck coefficients $S$ of sizes comparable to, and even exceeding, the best bulk semiconducting thermoelectric materials at room temperatures proved attainable. Moreover, the generation of pure spin currents as a result of an applied temperature gradient was predicted. Large superconductivity-mediated thermoelectric effects have also been found in more complex Zeeman-split hybrids [49], in superconductors doped with magnetic impurities [50], diffusive superconducting bilayers with magnetic interfaces [51], and in three-terminal superconductor-ferromagnet devices [52]. As a particle-hole asymmetry is key to obtaining these thermoelectric effects, merging superconducting spintronics with spin caloritronics and spin orbitronics could result in giant thermoelectric effects arising even at low applied magnetic field strengths.

Room temperature superconductors are not experimentally feasible as of yet. Consequently, application areas for the giant thermoelectric effects observed in spin-split superconducting hybrids currently need to allow for cryogenic temperatures. An appli-

cation area for such structures is as building blocks in phase-coherent thermal circuits [53]. Thermal nanovalves [54] and thermal transistors [55] based on different configurations of superconductors and normal metals exposed to magnetic fields have also been proposed. Thermoelectric superconducting hybrids could also be used as microcoolers for cooling to cryogenic temperatures on a chip [56], and for electron refrigeration [57]. A different major application area for the kind of device proposed in these articles is for thermal sensing and ultra-sensitive radiation detection [58].

A common denominator for all the superconducting hybrids which have so far been shown to exhibit large thermoelectric effects is their requirement for large externally applied magnetic fields of size order a of approximately 1 T. When considering potential practical application areas, this could pose a challenge.  Consequently, it would be desirable to obtain comparable thermoelectric effects without the requirement of strong magnetic fields. This, along with maximizing the thermoelectric effects in Zeeman-split superconducting hybrids, will be the main focus area of this thesis.

## 1.2    Objective and thesis organization

The goal of this thesis is the understanding and quantification of the giant thermoelectric effects arising through tunneling in superconducting hybrids.  We investigate the electronic properties necessary to achieving the particle-hole asymmetry allowing for thermoelectric phenomena to arise, and attempt to find the configurations maximizing said effects. We study the pure spin currents arising in spin-split superconducting hybrids upon applying temperature gradients, and study the thermoelectric figure of merit and Seebeck coefficient in order to compare our results to existing thermoelectric materials. As thermoelectric effects have already been discovered and offered much consideration in the case of Zeeman-split superconducting hybrids, we have chosen two major new routes which as of yet remain unexplored.  The first is the application of spin-dependent biases and the effect this has on thermoelectric effects. We study which thermoelectric currents can arise upon allowing spin-up and spin-down particles to have different temperatures and chemical potentials, and quantify said effects using numerical methods. We apply this framework, which is an extension of an already existing framework, to different material configurations than the ones that have already been studied. Secondly, we want to consider thermoelectric effects arising in materials with more exotic spin configurations than a homogeneous ferromagnet polarized along one direction, and derive a new mathematical framework based on quasiclassical theory and matrix currents for this purpose.  This is then applied to experimentally achievable superconducting hybrid structures. A major theme throughout all these considerations and calculations has been replicating the giant thermoelectric effects found in Zeeman-split superconducting hybrid structures using materials which do not require large applied magnetic fields.  Application areas could be much easier to identify if external fields could be omitted. Therefore, superconducting material systems in which only very low

or even no magnetic fields need to be applied are studied, and subsequently compared to the Zeeman-split systems. This is the primary goal of this work.

The structure of the thesis reflects the steps taken to achieve these goals. First we consider the fundamental theory crucial for understanding the physics and mathematics used in achieving the results. This will very briefly cover BCS superconductors, spin-orbit coupling and ferromagnets, along with providing a brief introduction to quasiclassical theory and the Keldysh formalism. Next, superconducting tunneling and thermoelectric currents will be described, followed by a motivation for the assumption of possible spin-dependent bias application. When the fundamental concepts have been covered, we will move on to deriving a complete framework for thermoelectric effects in superconducting hybrids with homogeneous magnetization. This framework will include the possibility of spin-dependent applied voltage and temperature biases, and the derivations will culminate in a $4 \times 4$ Onsager response matrix. The following chapter will seek to apply this framework to spin-split hybrid structures such as Zeeman-split superconducting bilayers and trilayers, superconductor/ferromagnet/superconductor (S/F/S) Josephson junctions with ferromagnetic domain walls and superconductor/ normal metal /superconductor (S/N/S) Josephson junctions with spin-active interfaces polarized homogeneously along the same axis. The focus point of this consideration will be upon maximizing the thermoelectric figure of merit $ZT$ and Seebeck coefficient $S$, along with maximizing the pure spin currents arising upon the application of a temperature gradient even in the absence of a polarized tunneling barrier. This is achieved through applying quasiclassical theory to the more complex structures to obtain values for the density of energy states, which is numerically integrated to obtain values for the thermoelectric coefficients. As this framework is not applicable to materials with more complex spin configurations, we also derive a framework for thermoelectric effects based on matrix currents and quasiclassical theory. Spin-dependent bias application will not be included here, but the effects of voltage and temperature biases upon spin, heat and charge currents are studied extensively. This framework is then applied to superconducting hybrid S/X/S structures with more complex spin polarization configurations such as conical ferromagnetism, spin-active interfaces with polarizations which may rotate in a plane and spin-orbit coupling. Once again, thermoelectric coefficients and figures of merit are quantified using numerical methods. Along with considerations of all specific structural configurations, an experimental discussion rooted in state of the art fabrication methods is included herein. The material parameters chosen are based on realistic values found for existing elements. Finally, the results will be summarized and conclusions presented. The more extensive analytical derivations can be found in the Appendices along with a thorough description of the numerical procedure.

# Chapter 2

# Fundamental theory

## 2.1 Notation conventions

This thesis will to a large degree employ mathematical notation conventions regularly used in physics. Rationalized natural units or Heaviside-Lorentz units [59][60] are chosen in order to simplify the calculations and considerations, and the most commonly used physical constants are defined to equal one. Accordingly,

$$\hbar = c = k_B = 4\pi G = \epsilon_0 = \mu_0 = 1, \tag{2.1}$$

where $\hbar$ is the Planck constant $h/2\pi$, $c$ is the speed of light in vacuum, $k_B$ is the Boltzmann constant, $4\pi G$ is the Newton gravitational constant, $\epsilon_0$ is the vacuum permittivity and $\mu_0$ is the vacuum permeability.

Vectors and matrices in three dimensions will throughout this thesis be written in a bold font. Hence, the Cartesian unit vectors are written as $\boldsymbol{x}$, $\boldsymbol{y}$ and $\boldsymbol{z}$. Matrices in $2 \times 2$ spin space are written with an underline, such as $\underline{A}$. Consequently, the Pauli matrices in spin space are

$$\underline{\sigma}_x = \begin{pmatrix} 0 & 1 \\ 1 & 0 \end{pmatrix}, \quad \underline{\sigma}_y = \begin{pmatrix} 0 & -i \\ i & 0 \end{pmatrix}, \quad \underline{\sigma}_z = \begin{pmatrix} 1 & 0 \\ 0 & -1 \end{pmatrix}. \tag{2.2}$$

The three-dimensional Pauli matrix vector thus becomes

$$\boldsymbol{\sigma} = \underline{\sigma}_x \boldsymbol{x} + \underline{\sigma}_y \boldsymbol{y} + \underline{\sigma}_z \boldsymbol{z}. \tag{2.3}$$

Matrices in the $4 \times 4$ particle-hole or Nambu space are written with a hat, as $\hat{A}$ or $\hat{\boldsymbol{A}}$. The Pauli matrices in Nambu space are

$$\hat{\sigma}_\nu = \text{diag}(\underline{\sigma}_\nu, \underline{\sigma}_\nu^*), \tag{2.4}$$

where $\nu = \{x, y, z\}$. Finally, we will need to consider these matrices in $8 \times 8$ Keldysh space, where matrices are specified using a check, as $\check{A}$ and $\check{\boldsymbol{A}}$. When the Pauli matrices need to be used in Keldysh space, they become $\check{\sigma}_\nu = \text{diag}(\hat{\sigma}_\nu, \hat{\sigma}_\nu)$. A last matrix worth noting is the $4 \times 4$ generalization of $\underline{\sigma}_z$,

$$\hat{\rho}_3 = \begin{pmatrix} 1 & 0 & 0 & 0 \\ 0 & 1 & 0 & 0 \\ 0 & 0 & -1 & 0 \\ 0 & 0 & 0 & -1 \end{pmatrix}. \tag{2.5}$$

As is already evident, an asterisk* is used to denote complex conjugation. A dagger† represents the Hermitian conjugate, and a $\mathrm{T}^T$ the matrix transpose. The partial derivative is written as $\partial_x = \partial/\partial_x$, $[\boldsymbol{A}, \boldsymbol{B}] = \boldsymbol{A}\boldsymbol{B} - \boldsymbol{B}\boldsymbol{A}$ is the commutator and $\{\boldsymbol{A}, \boldsymbol{B}\} = \boldsymbol{A}\boldsymbol{B} + \boldsymbol{B}\boldsymbol{A}$ the anticommutator.

## 2.2 Superconductivity

The celebrated BCS theory [2] explains superconductivity as a phonon-mediated attractive electron-electron interaction. The two electrons experiencing the mutual attraction reside in opposite spin states in conventional superconductors, and are known as a singlet Cooper pair [27]. The mean-field BCS Hamiltonian is [61] [62]

$$\mathcal{H} = \int \mathrm{d}^3\boldsymbol{r} \big[ \Delta^\dagger(\boldsymbol{r}, t)\psi_\downarrow(\boldsymbol{r}, t)\psi_\uparrow(\boldsymbol{r}, t) + \Delta(\boldsymbol{r}, t)\psi_\uparrow^\dagger(\boldsymbol{r}, t)\psi_\downarrow^\dagger(\boldsymbol{r}, t) \big], \tag{2.6}$$

with the mean field superconducting gap parameter defined as

$$\Delta(\boldsymbol{r}, t) = \lambda(\boldsymbol{r})\langle\psi_\downarrow(\boldsymbol{r}, t)\psi_\uparrow(\boldsymbol{r}, t)\rangle, \qquad \Delta^\dagger(\boldsymbol{r}, t) = \lambda(\boldsymbol{r})\langle\psi_\downarrow^\dagger(\boldsymbol{r}, t)\psi_\uparrow^\dagger(\boldsymbol{r}, t)\rangle. \tag{2.7}$$

$\lambda(\boldsymbol{r})$ encompasses the attractive interaction between electrons, and is modeled as a constant potential. The operator $\psi_\sigma^\dagger(\boldsymbol{r}, t)$ creates a quasiparticle with spin $\sigma$ at a given position and time, while $\psi_\sigma(\boldsymbol{r}, t)$ destroys such a particle, or conversely creates a quasihole. The complex gap parameter $\Delta = |\Delta|e^{i\theta}$ contains the size of the *superconducting energy gap* in $|\Delta|$, while $\theta$ describes the *superconducting phase*. The ratio $\frac{\Delta_0}{k_B T_c} = 1.76$ is used throughout this thesis, as it is correct for several low-$T_c$ BCS superconductors [63] [64, p. 89]. Unless the temperature is close to absolute zero, the superconducting gap $\Delta \neq \Delta_0$, which is the gap at zero temperature and magnetic field. A very good

approximation for the temperature dependence of the superconducting order parameter
is

$$\Delta = \Delta_0 \tanh\left(1.74\sqrt{\frac{T_{c,0}}{T} - 1}\right). \tag{2.8}$$
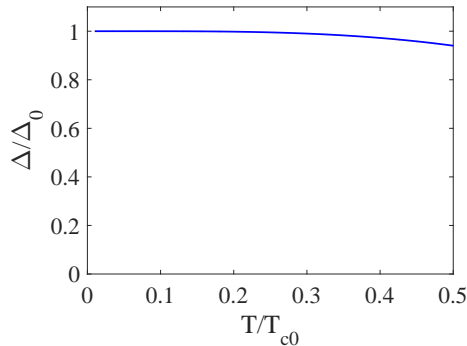


Figure 2.1: Temperature dependency of the superconducting gap $\Delta$.

The temperature evolution of the superconducting energy gap $\Delta$ according to this equa-
tion is represented graphically in Figure 2.1. The temperature dependency is quite weak,
and practically negligible up to around $T \approx 0.4 T_{c,0}$. When a superconductor is sub-
jected to a strong external magnetic field, the superconducting gap $\Delta$ depends on the
external field $h_S$ in addition to the temperature $T$ according to the self-consistency
relation [65]

$$1 - \frac{c}{2} \int_{-\omega_0}^{\omega_0} \mathrm{d}\varepsilon \frac{1 - f[E_\uparrow(\varepsilon)] - f[-E_\downarrow(\varepsilon)]}{\sqrt{\varepsilon^2 - \Delta^2}} = 0, \tag{2.9}$$

where $c$ is the weak-coupling constant and $E_\sigma = \sigma(\sqrt{\varepsilon^2 + \Delta^2} - h)$. The self-consistent
solution for the superconducting order parameter in Zeeman-split superconductors can
be found in Figure 2.2 for chosen values of $c$ and $\omega_0$.

A distinguishing feature of superconducting materials is discovered upon comparing
their densities of states to the normal-state situation. The density of states (DOS) for
a conventional superconductor (SC) is given by

$$\frac{D_{SC}(E)}{N_0(E)} = \left| \mathrm{Re}\left\{ \frac{E + i\Gamma}{\sqrt{(E + i\Gamma)^2 - \Delta^2}} \right\} \right|, \tag{2.10}$$

where the normal state density of states $N_0(E)$ is considered featureless and approxi-
mated as $N_0(E) \approx 1$ in the quasiclassical framework. This is done because the quasipar-
ticle energy is much smaller than the Fermi energy, and the normal state DOS therefore
hardly changes at all. Figure 2.3 shows the superconducting DOS at $T = 0$ K, with
$\Gamma = 0$ and $\Delta = \Delta_0 = 1$ meV. $\Gamma$ represents the Dynes parameter modeling inelastic
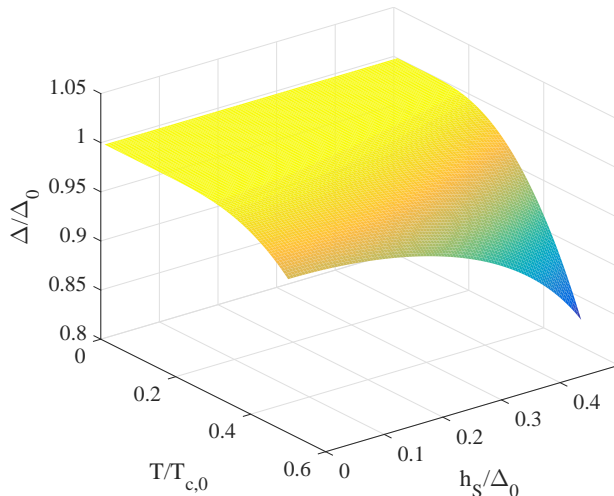
Figure 2.2: Self-consistent solution for $\Delta$ in a Zeeman-split superconductor. The weak-coupling constant is $c = 0.2$ and $\omega_0 = 0.5\Delta_0 e^{1/c}$.

scattering [66]. The Dynes model is here used to include the effect of subgap states on quasiparticle tunneling. The superconducting density of states exhibits several features separating the superconducting state from the normal state worth noticing. There is a gap in the DOS for $|E| < \Delta$, along with asymptotic behavior at the gap edges. As the energies become larger and $E \gg \Delta$, the superconducting DOS approaches the featureless normal-state DOS. When a superconductor is subjected to a strong external magnetic field, the BCS density of states is split into a spin-up and a spin-down part separated in energy [67], and

$$D^{\sigma}(E) = \left| \text{Re}\left\{ \frac{E + \sigma h_S + i\Gamma}{\sqrt{(E + \sigma h_S + i\Gamma)^2 - \Delta^2}} \right\} \right| \tag{2.11}$$

where $h_S$ denotes the applied exchange field. Figure 2.3 shows the density of states in a conventional BCS superconductor and the effect of exchange-splitting on the superconducting DOS, which also has been observed experimentally [68], is shown in Figures 2.4b and 2.4a.

The conventional BCS superconducting density of states exhibits a characteristic energy gap about zero energy up to the gap edges $E = \pm\Delta$. This gap reflects the properties of spin neutral so-called singlet superconductivity. When a superconductor is subjected to a spin-splitting Zeeman-field there is a great impact on the superconducting density of states as seen in Figure 2.4. Figure 2.4a shows the symmetric total density of states in a Zeeman-split superconductor $D_{ZS}^0(E) = 0.5(D^{\uparrow} + D^{\downarrow})$ while Figure 2.4b shows the spin-polarized $D_{ZS}^{\uparrow}(E)$ in red and $D_{ZS}^{\downarrow}(E)$ in blue. The difference in the Zeeman-split spin-dependent density of states $D_{ZS}^z(E) = D^{\uparrow} - D^{\downarrow}$ becomes antisymmetric about the
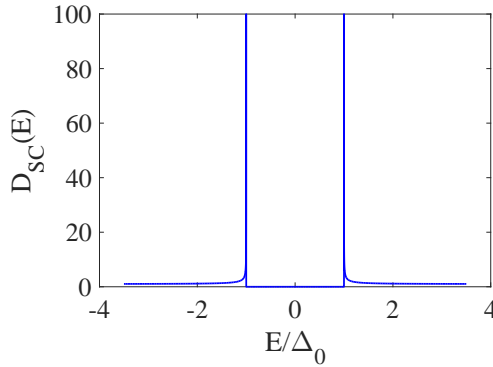
Figure 2.3: Density of energy states in a conventional BCS superconductor. $\Delta_0 = 1$ meV and inelastic scattering is neglected.
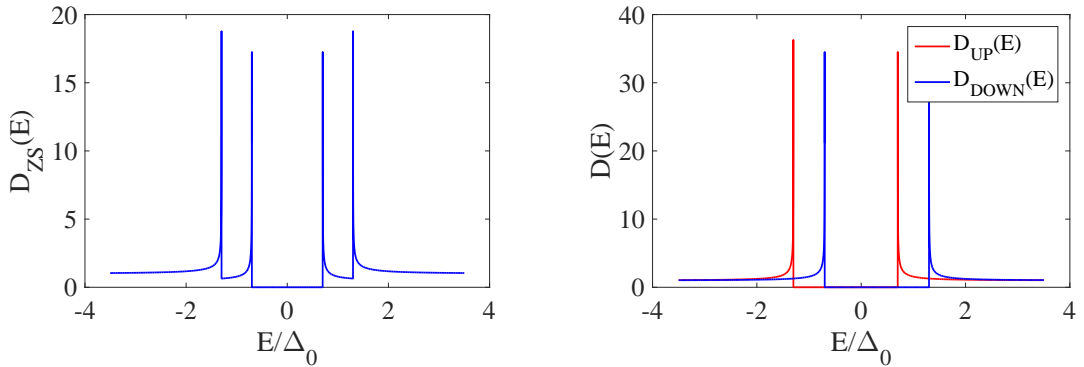


(a) Total density of states in a Zeeman-split superconductor.



(b) Spin-split density of states in a Zeeman-split superconductor.

Figure 2.4: Total density of states in a Zeeman-split BCS superconductor and spin-dependent DOS in a Zeeman-split supercodnuctor, respectively. $\Delta_0 = 1$ meV and $h_S = 0.3\Delta_0$. Inelastic scattering is neglected.

quasiparticle energy $E = 0$. The energy gap no longer occurs symmetrically about $E = 0$ and the peaks are no longer situated at the gap edges $E = \pm\Delta_0$, but are instead shifted with the exchange energy $h_S$. In the total Zeeman-split density of states in Figure 2.4a extra peaks arise, adding additional features to the superconducting density of states. In certain structures a zero-energy peak can arise, indicating the presence of triplet Cooper pairs and accordingly the possibility of spin-polarized supercurrents.

## 2.3    Ferromagnetism

Ferromagnetic materials can hold a permanent magnetic moment, known as a saturation moment, even in the absence of a magnetic field [69]. Such materials are normally organized in domains in order to reduce the energy cost of establishing and maintaining a net magnetic field [70]. Ferromagnetic spin ordering is favorable only as a result of the Pauli principle working in conjunction with the Coulomb repulsion. The Pauli principle demands that fermions occupy different quantum mechanical states, while Coulomb repulsion prevents electrons from occupying the same place in real space. Consequently, in some cases, electrons being of the same spin state while occupying different molecular orbitals is the energetically favorable electronic configuration [71]. Within a mean-field approximation ferromagnetic order can be described as

$$H = -\boldsymbol{h} \cdot \boldsymbol{\sigma}, \tag{2.12}$$

where the exchange field $\boldsymbol{h}$ encompasses the magnetic properties of the material and $\boldsymbol{\sigma}$ is the vector of Pauli matrices. Applying the second quantization formalism, the result is [72]

$$\mathcal{H} = -\int \mathrm{d}^3\boldsymbol{r} \sum_{\sigma\sigma'} \psi_\sigma^\dagger(\boldsymbol{r},t)[\boldsymbol{h}(\boldsymbol{r},t) \cdot \boldsymbol{\sigma}]_{\sigma\sigma'}\psi_{\sigma'}(\boldsymbol{r},t). \tag{2.13}$$

## 2.4    Spin-orbit coupling

When an electron moves in an electric field, it experiences an effective magnetic field which gives rise to a momentum-induced Zeeman-energy known as spin-orbit (SO) coupling, which is a relativistic effect [73]. The Hamiltonian for Rashba spin-orbit coupling is [74]

$$H_R = -\frac{\hbar}{4m_o^2c^2}\boldsymbol{\sigma} \cdot \boldsymbol{p} \times (\nabla V_0), \tag{2.14}$$

which in our consideration becomes $H_R = -\frac{\beta}{m}(\boldsymbol{\sigma} \times \boldsymbol{k}) \cdot \hat{z}$, where $\beta$ is the Rashba coefficient. This is commonly denoted $\alpha$, but as $\alpha$ is used for the thermoelectric coefficient we will employ $\beta$ instead. We will use the linearized single-particle Hamiltonian [38][39]

$$H_R = -\frac{\boldsymbol{p} \cdot \boldsymbol{A}}{m}, \tag{2.15}$$

where $\boldsymbol{A}$ is the spin-orbit field. This field is a vector in real space, as $\boldsymbol{A} = \underline{A}_x\boldsymbol{x} + \underline{A}_y\boldsymbol{y} + \underline{A}_z\boldsymbol{z}$, while $\underline{A}_\nu$ are $2 \times 2$ matrices in spin space. The Rashba spin-orbit coupling Hamiltonian is included in the total Hamiltonian for the system to be considered as an effective background field by redefining the covariant derivative as [75] $\tilde{\nabla}(\cdot) = \nabla(\cdot) - i[\hat{\boldsymbol{A}}, \cdot]$, where $\hat{\boldsymbol{A}} = \mathrm{diag}(\boldsymbol{A}, -\boldsymbol{A}^*)$.

## 2.5    Proximity effect

The proximity effect is the induction of the characteristic properties of one material in an adjacent material, if the systems are grown together and in good contact [4]. When considering a normal metal in contact with a superconductor, the proximity effect manifests itself through the leakage of Cooper pairs into the normal metal. In the normal metal, this is noticed as the emergence of superconducting order, while on the other side of the interface there is a reduction in superconductivity. This is known as the inverse proximity effect, and can be neglected when the interface transparency is low and the superconductors are sufficiently large compared to the other material. This approximation will be made throughout this thesis. Moreover, proximity effects will be considered solely in superconductor/ unknown material/ superconductor (S/X/S) Josephson junctions, where X is non-superconducting.

A robust approach to detecting the proximity effect in a system is through considering how the density of states in each material is altered as a consequence of the contact. If we once again consider the case of a normal metal and a superconductor, the proximity effect can be measured experimentally through considering the tunneling charge current [64]

$$I = \frac{2\pi}{\hbar} \int \mathrm{d}E D_L^0(E - \mu_L) D_R^0(E) [f_L(E - \mu_L) - f_R(E)], \qquad (2.16)$$

which arises as a result of applying different temperatures and voltage biases to the left (L) and right (R) sides of an interface with low transparency, a so-called tunneling interface. $D_j^0(E)$ is the density of energy states, $f_j(E - \mu_j)$ is the Fermi-Dirac distribution function, and $\mu_j$ is the chemical potential. If the left-hand material is a bulk normal metal with a featureless density of states, measuring the tunneling current gives a direct impression of the density of states of the right-hand-side material [76] which can be a complex proximity-coupled structure. This procedure essentially is the opposite of what we aim to achieve throughout this thesis. By obtaining exact measures for the densities of states of different proximity-coupled systems we are able to consider the resulting tunneling currents into other materials, along with the thermoelectric effects arising as a consequence.

One of the most famous superconducting hybrid structures relying on the proximity effect is the S/X/S Josephson junction mentioned above [77][78]. Such structures consist of two superconductors separated by a different material. The central layer can be for instance an insulator, a normal metal or a ferromagnet. What is observed in this case is a supercurrent traversing the central layer. When assuming the central material is not merely a tunneling barrier, this supercurrent is seen to modify the density of states of this material [79][80][81]. This current, and also the density of states in the central material, is greatly affected by both the superconducting phase difference and the interface transparency [82].

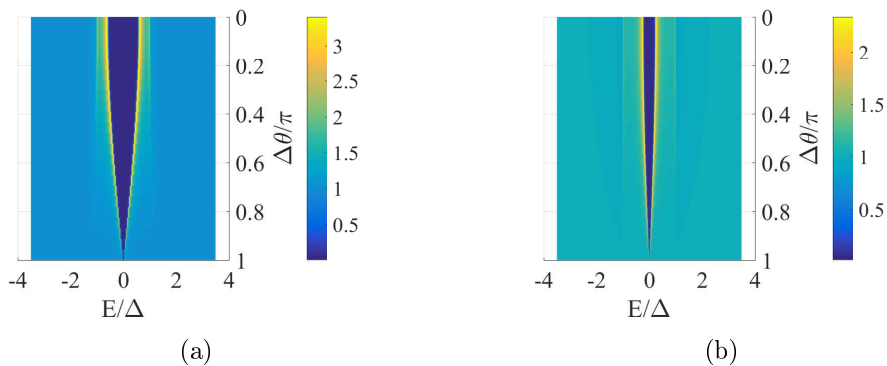(a)                                                      (b)

Figure 2.5: Density of states in the middle of the normal metal in a S/N/S Josephson junction for $L_N = 15$ nm and $L_N = 30$ nm, respectively. $\zeta = 3$ represents interface tunneling, $\xi = 30$ nm is the superconducting coherence length, $\Gamma/\Delta_0 = 0.005$ represents inelastic scattering and the temperature is $T/T_{c,0} = 0.2$.

Figure 2.5 shows the density of states at the center of the normal metal in a superconductor/ normal metal/ superconductor (S/N/S) Josephson junction. The interfaces have low transparencies, as determined by $\zeta = 3$. Figure 2.5a shows the DOS for a normal metal length of 15 nm, and figure 2.5b for $L_N = 30$ nm. A distinguishing feature here is the zero-energy gap in the normal-metal density of states, signifying the emergence of superconducting order throughout the non-superconducting material. The superconducting phase difference $\Delta\theta = \theta_L - \theta_R$ is the driving force for the transport of Cooper pairs. The superconducting gap persists for all energies and phase differences except for $\Delta\theta = \pi$. At this point, the Cooper pairs all have the same phase, and no net supercurrent traverses the system. For larger energies far from the gap edges, the DOS in the normal metal approaches the featureless normal-metal DOS. Moreover, when the superconducting phase difference $\Delta\theta = \pi$, the supercurrent passing through the normal metal is suppressed. The external tuning of the superconducting phase difference can be achieved experimentally by applying magnetic fields or passing currents through the system. Consequently, the Josephson current can be switched on and off by external means, in analogy to a field effect transistor (FET) [12].

When regular tunneling interfaces are situated between the normal metal and the superconductor, only spin-neutral singlet Cooper pairs with $S = 0$ and $\psi_{\text{singlet}} = \sqrt{\frac{1}{2}}\big(|\uparrow\downarrow\rangle - |\downarrow\uparrow\rangle\big)$ exist in the system when conventional BCS superconductors are considered. However, a process known as spin-mixing can occur at the interface between superconducting and magnetic materials. The Cooper pair wavefunction can oscillate between the singlet and the spinless triplet state, $\psi_{\text{triplet}} = \sqrt{\frac{1}{2}}\big(|\uparrow\downarrow\rangle + |\downarrow\uparrow\rangle\big)$, at the interface. These triplet Cooper pairs would, however, still be destroyed readily in a fully polarized ferromagnetic material such as a half metal. *Long range triplet Cooper pairs* $\psi_{\text{long}} = |\uparrow\uparrow\rangle$ and $\psi_{\text{long}} = |\downarrow\downarrow\rangle$ with $S_z = 1$ are generated through a process known

as *spin rotation*, which can occur when spin-splitting mechanisms such as inhomogeneous magnetic interfaces [33], spatially varying magnetic materials [83] and spin-orbit coupled materials [39] are employed.
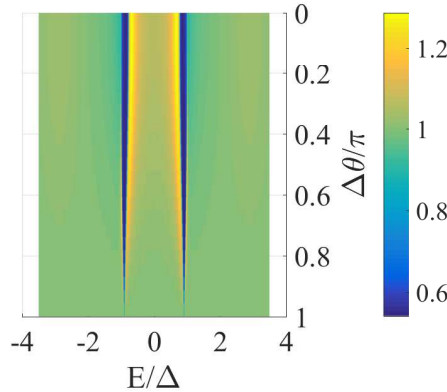


Figure 2.6: Density of states in an S/F/S Josephson junction, for $L_F = 15$ nm. $\zeta = 4$ represents interface tunneling, $\xi = 30$ nm is the superconducting coherence length, $\Gamma/\Delta_0 = 0.005$ represents inelastic scattering, $T/T_{c,0} = 0.2$ and $h/\Delta_0 = 3$. The ferromagnet polarization is aligned along the $z$-axis. Instead of a superconducting gap at energies $E < \Delta$, the DOS is now enhanced above its normal-state, a feature characteristic of odd-frequency triplet Cooper pairs.

Figure 2.6 shows the density of states in the middle of a superconductor/ ferromagnet/ superconductor (S/F/S) Josephson junction in comparison. There is no minigap about $E = 0$ but rather two gaps close to the gap edges.

Triplet superconductivity can be observed in the same manner as the singlet proximity effect, namely via the density of states within the material adjacent to a superconductor. Figure 2.7 shows the density of states at the middle of the normal metal in a Zeeman-split superconductor/normal metal/Zeeman-split superconductor (ZS/N/ZS) Josephson junction. Each figure displays the effect of a different value of the externally applied exchange field. For a certain value of the superconducting phase difference, the normal-metal density of states changes from having a zero-energy gap to instead containing a zero-energy peak. This peak signifies the switch from singlet to triplet superconductivity. A feature to be noticed concerns the fact that the stronger the applied magnetic field is, the smaller the superconducting phase difference needs to be for the singlet to triplet conversion to occur.

## 2.6  Quasiclassical theory

The Green function formalism is commonly employed when considering condensed matter physics phenomena. Green functions can be interpreted as propagators for the particle state, thus providing a measure of how much is left of the original particle state

(a)

(b)

(c)

(d)
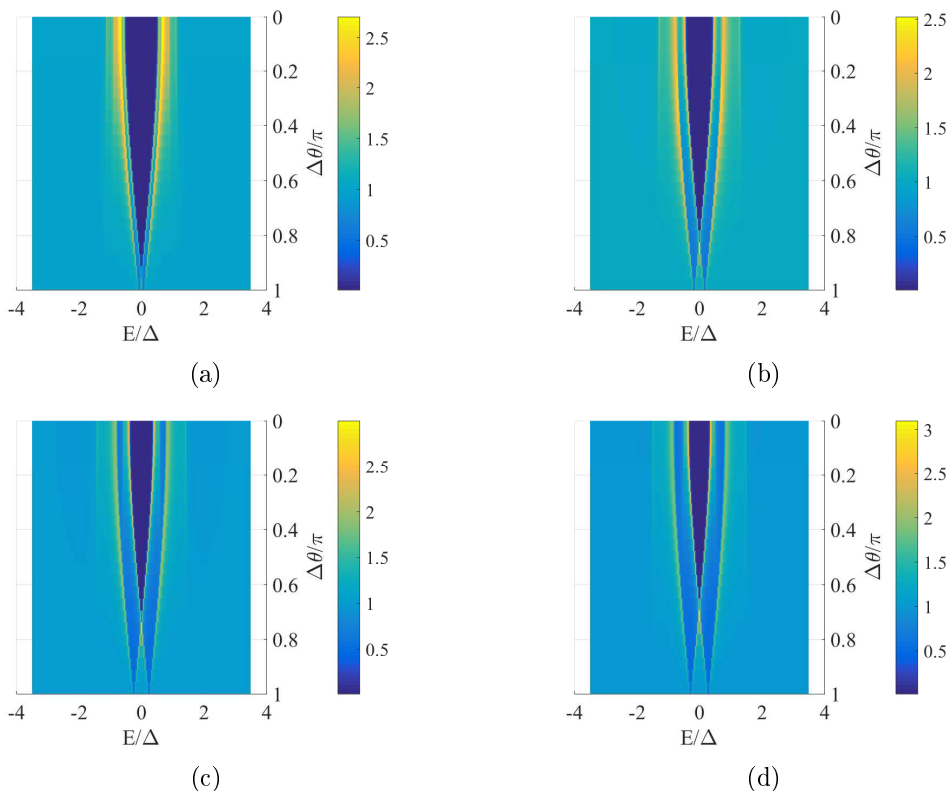
Figure 2.7: Density of states in a ZS/N/ZS Josephson junction, for $L_N = 15$ nm, $\zeta = 3$ represents interface tunneling, $\xi = 30$ nm is the superconducting coherence length, $\Gamma/\Delta_0 = 0.005$ represents inelastic scattering and $T/T_{c,0} = 0.2$. The spin-splitting exchange field is $h/\Delta_0 = 0.12$, $0.30$, $0.43$ and $0.50$, respectively.

[61][ch. 2]. This thesis is based on the Keldysh real-time Green function formalism, which he used to derive kinetic equations for electrons interacting with phonons [84][85]. Here, we only briefly outline the main steps of this theory and refer the reader to Refs. [86][87][88][89][90] for an in-depth review. The fermionic Green functions are

$$G^R_{\sigma\sigma'}(\boldsymbol{r}_1, t_1; \boldsymbol{r}_2, t_2) = -i\big\langle\big\{\psi_\sigma(\boldsymbol{r}_1, t_1), \psi^\dagger_{\sigma'}(\boldsymbol{r}_2, t_2)\big\}\big\rangle\Theta(t_1 - t_2) \tag{2.17}$$

$$G^A_{\sigma\sigma'}(\boldsymbol{r}_1, t_1; \boldsymbol{r}_2, t_2) = +i\big\langle\big\{\psi_\sigma(\boldsymbol{r}_1, t_1), \psi^\dagger_{\sigma'}(\boldsymbol{r}_2, t_2)\big\}\big\rangle\Theta(t_1 - t_2) \tag{2.18}$$

$$G^R_{\sigma\sigma'}(\boldsymbol{r}_1, t_1; \boldsymbol{r}_2, t_2) = -i\big\langle\big[\psi_\sigma(\boldsymbol{r}_1, t_1), \psi^\dagger_{\sigma'}(\boldsymbol{r}_2, t_2)\big]\big\rangle, \tag{2.19}$$

whereas their anomalous counterparts are

$$F^R_{\sigma\sigma'}(\boldsymbol{r}_1, t_1; \boldsymbol{r}_2, t_2) = -i\big\langle \big\{\psi_\sigma(\boldsymbol{r}_1, t_1), \psi_{\sigma'}(\boldsymbol{r}_2, t_2)\big\}\big\rangle \Theta(t_1 - t_2) \qquad (2.20)$$

$$F^A_{\sigma\sigma'}(\boldsymbol{r}_1, t_1; \boldsymbol{r}_2, t_2) = +i\big\langle \big\{\psi_\sigma(\boldsymbol{r}_1, t_1), \psi_{\sigma'}(\boldsymbol{r}_2, t_2)\big\}\big\rangle \Theta(t_1 - t_2) \qquad (2.21)$$

$$F^R_{\sigma\sigma'}(\boldsymbol{r}_1, t_1; \boldsymbol{r}_2, t_2) = -i\big\langle \big[\psi_\sigma(\boldsymbol{r}_1, t_1), \psi_{\sigma'}(\boldsymbol{r}_2, t_2)\big]\big\rangle. \qquad (2.22)$$

The retarded (R) and advanced (A) Green functions describe quantum transport of electrons and holes, respectively, as they are composed of sums of products of creation and annihilation operators. The dynamics of the Cooper pairs are thus encompassed by the anomalous Green functions $F^R$, $F^A$ and $F^K$. The retarded and advanced Green functions in both cases only contain equilibrium information, while the Keldysh components describe non-equilibrium transport. The propagators can now be combined to form $2 \times 2$ matrices in spin space,

$$\underline{\boldsymbol{G}}^R = \begin{pmatrix} G^R_{\uparrow\uparrow} & G^R_{\uparrow\downarrow} \\ G^R_{\downarrow\uparrow} & G^R_{\downarrow\downarrow} \end{pmatrix} \quad \underline{\boldsymbol{G}}^A = \begin{pmatrix} G^A_{\uparrow\uparrow} & G^A_{\uparrow\downarrow} \\ G^A_{\downarrow\uparrow} & G^A_{\downarrow\downarrow} \end{pmatrix} \quad \underline{\boldsymbol{G}}^K = \begin{pmatrix} G^K_{\uparrow\uparrow} & G^K_{\uparrow\downarrow} \\ G^K_{\downarrow\uparrow} & G^K_{\downarrow\downarrow} \end{pmatrix} \qquad (2.23)$$

$$\underline{\boldsymbol{F}}^R = \begin{pmatrix} F^R_{\uparrow\uparrow} & F^R_{\uparrow\downarrow} \\ F^R_{\downarrow\uparrow} & F^R_{\downarrow\downarrow} \end{pmatrix} \quad \underline{\boldsymbol{F}}^A = \begin{pmatrix} F^A_{\uparrow\uparrow} & F^A_{\uparrow\downarrow} \\ F^A_{\downarrow\uparrow} & F^A_{\downarrow\downarrow} \end{pmatrix} \quad \underline{\boldsymbol{F}}^K = \begin{pmatrix} F^K_{\uparrow\uparrow} & F^K_{\uparrow\downarrow} \\ F^K_{\downarrow\uparrow} & F^K_{\downarrow\downarrow} \end{pmatrix}, \qquad (2.24)$$

$4 \times 4$ matrices in particle-hole or Nambu space,

$$\widehat{\boldsymbol{G}}^R = \begin{pmatrix} \underline{\boldsymbol{G}}^R & \underline{\boldsymbol{F}}^R \\ \underline{\widetilde{\boldsymbol{F}}}^R & \underline{\widetilde{\boldsymbol{G}}}^R \end{pmatrix} \quad \widehat{\boldsymbol{G}}^A = \begin{pmatrix} \underline{\boldsymbol{G}}^A & \underline{\boldsymbol{F}}^A \\ \underline{\widetilde{\boldsymbol{F}}}^A & \underline{\widetilde{\boldsymbol{G}}}^A \end{pmatrix} \quad \widehat{\boldsymbol{G}}^K = \begin{pmatrix} \underline{\boldsymbol{G}}^K & \underline{\boldsymbol{F}}^K \\ -\underline{\widetilde{\boldsymbol{F}}}^K & -\underline{\widetilde{\boldsymbol{G}}}^K \end{pmatrix}, \qquad (2.25)$$

and finally the $8 \times 8$ matrix in Keldysh space

$$\widecheck{\boldsymbol{G}} = \begin{pmatrix} \widehat{\boldsymbol{G}}^R & \widehat{\boldsymbol{G}}^K \\ \boldsymbol{0} & \widehat{\boldsymbol{G}}^A \end{pmatrix}. \qquad (2.26)$$

The tilde-conjugation is interpreted as $\widetilde{G} = G^*(\boldsymbol{r}, -\epsilon)$ when $G$ depends on both the position and energy coordinate. The diagonal elements of $\underline{\boldsymbol{G}}^R$, $\underline{\boldsymbol{G}}^A$ and $\underline{\boldsymbol{G}}^K$ contain information regarding particle and hole dynamics while the anti-diagonal elements describe spin-flip scattering processes. The density of states of a system is consequently contained in these two diagonal elements of $\underline{\boldsymbol{G}}^R$. The motion of spin-singlet Cooper pairs is encompassed by the anti-diagonal elements of $\underline{\boldsymbol{F}}^R$, $\underline{\boldsymbol{F}}^A$ and $\underline{\boldsymbol{F}}^K$, with the long-range triplets being described by the diagonal elements of the same matrices.

Switching to the mixed coordinate or Wigner representation simplifies finding exact solutions for the Green functions. Finding such solutions has been a main objective of the work, as the Green functions contain information regarding the density of states.

As we need the DOS to quantify the thermoelectric effects, obtaining good approximations for the Green function presents itself as the first major obstacle to be overcome. The switch to the Wigner representation involves switching from specific coordinates $(\boldsymbol{r}_{1,2}, t_{1,2})$ to center of mass coordinates $(\boldsymbol{r}, t)$ and difference coordinates $(\boldsymbol{R}, T)$. Next, the dependence of the Green functions on the relative coordinate $|\boldsymbol{r}_1 - \boldsymbol{r}_2|$ is integrated out. The Green functions fluctuate with respect to this coordinate, but the rate of variation is on the scale of the Fermi wavelength $\lambda_F$, which is much smaller than characteristic length scales in superconducting systems. Moreover, the approximation relies on assuming that only particles near the Fermi surface contribute to transport in addition to a nearly non-directional or isotropic Green functions matrix. Applying the approximation and performing a Fourier transform results in the quasiclassical Green functions becoming

$$\check{\boldsymbol{g}}(\boldsymbol{r}, \boldsymbol{p}_F, \varepsilon, t) = \frac{i}{\pi} \int \mathrm{d}\xi \check{\boldsymbol{G}}(\boldsymbol{r}, \boldsymbol{p}, \varepsilon, t), \tag{2.27}$$

where $\xi = \frac{\boldsymbol{p}^2}{2m} - \mu$ is the kinetic energy with respect to the chemical potential, or Fermi level, $\mu$. Throughout this thesis, we also make the approximation of equilibrium or steady-state transport. Within the quasiclassical regime, we obtain the normalization condition $\check{\boldsymbol{g}}\check{\boldsymbol{g}} = \check{\boldsymbol{1}}$ and the Green function matrices in Nambu space become

$$\hat{\boldsymbol{g}}^R = \begin{pmatrix} \underline{\boldsymbol{g}}^R & \underline{\boldsymbol{f}}^R \\ -\underline{\tilde{\boldsymbol{f}}}^R & -\underline{\tilde{\boldsymbol{g}}}^R \end{pmatrix} \quad \hat{\boldsymbol{g}}^A = \begin{pmatrix} \underline{\boldsymbol{g}}^A & \underline{\boldsymbol{f}}^A \\ -\underline{\tilde{\boldsymbol{f}}}^A & -\underline{\tilde{\boldsymbol{g}}}^A \end{pmatrix} \quad \hat{\boldsymbol{g}}^K = \begin{pmatrix} \underline{\boldsymbol{g}}^K & \underline{\boldsymbol{f}}^K \\ \underline{\tilde{\boldsymbol{f}}}^K & \underline{\tilde{\boldsymbol{g}}}^K \end{pmatrix}. \tag{2.28}$$

The advanced quasiclassical Green function matrix depends on $\hat{\boldsymbol{g}}^R$ according to

$$\hat{\boldsymbol{g}}^A = -\hat{\rho}_3 \hat{\boldsymbol{g}}^{R\dagger} \hat{\rho}_3. \tag{2.29}$$

Non-equilibrium properties are, as mentioned, encompassed by the Keldysh component

$$\hat{\boldsymbol{g}}^K = \hat{\boldsymbol{g}}^R \hat{\boldsymbol{h}} - \hat{\boldsymbol{h}} \hat{\boldsymbol{g}}^A \tag{2.30}$$

with $\hat{\boldsymbol{h}}$ being the non-equilibrium matrix. When equilibrium conditions can be assumed, this becomes

$$\hat{\boldsymbol{g}}^K = \tanh\left(\frac{\beta\varepsilon}{2}\right)(\hat{\boldsymbol{g}}^R - \hat{\boldsymbol{g}}^A), \tag{2.31}$$

and all information regarding system dynamics resides within $\hat{\boldsymbol{g}}^R$, which also obeys the normalization condition $\hat{\boldsymbol{g}}^R \hat{\boldsymbol{g}}^R = \hat{1}$. The density of states of a system is defined as [91]

$$D(\varepsilon, \boldsymbol{r}) = \frac{1}{2} \mathrm{Re}\{\mathrm{Tr}\{\underline{\boldsymbol{g}}^R(\varepsilon, \boldsymbol{r})\}\}. \tag{2.32}$$

The next step thus concerns developing a matrix equation describing the system dynamics, and upon solving this equation we are able to quantify the Green function matrices with the goal of determining the density of states. This is achieved through applying the Heisenberg equation to the field operators,

$$i\partial_t\psi_\sigma(\boldsymbol{r},t) = [\psi_\sigma(\boldsymbol{r},t),\mathcal{H}] \tag{2.33}$$

$$i\partial_t\psi_\sigma^\dagger(\boldsymbol{r},t) = [\psi_\sigma^\dagger(\boldsymbol{r},t),\mathcal{H}], \tag{2.34}$$

where $\mathcal{H}$ is the total system Hamiltonian, in this case including superconductivity, ferromagnetism and spin-orbit coupling. Applying the anticommutation relation of fermionic field operators [61], differentiating the retarded Green function with respect to time and employing the quasiclassical approximation results in the *Usadel equation*

$$D\tilde{\nabla}(\check{\boldsymbol{g}}_s\tilde{\nabla}\check{\boldsymbol{g}}_s) = -i[\varepsilon\check{\rho}_3 + \check{\Delta} + \boldsymbol{h}\cdot\check{\sigma},\check{\boldsymbol{g}}_s]. \tag{2.35}$$

A complete derivation can be found in for instance [92] or [72]. $D = \frac{1}{3}\tau_0 v_F^2$ is the diffusion coefficient, $\check{\Delta}$ is the superconducting gap matrix, $\boldsymbol{h}$ describes the exchange field and $\tilde{\nabla}$ contains the spin-orbit field. As the inverse proximity effect is not considered in this thesis, the superconducting gap matrix will be neglected throughout. The Usadel equation is valid in the dirty or diffusive limit where impurity-scattering dominates and particles behave as if they are following a random walk. The subscript $\check{\boldsymbol{g}}_s$ will be neglected throughout the rest of this thesis, as all Green function matrices are assumed to be isotropic. One-dimensional transport in the $\boldsymbol{x}$-direction will be assumed throughout the rest of this thesis. Moreover, we will be able to assume equilibrium conditions for all cases in which the Usadel equation needs to be solved throughout this thesis, and consequently only need to consider the retarded Green function matrix,

$$D\tilde{\nabla}(\hat{\boldsymbol{g}}^R\tilde{\nabla}\hat{\boldsymbol{g}}^R) = -i[\varepsilon\hat{\rho}_3 + \widehat{\Sigma},\hat{\boldsymbol{g}}^R], \tag{2.36}$$

where $\widehat{\Sigma}$ contains the self-energy terms describing all material-specific parameters. In order to solve this equation, boundary conditions must be employed. Three different sets of boundary conditions are used, depending on the application. For regular tunneling interfaces with low transparency we can employ the Kuprianov-Lukichev tunneling boundary conditions [93]

$$2\zeta_n\check{\boldsymbol{g}}_n\partial_x\check{\boldsymbol{g}}_n = [\check{\boldsymbol{g}}_L,\check{\boldsymbol{g}}_R], \tag{2.37}$$

$n = \{L,R\}$ referring to the left (L) and right (R) side of the interface. When the interface barrier is weakly spin polarized, we instead use Cottet's boundary conditions [94]

$$2d\zeta_L \check{\boldsymbol{g}}_L \partial_x \check{\boldsymbol{g}}_L = [\check{\boldsymbol{g}}_L, \check{\boldsymbol{g}}_R] + G_{MR}\Big[\check{\boldsymbol{g}}_L, \{\widehat{\boldsymbol{M}}, \check{\boldsymbol{g}}_R\}\Big] + iG_\phi^L[\check{\boldsymbol{g}}_L, \widehat{\boldsymbol{M}}] \tag{2.38}$$

$$2d\zeta_R \check{\boldsymbol{g}}_R \partial_x \check{\boldsymbol{g}}_R = [\check{\boldsymbol{g}}_L, \check{\boldsymbol{g}}_R] - G_{MR}\Big[\check{\boldsymbol{g}}_R, \{\widehat{\boldsymbol{M}}, \check{\boldsymbol{g}}_L\}\Big] - iG_\phi^R[\check{\boldsymbol{g}}_R, \widehat{\boldsymbol{M}}]. \tag{2.39}$$

The matrix $\widehat{\boldsymbol{M}}$ contains the orientation and strength of the interface magnetization, and $G_\phi$ describes spin-dependent interface scattering. This parameter consequently is the key to spin mixing, as it determines the mechanism for how quasiparticles reflecting off magnetic interfaces acquire spin-dependent phase shifts. Thus, Cooper pairs may be converted from the singlet to the triplet state. The parameter $\zeta$ represents interface transparency, and is defined as $\zeta_n = R_B/R_n$, where $R_B$ is is the resistance of the interface and $R_n$ the bulk resistance of material $n$. For Cottet's boundary conditions to be valid, we require $G_{MR} \ll 1$, where $G_{MR}$ is directly proportional to the polarization. The most general boundary conditions currently available are valid for a tunneling interface and any polarization [95], and are

$$\check{\boldsymbol{g}}_R \partial_x \check{\boldsymbol{g}}_R = \frac{1}{4e^2 N_0 DA}[G_0 \check{\boldsymbol{g}}_L + G_{MR}\{\check{\boldsymbol{\kappa}}, \check{\boldsymbol{g}}_L\} + G_1 \check{\boldsymbol{\kappa}} \check{\boldsymbol{g}}_L \check{\boldsymbol{\kappa}} - iG_R^\phi \check{\boldsymbol{\kappa}}', \check{\boldsymbol{g}}_R] \tag{2.40}$$

$$\check{\boldsymbol{g}}_L \partial_x \check{\boldsymbol{g}}_L = -\frac{1}{4e^2 N_0 DA}[G_0 \check{\boldsymbol{g}}_R + G_{MR}\{\check{\boldsymbol{\kappa}}, \check{\boldsymbol{g}}_R\} + G_1 \check{\boldsymbol{\kappa}} \check{\boldsymbol{g}}_R \check{\boldsymbol{\kappa}} - iG_R^\phi \check{\boldsymbol{\kappa}}', \check{\boldsymbol{g}}_L]. \tag{2.41}$$

The boundary conditions are very similar to the ones defined in Equation 2.38, the only difference being the extra correction term including the prefactor $G_1$. The interface parameters are defined as

$$G_0 = G_q \sum_{nl} \tau_{nl}\big(1 + \sqrt{1 - P_{nl}^2}\big), \quad G_1 = G_q \sum_{nl} \tau_{nl}\big(1 - \sqrt{1 - P_{nl}^2}\big) \tag{2.42}$$

$$G_{MR} = G_q \sum_{nl} \tau_{nl} P_{nl}, \quad G_\phi = 2G_q \sum_n \theta_{nn}, \tag{2.43}$$

where $G_q = \frac{e^2}{h}$ is the conductance quantum. When a channel-diagonal scattering matrix is assumed, as will be done throughout this thesis, $n = l$, $\tau_{nl} = \tau$, $P_{nl} = P$ and $\check{\boldsymbol{\kappa}}' = \check{\boldsymbol{\kappa}}$. $\check{\boldsymbol{\kappa}}$ and $\widehat{\boldsymbol{A}}$ describe the magnetization of the interface, $P$ is the polarization and $\tau$ is the tunneling probability. When $\tau \ll 1$, it describes a highly non-transparent interface.

Upon initial consideration, the boundary conditions may seem unequal, but the boundary condition for generally polarized interfaces in Equation 2.40 reduces to the condition for weakly polarized interfaces defined in Eq. 2.38 in the limit where the polarization $P = 0$. In this limit, $G_{MR} = G_1 = 0$ while $G_0$ becomes independent of interface polarization. The interface parameters $\tau$ and $\zeta$ are both dimensionless, and the inverse of each other. The dimension of the left-hand-side of Eq. 2.40 is m$^{-1}$, and the same

should be the case for the right-hand-side for the two sets of boundary conditions to be equal. The prefactor to the right-hand-side of Eq. 2.40 is

$$\frac{G_q}{e^2 N_0 DA} = \frac{G_q}{\sigma A},$$
(2.44)

where $\sigma$ here denotes the conductivity per spin and $A$ the contact area. The unit of the conductivity $\sigma$ is $\frac{\text{A}^2\text{s}^3}{\text{m}^3\text{kg}}$, the unit of the conductance $G_q$ is $\frac{\text{A}^2\text{s}^3}{\text{m}^2\text{kg}}$, and the unit of the area is $\text{m}^2$. Consequently, the unit of the right-hand-side is also $\text{m}^{-1}$, and both sets of boundary conditions for polarized interfaces are dimensionless. The difference between the two sets of boundary conditions, when $P = 0$, can thereby be found within the definition of the interface parameter $\tau$ in relation to $\zeta$ .

All three sets of boundary conditions described here will be used throughout this thesis, depending on the application. When the Usadel equation is solved for non-spin active interfaces, the Kuprianov-Lukichev tunneling boundary conditions are used. When spin-active interfaces are assumed, we apply the boundary conditions for weak polarization with $G_{MR} \ll 1$. The most general boundary conditions, accepting tunneling interfaces but any polarization, will be used only upon consideration of matrix currents of the form

$$I = \frac{N_0 e DA}{4} \int_{-\infty}^{\infty} \mathrm{d}E\, \mathrm{Tr}\left\{ \hat{\rho}_3 [\check{\boldsymbol{g}}(\partial_x \check{\boldsymbol{g}})]^K \right\}$$
(2.45)

$$I_s^\nu = \frac{N_0 DA}{8} \int_{-\infty}^{\infty} \mathrm{d}E\, \mathrm{Tr}\left\{ \hat{\rho}_3 \hat{\tau}_\nu [\check{\boldsymbol{g}}(\partial_x \check{\boldsymbol{g}})]^K \right\}$$
(2.46)

$$\dot{Q} = \frac{N_0 DA}{4} \int_{-\infty}^{\infty} \mathrm{d}E (E - \mu)\, \mathrm{Tr}\left\{ [\check{\boldsymbol{g}}_L(\partial_x \check{\boldsymbol{g}}_L)]^K \right\},$$
(2.47)

where $I$ is the charge current in a material, $\dot{Q}$ is the heat current in a material and $I_s^\nu$ represents the spin current in each of the directions $\nu = \{x, y, z\}$. These currents can be calculated directly from the boundary conditions, without solving the Usadel equation [96][97]. In the cases where the Usadel equation does have to be solved, it would be beneficial to not have to consider a $4 \times 4$ matrix equation. By employing the Riccati parametrization [98]

$$\hat{\boldsymbol{g}}^R = \begin{pmatrix} \underline{N}(1 + \underleftarrow{\gamma \tilde{\gamma}}) & 2\underline{N}\gamma \\ -2\underline{\tilde{N}}\tilde{\gamma} & -\underline{\tilde{N}}(1 + \underline{\tilde{\gamma}\gamma}) \end{pmatrix}$$
(2.48)

where $\underline{N} = (1 - \underline{\gamma\tilde{\gamma}})^{-1}$ and $\underline{\tilde{N}} = (1 - \tilde{\gamma}\gamma)^{-1}$, the retarded Green function matrix can be expressed in terms of $2 \times 2$ matrices. Employing this formalism, the complete Riccati-parametrized Usadel equation, including ferromagnetism and spin-orbit coupling while excluding superconductivity, is [72][75][39]

$$D[\partial_x^2\gamma + 2\partial_x\gamma\tilde{N}\tilde{\gamma}\partial_x\gamma] = -2i\varepsilon\gamma - i\boldsymbol{h}(\boldsymbol{\sigma}\gamma - \gamma\boldsymbol{\sigma}^*)$$
$$+D[\boldsymbol{A}\boldsymbol{A}\gamma - \gamma\boldsymbol{A}^*\boldsymbol{A}^* + 2(\boldsymbol{A}\gamma + \gamma\boldsymbol{A}^*)\tilde{N}(\boldsymbol{A}^* + \tilde{\gamma}\boldsymbol{A}\gamma)] \qquad (2.49)$$
$$+2iD[\partial_x\gamma\tilde{N}(A_x^* + \tilde{\gamma}A_x\gamma) + (A_x + \gamma A_x^*\tilde{\gamma})N\partial_x\gamma],$$

where we have defined $\boldsymbol{A} = A_x\boldsymbol{x} + A_y\boldsymbol{y} + A_z\boldsymbol{z}$ to be the spin-orbit field vector and $\boldsymbol{h}$ contains the magnetization. We do not consider the inverse proximity effect here, as we assume bulk superconductors and tunneling S/X interfaces. If no exchange field is present, a spin-orbit field within the material X is unable to couple the singlet and triplet anomalous Green functions to lowest order in a diffusive structure. Consequently, the spin-orbit coupling cannot host a transformation from singlet to triplet superconductivity. The parametrization of the boundary conditions for tunneling interfaces including spin-orbit coupling results in [72]

$$\partial_x\gamma_1 = \frac{1}{L\zeta_1}(1 - \gamma_1\tilde{\gamma}_2)N_2(\gamma_2 - \gamma_1) + iA_x\gamma_1 + i\gamma_1 A_x^* \qquad (2.50)$$

$$\partial_x\gamma_2 = \frac{1}{L\zeta_2}(1 - \gamma_2\tilde{\gamma}_1)N_1(\gamma_2 - \gamma_1) + iA_x\gamma_2 + i\gamma_2 A_x^* \qquad (2.51)$$

for the left (1) and right (2) side of the interface, respectively, while the complete boundary conditions when considering weakly spin-polarized interfaces are [99]

$$4L\zeta_1\partial_x\gamma_1 = (1 - \gamma_1\tilde{\gamma}_2)N_2(\gamma_2 - \gamma_1) + 2iG_1^\phi[\gamma_1(\boldsymbol{m} \cdot \boldsymbol{\sigma}^*) - (\boldsymbol{m} \cdot \boldsymbol{\sigma})\gamma_1]$$
$$-4\cosh(\Theta)G_{MR}[(\boldsymbol{m} \cdot \boldsymbol{\sigma})\gamma_1 + \gamma_1(\boldsymbol{m} \cdot \boldsymbol{\sigma}^*)] \qquad (2.52)$$

$$4L\zeta_2\partial_x\gamma_2 = (1 - \gamma_2\tilde{\gamma}_1)N_1(\gamma_2 - \gamma_1) - 2iG_2^\phi[\gamma_2(\boldsymbol{m} \cdot \boldsymbol{\sigma}^*) - (\boldsymbol{m} \cdot \boldsymbol{\sigma})\gamma_2]$$
$$+4\cosh(\Theta)G_{MR}[(\boldsymbol{m} \cdot \boldsymbol{\sigma})\gamma_2 + \gamma_2(\boldsymbol{m} \cdot \boldsymbol{\sigma}^*)], \qquad (2.53)$$

when $\{1, 2\}$ means $\{L, R\}$, one side of the interface is a BCS superconductor, $\Theta = \tanh^{-1}\left(\frac{\Delta}{\varepsilon}\right)$ and $\Delta$ is the temperature-dependent superconducting gap. Within this framework, the density of states becomes

$$D(\varepsilon) = \frac{1}{2}\operatorname{Re}\{\operatorname{Tr}\{\underline{N}(1 + \underline{\gamma\tilde{\gamma}})\}\}. \qquad (2.54)$$

This is in reality a local quantity, as $\underline{\gamma}$ is position dependent. However, we will neglect this specification, as the density of states is always calculated at the center of the material in question. In the limit of weak superconductivity, the zero-energy DOS is

$$D(0) \approx 1 - \frac{1}{2}\left|f_s^R(0)\right|^2 + \frac{1}{2}\left|f_t^R(0)\right|^2, \qquad (2.55)$$

where $f_s^R$ describes singlet Cooper pairs and $f_t^R$ the triplet pairs. Thus, when no Cooper pairs are present the DOS equals the normal-state value represented by 1 constantly. Singlet Cooper pairs are accompanied by a zero-energy gap in the density of states, and triplet pairs give rise to a zero-energy peak.

## 2.7 Thermoelectric effects

The main focus of this thesis will be on spin-dependent thermoelectric effects associated with tunneling currents in superconducting hybrids. The system to be considered consists of two materials separated by an insulating polarizable barrier such as a ferromagnetic insulator. A temperature gradient or voltage bias is applied across this barrier. Proximity effects do not play a role when considering the thermoelectric effects specifically, as quasiparticle tunneling and not supercurrent tunneling is the main contributor. Moreover, we neglect the possibility of Josephson tunneling of Cooper pairs when calculating the thermoelectric effects. Quasiparticle tunneling in superconducting hybrid structures arises when a quasiparticle leaves an allowed state on the left side of an insulating barrier, tunnels through the interface and enters an allowed state on the other side [61][64]. If large-scale particle exchange across the barrier exists, and an external bias is applied to the system, net currents of charge and heat may arise. When considering single-particle tunneling only, the quasiparticle charge current between material $X$ and material $Y$ can be described by [64]

$$I_{XIY}^q = \frac{2\pi}{\hbar}|T_n|^2 \int_{-\infty}^{\infty} D_L(E)D_R(E+eV)[f_L(E) - f_R(E+eV)]\mathrm{d}E, \qquad (2.56)$$

where

$$f_j(E+eV_j) = \frac{1}{1 + e^{(E+eV_j)/k_B T_j}} \qquad (2.57)$$

is the Fermi-Dirac distribution function and $D_j(E)$ represents the density of energy states on each side of the junction. The superscript $q$ is present in order to ensure that only single quasiparticles, not Cooper pairs, are counted. When no voltage or temperature bias is applied $f_L(E) - f_R(E) = 0$, and the net current is zero.

Thermoelectric effects, such as the conversion of heat into electricity known as the Seebeck effect [100] [101] along with the opposite Peltier effect [102], have been known for a long time. This field of research shows great promise, as effective thermoelectric devices would allow for the conversion of useless waste heat into readily accessible electricity. The basis for large thermoelectric effects can be found in asymmetries in the electron-hole distribution. This can be visualized through considering a material in which there is a temperature gradient. The "hot" electrons and holes diffuse down the gradient, generating a heat current from the hot to the cold reservoir. When the material

in question contains perfect particle-hole symmetry, these currents will be equally large, resulting in zero net charge current [45]. Breaking the symmetry between electrons and holes is consequently a way in which one can enhance thermoelectric effects greatly [103]. For this reason, semiconducting materials often exhibit large thermoelectric effects [43] [104]. The phase transition from the normal to the superconducting state, on the other hand, is typically accompanied by a reduction in the thermoelectric properties of the material. As a temperature gradient is applied to a bulk superconductor, both a normal current and a supercurrent arise, which cancel each other out [105]. Regular BCS superconductors exhibit perfect particle hole symmetry in their density of states, as shown in Figure 2.3, and therefore cannot host thermoelectric phenomena [44]. However, if this symmetry can be broken, the asymptotic behavior of the superconducting density of states could contribute to large, even giant, thermoelectric effects.

There are several ways in which to break electron-hole symmetry when superconducting hybrids are used. One such method, which has been shown to result in giant thermo-electric effects when quasiparticle tunneling was studied [46] [52], involves applying a spin-splitting field to a conventional superconductor by coupling it to a spin polarized system, effectively breaking the electron-hole symmetry for each spin state [37]. An example of this is seen in figure 2.4a and 2.4b, showing first the total density of states and then the spin-split density of states for a Zeeman-split superconductor. Quasiparticle tunneling from a Zeeman-split superconductor (ZS) into for instance a normal metal (NM) will therefore give rise to large thermoelectric effects, and constitute one method for the achievement of superconducting thermoelectric effects. These are quantified through considering the spin-dependent heat and charge currents arising as a result of applied biases,

$$I_{\text{charge}}^{\sigma} = \frac{G_{\sigma}}{e} \int_{-\infty}^{\infty} \mathrm{d}E D_L^{\sigma}(E - \mu_L) D_R^{\sigma}(E - \mu_R) F(E) \tag{2.58}$$

$$I_{\text{heat}}^{\sigma} = \frac{G_{\sigma}}{e^2} \int_{-\infty}^{\infty} \mathrm{d}E (E - \mu_L) D_L^{\sigma}(E - \mu_L) D_R^{\sigma}(E - \mu_R) F(E), \tag{2.59}$$

where $F(E) = f_L(E - \mu_L) - f_R(E - \mu_R)$ and the heat current is defined from the left to the right electrode. A derivation of the expression for the heat current can be found in Ref. [106]. The total charge, spin, heat and spin heat currents driven by temperature and voltage biases are defined by

$$I_q = I_{\text{charge}}^{\uparrow} + I_{\text{charge}}^{\downarrow} \tag{2.60}$$

$$I_s = I_{\text{charge}}^{\uparrow} - I_{\text{charge}}^{\downarrow} \tag{2.61}$$

$$\dot{Q} = I_{\text{heat}}^{\uparrow} + I_{\text{heat}}^{\downarrow} \tag{2.62}$$

$$\dot{Q}_s = I_{\text{heat}}^{\uparrow} - I_{\text{heat}}^{\downarrow}. \tag{2.63}$$

In order to simplify further calculations and decouple the voltage and temperature

contributions to the thermoelectric effects, these biases can be Taylor expanded to linear order to obtain the Onsager response matrices [46][49]

$$\begin{pmatrix} I_q \\ \dot{Q} \end{pmatrix} = \begin{pmatrix} L_{11} & L_{12} \\ L_{12} & L_{22} \end{pmatrix} \begin{pmatrix} V \\ \Delta T/T \end{pmatrix} \tag{2.64}$$

and

$$\begin{pmatrix} I_s \\ \dot{Q}_s \end{pmatrix} = \begin{pmatrix} L'_{11} & L'_{12} \\ L'_{12} & L'_{22} \end{pmatrix} \begin{pmatrix} V \\ \Delta T/T \end{pmatrix}, \tag{2.65}$$

which obey the Onsager reciprocal relations [107] [108]. When considering thermoelectric coefficients, the Seebeck coefficient $S$ and dimensionless figure of merit $ZT$ are commonly considered accurate measures of thermoelectric effects. The Seebeck coefficient is defined as the potential difference developed per unit temperature difference when $I_{\text{charge}} = 0$ [109], and the figure of merit $ZT$ is considered a measure of how efficiently a system generates thermoelectric power. In this case, the coefficients are given by [110]

$$S = -\frac{L_{12}}{L_{11}T} \tag{2.66}$$

and

$$ZT = \left(\frac{L_{11}L_{22}}{L_{12}^2} - 1\right)^{-1}. \tag{2.67}$$

These parameters will be calculated at several points herein in order to allow for comparison to existing state-of-the-art thermoelectric materials. A major result of previous studies into superconducting thermoelectric effects, which will be expanded upon in this thesis, concerns the Onsager matrix for charge, spin and heat currents in hybrid structures consisting of a normal metal on the left side and a Zeeman-split superconductor on the right separated by a polarized insulating barrier [46]:

$$\begin{pmatrix} I_q \\ \dot{Q} \end{pmatrix} = \begin{pmatrix} G & P\alpha \\ P\alpha & G_Q \end{pmatrix} \begin{pmatrix} V \\ \Delta T/T \end{pmatrix} \tag{2.68}$$

$$\begin{pmatrix} I_s \\ \dot{Q}_s \end{pmatrix} = \begin{pmatrix} PG & \alpha \\ \alpha & PG_Q \end{pmatrix} \begin{pmatrix} V \\ \Delta T/T \end{pmatrix} \tag{2.69}$$

where $P$ is the polarization and

$$\alpha = \frac{G_T}{2e} \int_{-\infty}^{\infty} \frac{E D_R^z(E)}{4 k_B T \cosh^2\left(\frac{E}{2k_B T}\right)} \mathrm{d}E \tag{2.70}$$

$$G = G_T \int_{-\infty}^{\infty} \frac{D_R^0(E)}{4 k_B T \cosh^2\left(\frac{E}{2k_B T}\right)} \mathrm{d}E \tag{2.71}$$

$$G_Q = \frac{G_T}{e^2} \int_{-\infty}^{\infty} E^2 \frac{D_R^0(E)}{4 k_B T \cosh^2\left(\frac{E}{2k_B T}\right)} \mathrm{d}E. \tag{2.72}$$

$D_j^0(E) = 0.5(D_j^{\uparrow}(E) + D_j^{\downarrow}(E))$ and $D_j^z(E) = D_j^{\uparrow}(E) - D_j^{\downarrow}(E)$. A feature which quickly becomes evident is the possibility of a spin current $I_s = \alpha \Delta T / T$ arising as a consequence of an applied temperature gradient regardless of barrier polarization.

A major assumption underlying this derivation, however, concerns the polarization of the spins. All spins are here assumed to be polarized along the same axis, from here on out considered to be the $+z$-axis. This does not constitute a valid framework in all systems. A different approach to obtaining spin-split density of states while still exploiting the asymptotic behavior of the superconducting density of states is mediated by the proximity effect. By coupling two superconducting reservoirs to a nanowire, resulting in an S/X/S Josephson junction, a whole range of material parameters can be made to interfere with superconductivity. If the center of this nanowire is coupled to a normal metal electrode via a ferromagnetic insulator, a whole range of thermoelectric effects can be observed. The cases to be considered herein include materials with spatially varying magnetization, for example conical ferromagnetism and domain walls [83], spin-active interfaces with an alterable magnetization direction [33] and spin-orbit coupled semiconductor nanowires [39]. As superconducting Cooper pairs leak into these materials and undergo spin mixing and spin rotation, the resulting spin polarization for the quasiparticles is not necessarily uniaxial. Therefore, considering tunneling currents solely along one axis can result in loss of information, and two frameworks will be used when studying thermoelectric effects throughout this thesis. The first follows the approach outlined in this section, where the homogeneous spin-dependent density of states for each material is the starting point for our calculations. The hybrid structures considered within this line of thought are systems consisting of one or more Zeeman-split superconductors, Josephson junctions with spin-active interfaces aligned in the same direction coupled to normal metal electrodes, and ferromagnetic domain wall nanowires which are uniaxially polarized at $x = 0.5 L_F$. The second framework is based upon the idea hinted upon with the matrix currents defined in equations 2.45 - 2.47. Here, no particular spin-polarization is assumed, which enables us to consider spin-orbit coupled materials, conical ferromagnetism and changeable direction of the magnetization associated with the spin-active interfaces.

## 2.8   Spin-dependent bias

Hitherto, spin-dependency has been included only in the tunneling probabilities and densities of states. Throughout the recent years, the possibility of spin-dependent temperatures and voltages has been studied and reported. Non-equilibrium chemical potentials, different chemical potentials for different spin states, have become known under the name of spin accumulation and has been shown to be greatly enhanced in the superconducting state compared to the normal state [111]. Such a nonequilibrium spin accumulation can be induced in superconductors and normal metals through tunneling from ferromagnets in close proximity [112][113][114]. In addition to spin accumulation, ferromagnet tunneling has been predicted to induce spin heat accumulation, a spin-dependent temperature difference [115][116][117]. In Ref. [118] a spin-dependent heat conductance was measured in $F/N/F$ nanopillars. This was assumed to be caused by a spin-dependent heat difference, and based on this assumption they were able to extract a difference in effective spin temperature of up to 350 mK. The same effect was observed by Ref. [119] more recently, and the authors accepted the possibility of the heat conductance arising as a result of spin heat accumulation, but were more reluctant in coming to the certain conclusion.

As the evidence supports the possibility of spin-dependent voltages and temperature gradients we will henceforth allow for the application of spin-dependent biases. In the next chapter, a framework will be developed in which thermoelectric effects can arise from the application of spin-dependent biases.

# Chapter 3

# Thermoelectric Onsager matrix for homogeneously magnetized systems

In the following chapter we will present the first part of the analytical results obtained throughout the course of this work. The main goal has been the understanding and quantification of the giant thermoelectric effects arising within spin-split superconducting hybrids. This chapter focuses on the derivation of expressions for tunneling currents across barriers between two materials, along with the transformation of these currents into thermoelectric Onsager response matrices through Taylor expansion. We consider tunneling across a junction of the form X/I/Y, where I denotes an insulating material. The materials X and Y can be bulk materials, nanomaterials or more complex structures as long as at least one exhibits a particle-hole asymmetry capable of hosting thermoelectric phenomena. The material I can have some kind of polarization in addition to being a tunneling barrier. First we will derive complete expressions for the tunneling spin, heat, charge and spin heat currents, prior to performing a Taylor expansion to decouple the bias-dependent responses of the different currents. The novel part of this derivation concerns the generalization to include spin-dependent bias voltages and temperature gradients, which previously have not been found in Onsager response matrices. As the algebra performed here in some cases becomes rather extensive, only the primary results will be presented within this chapter. A more complete step-by-step methodology can be found in Appendix A.

In this chapter and the next we will limit our focus to material systems within which the spin-polarization exists homogeneously along one axis. Accordingly, we can employ the density of states-based approach outlined in Section 2.7, where the assumption of spin-polarization existing only along one axis is inherently made. The results in this chapter are presented in the form of mathematical expressions and matrix equations. A

discussion of the results will be included alongside the results themselves. The framework derived herein will be applied to experimentally realizable systems in the next chapter, Chapter 4. At the end of this chapter a discussion of possible material choices and realistic experimental procedures is included.

## 3.1 Tunneling currents

The currents for spin-$\sigma$ quasiparticles are given by

$$I_{\text{charge}}^{\sigma} = \frac{G^{\sigma}}{e} \int_{-\infty}^{\infty} \mathrm{d}E D_L^{\sigma}(E - \mu_L^{\sigma}) D_R^{\sigma}(E - \mu_R^{\sigma}) \big[ f_L^{\sigma}(E - \mu_L^{\sigma}) - f_R^{\sigma}(E - \mu_R^{\sigma}) \big] \qquad (3.1)$$

for the charge current and

$$I_{\text{heat}}^{\sigma} = \frac{G^{\sigma}}{e^2} \int_{-\infty}^{\infty} \mathrm{d}E(E - \mu_L^{\sigma}) D_L^{\sigma}(E - \mu_L^{\sigma}) D_R^{\sigma}(E - \mu_R^{\sigma}) \big[ f_L^{\sigma}(E - \mu_L^{\sigma}) - f_R^{\sigma}(E - \mu_R^{\sigma}) \big] \quad (3.2)$$

for the heat current traveling from the left to the right electrode. The heat current is not the same in both directions, and it therefore matters greatly in which direction and on which side of the barrier it is defined. The heat current traveling out of a material is determined by the energy of the moving particles in relation to the chemical potential on the originating side of the barrier. The heat current $I_{\text{heat}}^{L \to R}$ is determined by $(E - \mu_L)$, while the heat current in the opposite direction, $I_{\text{heat}}^{R \to L}$, is determined by $-(E - \mu_R)$. The quasiparticle energy $E$ is defined to be the energy in relation to the Fermi energy. The total charge and heat currents are

$$I = I_{\text{charge}}^{\uparrow} + I_{\text{charge}}^{\downarrow} \qquad (3.3)$$

$$\dot{Q} = I_{\text{heat}}^{\uparrow} + I_{\text{heat}}^{\downarrow} \qquad (3.4)$$

with the corresponding spin and spin heat currents being

$$I_s = I_{\text{charge}}^{\uparrow} - I_{\text{charge}}^{\downarrow} \qquad (3.5)$$

$$\dot{Q}_s = I_{\text{heat}}^{\uparrow} - I_{\text{heat}}^{\downarrow}. \qquad (3.6)$$

The spin currents considered here do not in fact describe the movement of the spin degree of freedom alone, but rather signifies migration of the spin polarization carried by the quasiparticle charge current. While the charge current describes the transport of all quasiparticles traversing the tunneling barrier regardless of their spin state, the

spin current only exists if more quasiparticles residing in one spin state than the other crosses the junction. Similarly the spin heat current is not the heat current carried by a pure spin current but rather the net spin polarization of the heat current. Throughout the rest of this thesis, $\left[ f_L^\sigma(E - \mu_L^\sigma) - f_R^\sigma(E - \mu_R^\sigma) \right]$ will be denoted by $F^\sigma$ and represents the spin-dependent distribution function. $D_j^\sigma(E - \mu_j^\sigma)$ will be shortened to $D_j^\sigma$ where $j = \{L, R\}$ and $(E - \mu_L^\sigma)$ is written as $\varepsilon^\sigma$. The main difference from previous differentiations, such as in [46] and [49], can be found in these factors. Here, all temperatures and bias voltages on both sides of the junction are assumed to be spin dependent. This greatly affects the Fermi-Dirac distribution functions. The main effect this has on the derivation of the Onsager response matrix is the fact that each of the current expressions needs to be differentiated with respect eight different variables $(T_L^\uparrow, T_R^\uparrow, V_L^\uparrow, V_R^\uparrow, T_L^\downarrow, T_R^\downarrow, V_L^\downarrow, V_R^\downarrow)$. First, we will construct general current expressions while retaining the spin-dependencies. The total charge current is

$$I = \frac{1}{e} \int_{-\infty}^{\infty} dE [G^\uparrow D_L^\uparrow D_R^\uparrow F^\uparrow + G^\downarrow D_L^\downarrow D_R^\downarrow F^\downarrow]. \tag{3.7}$$

We now want to express the charge current in terms of symmetric and antisymmetric expressions which are both easy to define for different material systems but also provide ease of differentiation in the next step. As we integrate over all energies, we are able to make certain simplifications by allowing all asymmetric terms within the integrals to equal zero. Consequently we expand the charge current in terms of symmetric and antisymmetric components as

$$I = \frac{1}{2e} \int_{-\infty}^{\infty} dE \left\{ \left[ (G^\uparrow + G^\downarrow)(F^\uparrow + F^\downarrow) + (G^\uparrow - G^\downarrow)(F^\uparrow - F^\downarrow) \right] \left( D_L^0 D_R^0 + \frac{1}{4} D_L^z D_R^z \right) + \right.$$
$$\left. \frac{1}{2} \left[ (G^\uparrow + G^\downarrow)(F^\uparrow - F^\downarrow) + (G^\uparrow - G^\downarrow)(F^\uparrow + F^\downarrow) \right] \left( D_L^0 D_R^z + D_L^z D_R^0 \right) \right\}. \tag{3.8}$$

The expression can now be further compressed according to

$$I = \frac{1}{e} \int_{-\infty}^{\infty} dE \left\{ \left( G_T F^0 + \frac{G_T P}{2} F^z \right) \left( D_L^0 D_R^0 + \frac{1}{4} D_L^z D_R^z \right) \right.$$
$$\left. + \frac{1}{2} \left( \frac{1}{2} G_T F^z + G_T P F^0 \right) \left( D_L^0 D_R^z + D_L^z D_R^0 \right) \right\} \tag{3.9}$$

by defining

$$G_T = G^\uparrow + G^\downarrow, \qquad P = \frac{G^\uparrow - G^\downarrow}{G^\uparrow + G^\downarrow} \tag{3.10}$$

$$F^0 = \frac{F^\uparrow + F^\downarrow}{2}, \qquad F^z = F^\uparrow - F^\downarrow \tag{3.11}$$

$$D_j^0 = \frac{D_j^\uparrow + D_j^\downarrow}{2}, \qquad D_j^z = D_j^\uparrow - D_j^\downarrow. \tag{3.12}$$

$G_T$ is the normal-state conductance of the tunnel junction and $P$ is the polarization providing the possibility of spin filtering if there are differing tunneling probabilities for the spin species. The charge current can now be seen to consist of sums of products of symmetric ($D_j^0(E)$) and antisymmetric ($D_j^z(E)$) components multiplied by the Fermi-Dirac distribution functions. The corresponding heat current leaving the left electrode and entering the right is

$$\dot{Q} = \frac{1}{e^2} \int_{-\infty}^{\infty} dE \Big[ \varepsilon^\uparrow G^\uparrow F^\uparrow D_L^\uparrow D_R^\uparrow + \varepsilon^\downarrow G^\downarrow F^\downarrow D_L^\downarrow D_R^\downarrow \Big], \tag{3.13}$$

which can be written as

$$\dot{Q} = \frac{1}{e^2} \int_{-\infty}^{\infty} dE \Bigg\{ \frac{1}{2} \Bigg[ \frac{\varepsilon^\uparrow + \varepsilon^\downarrow}{2} \big[ (G^\uparrow + G^\downarrow)(F^\uparrow + F^\downarrow) + (G^\uparrow - G^\downarrow)(F^\uparrow - F^\downarrow) \big] +$$
$$\frac{\varepsilon^\uparrow - \varepsilon^\downarrow}{2} \big[ (G^\uparrow + G^\downarrow)(F^\uparrow - F^\downarrow) + (G^\uparrow - G^\downarrow)(F^\uparrow + F^\downarrow) \big] \Bigg] \left( D_L^0 D_R^0 + \frac{1}{4} D_L^z D_R^z \right) +$$
$$\frac{1}{4} \Bigg[ \frac{\varepsilon^\uparrow + \varepsilon^\downarrow}{2} \big[ (G^\uparrow + G^\downarrow)(F^\uparrow - F^\downarrow) + (G^\uparrow - G^\downarrow)(F^\uparrow + F^\downarrow) \big] +$$
$$\frac{\varepsilon^\uparrow - \varepsilon^\downarrow}{2} \big[ (G^\uparrow + G^\downarrow)(F^\uparrow + F^\downarrow) + (G^\uparrow - G^\downarrow)(F^\uparrow - F^\downarrow) \big] \Bigg] \left( D_L^0 D_R^z + D_L^z D_R^0 \right) \Bigg\} \tag{3.14}$$

or

$$\dot{Q} = \frac{1}{e^2} \int_{-\infty}^{\infty} dE \left\{ \left[ \varepsilon^0 \left( G_T F^0 + \frac{G_T P}{2} F^z \right) + \frac{\varepsilon^z}{2} \left( \frac{G_T F^z}{2} + G_T P F^0 \right) \right] \right.$$
$$\cdot \left( D_L^0 D_R^0 + \frac{D_L^z D_R^z}{4} \right) + \frac{1}{2} \left[ \varepsilon^0 \left( \frac{G_T F^z}{2} + G_T P F^0 \right) + \frac{\varepsilon^z}{2} \left( G_T F^0 + \frac{G_T P}{2} F^z \right) \right]$$
$$\left. \cdot \left( D_L^0 D_R^z + D_L^z D_R^0 \right) \right\},$$

(3.15)

where

$$\varepsilon^0 = \frac{\varepsilon^\uparrow + \varepsilon^\downarrow}{2} \tag{3.16}$$

$$\varepsilon^z = \varepsilon^\uparrow - \varepsilon^\downarrow. \tag{3.17}$$

The spin current becomes

$$I_s = I^\uparrow - I^\downarrow \tag{3.18}$$

$$= \frac{1}{e} \int_{-\infty}^{\infty} dE [G^\uparrow D_L^\uparrow D_R^\uparrow F^\uparrow - G^\downarrow D_L^\downarrow D_R^\downarrow F^\downarrow]. \tag{3.19}$$

This can be expanded and then compressed in the same manner as the charge current according to

$$I_s = \frac{1}{2e} \int_{-\infty}^{\infty} dE \left\{ \left[ (G^\uparrow - G^\downarrow)(F^\uparrow + F^\downarrow) + (G^\uparrow + G^\downarrow)(F^\uparrow - F^\downarrow) \right] \left( D_L^0 D_R^0 + \frac{1}{4} D_L^z D_R^z \right) + \right.$$
$$\left. \frac{1}{2} \left[ (G^\uparrow - G^\downarrow)(F^\uparrow - F^\downarrow) + (G^\uparrow + G^\downarrow)(F^\uparrow + F^\downarrow) \right] \left( D_L^0 D_R^z + D_L^z D_R^0 \right) \right\},$$

(3.20)

and finally

$$I_s = \frac{1}{e} \int_{-\infty}^{\infty} dE \left\{ \left[ G_T P F^0 + \frac{G_T F^z}{2} \right] \left( D_L^0 D_R^0 + \frac{1}{4} D_L^z D_R^z \right) \right.$$
$$\left. + \frac{1}{2} \left[ \frac{G_T P}{2} F^z + G_T F^0 \right] \left( D_L^0 D_R^z + D_L^z D_R^0 \right) \right\}.$$

(3.21)

The spin heat current, which can be considered as the spin-polarization carried by the energy current in the same manner as the spin current is the polarization carried by the quasiparticle charge current, is defined by

$$\dot{Q}_s = \dot{Q}^\uparrow - \dot{Q}^\downarrow \tag{3.22}$$

$$= \frac{1}{e^2} \int_{-\infty}^{\infty} \mathrm{d}E \Big[ \varepsilon^\uparrow G^\uparrow F^\uparrow D_L^\uparrow D_R^\uparrow - \varepsilon^\downarrow G^\downarrow F^\downarrow D_L^\downarrow D_R^\downarrow \Big]. \tag{3.23}$$

As previously shown, this expression can be expanded as

$$\dot{Q}_s = \frac{1}{e^2} \int_{-\infty}^{\infty} \mathrm{d}E \bigg\{ \frac{1}{2} \bigg[ \frac{\varepsilon^\uparrow - \varepsilon^\downarrow}{2} \big[ (G^\uparrow + G^\downarrow)(F^\uparrow + F^\downarrow) + (G^\uparrow - G^\downarrow)(F^\uparrow - F^\downarrow) \big] +$$

$$\frac{\varepsilon^\uparrow + \varepsilon^\downarrow}{2} \big[ (G^\uparrow + G^\downarrow)(F^\uparrow - F^\downarrow) + (G^\uparrow - G^\downarrow)(F^\uparrow + F^\downarrow) \big] \bigg] \Big( D_L^0 D_R^0 + \frac{1}{4} D_L^z D_R^z \Big) +$$

$$\frac{1}{4} \bigg[ \frac{\varepsilon^\uparrow - \varepsilon^\downarrow}{2} \big[ (G^\uparrow + G^\downarrow)(F^\uparrow - F^\downarrow) + (G^\uparrow - G^\downarrow)(F^\uparrow + F^\downarrow) \big] +$$

$$\frac{\varepsilon^\uparrow + \varepsilon^\downarrow}{2} \big[ (G^\uparrow + G^\downarrow)(F^\uparrow + F^\downarrow) + (G^\uparrow - G^\downarrow)(F^\uparrow - F^\downarrow) \big] \bigg] \Big( D_L^0 D_R^z + D_L^z D_R^0 \Big) \bigg\} \tag{3.24}$$

and subsequently expressed in terms of the parameters $G_T$, $P$, $F^0$ and $F^z$ as

$$\dot{Q}_s = \frac{1}{2e^2} \int_{-\infty}^{\infty} \mathrm{d}E \bigg\{ \bigg[ \varepsilon^z \Big( G_T F^0 + \frac{G_T P}{2} F^z \Big) + \varepsilon^0 \Big( G_T F^z + 2 G_T P F^0 \Big) \bigg]$$

$$\cdot \Big( D_L^0 D_R^0 + \frac{D_L^z D_R^z}{4} \Big) + \bigg[ \frac{\varepsilon^z}{2} \Big( \frac{G_T F^z}{2} + G_T P F^0 \Big) + \varepsilon^0 \Big( G_T F^0 + \frac{G_T P}{2} F^z \Big) \bigg]$$

$$\cdot \Big( D_L^0 D_R^z + D_L^z D_R^0 \Big) \bigg\}. \tag{3.25}$$

We now have complete expressions for all four currents which depend almost exclusively on symmetric and antisymmetric components. The primary unknowns are the spin-dependent Fermi-Dirac distribution functions $F^0(E)$ and $F^z(E)$. Accordingly, the next stage in the procedure will be to assume a small voltage bias $V$ on one side of the junction or a small temperature difference $\Delta T$ across the barrier and perform a Taylor expansion to linear order about a certain point. This has several functions, as

it simplifies consideration of thermoelectric effects in different systems, yields a better grasp of the size of the thermoelectric effects through ease of quantification, and allows us to decouple the spin-dependent bias responses of the different currents.

## 3.2   Taylor expansion

The bias voltage and temperature gradients can be assumed to be very small. In this approximation, the expressions for the currents can be Taylor expanded up to linear order in $\Delta V$, $\Delta V_s$, $\Delta T/T$ and $\Delta T_s/T$. The goal is to express the currents in terms of Onsager coefficients as follows:

$$
\begin{pmatrix} I \\ \dot{Q} \\ I_s \\ \dot{Q}_s \end{pmatrix} = \begin{pmatrix} L_{11} & L_{12} & L_{13} & L_{14} \\ L_{21} & L_{22} & L_{23} & L_{24} \\ L_{31} & L_{32} & L_{33} & L_{34} \\ L_{41} & L_{42} & L_{43} & L_{44} \end{pmatrix} \begin{pmatrix} \Delta V \\ \Delta T \\ \Delta V_s \\ \Delta T_s \end{pmatrix}.
\tag{3.26}
$$

In analogy to the $2 \times 2$ Onsager response matrices we have seen previously we expect perfect diagonal symmetry. As outlined in the theory section (2.7), we can quantify the thermoelectric effects arising through considering the individual coefficients or parameters commonly used when comparing the efficiency of thermoelectric materials such as the Seebeck coefficient

$$
S = -\frac{L_{12}}{L_{11}T}
\tag{3.27}
$$

and the thermoelectric figure of merit

$$
ZT = \left( \frac{L_{11}L_{22}}{L_{12}^2} - 1 \right)^{-1}.
\tag{3.28}
$$

In order to quantify the thermoelectric effects in superconducting tunneling hybrids and obtain the $4 \times 4$ Onsager response matrix we first need to assume a small applied voltage or temperature bias and perform a Taylor expansion to the first order according to the formula

$$
f(x) = f(a) + \frac{f'(a)}{1!}(x - a) + \frac{f''(a)}{2!}(x - a)^2 + ...
\tag{3.29}
$$

In order to maintain the generality of the consideration, we will start with assuming spin-dependent temperatures and voltages on both sides of the junction. The currents are denoted $J = \{I, \dot{Q}, I_s, \dot{Q}_s\}$ and depend on $V_j^\sigma$ and $T_j^\sigma$, where $j = \{L, R\}$ refers to whether the left (L) or right (R) side of the tunneling junction is being considered. Each

of the currents is Taylor expanded with regard to each of the eight variables $V_j^\sigma$ and $T_j^\sigma$ in the following manner:

$$
\begin{aligned}
J \approx \ & \frac{\mathrm{d}J}{\mathrm{d}V_L^\uparrow}\bigg|_{V_{L,0}^\uparrow} (V_L^\uparrow - V_{L,0}^\uparrow) + \frac{\mathrm{d}J}{\mathrm{d}V_L^\downarrow}\bigg|_{V_{L,0}^\downarrow} (V_L^\downarrow - V_{L,0}^\downarrow) + \frac{\mathrm{d}J}{\mathrm{d}V_R^\uparrow}\bigg|_{V_{R,0}^\uparrow} (V_R^\uparrow - V_{R,0}^\uparrow) \\
& + \frac{\mathrm{d}J}{\mathrm{d}V_R^\downarrow}\bigg|_{V_{R,0}^\downarrow} (V_R^\downarrow - V_{R,0}^\downarrow) + \frac{\mathrm{d}J}{\mathrm{d}T_L^\uparrow}\bigg|_{T_{L,0}^\uparrow} (T_L^\uparrow - T_{L,0}^\uparrow) + \frac{\mathrm{d}J}{\mathrm{d}T_L^\downarrow}\bigg|_{T_{L,0}^\downarrow} (T_L^\downarrow - T_{L,0}^\downarrow) \\
& + \frac{\mathrm{d}J}{\mathrm{d}T_R^\uparrow}\bigg|_{T_{R,0}^\uparrow} (T_R^\uparrow - T_{R,0}^\uparrow) + \frac{\mathrm{d}J}{\mathrm{d}T_R^\downarrow}\bigg|_{T_{R,0}^\downarrow} (T_R^\downarrow - T_{R,0}^\downarrow).
\end{aligned} \tag{3.30}
$$

The Taylor coefficients will be evaluated in a specific point $(V_{j,0}^\sigma, T_{j,0}^\sigma) = (V_0, T_0) = (V, T)$. A dominant feature existing in all four currents is the Fermi-Dirac function

$$
F^\sigma = f_L^\sigma(E - eV_L^\sigma) - f_R^\sigma(E - eV_R^\sigma) \tag{3.31}
$$

$$
= \frac{e^{\frac{E - eV_R^\sigma}{k_B T_R^\sigma}} - e^{\frac{E - eV_L^\sigma}{k_B T_L^\sigma}}}{1 + e^{\frac{E - eV_R^\sigma}{k_B T_R^\sigma}} + e^{\frac{E - eV_L^\sigma}{k_B T_L^\sigma}} + e^{\frac{E - eV_R^\sigma}{k_B T_R^\sigma}} e^{\frac{E - eV_L^\sigma}{k_B T_L^\sigma}}}. \tag{3.32}
$$

As is apparent from this expression, when differentiating the expressions for the currents about $(V, T)$ only $F^\sigma$ needs to be differentiated. The reason for this is that $F^\sigma = 0$ when $V_j^\sigma = V$ and $T_j^\sigma = T$. Consequently, the $0^{\text{th}}$-order term equals zero, and we will only differentiate $F^0 = \frac{F^\uparrow + F^\downarrow}{2}$ and $F^z = F^\uparrow - F^\downarrow$. The results of differentiating $F^\sigma$ and thereafter allowing $(V_j^\sigma, T_j^\sigma) = (V_{j,0}^\sigma, T_{j,0}^\sigma) = (V, T)$ are

$$
\frac{\mathrm{d}F^\sigma}{\mathrm{d}V_R^\sigma} = -\frac{e}{4 k_B T \cosh^2\left(\frac{E - eV}{2 k_B T}\right)} \tag{3.33}
$$

$$
\frac{\mathrm{d}F^\sigma}{\mathrm{d}V_L^\sigma} = \frac{e}{4 k_B T \cosh^2\left(\frac{E - eV}{2 k_B T}\right)} \tag{3.34}
$$

$$
\frac{\mathrm{d}F^\sigma}{\mathrm{d}V_j^{-\sigma}} = 0. \tag{3.35}
$$

and

$$\frac{\mathrm{d}F^\sigma}{\mathrm{d}V_R^\sigma} = -\frac{E - eV}{4k_B T^2 \cosh^2\left(\frac{E-eV}{2k_B T}\right)} \tag{3.36}$$

$$\frac{\mathrm{d}F^\sigma}{\mathrm{d}V_L^\sigma} = \frac{E - eV}{4k_B T^2 \cosh^2\left(\frac{E-eV}{2k_B T}\right)} \tag{3.37}$$

$$\frac{\mathrm{d}F^\sigma}{\mathrm{d}V_j^{-\sigma}} = 0. \tag{3.38}$$

Combining these into the relevant sums $F_j^0(E)$ and $F_j^z(E)$, we are left with

$$\frac{\mathrm{d}F^0}{\mathrm{d}V_R^\sigma} = -\frac{1}{2}\frac{e}{4k_B T \cosh^2\left(\frac{E-eV}{2k_B T}\right)} \qquad \frac{\mathrm{d}F^z}{\mathrm{d}V_R^\sigma} = -\sigma\frac{e}{4k_B T \cosh^2\left(\frac{E-eV}{2k_B T}\right)} \tag{3.39}$$

$$\frac{\mathrm{d}F^0}{\mathrm{d}V_L^\sigma} = \frac{1}{2}\frac{e}{4k_B T \cosh^2\left(\frac{E-eV}{2k_B T}\right)} \qquad \frac{\mathrm{d}F^z}{\mathrm{d}V_L^\sigma} = \sigma\frac{e}{4k_B T \cosh^2\left(\frac{E-eV}{2k_B T}\right)} \tag{3.40}$$

and

$$\frac{\mathrm{d}F^0}{\mathrm{d}T_R^\sigma} = -\frac{1}{2}\frac{E - eV}{4k_B T^2 \cosh^2\left(\frac{E-eV}{2k_B T}\right)} \qquad \frac{\mathrm{d}F^z}{\mathrm{d}T_R^\sigma} = -\sigma\frac{E - eV}{4k_B T^2 \cosh^2\left(\frac{E-eV}{2k_B T}\right)} \tag{3.41}$$

$$\frac{\mathrm{d}F^0}{\mathrm{d}T_L^\sigma} = \frac{1}{2}\frac{E - eV}{4k_B T^2 \cosh^2\left(\frac{E-eV}{2k_B T}\right)} \qquad \frac{\mathrm{d}F^z}{\mathrm{d}T_L^\sigma} = \sigma\frac{E - eV}{4k_B T^2 \cosh^2\left(\frac{E-eV}{2k_B T}\right)} \tag{3.42}$$

where $\sigma = \{\uparrow, \downarrow\} = \pm 1$ and the temperature $T$ is defined as

$$T = \frac{T_L + T_R}{2} = \frac{T_L^\uparrow + T_L^\downarrow + T_R^\uparrow + T_R^\downarrow}{4}. \tag{3.43}$$

Now that all differentiations have been performed, we can allow one further simplification. In order to more easily apply the resulting expressions to actual systems, we define

$$V_{j,0}^\sigma = V = 0, \tag{3.44}$$

causing the point about which we perform the Taylor expansion, $(V, T)$, to become $(0, T)$. Consequently, $(E - eV) = (E)$ in the expressions above. This is to a large

part done in order to allow for symmetry considerations to be applied to the current expressions in the following sections.

The charge, heat, spin and spin heat currents are now Taylor expanded to the first order in terms of each of the eight variables while employing the differentiations presented in equations 3.39-3.42. As the computations are rather extensive, only the results are presented here. The reader is referred to Appendix A for a more complete derivation procedure. The main steps involve differentiating each current with respect to each of the eight variables, allowing $(V_j^\sigma, T_j^\sigma) = (0, T)$ and employing symmetry arguments to simplify expressions. The products of $dF^{0,z}/d(T, V)_j^\sigma$ and $D_j^0(E)$ and $D_j^z(E)$ are either symmetric or antisymmetric, and as the integral from $-\infty$ to $\infty$ of an antisymmetric argument equals zero this consideration simplifies the expressions rather drastically.

Upon differentiating the charge current with respect to each of the variables and allowing $(V_{j,0}^\sigma, T_{j,0}^\sigma) = (V, T) = (0, T)$ we observe that its dependency upon $(T_{j,0}^\sigma, V_{j,0}^\sigma)$ disappears and the total charge current becomes

$$
\begin{aligned}
I = & \frac{G_T}{2} \int_{-\infty}^{\infty} \frac{D_L^0 D_R^0 + \frac{D_L^z D_R^z}{4}}{4 k_B T \cosh^2\left(\frac{E}{2 k_B T}\right)} dE [(V_L^\uparrow + V_L^\downarrow) - (V_R^\uparrow + V_R^\downarrow)] \\
& + \frac{G_T P}{4e} \int_{-\infty}^{\infty} \frac{E(D_L^0 D_R^z + D_L^z D_R^0)}{4 k_B T \cosh^2\left(\frac{E}{2 k_B T}\right)} dE \frac{[(T_L^\uparrow + T_L^\downarrow) - (T_R^\uparrow + T_R^\downarrow)]}{T} \\
& + \frac{G_T P}{2} \int_{-\infty}^{\infty} \frac{D_L^0 D_R^0 + \frac{D_L^z D_R^z}{4}}{4 k_B T \cosh^2\left(\frac{E}{2 k_B T}\right)} dE [(V_L^\uparrow - V_L^\downarrow) - (V_R^\uparrow - V_R^\downarrow)] \\
& + \frac{G_T}{4e} \int_{-\infty}^{\infty} \frac{E(D_L^0 D_R^z + D_L^z D_R^0)}{4 k_B T \cosh^2\left(\frac{E}{2 k_B T}\right)} dE \frac{[(T_L^\uparrow - T_L^\downarrow) - (T_R^\uparrow - T_R^\downarrow)]}{T}.
\end{aligned}
\tag{3.45}
$$

Thermoelectric effects are the collective denotation of phenomena where charge currents arise due to applied temperature gradients and heat currents due to applied voltages. This can be generalized to include spin thermoelectric effects, where spin currents arise due to temperature gradients and spin heat currents due to voltage bias. The thermal response of the charge current is, according to Equation 3.45, encompassed by the coefficients

$$
L_{12} = \frac{G_T P}{4e} \int_{-\infty}^{\infty} \frac{E(D_L^0 D_R^z + D_L^z D_R^0)}{4 k_B T \cosh^2\left(\frac{E}{2 k_B T}\right)} dE
\tag{3.46}
$$

and

$$L_{14} = \frac{G_T}{4e} \int_{-\infty}^{\infty} \frac{E(D_L^0 D_R^z + D_L^z D_R^0)}{4k_B T \cosh^2\left(\frac{E}{2k_B T}\right)} \mathrm{d}E. \tag{3.47}$$

$L_{12}$ governs the charge current response to an applied temperature bias across the junction while $L_{14}$ controls the charge current arising as a result of an applied temperature difference for the spin species. A common feature of these two coefficients is the need for an asymmetry in the density of states on one side of the junction for them to be unequal to zero. This is dictated by the factors $D_L^z = D_L^\uparrow - D_L^\downarrow$ and $D_R^z = D_R^\uparrow - D_R^\downarrow$. If the density of states on both sides of the insulating barrier are equal for both spin up and spin down, the result will be $D_R^z = D_L^z = 0$ and $L_{12} = L_{14} = 0$. Consequently, no thermoelectric effects will arise in the system. A charge current is only able to arise across the barrier as a direct result of an applied temperature gradient, either spin dependent or otherwise, if a particle-hole asymmetry can be found. This can be understood from the description of thermoelectric effects in Section 2.7. When a temperature gradient is applied, electrons and holes from the warmer region will migrate towards the colder. If an equal amount of electrons and holes are in motion the net charge current will amount to zero. This describes the situation in conventional superconductors where there is perfect particle-hole symmetry around the Fermi level at $E = 0$ and thermoelectric effects to not occur. Applying an in-plane magnetic field or utilizing Josephson junctions with exotic spin configurations allows us to break the particle-hole symmetry for each spin separately, resulting in the possibility of thermoelectric transport. However, charge neutrality remains conserved, and if there is no spin-dependent difference in probability for tunneling across the barrier the total charge current will still equal zero. If the interface barrier is polarized with $P \neq 0$ and the tunneling probability differs for the spin species, charge currents are able to arise upon the application of a thermal gradient. If primarily one spin species is allowed through the barrier, and the particle-hole asymmetry for this spin is broken, the net amount of electrons passing through may differ from the net amount of holes and a nonzero charge current can exist. A feature worth noticing is the lack of polarization dependency in the response of the charge current to the application of a spin-dependent temperature gradient. If we consider a case where $T_R^\uparrow = T_R^\downarrow$ the spin gradient can be written as $\Delta T_s = T_L^\uparrow - T_L^\downarrow$. Even if no temperature difference exists across the barrier a polarization-independent charge current can arise as a result of applying different temperatures to the spin-up and spin-down particles on the left. This can result in a larger amount of temperature-driven migration of one spin species than the other, and when the particle-hole symmetry is broken for this spin species net nonzero charge currents are able to arise.

The voltage responses of the charge current,

$$L_{11} = \frac{G_T}{2} \int_{-\infty}^{\infty} \frac{D_L^0 D_R^0 + \frac{D_L^z D_R^z}{4}}{4k_B T \cosh^2\left(\frac{E}{2k_B T}\right)} \mathrm{d}E \tag{3.48}$$

and

$$L_{13} = \frac{G_T P}{2} \int_{-\infty}^{\infty} \frac{D_L^0 D_R^0 + \frac{D_L^z D_R^z}{4}}{4 k_B T \cosh^2\left(\frac{E}{2k_B T}\right)} \mathrm{d}E, \tag{3.49}$$

can be nonzero when no particle-hole asymmetry exists on either side of the junction. If a voltage bias $\Delta V$ is applied across the junction a net current will arise. This is due to the particles and holes moving in opposite directions in response to a voltage bias as opposed to in the case of a temperature bias, where both positive and negative charge particles move from the hot to the cold region. What is worth noticing in this case is the fact that a charge current can arise from applying a spin-dependent voltage bias on one side of the junction while keeping the total bias across the junction equal to zero. However, the polarization must be unequal to zero for this effect to arise. When a spin-dependent voltage bias is applied the spin species will move in opposite directions in response to the bias. As the symmetry breaking is equal and opposite for each spin species, the net current will disappear. If, however, a spin-dependent tunneling probability is present, $\Delta V_s \neq 0$ can result in a net charge current crossing the junction.

The heat current traversing the barrier from the left-hand-side to the right-hand-side electrode can be Taylor expanded in the same manner. Allowing $T_j^{\sigma} = T$ and $V_j^{\sigma} = V = 0$ following the differentiation of $F_j^{\sigma}$ causes

$$\varepsilon^0 = \frac{E + E}{2} = E \tag{3.50}$$

$$\varepsilon^z = E - E = 0 \tag{3.51}$$

and

$$\dot{Q} = \frac{1}{e^2} \int_{-\infty}^{\infty} E \left\{ \left( G_T F^0 + \frac{G_T P}{2} F^z \right) \left( D_L^0 D_R^0 + \frac{1}{4} D_L^z D_R^z \right) \right.$$
$$\left. + \frac{1}{2} \left( \frac{1}{2} G_T F^z + G_T P F^0 \right) \left( D_L^0 D_R^z + D_L^z D_R^0 \right) \right\} \mathrm{d}E. \tag{3.52}$$

One should note the extra asymmetric factor $E$, as this affects which parts of the expressions end up equaling zero. Defining $(V_{j,0}^{\sigma}, T_{j,0}^{\sigma}) = (0, T)$ results in the final heat current becoming

$$
\dot{Q} = \frac{G_T P}{4e} \int_{-\infty}^{\infty} \frac{E(D_L^0 D_R^z + D_L^z D_R^0)}{4k_B T \cosh^2\left(\frac{E}{2k_B T}\right)} \mathrm{d}E[(V_L^\uparrow + V_L^\downarrow) - (V_R^\uparrow + V_R^\downarrow)]
$$

$$
+ \frac{G_T}{2e^2} \int_{-\infty}^{\infty} \frac{E^2 \left(D_L^0 D_R^0 + \frac{D_L^z D_R^z}{4}\right)}{4k_B T \cosh^2\left(\frac{E}{2k_B T}\right)} \mathrm{d}E \frac{[(T_L^\uparrow + T_L^\downarrow) - (T_R^\uparrow + T_R^\downarrow)]}{T}
$$

$$
+ \frac{G_T}{4e} \int_{-\infty}^{\infty} \frac{E(D_L^0 D_R^z + D_L^z R_R^0)}{4k_B T \cosh^2\left(\frac{E}{2k_B T}\right)} \mathrm{d}E[(V_L^\uparrow - V_L^\downarrow) - (V_R^\uparrow - V_R^\downarrow)]
$$

$$
+ \frac{G_T P}{2e^2} \int_{-\infty}^{\infty} \frac{E^2 \left(D_L^0 D_R^0 + \frac{D_L^z D_R^z}{4}\right)}{4k_B T \cosh^2\left(\frac{E}{2k_B T}\right)} \mathrm{d}E \frac{[(T_L^\uparrow - T_L^\downarrow) - (T_R^\uparrow - T_R^\downarrow)]}{T}.
$$

(3.53)

Heat currents arise when there is a temperature difference across the system, as heat flows from a hot to a cold reservoir. This effect will exist regardless of barrier polarization, as is evident from $L_{22}$ being independent of polarization. The heat current is associated with quasiparticle transport. The heat current associated with transport of particles equals the heat transported by holes, and net heat currents arise when temperature gradients are applied regardless of barrier polarization. This occurs regardless of whether particle-hole asymmetries exist or not. If the temperature gradients applied are spin-dependent, and we consider for instance $\Delta T_s = T_L^\uparrow - T_L^\downarrow \neq 0$, the movement of spin up and spin down species can be opposite. If there is no barrier polarization present the net energy current consequently equals zero.

Applying a voltage difference to the junction results in zero net energy current if there is no interface polarization. The particles and holes move in opposite directions due to the voltage bias and their energy current components cancel each other out. If the particle-hole symmetry is broken for each spin species and polarization is present, the voltage difference can generate a net heat current. If the voltage bias only exists for different spin species and not across the junction a particle-hole asymmetry for each spin species allows for a different number of quasiparticles moving in each direction, resulting in a net energy current.

The spin current can be treated in the same manner. Performing the differentiations and applying the same assumptions to the spin current along with defining $(V_{j,0}^\sigma, T_{j,0}^\sigma) = (0, T)$ yields

$$
\begin{aligned}
I_s = {} & \frac{G_T P}{2} \int_{-\infty}^{\infty} \frac{D_L^0 D_R^0 + \frac{D_L^z D_R^z}{4}}{4 k_B T \cosh^2\left(\frac{E}{2 k_B T}\right)} \mathrm{d}E [(V_L^\uparrow + V_L^\downarrow) - (V_R^\uparrow + V_R^\downarrow)] \\
& + \frac{G_T}{4e} \int_{-\infty}^{\infty} \frac{E(D_L^0 D_R^z + D_L^z D_R^0)}{4 k_B T \cosh^2\left(\frac{E}{2 k_B T}\right)} \mathrm{d}E \frac{[(T_L^\uparrow + T_L^\downarrow) - (T_R^\uparrow + T_R^\downarrow)]}{T} \\
& + \frac{G_T}{2} \int_{-\infty}^{\infty} \frac{D_L^0 D_R^0 + \frac{D_L^z D_R^z}{4}}{4 k_B T \cosh^2\left(\frac{E}{2 k_B T}\right)} \mathrm{d}E [(V_L^\uparrow - V_L^\downarrow) - (V_R^\uparrow - V_R^\downarrow)] \\
& + \frac{G_T P}{4e} \int_{-\infty}^{\infty} \frac{E(D_L^0 D_R^z + D_L^z D_R^0)}{4 k_B T \cosh^2\left(\frac{E}{2 k_B T}\right)} \mathrm{d}E \frac{[(T_L^\uparrow - T_L^\downarrow) - (T_R^\uparrow - T_R^\downarrow)]}{T}.
\end{aligned}
\tag{3.54}
$$

Interestingly, the bias-specific polarization dependency for the spin current is opposite from the charge current case. Applying a voltage bias to the junction can generate a charge current in the absence of interface polarization, but this is not the case for the spin current. A particle-hole asymmetry is not necessary for spin currents to arise upon the application of a voltage bias, but barrier polarization must be present. As the voltage bias is applied the particle and hole currents move in opposite directions across the interface. If the same number of each spin species is allowed to pass through, the net spin current carried by the quasiparticles and quasiholes equals zero. If, however, differing probabilities for spin-dependent tunneling exist, a net spin tunneling current may arise. If the voltage bias applied only exists for the spin species and not across the barrier unequal numbers of spin-up and spin-down particles may cross the barrier regardless of whether the particle-hole asymmetry is broken or not, resulting in net spin currents.

If no particle-hole asymmetry exists on either side of the junction, applying a temperature gradient does not effect the spin or charge currents crossing the tunneling barrier. If there however is a particle-hole asymmetry present on one side of the junction, and the density of states of spin one spin state does not always equal that of the other, tunneling across the barrier can result in a spin current even in the absence of barrier polarization. Even though the net charge current resulting from the application of a temperature gradient equals zero, the broken particle-hole asymmetry may result in a net spin polarization passing through the system even in the absence of barrier polarization. If only a spin-dependent temperature gradient is applied there must be an unequal probability for spin-dependent tunneling present for the spin current to exist.

We can now, finally, differentiate the spin heat current with respect to each of the variables $T_j^\sigma$ and $V_j^\sigma$, followed by allowing $T_{j,0}^\sigma = T$ and $V_{j,0}^\sigma = V = 0$. Once again

$\varepsilon^0 = E$ and $\varepsilon^z = 0$, and

$$\dot{Q}_s = \frac{1}{2e^2} \int_{-\infty}^{\infty} E \left\{ \left( G_T F^z + 2 G_T P F^z \right) \left( D_L^0 D_R^0 + \frac{1}{4} D_L^z D_R^z \right) \right.$$
$$\left. + \left( G_T F^0 + \frac{G_T P}{2} F^z \right) \left( D_L^0 D_R^z + D_L^z D_R^0 \right) \right\} dE. \tag{3.55}$$

One should again note the extra asymmetric factor $E$, as this affects which parts of the expressions end up equaling zero. Performing the expansion and applying $(V_{j,0}^\sigma, T_{j,0}^\sigma) = (0, T)$ yields

$$\dot{Q}_s = \frac{G_T}{4e} \int_{-\infty}^{\infty} \frac{E(D_L^0 D_R^z + D_L^z D_R^0)}{4 k_B T \cosh^2\left(\frac{E}{2k_B T}\right)} dE [(V_L^\uparrow + V_L^\downarrow) - (V_R^\uparrow + V_R^\downarrow)]$$

$$+ \frac{G_T P}{2e^2} \int_{-\infty}^{\infty} \frac{E^2 \left( D_L^0 D_R^0 + \frac{D_L^z D_R^z}{4} \right)}{4 k_B T \cosh^2\left(\frac{E}{2k_B T}\right)} dE \frac{[(T_L^\uparrow + T_L^\downarrow) - (T_R^\uparrow + T_R^\downarrow)]}{T}$$

$$+ \frac{G_T P}{4e} \int_{-\infty}^{\infty} \frac{E(D_L^0 D_R^z + D_L^z R_R^0)}{4 k_B T \cosh^2\left(\frac{E}{2k_B T}\right)} dE [(V_L^\uparrow - V_L^\downarrow) - (V_R^\uparrow - V_R^\downarrow)] \tag{3.56}$$

$$+ \frac{G_T}{2e^2} \int_{-\infty}^{\infty} \frac{E^2 \left( D_L^0 D_R^0 + \frac{D_L^z D_R^z}{4} \right)}{4 k_B T \cosh^2\left(\frac{E}{2k_B T}\right)} dE \frac{[(T_L^\uparrow - T_L^\downarrow) - (T_R^\uparrow - T_R^\downarrow)]}{T}.$$

## 3.3 Onsager matrix

As is evident from the expressions for the currents, they can now be grouped together in the following Onsager matrix for bias response:

$$\begin{pmatrix} I \\ \dot{Q} \\ I_s \\ \dot{Q}_s \end{pmatrix} = \begin{pmatrix} L_{11} & L_{12} & L_{13} & L_{14} \\ L_{21} & L_{22} & L_{23} & L_{24} \\ L_{31} & L_{32} & L_{33} & L_{34} \\ L_{41} & L_{42} & L_{43} & L_{44} \end{pmatrix} \begin{pmatrix} \Delta V \\ \frac{\Delta T}{T} \\ \Delta V_s \\ \frac{\Delta T_s}{T} \end{pmatrix}. \tag{3.57}$$

When the matrix is assembled in this manner, there is perfect symmetry about the diagonal. This corresponds perfectly with what we would expect for Onsager coefficients such as these. The complete current expressions to linear order are

$$
\begin{pmatrix} I \\ \dot{Q} \\ I_s \\ \dot{Q}_s \end{pmatrix} = \begin{pmatrix} G & P\alpha & PG & \alpha \\ P\alpha & G_Q & \alpha & PG_Q \\ PG & \alpha & G & P\alpha \\ \alpha & PG_Q & P\alpha & G_Q \end{pmatrix} \begin{pmatrix} \Delta V \\ \Delta T/T \\ \Delta V_s/2 \\ \Delta T_s/2T \end{pmatrix}. \tag{3.58}
$$

We have defined the biases as

$$
\Delta V = \frac{V_L^\uparrow + V_L^\downarrow}{2} - \frac{V_R^\uparrow + V_R^\downarrow}{2} \tag{3.59}
$$

$$
\Delta T = \frac{T_L^\uparrow + T_L^\downarrow}{2} - \frac{T_R^\uparrow + T_R^\downarrow}{2} \tag{3.60}
$$

$$
\Delta V_s = (V_L^\uparrow - V_L^\downarrow) - (V_R^\uparrow - V_R^\downarrow) \tag{3.61}
$$

$$
\Delta T_s = (T_L^\uparrow - T_L^\downarrow) - (T_R^\uparrow - T_R^\downarrow), \tag{3.62}
$$

and the thermoelectric coefficients are

$$
G = G_T \int_{-\infty}^{\infty} dE \frac{D_L^0 D_R^0 + \frac{D_L^z D_R^z}{4}}{4k_B T \cosh^2(\frac{E}{2k_B T})} \tag{3.63}
$$

$$
\alpha = \frac{G_T}{2e} \int_{-\infty}^{\infty} dE \frac{E(D_L^0 D_R^z + D_L^z D_R^0)}{4k_B T \cosh^2(\frac{E}{2k_B T})} \tag{3.64}
$$

$$
G_Q = \frac{G_T}{e^2} \int_{-\infty}^{\infty} dE \frac{E^2 \left( D_L^0 D_R^0 + \frac{D_L^z D_R^z}{4} \right)}{4k_B T \cosh^2(\frac{E}{2k_B T})}. \tag{3.65}
$$

Here, $G$ represents the conductance, $\alpha$ is the thermoelectric coefficient and $G_Q$ is the heat conductance. The temperature is defined as

$$
T = \frac{T_L + T_R}{2} = \frac{T_L^\uparrow + T_L^\downarrow + T_R^\uparrow + T_R^\downarrow}{4}. \tag{3.66}
$$

The derivation of the Onsager matrix is completely general until the assumption $(V, T) = (0, T)$ is made. The matrix describes the response of the charge, spin, heat and spin heat currents to both spin-dependent and spin-independent voltage and temperature biases. Moreover, the derived framework allows for particle-hole asymmetries to exist on either one or both sides of the tunneling junction, granting further flexibility.

Equations 3.58 - 3.65 are the central analytical results of the first part of this thesis.

All the thermoelectric coefficients in the Onsager matrix are in some way proportional to $\alpha$ and equation 3.64. This is persistent with previous results, such as Ref. [46]. The thermoelectric coefficient $\alpha$ therefore governs the temperature response of the charge and spin currents, as $I = P\alpha\Delta T/T$ and $I_s = \alpha\Delta T/T$ when $\Delta V = \Delta V_s = \Delta T_s = 0$, along with the voltage bias response of the heat and spin heat currents. $\alpha$ is only unequal to zero when there is a particle-hole asymmetry on at least one side of the tunneling barrier. This can, for the cases studied in the following chapter, be achieved by applying strong external magnetic fields to superconducting materials [37], or proximity-coupling superconductors to ferromagnetic insulators [120][24][121][122] or thin ferromagnetic metallic layers [30][123]. The magnetic exchange field should be applied in-plane of the superconductor and perpendicularly to the transport direction, to minimize the destructive effect of the field on superconducting order [67].

Structures containing particle-hole asymmetries will constitute the focus point of the subsequent chapter. In Chapter 4, the framework presented herein will be used to study the thermoelectric effects arising in spin-split superconducting hybrids. The systems considered contain Zeeman-split superconductors, ferromagnetic domain walls and Josephson junctions with spin-active interfaces. Numerical methods and MATLAB are applied when quantifying the thermoelectric effects arising. See Appendix C for further details. As the thermoelectric coefficient $\alpha$ is shown to govern thermoelectric response even when spin-dependent biases are applied, this coefficient will dominate a large number of the considerations made. We therefore limit our concern to this coefficient along with the Seebeck coefficient

$$S = \frac{P\alpha}{GT} \tag{3.67}$$

and the thermoelectric figure of merit

$$ZT = \left(\frac{G_Q G}{(P\alpha)^2} - 1\right)^{-1}. \tag{3.68}$$

The main limitation of the framework presented herein is the fact that spin-polarization existing homogeneously along only one axis is inherently assumed. Therefore, only materials exhibiting such spin configurations can be studied using the expressions presented here. The consideration within the next chapter is consequently devoted to structures fulfilling these demands. This problem is solved in Chapter 5, where we present a framework allowing for the quantification of thermoelectric effects in superconducting hybrids with arbitrary spin-dependent fields.

# Chapter 4

# Thermoelectric effects in homogeneously magnetized systems

In this chapter we explore the plethora of thermoelectric effects arising in superconducting tunneling junctions consisting of homogeneously magnetized spin-split materials. Consequently, we can employ the framework derived in Chapter 3 when quantifying these effects. We will study the thermoelectric figure of merit and Seebeck coefficient for easy comparison to more common thermoelectric materials, but also bestow great focus upon the thermoelectric coefficient $\alpha$. This coefficient governs the generation of charge currents and spin currents from applied temperature gradients, along with the induction of heat and spin heat currents as a result of applied voltage biases. As shown when deriving the $4 \times 4$ Onsager matrix in the preceding chapter, the consistency in $\alpha$ governing thermoelectric effects persists also when the applied biases exist for different spin species and not across the tunneling junction.

The material systems studied in this chapter can be divided into two categories: Zeeman-split superconducting hybrids and normal metal/insulator/(SXS) structures. The superconductor/X/superconductor (S/X/S) Josephson junctions exhibit a homogeneous particle-hole asymmetry for each spin species. The two Josephson junctions considered within this chapter are a superconductor/normal metal/superconductor Josephson junction with spin-active interfaces polarized along the same axis, and a superconductor/ferromagnet/superconductor Josephson junction with a head-to-head domain wall structure within the ferromagnetic nanowire.

An important thing to note with regard to all the results in this chapter is the validity of the model as the temperature is reduced. When considering heat transport in tunneling junctions consisting of superconducting materials we have made a crucial assumption concerning the heat only being carried by the quasiparticles tunneling across the barrier

interfaces. As heat supercurrents do not exist, and Cooper pairs do not carry heat, this assumption is not valid for low temperatures. When the temperature is close to 0 K, practically all the electrons in a superconductor are bound in Cooper pairs. Consequently, the amount of Cooper pairs which can contribute to heat transport diminishes as the temperature is lowered. When this occurs, the phonon contribution will dominate heat transport. As this contribution has been neglected in all the considerations so far, low temperatures lowers the validity of our model. Therefore, in this chapter, we will mainly consider temperatures above $T = 0.2T_{c,0}$, where our models prove good approximations. The results which show current responses for temperatures lower than $T = 0.2T_{c,0}$ should therefore be accepted as somewhat uncertain.

The primary goal of the numerical calculations performed herein is to determine and quantify the thermoelectric effects arising in homogeneously polarized spin-split superconducting tunneling junctions. Within this chapter and Chapter 6 we study different hybrid systems in order to maximize the thermoelectric phenomena arising. We study the thermoelectric coefficient $\alpha$ governing pure thermal spin currents along with the Seebeck coefficient $S$ and thermoelectric figure of merit $ZT$ which both allow us to compare the thermoelectric effects arising here to the best bulk thermoelectric materials presently available. We first study different configurations of Zeeman-split superconducting materials, which have previously been shown to give rise to giant thermoelectric effects [46], before switching our focus to various configurations of Josephson junctions spin-split along one axis requiring no or low applied magnetic fields to generate thermoelectric phenomena.

All results within this chapter are presented in the form of three-dimensional MATLAB *surf*-plots. In order to simplify reading this thesis, we have implemented a color-coding for the different material systems. The color systems used so far for the density of states and superconducting gap parameter in Chapter 2 will not be employed for the thermoelectric effects, but only for density of states. The color coding commenced here will be continued also in the next chapter studying numerical results, Chapter 6. In this chapter, thermoelectric coefficients connected to Zeeman-split bilayers will be presented in light purple and blue, Zeeman-split Josephson junction hybrids in pink, S/F/S junctions with ferromagnetic domain walls in copper, and S/N/S Josephson junctions with magnetic interfaces in pink and yellow.


## 4.1   Zeeman-split hybrids


Applying in-plane magnetic fields to conventional BCS superconductors has, as previously mentioned, been seen to lift the superconducting particle-hole asymmetry for each spin and allow such materials to host giant thermoelectric effects. Particularly normal metal/polarized insulator/Zeeman-split superconductor bilayers have been studied. Within this section, we apply the framework presented in Chapter 3 to different hy-

brid structures containing Zeeman-split superconductors with the goal of quantifying the thermoelectric phenomena arising. Approximate analytic formulas for the spin-dependent densities of states exist for all the Zeeman-split systems considered. and numerical integration in MATLAB is therefore applied to the expressions for the thermoelectric effects. The Zeeman-fields considered are all defined to be applied in-plane and not in the transport direction. Otherwise, superconductivity would be more readily destroyed due to orbital depairing. The thermoelectric coefficient

$$\alpha = \frac{G_T}{2e} \int_{-\infty}^{\infty} dE \frac{E(D_L^0 D_R^z + D_L^z D_R^0)}{4k_B T \cosh^2(\frac{E}{2k_B T})} \tag{4.1}$$

has been shown to be the main governing factor for thermoelectric effects in X/I/Y junctions, both when spin-dependent biases are present and when they are not. A necessary feature for such junctions to exhibit thermoelectric effects is a particle-hole asymmetry on at least one side of the junction. Aside form this, no assumptions have been made regarding the nature of the junction. Polarization at the isolator interfaces can be present, but this is not necessary in order to observe thermoelectric effects. For instance, a spin-dependent temperature gradient can induce a charge current across the junction even when $P = 0$, as evident from

$$I = \alpha \frac{\Delta T_s}{2T} \tag{4.2}$$

when $\Delta V = \Delta T = \Delta V_s = 0$. The thermoelectric coefficient $\alpha$ defines the size of the charge current if $\Delta T_s$ is assumed constant. Moreover, $\alpha$ governs the existence of a similar spin-polarized tunneling current when $\Delta T_s = \Delta V = \Delta V_s = 0$, as

$$I_s = \alpha \frac{\Delta T}{T}. \tag{4.3}$$

Additionally, the thermal response of the tunneling charge current is

$$I = P\alpha \frac{\Delta T}{T}. \tag{4.4}$$

In this subsection, analytical expressions for the density of states will be employed for the considerations of thermal spin currents and the thermoelectric coefficient $\alpha$. Consequently, the right-hand-side structure will contain Zeeman-split superconductors, and therefore display a particle-hole asymmetry in the density of states. The thermoelectric coefficient is calculated through using a MATLAB function for numerical integration

called *integral*. For a more rigorous description of the numerical methods employed for the calculations, see Appendix C. The structures to be considered analytically can be divided into two categories: superconducting bilayer structures and more complicated systems containing Josephson junctions. Both these cases where also briefly discussed in an article recently published, Ref. [49], included in Appendix D.

### 4.1.1 Zeeman-split bilayers

This section will focus on thermal spin currents and thermoelectric effects in general in Zeeman split superconducting bilayers. The three systems considered here are normal metal/insulator/Zeeman-split superconductor (N/I/ZS), superconductor/insulator/Zeeman-split superconductor (S/I/ZS) and Zeeman-split superconductor/insulator/Zeeman-split superconductor (ZS/I/ZS) bilayers. The setup is shown in Figure 4.1.
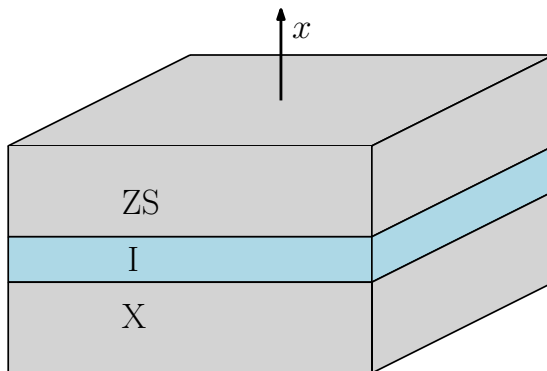


Figure 4.1: Schematic of the experimental setup considered. A tunneling barrier (I) separates a normal metal (N), superconductor (S) or Zeeman-split superconductor (ZS), denoted X, on the left-hand-side from a Zeeman-split superconductor (ZS) on the right. Tunneling takes place across the barrier in the $\boldsymbol{x}$-direction.

The parameters to be considered are the thermoelectric coefficient $\alpha$, the Seebeck coefficient $S$ and the dimensionless figure of merit $ZT$. Defined in terms of the Onsager matrix in equation 3.58, the last two are defined as

$$S = -\frac{P\alpha}{GT} \tag{4.5}$$

and

$$ZT = \left(\frac{G_Q G}{(P\alpha)^2} - 1\right)^{-1}. \tag{4.6}$$

The coefficients $S$ and $ZT$ are commonly used when characterizing the size of thermoelectric effects and allow us to compare our results to existing state-of-the-art thermoelectric materials. The coefficients considered are, as before,

$$\alpha = \frac{G_T}{2e} \int_{-\infty}^{\infty} \frac{E(D_L^0 D_R^z + D_L^z D_R^0)}{4k_B T \cosh^2\left(\frac{E}{2k_B T}\right)} \mathrm{d}E \tag{4.7}$$

$$G = G_T \int_{-\infty}^{\infty} \frac{D_L^0 D_R^0 + \frac{D_L^z D_R^z}{4}}{4k_B T \cosh^2\left(\frac{E}{2k_B T}\right)} \mathrm{d}E \tag{4.8}$$

$$G_Q = \frac{G_T}{e^2} \int_{-\infty}^{\infty} E^2 \frac{D_L^0 D_R^0 + \frac{D_L^z D_R^z}{4}}{4k_B T \cosh^2\left(\frac{E}{2k_B T}\right)} \mathrm{d}E \tag{4.9}$$

with the densities of states being defined as

$$D_j^0 = \frac{D_j^\uparrow + D_j^\downarrow}{2} \tag{4.10}$$

$$D_j^z = D_j^\uparrow - D_j^\downarrow. \tag{4.11}$$

For a conventional BCS superconductor the density of states becomes

$$D_{SC}^0 = \left| \mathrm{Re}\left\{ \frac{E + i\Gamma}{\sqrt{(E + i\Gamma)^2 - \Delta^2}} \right\} \right| \tag{4.12}$$

$$D_{SC}^z = 0, \tag{4.13}$$

where $\Delta = \Delta(T)$ is the temperature-dependent superconducting gap. $\Gamma$ represents inelastic scattering and is in all cases throughout this thesis defined as $\Gamma = 0.005\Delta_0$, while $\Delta_0$ is the superconducting gap parameter when $h_S = T = 0$. This is defined as $\Delta_0 = 1$ meV herein. The value choice for the superconducting gap parameter was made without a specific material in mind, but is not unreasonable as it takes the values 0.18, 1.35 and 1.50 meV for Al, Pb and Nb, respectively [124, p. 79]. The density of states for each spin species $\sigma$ in a Zeeman-split superconductor is defined by

$$D_{ZS}^\sigma = \left| \mathrm{Re}\left\{ \frac{E + \sigma h_S + i\Gamma}{\sqrt{(E + \sigma h_S + i\Gamma)^2 - \Delta^2}} \right\} \right|, \tag{4.14}$$

where $h_S$ is the induced Zeeman-field in the superconductor and the superconducting gap $\Delta = \Delta(h_S, T)$ depends on the field and the temperature [37] according to the gap equation 2.9. The self-consistent solution for the superconducting order parameter in Zeeman-split superconductors can be found in Figure 2.2.

Figure 4.2 shows the thermoelectric coefficient $\alpha$ for the three structures N/I/ZS, S/I/ZS and ZS/I/ZS, while Figure 4.3 shows the Seebeck coefficient and thermoelectric figure

(a) $\alpha e/(G_T \Delta_0)$



(b) $\alpha e/(G_T \Delta_0)$



(c) $\alpha e/(G_T \Delta_0)$
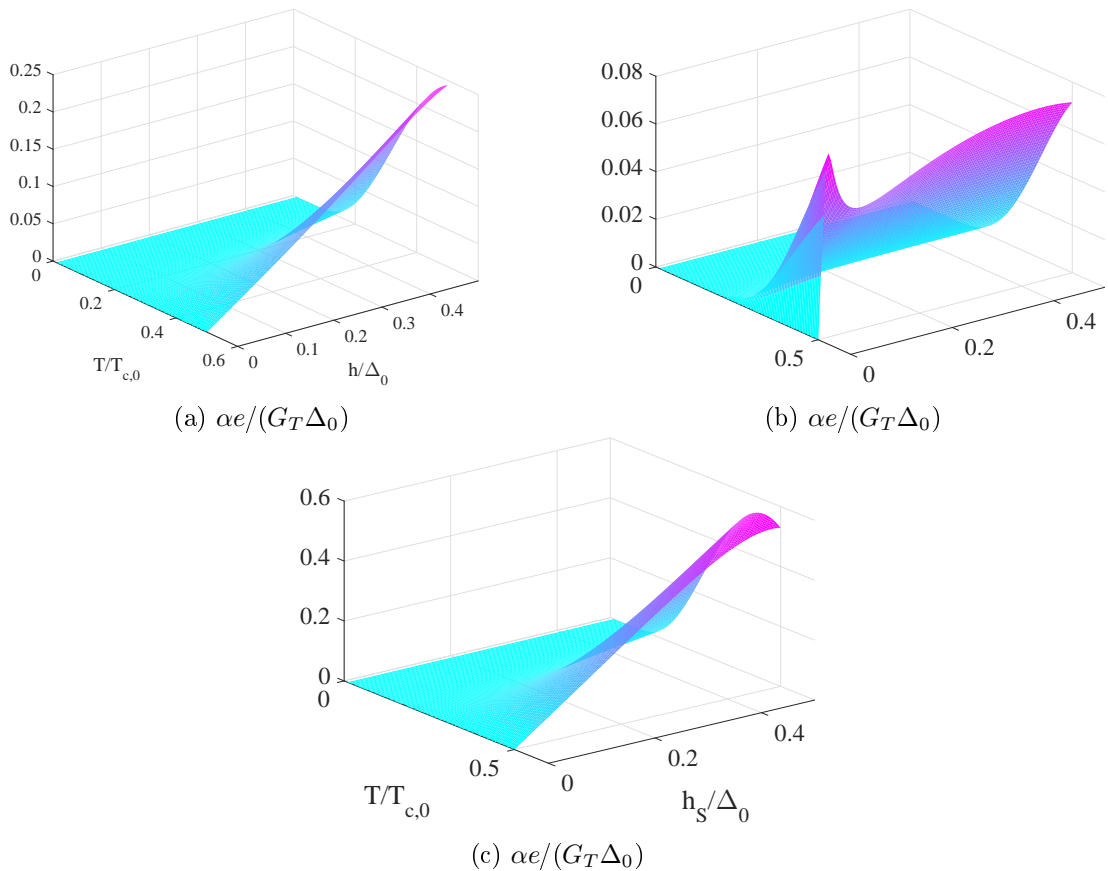
Figure 4.2: Dimensionless thermoelectric coefficient $\alpha e/(G_T\Delta_0)$ in (a) normal metal/I/ZS, (b) superconductor/I/ZS and (c) Zeeman-split superconductor/I/ZS bilayers. Inelastic scattering is governed by $\Gamma = 0.005\Delta_0$ where $\Delta_0 = 1$ meV is the superconducting energy gap. The polarization of the tunneling interface is defined as $P = 97\%$.

of merit for the same systems. The parameters chosen are $\Delta_0 = 1$ meV for the super-conducting energy gap, $\Gamma = 0.005\Delta_0$ represents inelastic scattering and $P = 97\%$ is the interface polarization. This value was chosen as similar polarizations are attainable in ferromagnetic insulators such as at GdN 3 K [68]. Interestingly, having a particle-hole asymmetry on both sides of the junction is seen to maximize all the effects being considered when the Zeeman-split superconductors are identical. The largest Seebeck coefficient, thermoelectric coefficient and thermoelectric figure of merit can be found for the case of ZS/I/ZS. This trend is maintained also when other parameters than the ones displayed here are used. When $h_S = 0$ no asymmetry exists, and no thermoelectric effects arise. This is as we expect, and $\alpha$, $S$ and $ZT = 0$ in all cases when this is true. As soon as the temperature and fields are increased somewhat $\alpha$ no longer identically equals zero, but is still very small compared to the maximum value. Because $S$ and $ZT$ are governed by the relationships between $\alpha$ and the other thermoelectric coefficients,
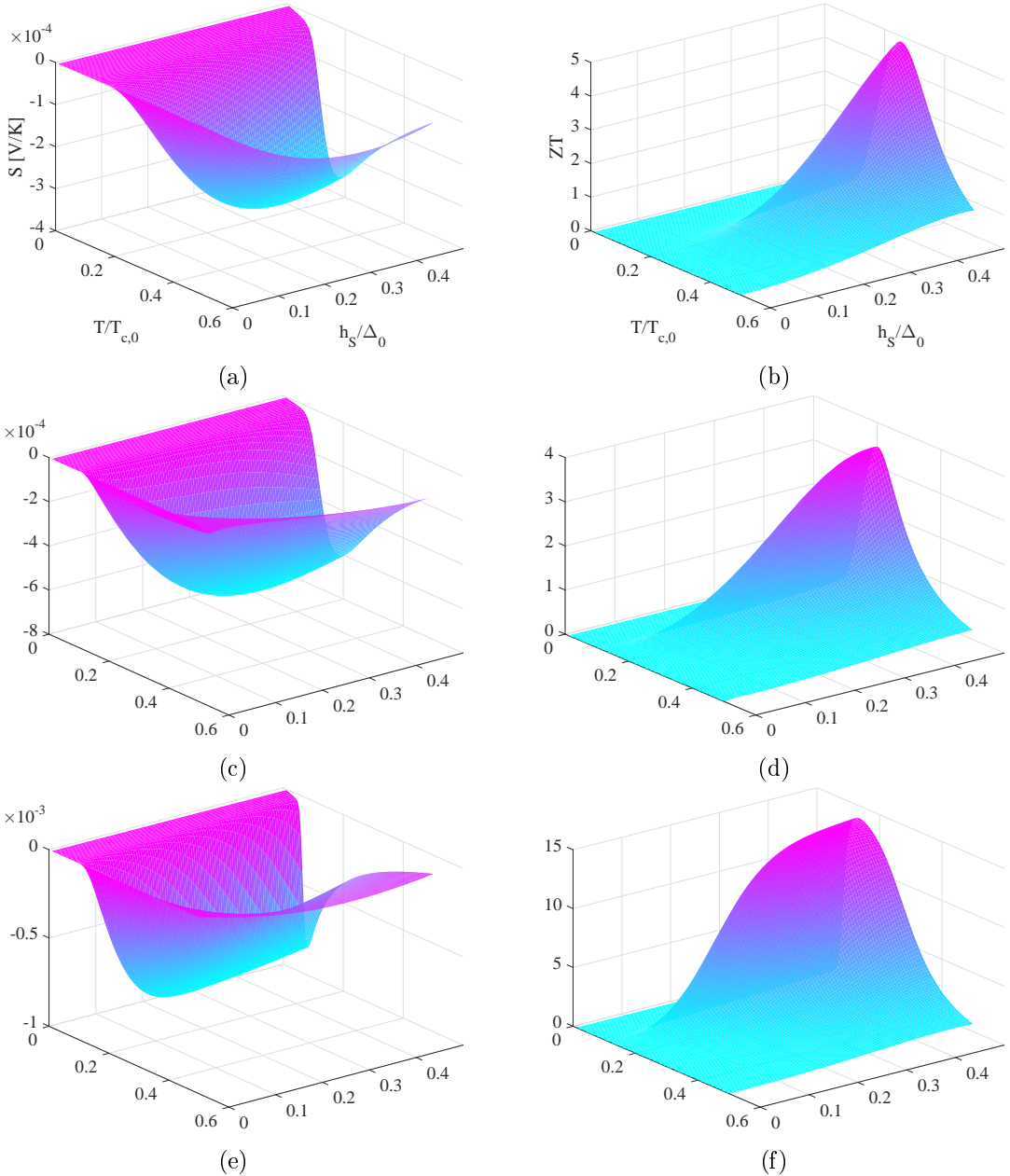
Figure 4.3: Seebeck coefficient $S$ (first column) and thermoelectric figure of merit $ZT$ (second column) in X/I/ZS bilayers. The left hand side is occupied by a (a)-(b) normal metal, (c)-(d) superconductor and (e)-(f) Zeeman-split superconductor. Inelastic scattering is governed by $\Gamma = 0.005\Delta_0$ where $\Delta_0 = 1$ meV, and the polarization is $P = 97\%$.

theys tart to increase rapidly as soon as $(h_S, T) \neq (0,0)$ and $\alpha \neq 0$.

A notable trend in Figure 4.2 concerns the temperature dependency of $\alpha$. The thermo-electric coefficient increases along with the temperature and the applied exchange field. This can be understood in terms of the distribution function within the expression for $\alpha$, $C(E) = [4k_B T \cosh^2\left(\frac{E}{2k_B T}\right)]^{-1}$. This factor functions as a weight upon the densities of states on each side of the barrier and determines the probability for an available energy state actually being occupied.
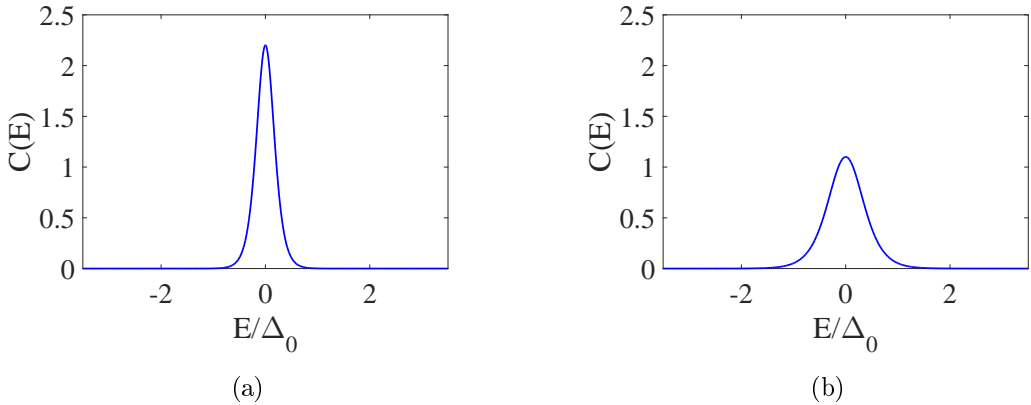


Figure 4.4: The figures show $C(E) = [4k_B T \cosh^2\left(\frac{E}{2k_B T}\right)]^{-1}$ for (a) $T = 0.2T_{c,0}$ and (b) $T = 0.4T_{c,0}$.

Figure 4.4 shows the distribution function C(E) for (a) $T = 0.2T_{c,0}$ and (b) $T = 0.4T_{c,0}$. The peak broadens as the temperature increases, allowing for a larger number of energies to be accompanied by occupied states. Accordingly, when the temperature is higher, the thermoelectric coefficient increases in size. When the temperature approaches zero very few energies aside from the Fermi energy (represented by $E = 0$) are accompanied by occupied states. If the density of states on either side of the tunneling barrier were to exhibit a zero-energy peak this could accordingly contribute to enhancing the thermoelectric coefficient significantly, even at lower temperatures. This has previously been stated to indicate triplet Cooper pairs being present instead of singlet Cooper pairs. This weighting function also holds an explanation for why the larger exchange fields are accompanied by a larger corresponding $\alpha$. The smaller the exchange field is, the closer will the extra Zeeman-split peaks in the superconducting density of states be to the BCS coherence peak at the gap edges. This will be far away from the weighting function, and small fields accordingly do not give rise to thermoelectric effects. When the fields become larger, the Zeeman-split peaks will approach $E = 0$ and consequently interfere with the probability function C(E). If the temperature increases at the same time these will enhance each other, resulting in very large pure thermal spin currents $I_s = \alpha \Delta T/T$. It is important to note, however, that this temperature dependency may not continue

for even larger temperatures than the once shown in Figure 4.2, where the maximum temperature studied is $T = 0.5T_{c,0}$. As the temperature increases the distribution function broadens, and more energies have a probability of having occupied states, but the weight upon each energy state becomes smaller. For this reason, once some threshold temperature is passed the thermoelectric coefficient may begin to decrease as the temperature is further increased. The evolution of $S$ and $ZT$ with temperature is quite different as these depend on $G$ and $G_Q$ in addition to $\alpha$. These coefficients depend on the temperature in the same manner as $\alpha$, but evolve differently with respect to the quasiparticle energy. This results in the temperature dependency of $S$ and $ZT$ not being as readily determinable as for $\alpha$. Moreover, $S \propto T^{-1}$, and should therefore not be largest for large temperatures.

When considering Figure 4.2b, we notice that using a superconductor rather than another material on the left side of the barrier reduces the size of the spin current governed by $I_s = \alpha \Delta T/T$. The smallest values for $\alpha$ are consistently found in the case of S/I/ZS rather than N/I/ZS. Mathematically this can be explained as a result of destructive interference between $D_j^0(E)$ and $D_j^z(E)$ in the expression for $\alpha$. The density of states for the superconductor and Zeeman-split superconductor used in these bilayer considerations are shown in Figure 4.5 for $h_S = 0.3\Delta_0$.

When the left hand side material is a normal metal or a conventional non-split superconductor, $D_L^z = 0$. Therefore, how $D_L^0$ and $D_R^z$ affect each other as the temperature and field are altered governs the thermoelectric response of the system. The giant thermoelectric effects seen in the cases of N/I/ZS and ZS/I/ZS are made possible through the asymptotic nature of the superconducting density of states, shown for a Zeeman-split superconductor in Figure 4.5b. When considering N/I/ZS the normal-state density of states is neglected, and therefore cannot influence the eventual size and shape of $\alpha$. When S/I/ZS is considered, the asymptotic nature of the superconducting density of states on one side of the barrier can be suppressed by the superconducting energy gap on the other side of the tunneling junction, as seen when comparing Figures 4.5a and 4.5c. The larger the amount of energies for which the DOS equals zero on one side of the junction is, the smaller $\alpha$ will be. The superconducting density of states, which does not change much qualitatively with temperature, is shown in Figure 2.3. The difference in spin-up and spin-down density of states for a Zeeman-split superconductor, which is not greatly affected by temperature either, is shown in Figure 4.5c for $h_S/\Delta_0 = 0.3$. When $D_{ZS}^z(E)$ displays its largest absolute values, at $|E| < \pm 1$, the superconducting DOS equals zero. Consequently, the largest peaks in $D_{ZS}^z(E)$ cannot contribute to $\alpha$. Moreover, $D_{ZS}^z(E)$ is fairly small at $E = \pm 1$ where $D_{SC}^0(E)$ displays asymptotic behavior, and $D_{SC}^0(E) = 1$ for $|E| > 1$ where $D_{ZS}^z(E)$ is again large. Accordingly, the largest values of the density of states on each side of the junction are suppressed when considering tunneling between a conventional BCS superconductor and a Zeeman-split superconductor. This trend persists also for other values of the exchange field. The largest maximum values for $\alpha$ are attained for the doubly Zeeman-split bilayer. The two Zeeman-split superconductors used are equal, and the peaks in the density of states at

(a)



(b)



(c)
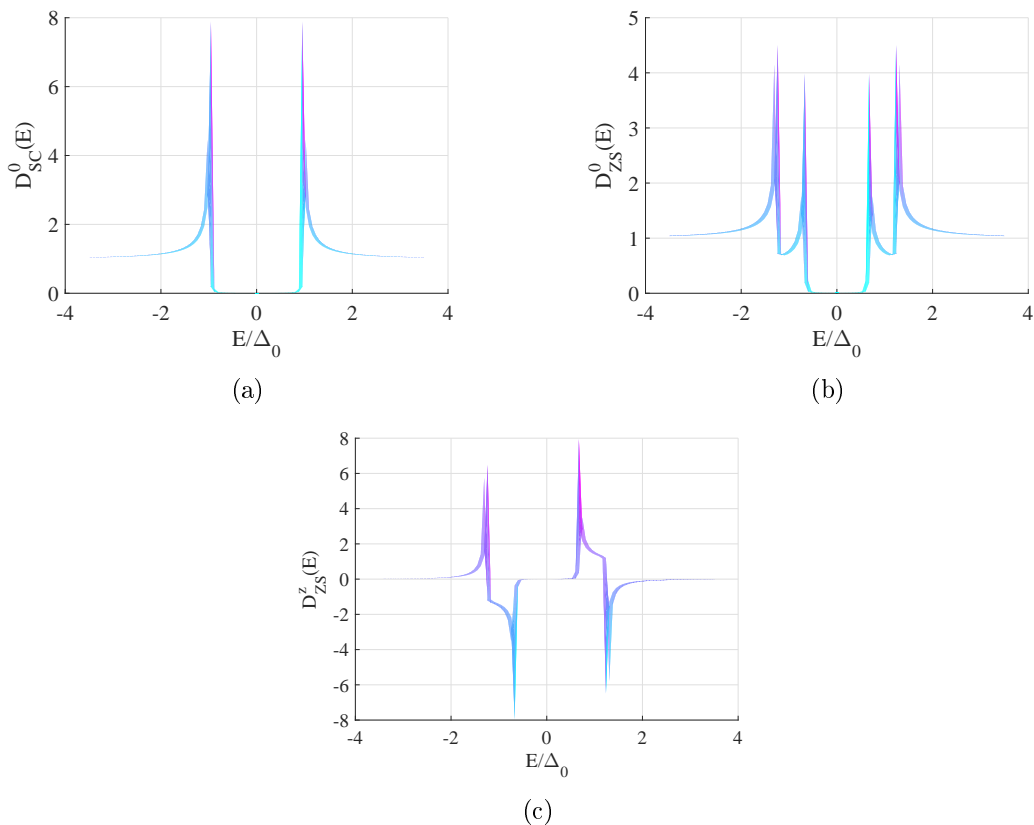
Figure 4.5: The figures show the density of states vs. energy for (a) a normal superconductor, (b) a Zeeman-split superconductor and (c) the difference in the DOS for spin up and spin down species in a Zeeman-split superconductor when $h_S = 0.3\Delta_0$ and $\Gamma = 0.005\Delta_0$.

the gap edges occur at identical energies. Consequently, the peaks enhance each other, and $\alpha$ can become very large for certain fields and temperatures. If the superconductors used did not display the same energy gap the situation could change drastically.

Interestingly, only the thermoelectric coefficient $\alpha$ is suppressed in this manner in the case of S/I/ZS. The thermoelectric figure of merit $ZT$ and the Seebeck coefficient $S$ are almost equal both when considering a normal metal and a superconductor to the left of the barrier. These are governed not only by $\alpha$, but by the relationship between $\alpha$ and $G$ and $G_Q$. If these are close in size, $S$ and $ZT$ can become large regardless of the size of $\alpha$. Therefore, even when the pure thermal spin currents are suppressed when replacing the normal metal with a superconductor, the normally considered thermoelectric effects are not. These are still maximized by employing two spin-split superconductors separated by a tunneling barrier, but are quite significant also when the asymmetry exists only in the right hand side material. The best bulk thermoelectric materials, among others $CsBi_4Te_8$ and $Bi_2Te_3$, have thermoelectric figures of merit $ZT \approx 2$ and Seebeck

coefficients $S \approx 1$ meV [42, p. 82]. Figure 4.3 shows that this is far surpassed in the Zeeman-split bilayers for the thermoelectric figure of merit, particularly in the case of double asymmetry. The doubly Zeeman-split bilayer can match the Seebeck coefficient of the best thermoelectric semiconductors.

### 4.1.2 Zeeman-split Josephson junction

Exchanging one of the materials in the bilayer considered so far for a Josephson junction allows for a whole new element of control over the tunneling thermoelectric effects arising in the system, and results in new phenomena previously not observed. A schematic of the setup is shown in Figure 4.6. The new control parameter is the superconducting phase difference. As this can be controlled by applying external magnetic fields or passing currents through the system we now have an additional method for tuning the thermoelectric effects. The density of states for each spin species in the normal metal part of a Zeeman-split Josephson junction (ZS/N/ZS) is given by

$$D^{\sigma}_{ZS/N/ZS} = \left| \text{Re} \left\{ \frac{E + \sigma h_S + i\Gamma}{\sqrt{(E + \sigma h_S + i\Gamma)^2 - \Delta^2 \cos^2\left(\frac{\Delta\theta}{2}\right)}} \right\} \right|, \qquad (4.15)$$

where $\Delta\theta$ is the superconducting phase difference found in the Josephson junction. This model is valid to a good approximation when $L_N \ll \xi$, with $\xi$ being the superconducting coherence length. When this is true the density of states hardly changes throughout the normal metal nanowire.
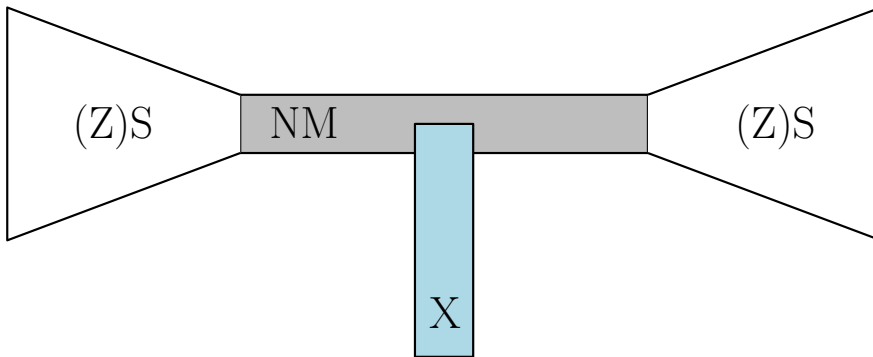


Figure 4.6: Schematic of the experimental setup considered, where a tunneling barrier (I) separates a normal metal, superconductor or Zeeman-split superconductor (X) on the left-hand-side from a Zeeman-split (ZS/NM/ZS) or normal superconductor (S/NM/S) Josephson junction on the right.

We begin by considering the effect of adding one Josephson junction to the bilayer structure. Figure 4.7 shows $\alpha$ in the case of tunneling between a normal metal, a super-

(a)                                                                              (b)



(c)
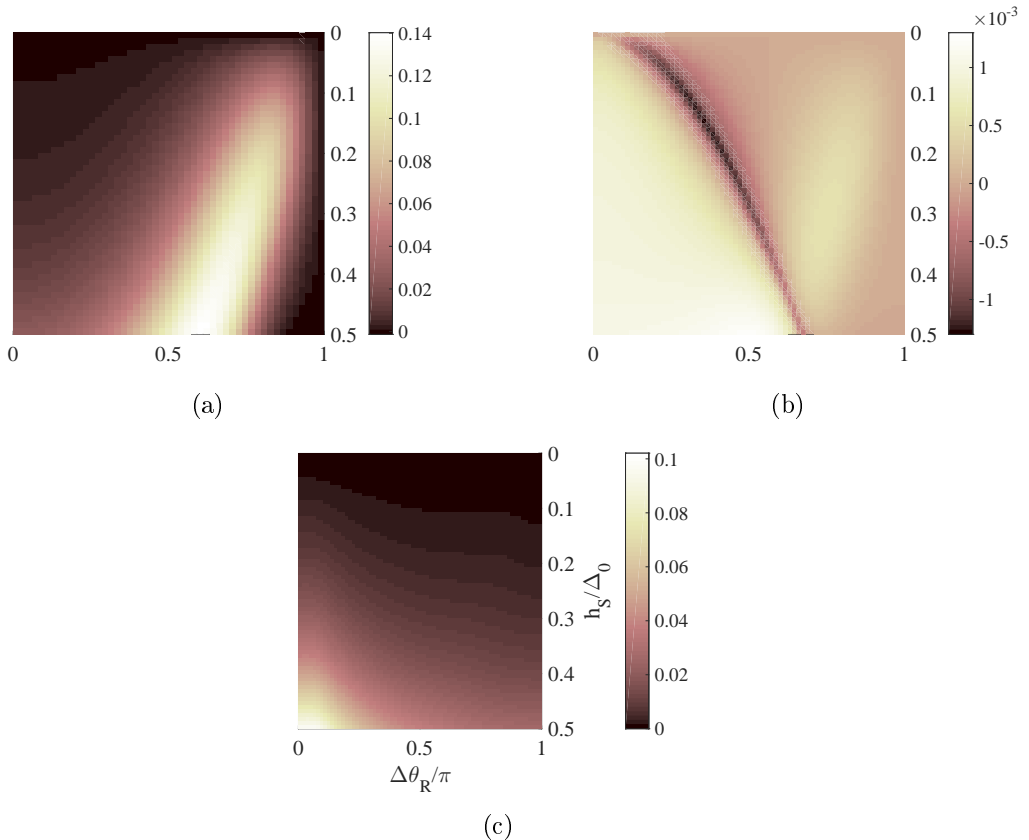
Figure 4.7: The figures show the thermoelectric coefficient $\alpha e/(G_T\Delta_0)$ arising in X/I/ZSNZS structures. Inelastic scattering is governed by $\Gamma = 0.005\Delta_0$ where $\Delta_0 = 1$ meV, $T = 0.2T_{c,0}$ and the polarization is $P = 97\%$. The figures show (a) a normal metal, (b) a superconductor and (c) a Zeeman-split superconductor occupying the left hand side of the interface. The right side of the barrier is occupied by a ZS/N/ZS Josephson junction where $L_{NM} \ll \xi$.

conductor or a Zeeman-split superconductor and the normal metal part of a Zeeman-split superconductor/normal metal/Zeeman-split superconducor (ZS/N/ZS) Josephson junction. In stark contrast to the bilayer case, the qualitative change in the thermo-electric coefficient is immense as the material to the left of the interface is changed. Where $\alpha$ was maximized for approximately the same parameters in the bilayer case, the extra element of control that is the superconducting phase difference results in the thermoelectric coefficient having radically different shapes depending on which material is on the left. As before the case of a conventional BCS superconductor minimizes $\alpha$ significantly when compared to the other two cases. Now, however, $\alpha$ is largest when a normal metal is on the left. This is however only true at the given temperature, and changes as the temperature is increased. When $T = 0.4T_{c,0}$, for instance, $\alpha$ is significantly larger in the X = ZS case than in the X = NM or the X = SC cases. As the temperature is increased, $\alpha$ increases and $ZT$ and $S$ decrease. The temperature

evolution of $\alpha$, $S$ and $ZT$ along with the fact that $\alpha = 0$ when $h_S = 0$ can be explained in the same manner as before.

A new feature to be noticed concerns $\alpha = 0$ when $\Delta\theta = \pi$ in the cases X = NM and X = SC. In both these cases the particle-hole asymmetry only exists in the Josephson junction to the right of the tunneling barrier. The thermoelectric coefficient therefore only exists if $D_R^z(E) \neq 0$. When $\Delta\theta = \pi$, the factor $\Delta^2 \cos^2\left(\frac{\Delta\theta}{2}\right) = 0$ from Eq. 4.15. The spin-dependent density of states in the normal-metal part of the Zeeman-split Josephson junction is

$$D_{ZS/N/ZS}^\sigma = \left| \text{Re}\left\{ \frac{E + \sigma h_S + i\Gamma}{\sqrt{(E + \sigma h_S + i\Gamma)^2 - 0}} \right\} \right| \tag{4.16}$$

$$= \left| \text{Re}\left\{ \frac{E + \sigma h_S + i\Gamma}{E + \sigma h_S + i\Gamma} \right\} \right| \tag{4.17}$$

$$= 1 \tag{4.18}$$

when the superconducting phase difference equals $\pi$, causing

$$D_R^z(E) = D_{ZS/N/ZS}^z(E) = 1 - 1 = 0 \tag{4.19}$$

for all values of $h_S$ and $T$. Accordingly, $\alpha = S = ZT = 0$ whenever $\Delta\theta = \pi$ if a particle-hole asymmetry exists on only one side of the junction. If a particle-hole asymmetry is present also to the left of the barrier, as in the case of a Zeeman-split superconductor on the left, $\alpha \neq 0$ when the superconducting phase difference on the right equals $\pi$. Accordingly, neither $\alpha$ nor $S$ and $ZT$ equal zero at $\Delta\theta = \pi$ if the difference in spin-dependent density of states to the left of the barrier is unequal to zero.

Another feature to notice can be found in Figure 4.7b. The sign of the thermoelectric coefficient can be switched upon tuning the magnetic exchange field and the superconducting phase difference. This was not possible without the Josephson junction, and also does not happen when the material to the left of the barrier was a normal metal or a Zeeman-split Josephson junction for the parameters chosen. The structure choice of superconductor/tunneling barrier/Zeeman-split Josephson junction, however, can result in pure thermal spin currents in which the dominating polarization direction can be changed by altering the superconducting phase difference. These spin currents are defined by $I_s = I_{\text{charge}}^\uparrow - I_{\text{charge}}^\downarrow = \alpha\Delta T/T$ when no other biases are applied, and if $\Delta T$ and $T$ are kept constant the entire spin current is governed by $\alpha$. If the sign of $\alpha$ changes so does the sign of $I_s$, and accordingly so does the spin current polarization. Mathematically, this can be explained by the integrand of $\alpha$. The superconducting DOS is able to enhance the negative aspects of the product of the factor $E$ and $D_{ZS}^z(E)$ sufficiently for $\alpha$ to be able to become negative. $D_{ZS}^z(E)$ is shown in Figure 4.8b for $h_S/\Delta_0 = 0.15$.

The thermoelectric coefficient governs the pure thermal spin current. As the density of states is unequal for the particles of each spin, the migration of species at the application of a thermal bias may be accompanied by a finite spin polarization. The amount of particles with enough energy to traverse the barrier with spin up may be greater or smaller than the particles with the same energies and the opposite spin state. Even though the charge current equals zero when the tunneling barrier is unpolarized, a spin current may exist. The fascinating feature studied here concerns the exchange field and superconducting phase difference being able to control the dominating polarization of the spin current. Both these parameters affect the density of states for each spin directly, and accordingly are able to control which spin species has the largest probability of occupation. This effect is not limited to the case of superconductor/insulator/Zeeman-split normal metal Josephson junction, as will be shown later on.





(a)                                                                   (b)
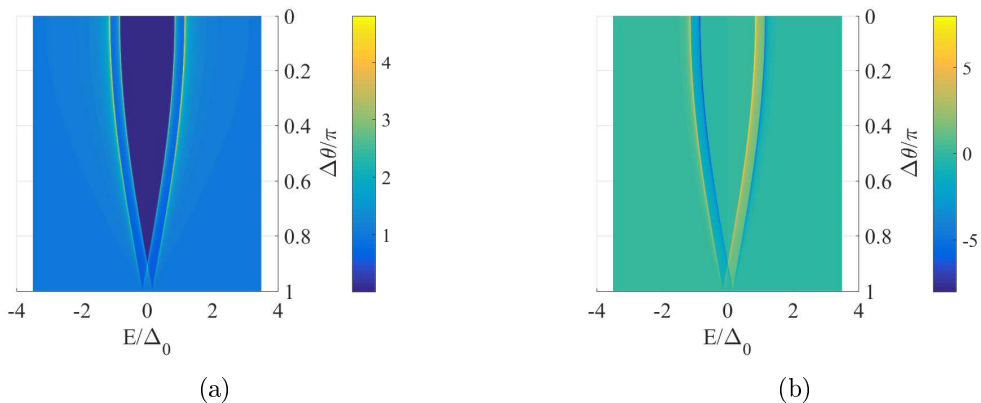
Figure 4.8:   (a) Density of states $D^0(E)$ and (b) difference in spin-dependent density of states $D^z(E)$ in a Zeeman-split superconductor/normal metal/Zeeman-split superconductor (ZS/N/ZS) Josephson junction where $L \ll \xi$, $T/T_{c0} = 0.2$, $\Gamma/\Delta_0 = 0.005$ representns inelastic scattering and $h_S/\Delta_0 = 0.15$ is the Zeeman field.

Figure 4.8 shows the (a) density of states and (b) difference in spin-dependent difference in the density of states within the normal metal of a Zeeman-split superconductor/normal metal/Zeeman-split superconductor Josephson junction with $h_S = 0.15\Delta_0$, as defined by Eq. 4.15. When the assumption is made that $L_N \ll \xi$, the density of states is assumed to be constant throughout the entirety of the normal metal nanowire. There is an asymmetry in the density of states which persists for all parameter choices until $\Delta\theta = \pi$, and at approximately $\Delta\theta = 0.9\pi$ a peak occurs, indicating triplet superconductivity within the normal metal nanowire. This is shown in Figure 4.8a. The interference of $D_{ZS}^z(E)$, shown in Figure 4.8b, with $D_L^0(E)$, $E$ and $C(E)$ can result in the sign of $\alpha$ changing with varying exchange field and phase difference.

Figure 4.9 shows $S$ and $ZT$ resulting from thermoelectric currents through tunneling from a doubly Zeeman-split Josephson junction to a material X, where X is (a)-(b) a normal metal, (c)-(d) a superconductor or (e)-(f) a Zeeman-split superconductor.
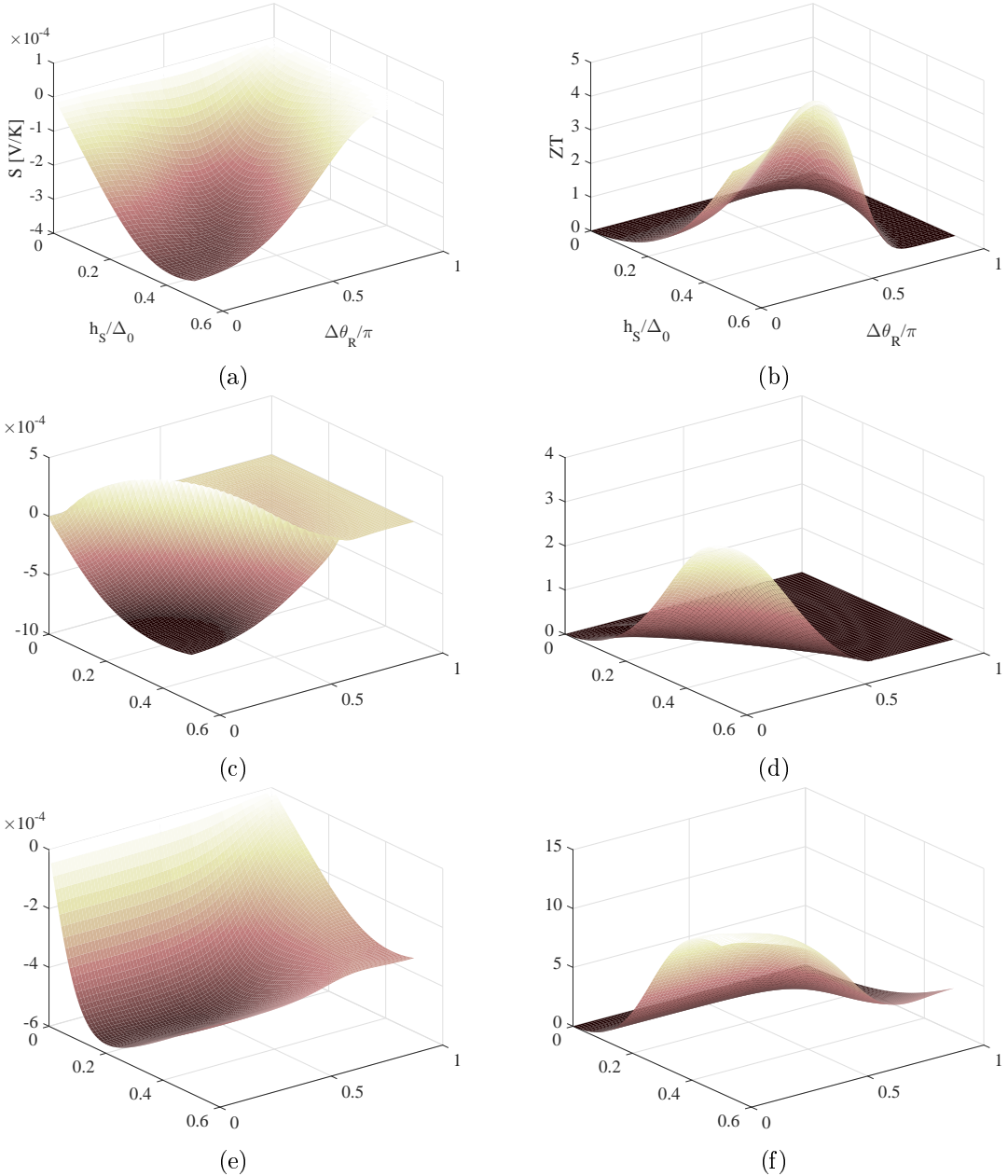
Figure 4.9: Seebeck coefficient $S$ (first column) and thermoelectric figure of merit $ZT$ (second column) in X/I/ZSNZS junction where X denotes (a)-(b) a normal metal, (c)-(d) a superconductor or (e)-(f) a Zeeman-split superconductor. Inelastic scattering is governed by $\Gamma = 0.005\Delta_0$ where $\Delta_0 = 1$ meV, $T = 0.2T_{c,0}$ and the polarization is $P = 97\%$.

When the Josephson junction is included, including spin-splitting on both sides of the tunneling barrier does not maximize all effects at the given temperature. At higher temperatures, assuming Zeeman-splitting on both sides of the junction does increase the thermoelectric effects when compared to considering normal metals or superconductors to the left of the barrier. At the temperature considered here, however, $\alpha$ is largest when the material on the left is a normal metal, $S$ is largest when it is a superconductor and $ZT$ is largest when a Zeeman-split superconductor is used.

The sizes of the thermoelectric effects arising in the hybrid structures containing Josephson junctions are remarkably large when considering the complexity of the systems. The thermoelectric figure of merit approaches 10 and the Seebeck coefficient is close to $-0.6$ meV in Figure 4.9f at zero superconducting phase difference, which approaches the maximum values of $ZT \approx 13$ and $S \approx -0.8$ meV found in the doubly Zeeman-split superconducting bilayer. However, as the largest thermoelectric effects are still to be found in the doubly-split superconducting bilayer the primary advantage to adding Josephson junctions to the mix would be the possibility of switching the polarization of a spin current *in situ* through tuning the exchange field or superconducting phase difference. Unfortunately $\alpha_{\max} \approx 10^{-3}$ at $T = 0.2T_{c,0}$ in the case where this occurs, with a superconductor to the left, which might not be sufficient to be useful.

### 4.1.3   Double Josephson junction

Following the consideration of the addition of one Josephson junction to the tunneling regime, we wanted to consider the effect of adding two. We therefore studied the effect of tunneling between the normal metal in a superconductor/normal metal/superconductor (S/N/S) Josephson junction and the normal metal in a Zeeman-split superconductor/normal metal/Zeeman-split superconductor (ZS/N/ZS) Josephson junction. A graphical visualization of the double Josephson junction structure can be found in Figure 4.10. The tunneling is supposed to occur in the purple area, where the centers of the normal metal parts of each Josephson junction are separated by an insulating material which can be polarized. The actual tunneling junction is accordingly a normal metal/insulator/normal metal (N/I/N) junction. The superconductors should not be in contact. We acknowledge that the experimental realization of such structures may result in significant challenges, but we nonetheless include the results due to their interesting nature. The density of states in a regular S/N/S Josephson junction is similar to the DOS in a Zeeman-split Josephson junction and given by

$$D_{S/N/S}^{\sigma} = \left| \mathrm{Re}\left\{ \frac{E + i\Gamma}{\sqrt{(E + i\Gamma)^2 - \Delta^2 \cos^2\left(\frac{\Delta\theta}{2}\right)}} \right\} \right|. \tag{4.20}$$

This is valid when the normal metal length $L_N$ is much smaller than the superconducting

coherence length $\xi$, and the density of states can be assumed constant across the entire length of the normal metal.
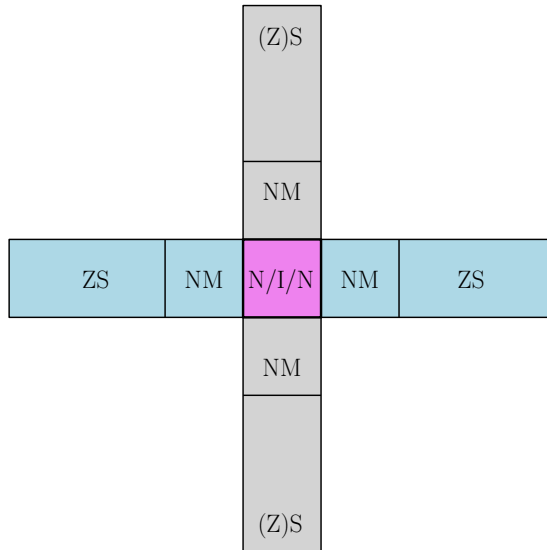


Figure 4.10: Schematic of the experimental setup considered, where a tunneling barrier (I) separates the normal metal parts of two Josephson junctions, at least one of which containing Zeeman-split superconductors.

Figure 4.11 shows (a)-(b) the thermoelectric coefficient, (c)-(d) the Seebeck coefficient and (e)-(f) the thermoelectric figure of merit resulting from quasiparticle tunneling between two Josephson junctions. The first column shows the case where the left-side junction is a superconductor/normal metal/superconductor (S/N/S) Josephson junction, while the right column shows the case where both structures are Zeeman-split normal-metal Josephson junctions. The results are qualitatively the same for different values of the exchange field $h_S$ and the temperature $T$, and therefore only one set of figures is included. The thermoelectric effects arising are seen to be almost equally large in both cases, surpassing the best semiconducting thermoelectric materials available and rivaling the Zeeman-split superconducting bilayers studied in the preceding section.

In addition to providing an extra element of control to the system the superconducting phase difference is shown to singlehandedly control both the size, shape and sign of the thermal spin currents arising as a result of tunneling across the junction between the two central normal metals. This phenomenon is quantitatively almost identical regardless of whether a S/N/S or ZS/N/ZS Josephson junction is situated to the right of the tunneling barrier and $\alpha$ varies between approximately the same values in both cases. Qualitatively, on the other hand, the effects vary radically. When tunneling between two Zeeman-split Josephson junctions is being considered, $\alpha$ is maximized when $\Delta\theta_L = \Delta\theta_R = \pi/2$. The Seebeck coefficient $S$ and thermoelectric figure of merit

(a)

(b)

(c)

(d)

(e)

(f)
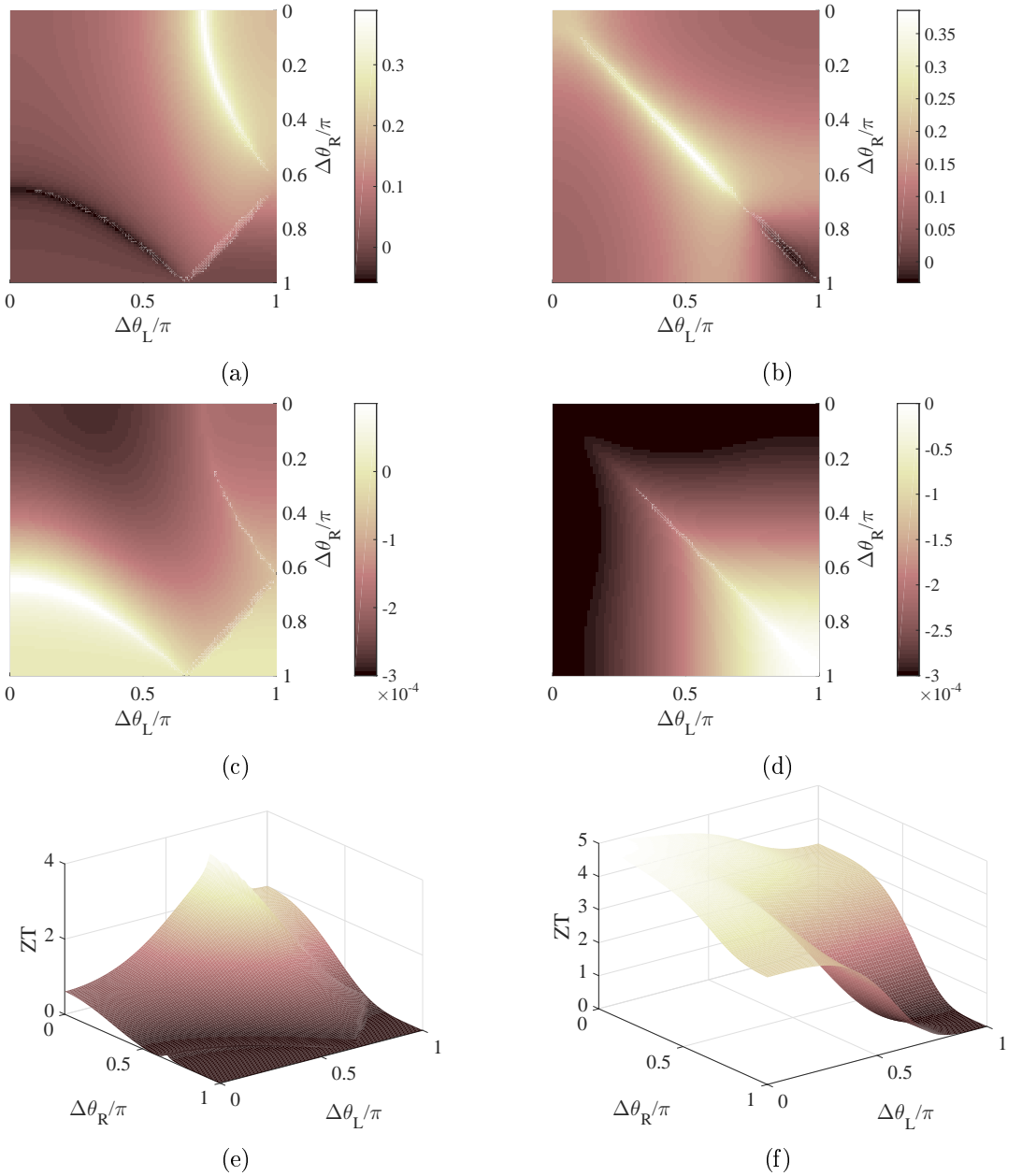
Figure 4.11: (a)-(b) Thermoelectric coefficient $\alpha e/(G_T \Delta_0)$, (c)-(d) Seebeck coefficient $S$ and (e)-(f) thermoelectric figure of merit $ZT$ for tunneling between (first column) a S/N/S Josephson junction and a ZS/N/ZS Josephson junction separated by a tunneling barrier between the normal metals and (second coulmn) two Zeeman-split ZS/N/ZS Josephson junctions where the normal metal nanowires are separated by a tunneling barrier. Inelastic scattering is governed by $\Gamma = 0.005\Delta_0$ where $\Delta_0 = 1$ meV and the polarization is $P = 97\%$. $L_N \ll \xi$ on both sides of the tunneling barrier. For the situation where only one Josephson junction contains Zeeman-split superconductors $T = 0.4T_{c,0}$ and $h_S = 0.5\Delta_0$, while in the other case $T = 0.3T_{c,0}$ and $h_S = 0.4\Delta_0$.

$ZT$ reach their maximum values when the superconducting phase difference equals zero on both sides of the insulating barrier.

As we would expect with respect to previous discussions the thermoelectric coefficient $\alpha$ equals zero when the superconducting phase difference on the right equals $\pi$ in the case of a S/N/S Josephson junction being present to the left of the barrier. When particle-hole asymmetry exists on both sides of the junction the thermoelectric coefficient is never identically equal to zero for all other parameters when one phase difference is set to $\pi$.

## 4.2 Low-field considerations

The substantial thermoelectric effects studied so far all require the application of large magnetic fields to arise. In light of possible application areas this is not desirable. Consequently, a goal of this work has been attempting to replicate the phenomena observed within Zeeman-split systems using other superconducting hybrid structures not requiring large applied fields. Thus, other ways of lifting the particle-hole symmetry for each spin had to be found. Within this section we will apply the framework for thermoelectric effects arising in systems with homogeneous magnetization derived in Chapter 3, and consider superconductor/normal metal/superconductor (S/N/S) Josephson junctions with aligned spin-active interfaces and superconductor/ferromagnet/superconductor (S/F/S) Josephson junctions where the ferromagnet has a head-to-head domain wall structure.

Analytical expressions for the superconducting density of states could be inserted directly into the formulas for the thermoelectric coefficients in order to obtain the results presented in the previous section. Here, we will consider thermoelectric phenomena in more complex hybrids with features that cannot be as simply described. The Keldysh Green function formalism outlined in Section 2.6 was employed when solving the Riccati parametrized Usadel equation in the middle of the normal metal or ferromagnet nanowire. The resulting values for the density of states were subsequently numerically integrated in order to quantify the thermoelectric parameters.

This section will focus on tunneling currents between normal metals on the one side of a tunneling barrier and more complex S/X/S Josephson junctions on the other as shown in Figure 4.12. Similar realized experimental setups can be found in Refs. [125] [126] [127]. The first step made when studying the thermoelectric response of complex superconducting hybrids is defining material parameters and boundary conditions at the S/X/S interfaces. Next, the Riccati-parametrized Usadel equation is solved in the middle of the central material. Following the calculation of the density of states at $x = 0.5L_X$, numerical integration in MATLAB was used to calculate the relevant thermoelectric coefficients. Accordingly, the results for the tunneling coefficients are primarily valid in the middle of the central Josephson junction material (X). Ideally,

the normal metal contact should be centered at $x = 0.5L_X$ and only be a few nanometers wide for the results presented herein to be as valid as possible. We realize that this may cause experimental concern, as metallic contacts of $5 - 6$ nm size are hard to achieve even using cutting-edge electron beam lithography technology. This will be discussed further at the end of this section. For a more thorough qualitative description of the numerical methods employed, see Appendix C.
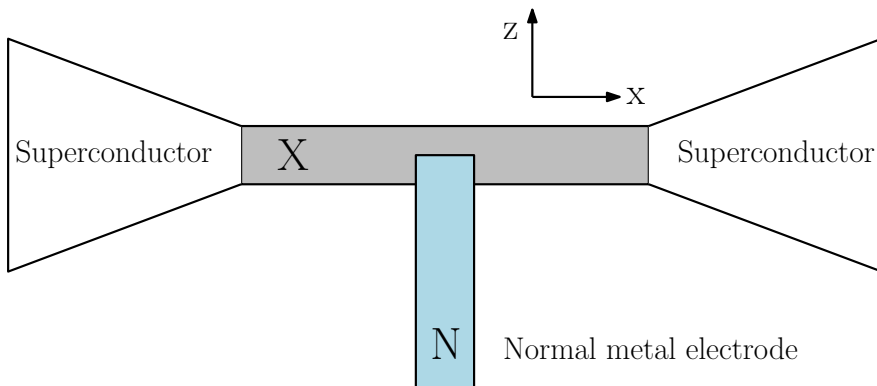


Figure 4.12: Schematic of the experimental setup considered whenever low-field thermoelectric effects are studied within this thesis. There is a tunneling barrier, which can be fully polarized, between the normal metal electrode N and the nanowire X centered between two superconducting reservoirs.

### 4.2.1   Josephson junction with spin-active interfaces

Superconductor/normal metal/superconductor Josephson junctions with magnetic or spin-active interfaces have been shown to give rise to particle-hole asymmetries, with densities of states which differ for the spin species [33][51][99]. The S/N interfaces are herein considered to be occupied by weakly polarized ferromagnetic insulators which are both polarized along the $+z$-axis. The Usadel equation was solved numerically using MATLAB to procure the density of states in the middle of the normal metal, utilizing the Kuprianov-Lukichev tunneling boundary conditions along with Cottet's boundary conditions for weakly polarized interfaces. To fulfill the demand of weakly polarized spin-active interfaces the parameters $G_{MR} = 0.1$ and $\zeta = 3$ were chosen to describe the magnetic tunneling interface. Moreover, the superconducting coherence length was defined as $\xi = 30$ nm. A schematic showing the spin-polarized Josephson junction and highlighting the polarization at the interfaces is presented in Figure 4.13.

The primary reason for using the boundary conditions for weakly polarized interfaces can be attributed to reducing the computation time. In order to ensure accuracy in the numerical integration, the Usadel equation was solved for 3500 energies and 24 phase differences for every single value of $G_\varphi$. Using the complete boundary conditions would have increased the computation time significantly, as the whole system would
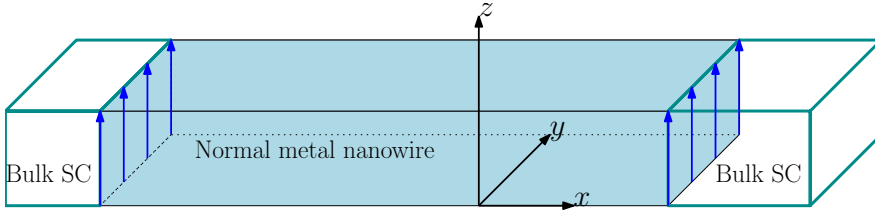
Figure 4.13: Schematic of a superconductor/normal metal/superconductor ($S/N/S$) Josephson junction with $z$-polarized spin-active interfaces. The superconductors are in reality very large when compared to the normal metal nanowire.

have become much more complex to solve numerically. The interface across which we consider the actual tunneling current can be completely polarized with $P = 100\%$, and we therefore do not consider the choice of weakly polarized interfaces to be a major limitation to the generality of the work.
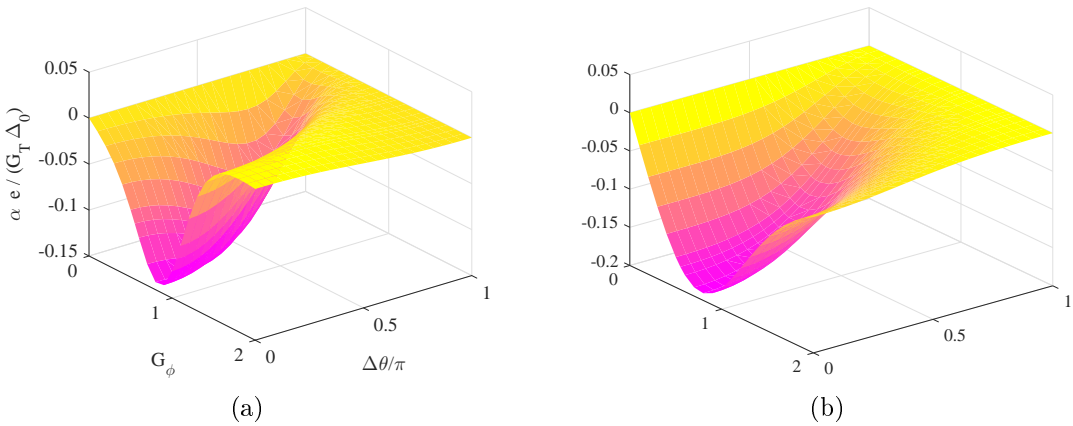


Figure 4.14: Thermoelectric coeffcient $\alpha$ in a N/I/SNS structure where the Josephson junction has $L_N = 15$ nm and spin active interfaces, both aligned in the $+z$-direction. (a) shows $T = 0.2T_{c,0}$, and (b) $T = 0.4T_{c,0}$. We have also used $\zeta = 3$, $\xi = 30$ nm, $P = 97\%$ for the N/I/N tunneling and $G_{MR} = 0.1$ for the S/N/S-tunneling.

Using numerical integration, the thermoelectric coefficients, Seebeck coefficient and thermoelectric figure of merit were calculated for various parameters. The thermoelectric coefficient $\alpha$ is presented for different temperatures in Figure 4.14, with (a) showing $T/T_{c,0} = 0.2$ and (b) showing $T/T_{c,0} = 0.4$. Here, the size of the thermoelectric coefficient $\alpha$ can become as large as $-0.2$ when $T = 0.4T_{c,0}$. This approaches the value attained in the $N/I/ZS$-bilayer, as shown in Figure 4.2a. However, when spin active interfaces in normal metal Josephson junctions are used, external magnetic fields need not be applied. This would be highly beneficial in light of possible application areas. Moreover, the superconducting phase difference provides an additional means of external control.
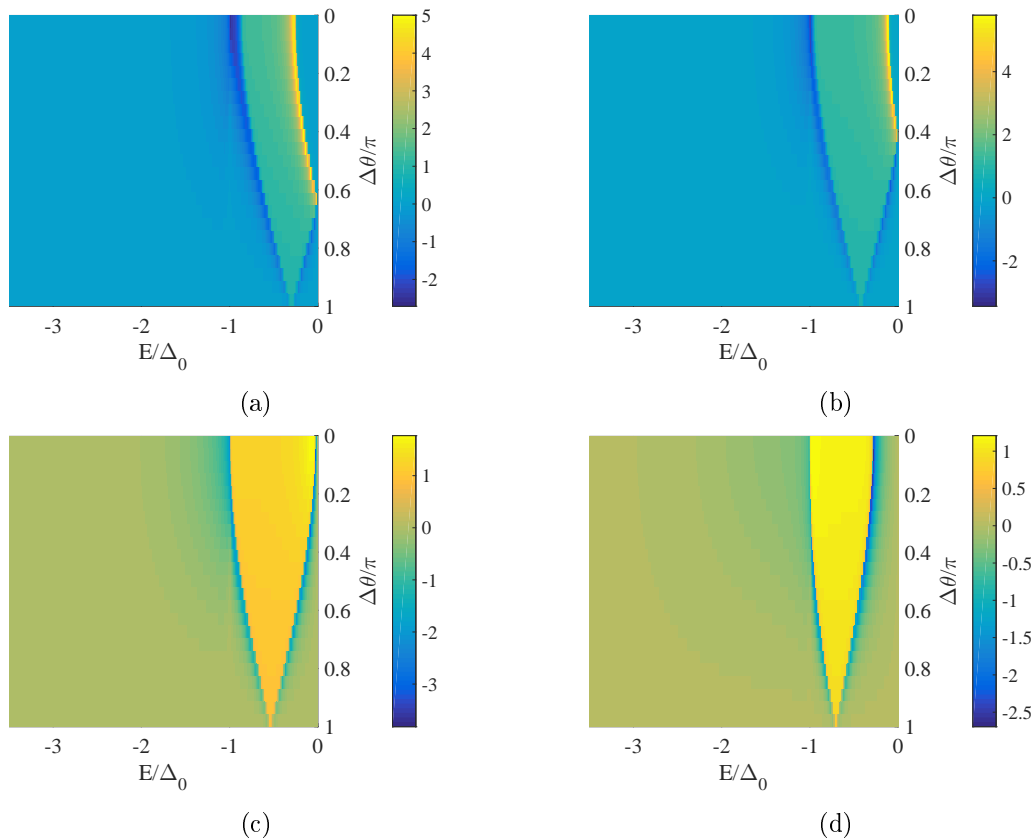
Figure 4.15: Difference in spin-dependent density of states, $D^z(E)$, in the middle of the normal metal of a S/N/S Josephson junction with spin-active interfaces. $L_N = 15$ nm, $\zeta = 3$, $\Gamma = 0.005\Delta_0$ The spin-dependent phase-shifts at the interfaces are governed by (a) $G_\phi = 0.55$, (b) $G_\phi = 0.8$ (c) $G_\phi = 1.05$ and (d) $G_\phi = 1.55$.

The thermoelectric coefficient varies with the superconducting phase difference and $G_\phi$, which represents the spin-dependency of the phase shifts arising due to scattering at the interfaces. This is not an ideal parameter to vary, as it is material specific and cannot be altered *in situ* or during operation. However, how $\alpha$ varies with $G_\phi$ is quite interesting. There seems to be an ideal value of $G_\phi$ where $|\alpha|$ is maximized, and this occurs at $G_\phi \approx 0.8$ and $\Delta\theta = 0$. When there is no superconducting phase difference, the supercurrents exiting both superconductors seem to enhance each other, generating large thermal spin currents or charge currents when $P \neq 0$. Once again, $\alpha$ is seen to increase with temperature as the distribution function broadens. The maximum value of $\alpha$ occurring at approximately $G_\phi = 0.8$ can be understood from considering the difference in the spin-dependent density of states, $D^z(E)$, in the middle of the normal metal. This is due to the thermoelectric coefficient becoming

$$\alpha = \frac{G_T}{2e} \int_{-\infty}^{\infty} \mathrm{d}E E D_L^z(E) C(E) \tag{4.21}$$

when the right-side electrode is a normal metal, and $D_L^z(E)$ is shown in Figure 4.15. The figure displays the difference in the density of states for the spin species at $x = 0.5L_N$ from $E = -3.5\Delta_0$ to $E = 0$, where $D_L^z(E)$ is antisymmetric about the zero-energy point. The thermoelectric coefficients are largest for zero superconducting phase difference because this is where the superconducting order in the normal metal is the strongest. As $G_\phi$ is increased from 0.55 in Fig. 4.15a to 0.8 in Fig. 4.15b, the asymptotic peaks approach $E = 0$ when $\Delta\theta = 0$. Consequently, the peaks become more likely to be encompassed by the distribution function $C(E)$ when $G_\phi = 0.8$ than when $G_\phi = 0.55$. As $G_\phi$ is increased further the zero-energy gap closes and is replaced by a zero-energy peak for all phase differences, indicating the presence of triplet superconductivity within the normal metal. Here, however, only one asymptotic peak contributes to the thermoelectric effects, and $D^z(E) = 0$ when the quasiparticle energy is just slightly greater than $E = 0$. Moreover, the actual size of the peaks is seen to decrease as $G_\phi$ is increased, and consequently make a smaller contribution to the total thermoelectric coefficient. At higher temperatures the distribution function is broader and able to encompass more and larger asymptotic peaks also for smaller and greater values of $G_\phi$ than 0.8, causing a larger maximum value for $\alpha$ persisting over a broader region of $G_\phi$. The densities of states do not change much as the temperature is increased, and are therefore only shown here for one temperature, $T = 0.2T_{c,0}$.

The size of the thermoelectric effects are further studied in Figure 4.16, which shows the (a)-(b) Seebeck coefficient and (c)-(d) thermoelectric coefficient at different temperatures. When $T = 0.2T_{c,0}$ $ZT$ can approach 2.5 and $S \approx 0.25$ meV. This rivals the capabilities of the best bulk room-temperature thermoelectrics presently available. As the temperature is further increased, these effects are once again diminished even as the thermal spin currents are enhanced. If the normal metal electrode is replaced by a superconducting electrode the sign of $\alpha$ can be altered through changing $G_\phi$ and the superconducting phase difference in the spin-active Josephson junction when $T = 0.2T_{c,0}$ and the remaining parameters are set as in Figure 4.14. This effect is however extremely small, and $\frac{\alpha e}{G_T \Delta_0} \approx 10^{-3}$ at best. Consequently this plot has not been included, but the effect should nonetheless be noted. The maximum values of $S$ and $ZT$ occur approximately at the same values of $G_\phi$ and $\Delta\theta$ as the maximum values of $\alpha$. As the thermoelectric coefficient vanishes when $G_\phi = 0$, $G_\phi = 2$ and $\Delta\theta = \pi$, so does $S$ and $ZT$.

At very small and very large values of $G_\phi$, the thermoelectric coefficient $\alpha$ approaches zero. This effect also occurs when $\Delta\theta = \pi$. As both these parameters are modified on the right-hand-side, the spin-active interface Josephson junction must be responsible. As $D_{NM}^0(E) = 1$ and does not equal zero in either of these cases, this implies $D_R^z(E) = D_{SNS}^z(E) = 0$ when $G_\phi = 0$, $G_\phi = 2$ and $\Delta\theta = \pi$. Consequently, in these cases,
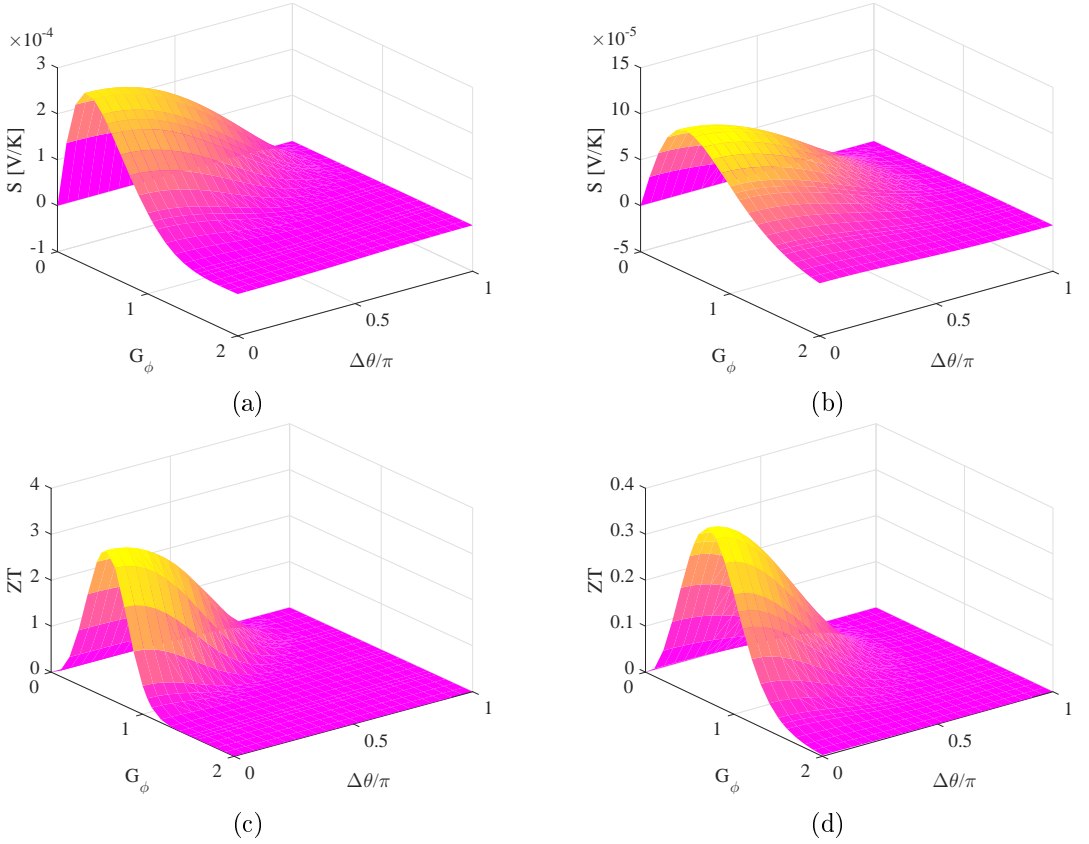
Figure 4.16: Seebeck coeffcient $S$ in the first row and thermoelectric figure of merit $ZT$ in the second in a N/I/SNS structure where the Josephson junction has spin active interfaces, both aligned in the $+\boldsymbol{z}$-direction, and $L_N = 15$ nm. The first column shows $T/T_{c,0} = 0.2$ and the second $T/T_{c,0} = 0.4$. We have also used $\zeta = 3$, $\xi = 30$ nm, $P = 97\%$ for the N/I/N tunneling and $G_{MR} = 0.1$ for the S/N/S-tunneling.

$D_{SNS}^{\uparrow} = D_{SNS}^{\downarrow}$ whenever these conditions are met. This could either mean that no supercurrent exists in the Josephson junction, as is the case when the interfaces are not spin-active, or simply that the particle-hole asymmetry necessary for thermoelectric effects to arise is suppressed at these values for the phase difference and the spin-dependent phase shifts. Figure 4.15 indicates that the features in the densities of states become vanishingly small at all four values of $G_\phi$ considered when the superconducting phase difference equals $\pi$. Accordingly, the corresponding features in $\alpha$ become minute when compared to the maximum values. When $G_\phi = 0$ and $G_\phi = 2$ there are no features within the scope of the distribution function $C(E)$ capable of contributing to the thermoelectric effects.

### 4.2.2 Spatially varying magnetization

Spatially varying magnetization within a superconductor/ferromagnet/superconductor Josephson junction should be capable of lifting the superconducting particle-hole symmetry and generating thermoelectric effects. The possible thermoelectric effects arising are however not necessarily expected to be very large, as the ferromagnetic exchange field is known to reduce or even destroy superconducting order leaking through the S/F interfaces. The magnetization in the ferromagnet nanowire varies spatially, and is in the shape of a head-to-head domain wall. Head-to-head domain wall ferromagnetism exists in, among others, magnetic strips of $Ni_{80}Fe_{20}$ [128] and Co rings [129]. We have chosen $L_F = 15$ nm as the ferromagnet nanowire length, $\zeta = 3$ to denote a tunneling interface and $\xi = 30$ nm as the superconducting coherence length. The domain wall is situated at $x_0 = L_F/2 = 7.5$ nm and the thickness of the domain wall is $\lambda = L_F/2 = 7.5$ nm. When considering thermoelectric phenomena in S/F/S Josephson junctions, the Usadel equation including ferromagnetic order was solved in the middle of the ferromagnetic nanowire. Regular Kuprianov-Lukichev tunneling boundary conditions were applied. The thermoelectric coefficient were subsequently calculated using numerical integration. Inverse proximity effects are once again disregarded.
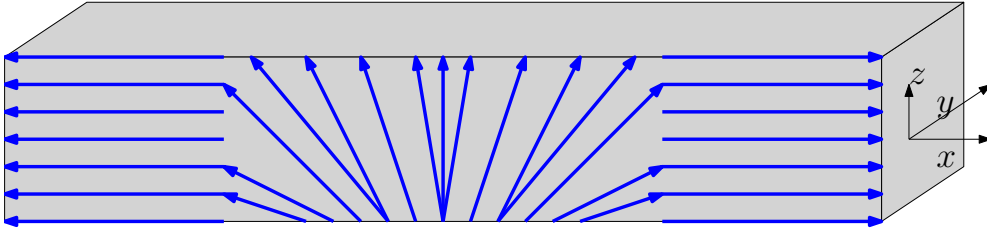


Figure 4.17: Schematic of the polarization in the ferromagnetic nanowire, where the shape of the polarization is that of a head-to-head domain wall. The length of the domain wall is $\lambda = L_F/2$.

The head-to-head domain wall is assumed to permeate the entire material, also in the **y**-direction, and is shown in Figure 4.17. The magnetization vector describing head-to-head domain wall ferromagnetism is defined by [83]

$$\boldsymbol{h}_{\mathrm{h2h}} = h_x \boldsymbol{x} + h_y \boldsymbol{y} + h_z \boldsymbol{z} \tag{4.22}$$

$$h_x = h \tanh\left(\frac{x - x_0}{\lambda}\right), \qquad h_y = 0, \qquad h_z = h \operatorname{sech}\left(\frac{x - x_0}{\lambda}\right). \tag{4.23}$$

Solving the Usadel equation in the middle of the ferromagnetic nanowire and applying the framework for thermoelectric tunneling currents in systems with homogeneous magnetization derived in Chapter 3 results in quantified thermoelectric coefficients. Figure 4.18 shows $\alpha$ for the head-to-head domain wall shown in Figure 4.17. The thermoelectric coefficient is essentially calculated at $x = 0.5L_F$. The maximum values for the

(a)                                        (b)
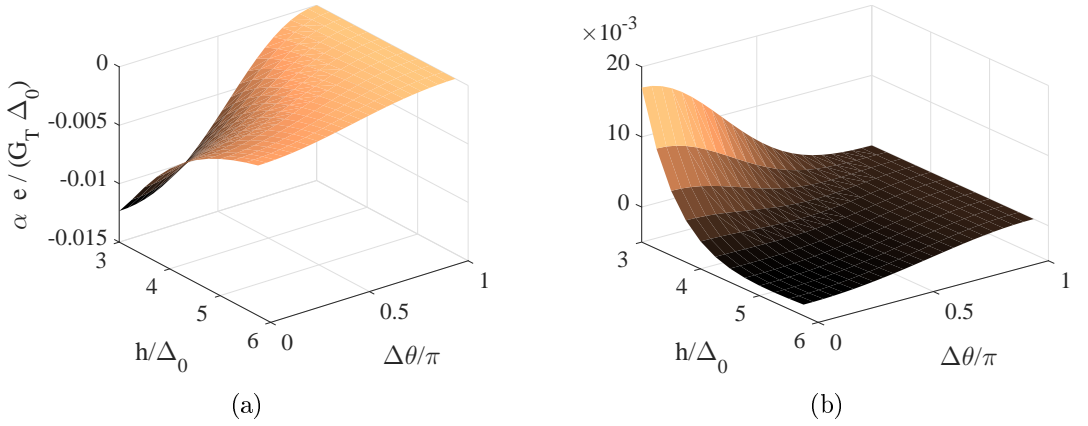
Figure 4.18: Thermoelectric coefficient $\alpha$ in a $N/I/SFS$ setup where (a) $T = 0.2T_{c,0}$ and (b) $T = 0.4T_{c,0}$. The ferromagnet nanowire contains a head to head domain wall where $\lambda = L_F/2$, $x_0 = L_F/2$, $\Gamma = 0.005\Delta_0$, and $L_F = 15$ nm.

thermoelectric coefficients can be found when the ferromagnetic exchange field strength if as small as possible. This is intuitively understandable from the pair-breaking effect of the ferromagnetic exchange field. Once again, increasing the temperature is seen to increase the size of $\alpha$. What is more, increasing the temperature actually changes the sign of $\alpha$ and consequently also of the thermal spin currents which can arise. As an increase in temperature from $0.2T_{c,0}$ to $0.4T_{c,0}$ does not alter the superconducting energy gap much, this is attributed to the influence of the distribution function $C(E) = [4k_BT \cosh^2\left(\frac{E}{2k_BT}\right)]^{-1}$ on the spin-dependent density of states.



(a)                                        (b)
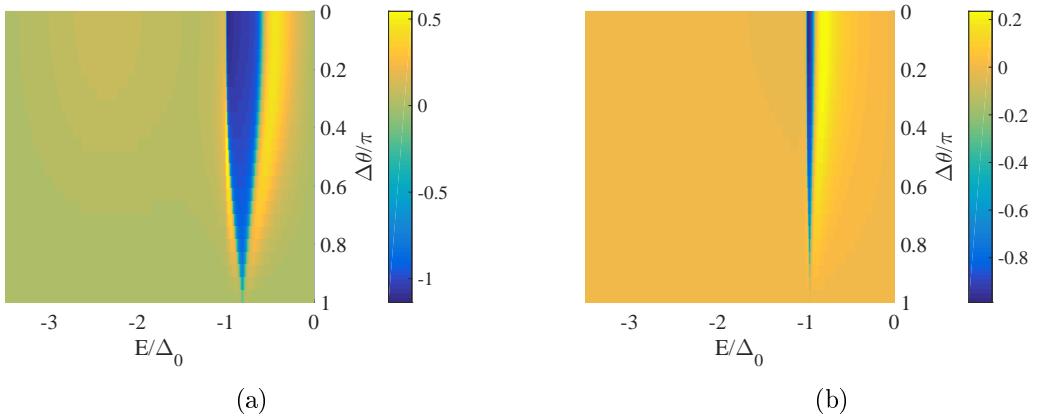
Figure 4.19: Difference in spin-dependent density of states $D^z(E)$ in the middle of the ferromagnet in a superconductor/ferromagnet/superconductor Josephson junction. The ferromagnetic exchange field is (a) $h = 3\Delta_0$ and (b) $h = 5.75\Delta_0$. The ferromagnet nanowire contains a head to head domain wall where $\lambda = L_F/2$, $x_0 = L_F/2$, $\Gamma = 0.005\Delta_0$, $T = 0.2T_{c,0}$ and $L_F = 15$ nm.

Figure 4.19 shows the difference in spin-dependent density of states $D^z(E)$ in the mid-

dle of the head-to-head domain wall ferromagnet in the superconductor/ ferromagnet/ superconductor Josephson junction. Figure 4.19a shows $D^z(E)$ when the ferromagnetic exchange field is at its lowest, $h = 3\Delta_0$, and Figure 4.19b shows the spin-dependent difference in density of states for the strongest ferromagnetic exchange field considered in this case, $h = 5.75\Delta_0$. The figures depict the densities of states, which are antisymmetric about $E = 0$, between the quasiparticle energies $-3.5\Delta_0$ and $0$. The superconducting order within the ferromagnet is seen to decrease as the exchange field strength increases. The thermoelectric coefficient $\alpha$ depends on the spin-dependent difference in density of states as $\alpha = \frac{G_T}{2e} \int_{-\infty}^{\infty} \mathrm{d}E E D_L^z(E) C(E)$, and consequently is reduced along with the reduction in $D^z(E)$. As the superconducting peaks within $D^z(E)$ become smaller with increasing exchange field, so does $\alpha$. Moreover, the peaks are seen to occur further from the zero energy point as the field becomes larger. Accordingly, they are encompassed by the distribution function $C(E)$ to a lesser degree, leading to smaller thermoelectric effects. The thermoelectric coefficient does not vanish entirely when $h = 5.75\Delta_0$ as long as the superconducting phase difference is small, but is seen to equal zero at phase difference $\pi$ for both temperatures considered. As the temperature is increased from $0.2T_{c,0}$ to $0.4T_{c,0}$ the distribution function widens, encompassing more of the superconducting peaks in the densities of states, allowing the thermoelectric coefficient to increase with temperature.

When $\Delta\theta = 0$, the thermoelectric coefficient reaches its maximum value as superconducting order in the middle of the ferromagnetic nanowire is at its strongest. When the superconducting phase difference equals $\pi$, however, the thermoelectric coefficient is seen to vanish and $\alpha = 0$. If we were to consider a case where the left-hand-side material contained a particle-hole asymmetry this would not necessarily be the case, as $D_{SFS}^z(E) = 0$ at $\Delta\theta = \pi$ is probably the explanation for the vanishing thermoelectric effects at this particular superconducting phase difference. However, this could significantly increase the complexity of the problem if for instance another Josephson junction was to be added. One could of course exchange the normal metal or superconducting electrode for a Zeeman-split superconductor, but this would require large applied magnetic fields and completely negate the purpose of considering Josephson junctions containing ferromagnetic domain wall nanowires in the first place.

The value of the exchange field $h$ greatly affects the thermoelectric coefficient. This is to a large degree as expected as a large ferromagnetic exchange field can tear the superconducting Cooper pairs leaking into the ferromagnetic nanowire apart, and thereby greatly diminish the proximity effect. As the existence of giant thermoelectric effects is largely dependent on the asymptotic nature of the superconducting density of states being present and sufficiently large, the ferromagnetic destruction of the supercurrent should be expected to result in fairly minute thermoelectric effects. The ferromagnetic exchange field strengths considered within this section range between $3\Delta_0$ and $5.75\Delta_0$. The end point was chosen as beyond this the thermoelectric features become vanishing. The starting point, on the other hand, could have been chosen to be smaller. This might have contributed to the thermoelectric effects becoming greater. However, the

choice was made to only consider fields greater than $3\Delta_0$ as this seems reasonable with what has shown to be experimentally feasible, exemplified by Ref. [130].
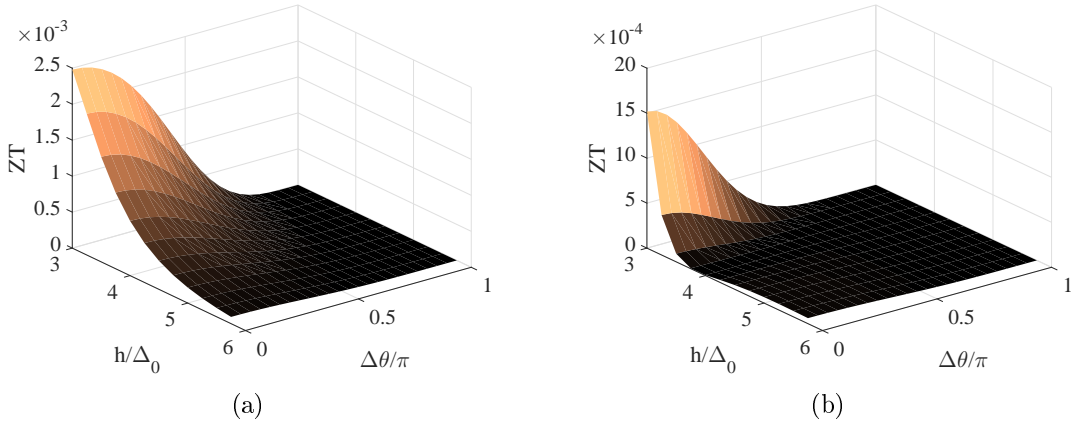


(a)                                              (b)

Figure 4.20: Dimensionless thermoelectric figure of merit $ZT$ in a $N/I/SFS$ setup where (a) $T = 0.2T_{c,0}$ and (b) $T = 0.4T_{c,0}$. The ferromagnetic nanowire contains a head to head domain wall where $\lambda = L_F/2$. $\Gamma = 0.005\Delta_0$ models the inelastic scattering, $P = 97\%$ and $L_F = 15$ nm.
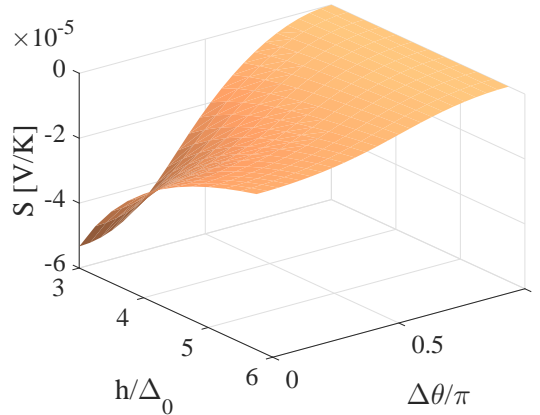


Figure 4.21: Seebeck coefficient $S$ for tunneling across the interface in a $S/I/SFS$ structure. The ferromagnet has a head-to-head domain wall structure with $\lambda = L_F/2$, $L_F = 15$ nm, $\Gamma = 0.005\Delta_0$, $T = 0.4T_{c,0}$ and $P = 97\%$.

Figure 4.20 shows the thermoelectric figure of merit $ZT$ for the same temperatures as $\alpha$. These are extremely small, just like $\alpha$, and the structures considered do not seem to be good hosts for thermoelectric phenomena. The largest values for the Seebeck coefficient are found when the normal metal is exchanged for a superconductor and the temperature is $T = 0.4T_{c,0}$, as shown in Figure 4.21. The Seebeck coefficients attained are not negligible, in contradiction to $\alpha$ and $ZT$, but are still not as prominent as we would like. The sizes of both $\alpha$, $S$ and $ZT$ are small enough for the structures considered to not be directly utilizable for practical applications. However, the results included

herein show how a ferromagnetic domain wall is able to generate an asymmetry for spin up and spin down particles. Different material parameters and magnetic configurations could counteract the pair-breaking effect of the ferromagnetic exchange field to a larger degree and contribute to enhancing the thermoelectric effects arising even further.

The reason for choosing the particular type of domain wall portrayed above concerns the nature of the expressions for the thermoelectric coefficients used in this chapter. As homogeneously polarization along only one is assumed, we need to consider structures where we can assume the polarization to be aligned in a certain direction, here defined as the $z$-direction, at $x = 0.5L_F$, the point at which the Usadel equation is solved numerically. The head-to-head domain wall satisfies these conditions. If we possessed a framework capable of describing thermoelectric effects within material systems having different and more complicated polarization configurations, we could study thermoelectric effects arising in Josephson junctions with even more exotic spatially varying magnetization structures, such as for instance conical ferromagnetism. This is done in Chapter 6, using the framework to be derived in Chapter 5.

## 4.3  Experimental considerations

This section provides a brief consideration of possible fabrication methods for the structures examined herein as well as a summary of the parameter choices made in the numerical calculations for the thermoelectric coefficients. The values used for the material-specific parameters such as the superconducting coherence length and energy gap are motivated by the corresponding parameters obtainable in existing materials.

Electron beam lithography (EBL) is commonly used when fabricating nanostructures. There are limits to how good the resolution can be in all nanofabrication methods, and EBL is no exception. The exact physical principles governing the EBL resolution limit are not thoroughly understood as of yet [131], but vast studies into this area are being conducted with the goal of pushing EBL resolution limits toward the sub-5 nm scale. Already in the year 2000 resolution of writing in the resist as small as 3 nm was possible, but actual practical resolution was limited by exposure, pattern transfer and development. 2 nm isolated featured sizes in the resist were obtained in 2013 [132]. Normal metal electrode widths of $3 - 5$ nm therefore seem to be extremely difficult to achieve, but not necessarily entirely impossible. Another possibility seems to be Extreme Ultraviolet Lithography (EUVL), where resolutions of 7 nm with possibilities of smaller nodes towards 2.5 nm were recently reported [133].

The structures considered within the first part of this chapter demand $L_N \ll \xi$ when Josephson junctions are considered. If materials with long superconducting coherence lengths are used, so $L_{NM} \ll \xi$ even when the normal metal length is around 15 nm, we believe most of the structures proposed to be achievable. The main problem is the right-hand-side normal metal electrode, as the tunneling currents are calculated at

$x = 0.5L_{NM}$. The density of states in the normal metals seems to be fairly consistent over a range of a few nanometers, but this electrode should ideally not be much wider than 5 nm in order to obtain good coherence between theory and experiment.

The thermoelectric effects predicted herein can easily be compared to the best values for $S$ and $ZT$ shown for state-of-the-art bulk thermoelectric materials. The best bulk thermoelectric materials, among others $CsBi_4Te_8$ and $Bi_2Te_3$, have thermoelectric figures of merit $ZT \approx 2$ [42, p. 82]. Figure 4.3 shows that this is far surpassed in the Zeeman-split bilayers, particularly in the case of double asymmetry, even when the Dynes parameter [66] $\Gamma = 0.005\Delta_0$ and inelastic scattering occurs at a fairly large rate. The use of such a large scattering rate could simplify the experimental realization of the effects theoretically shown, as it opens for a much broader range of possible materials than using for instance $\Gamma = 10^{-6}\Delta_0$ would. The choice of $\Gamma = 0.005\Delta_0$ for the Dynes parameter modeling inelastic scattering is quite large, and results in fairly heavy suppression of the BCS coherence peaks. However, this choice allows for a wider range of possible materials to choose from for experimental realization. The Dynes parameter in Al, for instance, is often modeled as $\Gamma \approx 10^{-4}\Delta_0$. The superconducting gap parameter is chosen as $\Delta_0 = 1$ meV for all calculations within this thesis. The value choice for the superconducting gap parameter was made without a specific material in mind, but is not unreasonable as it takes the values 0.18, 1.35 and 1.50 meV for Al, Pb and Nb, respectively [124, p. 79].

The superconducting coherence length $\xi$ plays an important role when choosing superconductors for possible experimental realization of the various setups suggested throughout this thesis. This is particularly true in Sections 4.1.2 and 4.1.3, where a number of the structures considered consist of Josephson junctions with $L_N \ll \xi$. If $\xi = 30$ nm, which is close to the coherence length of Niobium (Nb) with $\xi_0 = 35$ nm [63], the accurate realization of the theories presented requires $L_N \approx 2$ nm. This may pose significant problems from a fabrication perspective. However, if one chooses a material with a larger $\xi$, this problem is diminished. Possible material choices, which are still type I superconductors and adhere to the BCS theory of superconductivity, are for instance aluminum (Al) with $\xi_0 = 1600$ nm, and lead (Pb) with $\xi_0 = 90$ nm [124, p. 79]. $\xi_0$ is the bulk superconducting coherence length at zero temperature, and depends on temperature [134] and thickness if the superconductor is a thin film [24]. For thin film Al, coherence lengths are typically around $\xi \approx 100$ nm [135].

When considering S/N/S Josephson junctions with spin-active interfaces in Section 4.2.1 the superconducting coherence length was defined as $\xi = 30$ nm in analogy with NbN. Magnetic insulators such as EuS [24] or EuO [136] could be used at the S/N interfaces. The superconducting critical temperature of NbN is $T_c = 14$ K, which is easier to achieve experimentally than when using for instance Al, which has $T_c = 1.2$ K. The tunneling from the center of the normal metal nanowire in the Josephson junction and into the normal metal electrode is governed by $P = 97\%$ as the interface polarization, when we consider $P \neq 0$. This value was chosen as similar polarizations

are attainable in ferromagnetic insulators such as GdN at 3 K [68]. This is well within the superconducting critical temperature of NbN with $T_c = 14K$. As we primarily consider $T = 0.2T_{c0} = 2.8$ K for NbN, the achievement of $P = 97\%$, $T = 0.2T_{c,0}$ and $\xi = 30$ nm at the same time does not seem impossible. This is, of course, dependent on the growth compatibility of the materials chosen.

From en experimental perspective, the temperature gradient crucial to attaining the thermoelectric effects which are the focus point of this chapter can be applied through shining a laser onto the material on one side of the tunneling interface. For instance, in the case of a normal metal on the right-hand-side and an S/X/S structure on the left-hand-side as shown in Figure 4.12, the normal metal can be heated through using a laser while the more complex S/X/S structure is kept at a constant temperature. The possible application of spin-dependent biases complicates matters greatly. In addition to already considering a fairly complicated N/I/SXS-structure, ferromagnetic materials need to be added to the normal metal electrode and subsequently heated to different temperatures. This could, understandably, induce significant concern for the possibility of experimental realization.

## 4.4 Summary and discussion

The goal of this chapter was to study the thermoelectric effects arising in homogeneously magnetized superconducting tunneling hybrids in which the particle-hole symmetry is broken. The framework used for the relevant thermoelectric coefficient was presented and derived in Chapter 3. The tunneling junctions can be divided into two categories, one including Zeeman-split superconductors and one focusing on low-field thermoelectric effects. The Zeeman-split hybrids were all described using analytical expressions for the densities of states. The low-field hybrids studied herein were considered using numerical methods, and include superconductor/ferromagnet/superconductor Josephson junctions coupled to a normal-metal electrode where the ferromagnet has a head-to-head domain wall structure, and superconductor/normal metal/superconductor Josephson junctions coupled to a normal-metal electrode where magnetic insulators, weakly polarized along the same axis, are situated at the superconductor/normal metal interfaces.

The largest thermoelectric effects are seen to arise in doubly Zeeman-split superconducting bilayers, where two Zeeman-split superconductors are separated by a polarized tunneling interface (ZS/I/ZS). The thermoelectric coefficient is in this case able to reach values of $\alpha e/(G_T \Delta_0) \approx 0.6$, whereas the normal metal/insulator/Zeeman-split superconductor (N/I/ZS) thermoelectric coefficient can approach $\alpha e/(G_T \Delta_0) \approx 0.25$. This coefficient is able to govern the thermal spin currents $I_s = \alpha \Delta T/T$. In order to compare the thermoelectric efficiency of the Zeeman-split bilayers to state-of-the-art thermoelectric materials the Seebeck coefficient and thermoelectric figure of merit are studied, which can reach $S = -0.8$ meV and $ZT = 15$ in the Zeeman-split ZS/I/ZS

bilayer, and $S = -0.3$ meV and $ZT = 5$ in the N/I/ZS bilayer. The thermoelectric effects in both these bilayer configurations are seen to rival or surpass those achievable in state-of-the-art bulk thermoelectric materials at room temperature.

Adding Zeeman-split Josephson junctions (ZS/N/ZS) to the mix allows for the additional element of control which is the superconducting phase difference while retaining large Seebeck coefficients and thermoelectric figures of merit. The most interesting effect of this addition is the possibility of switching the sign of the thermoelectric coefficient $\alpha$, and thereby also of the thermal spin current, by altering the superconducting phase difference. This is seen to be possible for tunneling between a superconductor and the normal metal in a ZS/N/ZS Josephson junction, between a S/N/S and a ZS/N/ZS Josephson junction and between the normal metals of two ZS/N/ZS Josephson junctions.

Other notable trends throughout include the thermoelectric coefficient increasing and the Seebeck coefficient and thermoelectric figure of merit decreasing as the temperature is raised. This was attributed to the broadening of the distribution function $C(E) = [4k_BT\cosh^2\left(\frac{E}{2k_BT}\right)]^{-1}$ as the temperature is increased. Additionally, when Josephson junctions are considered, the thermoelectric effects disappear when the superconducting phase difference equals $\pi$ if the particle-hole asymmetry exists on only one side of the tunneling interface. This should be true as long as triplet superconductivity does not arise when $\Delta\theta = \pi$, which is not observed within this chapter.

The main drawback to using Zeeman-splitting to obtain the large thermoelectric effects observed herein is related to the large magnetic fields which must be applied for the necessary particle-hole asymmetry to arise. Consequently, structures containing spin-active Josephson junction interfaces and spatially varying magnetization were studied with the goal of obtaining large thermoelectric effects. The superconductor/ferromagnet/superconductor Josephson junction with a head-to-head domain wall centered in the middle of the ferromagnetic nanowire did display small thermoelectric effects, but they are far away from the desired size. Spatially varying magnetization shows promise, but the ferromagnetic exchange field destroys superconducting order too rapidly for large thermoelectric effects to arise in the domain wall configuration. Spin-active interfaces in superconductor/normal metal/superconductor Josephson junctions, however, display large thermoelectric effects. When the temperature is $T = 0.4T_{c,0}$ the thermoelectric coefficient can reach the value $\alpha_{\max} = -0.2$ for a spin-dependent interface phase shift parameter choice of $G_\phi \approx 0.8$. At this temperature the Seebeck coefficient and thermoelectric figure of merit are not very large, but when $T = 0.2T_{c,0}$ they can reach $S = 0.25$ meV and $ZT = 3$. This rivals what is achievable in the normal metal/insulator/Zeeman-split superconductor (N/I/ZS) configuration, and is close to surpassing effects in existing state-of-the-art thermoelectric materials. Of the two control parameters for the Josephson junction with spin-active interfaces $G_\phi$ and $\Delta\theta$, only the superconducting phase difference can be altered *in situ*. Accordingly, we have only one element of experimental control as $G_\phi$ is a material parameter. However, the

superconducting phase difference is able to cause large changes in the thermoelectric effects, as large variations are seen upon tuning the phase difference between 0 and $\pi$. What is more, the suppression of the thermoelectric effects at the superconducting phase difference of $\pi$ allows us to turn the large thermal charge and spin currents on and off merely through tuning the superconducting phase difference. As mentioned briefly previously, this can be compared to the working principle of a transistor. Especially the configuration of a normal metal coupled via a tunneling interface to the middle of the normal metal in a superconductor/normal metal/superconductor Josephson junction with spin-active interfaces, harbors the potential of functioning as a spin transistor driven by a thermal bias and controlled by the superconducting phase difference.

Within this chapter, we have only studied Josephson junctions where the lengths of the central material either is much smaller than the superconducting coherence length, or where the length of the central material equals 15 nm. The latter choice was made in order to remain closer to what is experimentally achievable, as was discussed in the previous section. If smaller central nanowire lengths than 15 nm were to be used, however, the thermoelectric effects calculated for the S/F/S domain wall Josephson junction and the S/N/S Josephson junction with spin-active interfaces are expected to increase significantly. Consequently, there is a chance that the thermoelectric effects in structures with critical dimensions approaching the sub-5 nm regime may surpass even those achievable in the doubly Zeeman-split ZS/I/ZS bilayers.

# Chapter 5

# Quasiclassical approach to thermoelectric effects for arbitrary spin-dependent fields

The method outlined in Chapter 3 depends on a very important assumption. Throughout the entire derivation, all spins have been assumed to be polarized along the same axis. When considering materials such as conical ferromagnets or nanowires exhibiting spin-orbit coupling, this course of action will not yield accurate results as the spin polarization must here be considered along more than one axis. Therefore, it is desirable to consider tunneling currents of spin, heat and charge without needing to consider the spin-dependent density of states explicitly. We have therefore applied the approach suggested in Refs. [96] and [137]. The tunneling charge, spin and heat currents are here expressed in terms of the quasiclassical Green function matrices presented in Section 2.6 instead of in terms of the densities of states. The currents are subsequently Taylor expanded to the first order with the goal of obtaining expressions for the thermoelectric coefficients, Seebeck coefficient and the thermoelectric figure of merit. The resulting expressions will be applied to theoretical material systems in Chapter 6.

The material systems to be considered are tunneling hybrids, where an electrode on the right is separated from a superconductor/X/superconductor Josephson junction on the left via an insulating barrier. This barrier has a transparency in the tunneling limit, and any interface polarization. We therefore apply Eschrig's boundary conditions, derived in Ref. [95] and presented in Equation 2.40. The thermoelectric coefficients derived will first be presented as generally as possible, where nothing is assumed about the left or right side materials. Thereafter, the right hand side electrode will be assumed to be a normal metal. This simplifies the expressions a great deal, and is done as these are the material systems to be considered in Chapter 6.

## 5.1   Initial definitions

The charge, spin and heat currents to be considered are defined by

$$
I_q = \frac{N_0 e D A}{4} \int_{-\infty}^{\infty} \mathrm{d}E \, \mathrm{Tr} \left\{ \hat{\rho}_3 [\check{\boldsymbol{g}}_R (\partial_x \check{\boldsymbol{g}}_R)]^K \right\} \tag{5.1}
$$

$$
I_s^\nu = \frac{N_0 D A}{8} \int_{-\infty}^{\infty} \mathrm{d}E \, \mathrm{Tr} \left\{ \hat{\rho}_3 \hat{\tau}_\nu [\check{\boldsymbol{g}}_R (\partial_x \check{\boldsymbol{g}}_R)]^K \right\} \tag{5.2}
$$

$$
\dot{Q} = \frac{N_0 D A}{4} \int_{-\infty}^{\infty} \mathrm{d}E (E - \mu_L) \, \mathrm{Tr} \left\{ [\check{\boldsymbol{g}}_L (\partial_x \check{\boldsymbol{g}}_L)]^K \right\}. \tag{5.3}
$$

$I_q$ is the charge current within the electrode to the right of the barrier and $I_s^\nu$ represents the spin current in each of the directions $\nu = \{x, y, z\}$ within the electrode to the right of the barrier. The energy or heat current $\dot{Q}$ is defined as traveling from the left to the right side of the barrier. The spin currents described herein are not the same currents as the ones studied in Chapters 3 and 4. The tunneling spin currents studied within the framework for homogeneously magnetized systems encompassed the net spin polarization accompanying the tunneling quasiparticle charge current. Within this section, the starting point for the charge and spin thermoelectric coefficients is not the same, as seen from equations 5.1-5.3. Accordingly, the prefactors of the charge and spin thermoelectric coefficients are expected to differ. In order to be able to describe even strongly spin-polarized tunneling interfaces, we will use Eschrig's boundary conditions:

$$
\check{\boldsymbol{g}}_R \partial_x \check{\boldsymbol{g}}_R = \frac{1}{4e^2 N_0 D A} [G_0 \check{\boldsymbol{g}}_L + G_{MR} \{\check{\boldsymbol{\kappa}}, \check{\boldsymbol{g}}_L\} + G_1 \check{\boldsymbol{\kappa}} \check{\boldsymbol{g}}_L \check{\boldsymbol{\kappa}} - i G_\phi \check{\boldsymbol{\kappa}}', \check{\boldsymbol{g}}_R] \tag{5.4}
$$

$$
\check{\boldsymbol{g}}_L \partial_x \check{\boldsymbol{g}}_L = -\frac{1}{4e^2 N_0 D A} [G_0 \check{\boldsymbol{g}}_R + G_{MR} \{\check{\boldsymbol{\kappa}}, \check{\boldsymbol{g}}_R\} + G_1 \check{\boldsymbol{\kappa}} \check{\boldsymbol{g}}_R \check{\boldsymbol{\kappa}} - i G_\phi \check{\boldsymbol{\kappa}}', \check{\boldsymbol{g}}_L]. \tag{5.5}
$$

This is done as the Usadel equation does not need to be solved in this case, and therefore the complexity of the expression does not pose a problem. The charge, spin and heat currents thus become

$$
I_q = \frac{1}{16e} \int_{-\infty}^{\infty} \mathrm{d}E \, \mathrm{Tr} \{ \hat{\rho}_3 [G_0 \check{\boldsymbol{g}}_L + G_{MR} \{\check{\boldsymbol{\kappa}}, \check{\boldsymbol{g}}_L\} + G_1 \check{\boldsymbol{\kappa}} \check{\boldsymbol{g}}_L \check{\boldsymbol{\kappa}} - i G_\phi \check{\boldsymbol{\kappa}}', \check{\boldsymbol{g}}_R]^K \} \tag{5.6}
$$

$$
I_s^\nu = \frac{1}{32e^2} \int_{-\infty}^{\infty} \mathrm{d}E \, \mathrm{Tr} \{ \hat{\rho}_3 \hat{\tau}_\nu [G_0 \check{\boldsymbol{g}}_L + G_{MR} \{\check{\boldsymbol{\kappa}}, \check{\boldsymbol{g}}_L\} + G_1 \check{\boldsymbol{\kappa}} \check{\boldsymbol{g}}_L \check{\boldsymbol{\kappa}} - i G_\phi \check{\boldsymbol{\kappa}}', \check{\boldsymbol{g}}_R]^K \} \tag{5.7}
$$

$$
\dot{Q} = -\frac{1}{16e^2} \int_{-\infty}^{\infty} \mathrm{d}E E \, \mathrm{Tr} \{ [G_0 \check{\boldsymbol{g}}_R + G_{MR} \{\check{\boldsymbol{\kappa}}, \check{\boldsymbol{g}}_R\} + G_1 \check{\boldsymbol{\kappa}} \check{\boldsymbol{g}}_R \check{\boldsymbol{\kappa}} - i G_R^\phi \check{\boldsymbol{\kappa}}', \check{\boldsymbol{g}}_L]^K \}. \tag{5.8}
$$

The interface parameters are defined as

$$G_0 = G_q \sum_{nl}^{N} \tau_{nl}(1 + \sqrt{1 - P_{nl}^2}), \quad G_1 = G_q \sum_{nl}^{N} \tau_{nl}(1 - \sqrt{1 - P_{nl}^2}) \quad (5.9)$$

$$G_{MR} = G_q \sum_{nl}^{N} \tau_{nl} P_{nl}, \quad G_\phi = 2G_q \sum_{n}^{N} \theta_{nn} \quad (5.10)$$

where $G_q = e^2/h$ is the conductance quantum. By assuming a channel-diagonal scattering matrix, where the scattering is equal for all channels and $n = l$, $\kappa' = \kappa$. Consequently, we only have to consider

$$G_0 = NG_q\tau(1 + \sqrt{1 - P^2}), \quad G_1 = NG_q\tau(1 - \sqrt{1 - P^2}) \quad (5.11)$$

$$G_{MR} = NG_q\tau P, \quad G_\phi = 2G_q \sum_{n}^{N} \theta_{nn}. \quad (5.12)$$

The procedure to be used when obtaining expressions for the thermoelectric coefficients within this section is identical to the one used in the previous section. The currents $J = \{I_q, I_s^\nu, \dot{Q}\}$ will be Taylor expanded to linear order as

$$J \approx \frac{\mathrm{d}J}{\mathrm{d}V_R}(V_R - V_{R,0}) + \frac{\mathrm{d}J}{\mathrm{d}V_L}(V_L - V_{L,0}) + \frac{\mathrm{d}J}{\mathrm{d}T_R}(T_R - T_{R,0}) + \frac{\mathrm{d}J}{\mathrm{d}T_L}(T_L - T_{L,0}) \quad (5.13)$$

$$= \frac{\mathrm{d}J}{\mathrm{d}V_R}\Big|_{(V_0,T_0)}(V_R) + \frac{\mathrm{d}J}{\mathrm{d}T_R}\Big|_{(V_0,T_0)}(T_R - T) + \frac{\mathrm{d}J}{\mathrm{d}T_L}\Big|_{(V_0,T_0)}(T_L - T) \quad (5.14)$$

about the point $(V_{j,0}, T_{j,0}) = (V_0, T_0) = (0, T)$. Spin dependent biases are not regarded within this section. Accordingly, as a $4 \times 4$ Onsager response matrix will not be derived regardless, the spin heat current is not considered within this framework. The spin heat current is not essential when considering thermoelectric effects, and is not needed when deriving the thermoelectric coefficients.

The $8 \times 8$ Green function matrices $\check{\boldsymbol{g}}_j$ are defined as

$$\check{\boldsymbol{g}}_j = \begin{pmatrix} \hat{\boldsymbol{g}}_j^R & \hat{\boldsymbol{g}}_j^K \\ \boldsymbol{0} & \hat{\boldsymbol{g}}_j^A \end{pmatrix}, \quad (5.15)$$

where $j = \{L, R\}$. We are considering the case of non-equilibrium tunneling across a barrier. Therefore, the $4 \times 4$ Green function matrices must be expressed in terms of each other as

$$\hat{\boldsymbol{g}}_j^A = -\hat{\rho}_3 \hat{\boldsymbol{g}}_j^{R\dagger} \hat{\rho}_3 \quad (5.16)$$

and

$$\hat{g}_j^K = \hat{g}_j^R \hat{h}_j - \hat{h}_j \hat{g}_j^A. \tag{5.17}$$

First, each of the currents will be expressed in therms of the retarded Green function matrices $\hat{g}^R$. This procedure is rather extensive, and can be found in Appendix B. Thereafter, a Taylor expansion in each of the four variables $(V_j, T_j)$ will be performed about the point $(0, T)$ in order to obtain the new thermoelectric coefficients. The form of $\hat{h}_L$ and $\hat{h}_R$ depends on the electronic structure of the material to be considered. Prior to differentiation, the voltage biases are defined as

$$\mu_L = 0, \qquad \mu_R = eV_R. \tag{5.18}$$

The left-hand-side bias is defined to be zero for reference due to the fact that we do not know the electronic structure of this material. Furthermore, local thermal equilibrium on each side of the tunneling barrier is assumed. Consequently, $\hat{h}_L$ becomes the equilibrium matrix

$$\hat{h}_L = \tanh\left(\frac{E}{2k_B T_L}\right)\hat{1} = \tanh\left(\frac{\beta_L E}{2}\right)\hat{1}. \tag{5.19}$$

The right-hand-side material, a normal metal electrode in Chapter 6, is described by the non-equilibrium matrix

$$\hat{h}_R = \begin{pmatrix} \tanh\left(\frac{\beta_R}{2}(E + eV)\right)\bar{1} & \bar{0} \\ \bar{0} & \tanh\left(\frac{\beta_R}{2}(E - eV)\right)\bar{1} \end{pmatrix}. \tag{5.20}$$

The framework derived can be applied to all material systems which can be described by these two matrices. The polarization matrix of the interface I between the electrode and the S/X/S Josephson junction, $\check{\kappa}$, is defined as

$$\check{\kappa} = \vec{m}\vec{\check{\sigma}}. \tag{5.21}$$

$\vec{\check{\sigma}}$ is the Pauli vector in $8 \times 8$ Keldysh space, $\vec{\check{\sigma}} = \vec{\hat{\sigma}}\check{1}$ and

$$\vec{\hat{\sigma}} = \begin{pmatrix} \vec{\sigma} & \bar{0} \\ \bar{0} & \vec{\sigma}^* \end{pmatrix}. \tag{5.22}$$

Defining the magnetization vector $\vec{m}$ of the barrier to be aligned in the $z$-direction, the polarization matrix $\check{\kappa}$ in $8 \times 8$ Keldysh space becomes

$$\check{\boldsymbol{\kappa}} = \begin{pmatrix} \sigma_z & \bar{0} & \bar{0} & \bar{0} \\ \bar{0} & \sigma_z & \bar{0} & \bar{0} \\ \bar{0} & \bar{0} & \sigma_z & \bar{0} \\ \bar{0} & \bar{0} & \bar{0} & \sigma_z \end{pmatrix}. \tag{5.23}$$

## 5.2 Charge current

### 5.2.1 Thermoelectric coefficients

As the commutators contain a lot of terms, most of the derivation of the matrix current coefficients is moved to Appendix B, and only the results can be found here. The procedure involves expressing each of the commutators in terms of the retarded Green function matrices on both sides of the interface barrier. This is done through employing the relations 5.16 and 5.17, and differentiating with respect to the voltage and temperature on both sides of the junction about the point $(V_0, T_0) = (0, T)$. In this point, $\hat{\boldsymbol{h}}_L = \hat{\boldsymbol{h}}_R = \tanh(E/2k_B T)$. All current terms become zero in this case, and the zeroth order term of the Taylor expansion therefore disappears. The only factors which depend on the temperature and voltage are $\hat{\boldsymbol{h}}_L$ and $\hat{\boldsymbol{h}}_R$, and therefore only these factors are differentiated. Differentiating the non-equilibrium matrices with respect to temperature yields

$$\frac{\mathrm{d}\boldsymbol{h}_j}{\mathrm{d}T_j} = -\frac{E}{2k_B T^2 \cosh^2\left(\frac{E}{2k_B T}\right)} \hat{\mathbf{1}} \tag{5.24}$$

$$\frac{\mathrm{d}\boldsymbol{h}_{L,R}}{\mathrm{d}T_{R,L}} = 0. \tag{5.25}$$

When Taylor expanding in voltage we only need to focus on $V_R$, as the term containing $V_L$ becomes zero as $V_L = 0$. Moreover, only $\hat{\boldsymbol{h}}_R$ depends on voltage, and

$$\frac{\mathrm{d}\hat{\boldsymbol{h}}_R}{\mathrm{d}V_R} = \frac{e}{2k_B T \cosh^2\left(\frac{E}{2k_B T}\right)} \hat{\rho}_3. \tag{5.26}$$

The complete conductance coefficient, prior to assuming the right-hand material to be a normal metal and defining $\hat{\boldsymbol{g}}_R = \hat{\rho}_3$, is

$$
\begin{aligned}
G' = \frac{\mathrm{d}I_q}{\mathrm{d}V_R} = \frac{G_q N\tau}{4} \int_{-\infty}^{\infty} & \frac{\mathrm{d}E}{4k_B T \cosh^2\left(\frac{E}{2k_B T}\right)} \operatorname{Tr}\left\{(1+\sqrt{1-P^2})\operatorname{Re}\left\{\hat{\boldsymbol{g}}_L\hat{\boldsymbol{g}}_R + \hat{\boldsymbol{g}}_L\hat{\boldsymbol{g}}_R^{\dagger}\right\}\right. \\
& + P\operatorname{Re}\left\{\hat{\sigma}_z\hat{\boldsymbol{g}}_L\hat{\boldsymbol{g}}_R + \hat{\sigma}_z\hat{\boldsymbol{g}}_R\hat{\boldsymbol{g}}_L + \hat{\sigma}_z\hat{\boldsymbol{g}}_L\hat{\boldsymbol{g}}_R^{\dagger} + \hat{\sigma}_z\hat{\boldsymbol{g}}_R^{\dagger}\hat{\boldsymbol{g}}_L\right\} \\
& \left. + (1-\sqrt{1-P^2})\operatorname{Re}\left\{\hat{\sigma}_z\hat{\boldsymbol{g}}_L\hat{\sigma}_z\hat{\boldsymbol{g}}_R + \hat{\sigma}_z\hat{\boldsymbol{g}}_L\hat{\sigma}_z\hat{\boldsymbol{g}}_R^{\dagger}\right\}\right\}
\end{aligned}
$$
$$(5.27)$$

The non-equilibrium matrices $\hat{\boldsymbol{h}}_L$ and $\hat{\boldsymbol{h}}_R$ must behave according to Equations 5.19 and 5.20, but otherwise no assumptions regarding $\hat{\boldsymbol{g}}_L$ and $\hat{\boldsymbol{g}}_R$ have been made. The complete expressions for the thermoelectric coefficients prior to allowing the right-side electrode to become a normal metal are

$$
\begin{aligned}
\alpha_1' = T\frac{\mathrm{d}I_q}{\mathrm{d}T_L} = \frac{G_q N\tau}{4e} \int_{-\infty}^{\infty} & \frac{E\,\mathrm{d}E}{4k_B T \cosh^2\left(\frac{E}{2k_B T}\right)} \operatorname{Tr}\left\{(1+\sqrt{1-P^2})\Big(\operatorname{Re}\{\hat{\rho}_3\hat{\boldsymbol{g}}_R\hat{\boldsymbol{g}}_L\}\right. \\
& + \operatorname{Re}\left\{\hat{\rho}_3\hat{\boldsymbol{g}}_R^{\dagger}\hat{\boldsymbol{g}}_L\right\}\Big) + P\operatorname{Re}\left\{\hat{\rho}_3\hat{\sigma}_z\hat{\boldsymbol{g}}_R\hat{\boldsymbol{g}}_L + \hat{\rho}_3\hat{\sigma}_z\hat{\boldsymbol{g}}_R^{\dagger}\hat{\boldsymbol{g}}_L + \hat{\rho}_3\hat{\boldsymbol{g}}_R\hat{\sigma}_z\hat{\boldsymbol{g}}_L + \hat{\rho}_3\hat{\boldsymbol{g}}_R^{\dagger}\hat{\sigma}_z\hat{\boldsymbol{g}}_L\right\} \\
& \left. + (1-\sqrt{1-P^2})\operatorname{Re}\left\{\hat{\rho}_3\hat{\sigma}_z\hat{\boldsymbol{g}}_R\hat{\sigma}_z\hat{\boldsymbol{g}}_L + \hat{\rho}_3\hat{\sigma}_z\hat{\boldsymbol{g}}_R^{\dagger}\hat{\sigma}_z\hat{\boldsymbol{g}}_L\right\}\right\}
\end{aligned}
$$
$$(5.28)$$

and

$$
\begin{aligned}
\alpha_2' = T\frac{\mathrm{d}I_q}{\mathrm{d}T_R} = -\frac{G_q N\tau}{4e} \int_{-\infty}^{\infty} & \frac{E\,\mathrm{d}E}{4k_B T \cosh^2\left(\frac{E}{2k_B T}\right)} \operatorname{Tr}\left\{(1+\sqrt{1-P^2})\Big(\operatorname{Re}\{\hat{\rho}_3\hat{\boldsymbol{g}}_L\hat{\boldsymbol{g}}_R\}\right. \\
& + \operatorname{Re}\left\{\hat{\rho}_3\hat{\boldsymbol{g}}_R^{\dagger}\hat{\boldsymbol{g}}_L\right\}\Big) + P\operatorname{Re}\left\{\hat{\rho}_3\hat{\sigma}_z\hat{\boldsymbol{g}}_L\hat{\boldsymbol{g}}_R + \hat{\rho}_3\hat{\sigma}_z\hat{\boldsymbol{g}}_R^{\dagger}\hat{\boldsymbol{g}}_L + \hat{\rho}_3\hat{\boldsymbol{g}}_L\hat{\sigma}_z\hat{\boldsymbol{g}}_R^{\dagger} + \hat{\rho}_3\hat{\boldsymbol{g}}_R^{\dagger}\hat{\sigma}_z\hat{\boldsymbol{g}}_L\right\} \\
& \left. + (1-\sqrt{1-P^2})\operatorname{Re}\left\{\hat{\rho}_3\hat{\sigma}_z\hat{\boldsymbol{g}}_L\hat{\sigma}_z\hat{\boldsymbol{g}}_R + \hat{\rho}_3\hat{\sigma}_z\hat{\boldsymbol{g}}_R^{\dagger}\hat{\sigma}_z\hat{\boldsymbol{g}}_L\right\}\right\}.
\end{aligned}
$$
$$(5.29)$$

The three expressions for thermoelectric coefficients defined here, for $G'$, $\alpha_1'$ and $\alpha_2'$, are completely general and should be applicable to a wide range of systems. Depending on the material included as the electrode to the right of the barrier, the entirety of

the Green function matrix could now contribute to the tunneling thermoelectric effects. Previously, only the diagonal elements in the $2 \times 2$ retarded Green function matrix $\boldsymbol{g}^R$ contributed to the tunneling currents. This matrix is encompassed by the $4 \times 4$ retarded Green function matrix as

$$\hat{\boldsymbol{g}}^R = \begin{pmatrix} \underline{\boldsymbol{g}}^R & \underline{\boldsymbol{f}}^R \\ -\underline{\tilde{\boldsymbol{f}}}^R & -\underline{\tilde{\boldsymbol{g}}}^R \end{pmatrix}, \tag{5.30}$$

and contributes to the tunneling currents studied in Chapter 3 via the density of states definition

$$D^0(E) = \frac{1}{2} \operatorname{Tr} \operatorname{Re}\{\underline{\boldsymbol{g}}^R\}. \tag{5.31}$$

Within the new framework, however, the entire retarded Green function matrix can contribute to the arising thermoelectric effects. Consequently, it is not only the **z**-polarized elements which determine system dynamics. This, however, depends greatly upon the choice of materials. If one of the materials is a normal metal, only the diagonal elements of the Green function matrices play a role, and the expressions derived for the charge current quickly reduce to including traces over the retarded Green function matrices on one side of the junction, which is very similar to the integrals over the densities of states defining the thermoelectric coefficients derived in Chapter 3. When $\hat{\boldsymbol{g}}_R = \hat{\boldsymbol{g}}_{NM} = \hat{\rho}_3$ the differentiated charge current with respect to the voltage can be written as

$$\begin{aligned}
\frac{\mathrm{d}I_q}{\mathrm{d}V_R} = G_q N\tau \int_{-\infty}^{\infty} \frac{\mathrm{d}E}{4k_B T \cosh^2\left(\frac{E}{2k_B T}\right)} \operatorname{Tr}\Big\{ \operatorname{Re}\Big\{ \frac{1}{2}(1 + \sqrt{1 - P^2})\hat{\rho}_3\hat{\boldsymbol{g}}_L \Big\} \\
+ \operatorname{Re}\Big\{ P\hat{\rho}_3\hat{\sigma}_z\hat{\boldsymbol{g}}_L + \frac{1}{2}(1 - \sqrt{1 - P^2})\hat{\rho}_3\hat{\boldsymbol{g}}_L \Big\} \Big\},
\end{aligned} \tag{5.32}$$

and the conductance coefficient for tunneling in a unknown material(X)/ insulator(I)/ normal metal(N) structure becomes

$$G' = \frac{\mathrm{d}I_q}{\mathrm{d}V_R} = G_q N\tau \int_{-\infty}^{\infty} \frac{\mathrm{d}E}{4k_B T \cosh^2\left(\frac{E}{2k_B T}\right)} \operatorname{Tr}\Big\{ \operatorname{Re}\{\hat{\rho}_3\hat{\boldsymbol{g}}_L + P\hat{\rho}_3\hat{\sigma}_z\hat{\boldsymbol{g}}_L\} \Big\}. \tag{5.33}$$

This does not equal the conductance coefficient $G$ derived in Section 3 in all cases, and the superscript in $G'$ is included to highlight this fact. When $P = 0$, $G' \propto G$ as defined

in Equation 3.63. This is due to $\text{Tr}\{\hat{\rho}_3\hat{\boldsymbol{g}}_L\}$ becoming equal to $D^0(E)$, the total density of states for all spin species. However, when the polarization does not equal zero, other effects may arise depending on the content of $\hat{\boldsymbol{g}}_L$. In several approximate cases, however, $\text{Tr}\{\hat{\rho}_3\hat{\sigma}_z\hat{\boldsymbol{g}}_L\} = 0$, and equation 5.33 for $G'$ reduces to the expression for the conductance coefficient $G$. The only case for which these are not identical, is when $\text{Tr}\{\hat{\rho}_3\hat{\sigma}_z\hat{\boldsymbol{g}}_L\} \neq 0$. If this occurs, the additional correction term accounts for increased or reduced tunneling probability depending on the spin species. When allowing $\hat{\boldsymbol{g}}^R = \hat{\rho}_3$ and considering the thermal response of the charge current, it becomes evident that

$$\frac{\mathrm{d}I_q}{\mathrm{d}T_R} = -\frac{\mathrm{d}I}{\mathrm{d}T_L} \tag{5.34}$$

and

$$\begin{aligned}
\frac{\mathrm{d}I_q}{\mathrm{d}T_L} = \frac{G_q N\tau}{e} \int_{-\infty}^{\infty} \frac{E\,\mathrm{d}E}{4k_B T^2 \cosh^2\left(\frac{E}{2k_B T}\right)} \text{Tr}\Bigg\{ &\Bigg( \text{Re}\Big\{\frac{1}{2}(1+\sqrt{1-P^2})\hat{\boldsymbol{g}}_L\Big\} \\
&+ \text{Re}\Big\{ P\hat{\sigma}_z\hat{\boldsymbol{g}}_L + \frac{1}{2}(1-\sqrt{1-P^2})\hat{\boldsymbol{g}}_L\Big\}\Bigg)\Bigg\}.
\end{aligned} \tag{5.35}$$

Consequently, the thermoelectric coefficient for the charge current becomes

$$\alpha' = T\frac{\mathrm{d}I_q}{\mathrm{d}T_L} = \frac{G_q N\tau}{e} \int_{-\infty}^{\infty} \frac{E\,\mathrm{d}E}{4k_B T \cosh^2\left(\frac{E}{2k_B T}\right)} \text{Tr}\Big\{ \text{Re}\{\hat{\boldsymbol{g}}_L + P\hat{\sigma}_z\hat{\boldsymbol{g}}_L\}\Big\}. \tag{5.36}$$

$\text{Tr}\{\hat{\boldsymbol{g}}_L\} = 0$ due to charge conservation. Accordingly, the expression for $\alpha'$ should reduce to the expression for the previously derived thermoelectric coefficient $\alpha$ (Eq. 3.64). When $P = 0$, the result is $\alpha' = \alpha = 0$, as we would expect for the temperature-driven total charge current. Moreover, we observe that $\alpha$ is merely the integral over $P\,\text{Tr}\{\hat{\sigma}_z\hat{\boldsymbol{g}}_L\}$, which is the difference between the z-polarized spin up and spin down density of states, or $D^z(E)$. Consequently, unless $\text{Tr}\{\hat{\rho}_3\hat{\sigma}_z\hat{\boldsymbol{g}}_L\} \neq 0$, not much new information is gained through the quasiclassical thermoelectric consideration of the charge current when the material to the right of the tunneling barrier is a normal metal.

Two tests for the quasiclassical conductance and thermoelectric charge current coefficients are included, considering both the case where the right-hand-side material is a normal metal as well as when it is not. When using materials for which there are analytic expressions for the retarded Green function matrix available the expressions derived for $\alpha'$ and $G'$ should reduce to the expressions derived in Chapter 3.

### 5.2.2 Test for non-polarized S/I/ZS tunneling

When considering $P = 0$, only the expression for $G'$ should be unequal to zero. Here, the structure considered is a superconductor/insulator/Zeeman-split superconductor bilayer. The right-hand-side material is consequently not a normal metal, but the expressions for $\hat{h}_L$ and $\hat{h}_R$ remain valid. When no polarization is present, $G_1 = G_{\mathrm{MR}} = 0$. Therefore, only the term preceded by $G_0$ survives. Additionally, we do not need to consider the polarization matrix at it is not involved in the first term, and the conductance coefficient becomes

$$G' = \frac{\mathrm{d}I_q}{\mathrm{d}V_R} = \frac{G_0}{4}\int_{-\infty}^{\infty}\frac{\mathrm{d}E}{4k_BT\cosh^2\left(\frac{E}{2k_BT}\right)}\,\mathrm{Tr}\left\{\mathrm{Re}\left\{\hat{\boldsymbol{g}}_L^R(\hat{\boldsymbol{g}}_R^R + \hat{\boldsymbol{g}}_R^{R\dagger})\right\}\right\}. \tag{5.37}$$

Using the old expression for $G$,

$$G = G_T\int_{-\infty}^{\infty}\frac{D_L^0 D_R^0 + \frac{D_L^z D_R^z}{4}}{4k_BT\cosh^2\left(\frac{E}{2k_BT}\right)}\mathrm{d}E, \tag{5.38}$$

the result for the conductance coefficient should be

$$\begin{aligned}
G = \frac{G_T}{2}\int_{-\infty}^{\infty}&\frac{\mathrm{d}E}{4k_BT\cosh^2\left(\frac{E}{2k_BT}\right)}\,\mathrm{Re}\left\{\frac{E}{\sqrt{E^2 - \Delta^2}}\right\}\\
&\cdot\mathrm{Re}\left\{\frac{E+h}{\sqrt{(E+h)^2 - \Delta^2}} + \frac{E-h}{\sqrt{(E-h)^2 - \Delta^2}}\right\}.
\end{aligned} \tag{5.39}$$

The retarded Green function matrix for a conventional BCS superconductor is defined as

$$\hat{\boldsymbol{g}}_{SC} = \hat{\boldsymbol{g}}_L = \begin{pmatrix} c & 0 & 0 & s \\ 0 & c & s & 0 \\ 0 & -s & -c & 0 \\ -s & 0 & 0 & -c \end{pmatrix}, \tag{5.40}$$

where $c = \cosh(\Theta)$, $s = \sinh(\Theta)$ and $\Theta = \tanh^{-1}\left(\frac{\Delta}{E}\right)$. This causes $c = |E|/\sqrt{E^2 - \Delta^2}$. Furthermore, the retarded Green function matrix for a Zeeman-split BCS superconductor is [138]

$$\hat{\boldsymbol{g}}_{ZS} = \hat{\boldsymbol{g}}_R = \begin{pmatrix} c\uparrow & 0 & 0 & s\uparrow \\ 0 & c\downarrow & s\downarrow & 0 \\ 0 & -s\downarrow & -c\downarrow & 0 \\ -s\uparrow & 0 & 0 & -c\uparrow \end{pmatrix}. \tag{5.41}$$

Calculating the Hermitian transpose

$$\hat{\boldsymbol{g}}_R^{\dagger} = \begin{pmatrix} c\uparrow^{*} & 0 & 0 & -s\uparrow^{*} \\ 0 & c\downarrow^{*} & -s\downarrow^{*} & 0 \\ 0 & s\downarrow^{*} & -c\downarrow^{*} & 0 \\ s\uparrow^{*} & 0 & 0 & -c\uparrow^{*} \end{pmatrix}, \tag{5.42}$$

where $c_{\sigma} = (E + \sigma h)/\sqrt{(E + \sigma h)^2 - \Delta^2}$, we can now compute

$$\hat{\boldsymbol{g}}_R + \hat{\boldsymbol{g}}_R^{\dagger} = 2 \begin{pmatrix} \mathrm{Re}\{c\uparrow\} & 0 & 0 & i\,\mathrm{Im}\{s\uparrow\} \\ 0 & \mathrm{Re}\{c\downarrow\} & i\,\mathrm{Im}\{s\downarrow\} & 0 \\ 0 & -i\,\mathrm{Im}\{s\downarrow\} & -\,\mathrm{Re}\{c\downarrow\} & 0 \\ -i\,\mathrm{Im}\{s\uparrow\} & 0 & 0 & -\,\mathrm{Re}\{c\uparrow\} \end{pmatrix} \tag{5.43}$$

and

$$\mathrm{Re}\left\{\hat{\boldsymbol{g}}_L(\hat{\boldsymbol{g}}_R + \hat{\boldsymbol{g}}_R^{\dagger})\right\} = 2 \begin{pmatrix} c\,\mathrm{Re}\{c\uparrow\} & 0 & 0 & -s\,\mathrm{Re}\{c\uparrow\} \\ 0 & c\,\mathrm{Re}\{c\downarrow\} & -s\,\mathrm{Re}\{c\downarrow\} & 0 \\ 0 & -s\,\mathrm{Re}\{c\downarrow\} & c\,\mathrm{Re}\{c\downarrow\} & 0 \\ -s\,\mathrm{Re}\{c\uparrow\} & 0 & 0 & c\,\mathrm{Re}\{c\uparrow\} \end{pmatrix}. \tag{5.44}$$

Inserting this into the expression for the quasiclassical conductance coefficient results in

$$G' = \frac{G_0}{4} \int_{-\infty}^{\infty} \frac{\mathrm{d}E}{4k_B T \cosh^2\left(\frac{E}{2k_B T}\right)} 2\,\mathrm{Re}\{c\,\mathrm{Re}\{c\uparrow + c\downarrow + c\downarrow + c\uparrow\}\} \tag{5.45}$$

$$= G_0 \int_{-\infty}^{\infty} \frac{\mathrm{d}E}{4k_B T \cosh^2\left(\frac{E}{2k_B T}\right)} \mathrm{Re}\{c\,\mathrm{Re}\{c\uparrow + c\downarrow\}\}. \tag{5.46}$$

Considering $\mathrm{Re}\{AB\} = \mathrm{Re}\{A\}\,\mathrm{Re}\{B\} - \mathrm{Im}\{A\}\,\mathrm{Im}\{B\}$, this becomes

$$\mathrm{Re}\{c\,\mathrm{Re}\{c\uparrow + c\downarrow\}\} = \mathrm{Re}\{c\}\,\mathrm{Re}\{\mathrm{Re}\{c\uparrow + c\downarrow\}\} - \mathrm{Im}\{c\}\,\mathrm{Im}\{\mathrm{Re}\{c\uparrow + c\downarrow\}\} \tag{5.47}$$

$$= \mathrm{Re}\{c\}\,\mathrm{Re}\{\mathrm{Re}\{c\uparrow + c\downarrow\}\} \tag{5.48}$$

$$= \mathrm{Re}\{c\}\,\mathrm{Re}\{c\uparrow + c\downarrow\}. \tag{5.49}$$

Inserting the identities for $c$ and $c_\sigma$ yields

$$G' = G_0 \int_{-\infty}^{\infty} \frac{\mathrm{d}E}{4k_B T \cosh^2\left(\frac{E}{2k_B T}\right)} \mathrm{Re}\left\{ \frac{E}{\sqrt{E^2 - \Delta^2}} \right\}$$
$$\cdot \mathrm{Re}\left\{ \frac{E+h}{\sqrt{(E+h)^2 - \Delta^2}} + \frac{E-h}{\sqrt{(E-h)^2 - \Delta^2}} \right\}, \tag{5.50}$$

which by defining $2G_0 = G_T$ is exactly equal to equation 5.39. Considering the thermoelectric coefficient,

$$\alpha_1' = \frac{G_0}{4e} \int_{-\infty}^{\infty} \mathrm{d}E \frac{E}{4k_B T \cosh^2\left(\frac{E}{2k_B T}\right)} \mathrm{Tr}\left\{ \mathrm{Re}\left\{ \hat{\boldsymbol{g}}_L \hat{\rho}_3 (\hat{\boldsymbol{g}}_R + \hat{\boldsymbol{g}}_R^\dagger) \right\} \right\} \tag{5.51}$$

$$= \frac{G_0}{4e} \int_{-\infty}^{\infty} \mathrm{d}E \frac{E}{4k_B T \cosh^2\left(\frac{E}{2k_B T}\right)} (c\,\mathrm{Re}\{c\uparrow\} + c\,\mathrm{Re}\{c\downarrow\} - c\,\mathrm{Re}\{c\downarrow\} - c\,\mathrm{Re}\{c\uparrow\})$$
$$\tag{5.52}$$

$$= 0 \tag{5.53}$$

and

$$\alpha_2' = -\frac{G_0}{4e} \int_{-\infty}^{\infty} \mathrm{d}E \frac{E}{4k_B T \cosh^2\left(\frac{E}{2k_B T}\right)} \mathrm{Tr}\left\{ \mathrm{Re}\left\{ \hat{\boldsymbol{g}}_R \hat{\rho}_3 (\hat{\boldsymbol{g}}_L + \hat{\boldsymbol{g}}_L^\dagger) \right\} \right\} \tag{5.54}$$

$$= -\frac{G_0}{4e} \int_{-\infty}^{\infty} \mathrm{d}E \frac{E}{4k_B T \cosh^2\left(\frac{E}{2k_B T}\right)} 2(c\uparrow\mathrm{Re}\{c\} + c\downarrow\mathrm{Re}\{c\} - c\downarrow\mathrm{Re}\{c\} - c\uparrow\mathrm{Re}\{c\})$$
$$\tag{5.55}$$

$$= 0, \tag{5.56}$$

as is to be expected when the polarization $P = 0$.

### 5.2.3   Test for fully polarized ZS/I/N tunneling

The second test performed is for a Zeeman-split superconductor/insulator/normal metal bilayer when the interface is fully polarized and $P = 1$. Inserting $P = 1$ and the expression for the retarded Green function matrix of a Zeeman-split superconductor to

the expression for the quasiclassical thermoelectric coefficient when the right-hand-side material is a normal metal results in

$$
\alpha' = \frac{G_q N \tau}{e} \int_{-\infty}^{\infty} \frac{E \mathrm{d}E}{4 k_B T \cosh^2\left(\frac{E}{2k_B T}\right)} \operatorname{Tr} \left\{ \operatorname{Re}\{ \hat{\boldsymbol{g}}_L + \hat{\sigma}_z \hat{\boldsymbol{g}}_L \} \right\}  \tag{5.57}
$$

$$
= \frac{2 G_q N \tau}{e} \int_{-\infty}^{\infty} \frac{E \mathrm{d}E}{4 k_B T \cosh^2\left(\frac{E}{2k_B T}\right)} \operatorname{Tr} \left\{ \operatorname{Re}\{ c \uparrow - c \downarrow \} \right\}  \tag{5.58}
$$

$$
= \frac{2 G_q N \tau}{e} \int_{-\infty}^{\infty} \frac{E \mathrm{d}E}{4 k_B T \cosh^2\left(\frac{E}{2k_B T}\right)} \operatorname{Re} \left\{ \frac{E+h}{\sqrt{(E+h)^2 - \Delta^2}} - \frac{E-h}{\sqrt{(E-h)^2 - \Delta^2}} \right\}.  \tag{5.59}
$$

Moreover, the conductance coefficient becomes

$$
G' = 4 G_q N \tau \int_{-\infty}^{\infty} \frac{\mathrm{d}E}{4 k_B T \cosh^2\left(\frac{E}{2k_B T}\right)} \operatorname{Re}\{ c \uparrow + c \downarrow \}  \tag{5.60}
$$

$$
= \frac{2 G_q N \tau}{e} \int_{-\infty}^{\infty} \frac{E \mathrm{d}E}{4 k_B T \cosh^2\left(\frac{E}{2k_B T}\right)} \operatorname{Re} \left\{ \frac{E+h}{\sqrt{(E+h)^2 - \Delta^2}} + \frac{E-h}{\sqrt{(E-h)^2 - \Delta^2}} \right\}.  \tag{5.61}
$$

This is identical to what we expect for this material system when applying the framework assuming homogeneously magnetized materials derived in Chapter 3, and the new expressions are seen to reduce to the old ones in the required limiting cases.

## 5.3   Spin current

Taylor expanding the expression for the spin current on the right side of the interface barrier to the first order about the point $(0, T)$ results in the complete expressions for the thermoelectric spin current coefficients becoming

$$
\frac{\mathrm{d}I_s^\nu}{\mathrm{d}V_R} = \frac{1}{16e} \int_{-\infty}^{\infty} \frac{\mathrm{d}E}{4k_B T \cosh^2\left(\frac{E}{2k_B T}\right)} \operatorname{Tr}\left\{\hat{\rho}_3\hat{\tau}_\nu\Big[G_0(\hat{\boldsymbol{g}}_L\hat{\boldsymbol{g}}_R\hat{\rho}_3 + \hat{\boldsymbol{g}}_L\hat{\boldsymbol{g}}_R^\dagger\hat{\rho}_3 + \hat{\boldsymbol{g}}_R\hat{\boldsymbol{g}}_L^\dagger\hat{\rho}_3 + \hat{\boldsymbol{g}}_R^\dagger\hat{\boldsymbol{g}}_L^\dagger\hat{\rho}_3)\right.
$$
$$
+G_{MR}(\hat{\sigma}_z\hat{\boldsymbol{g}}_L\hat{\boldsymbol{g}}_R\hat{\rho}_3 + \hat{\sigma}_z\hat{\boldsymbol{g}}_L\hat{\boldsymbol{g}}_R^\dagger\hat{\rho}_3 + \hat{\boldsymbol{g}}_L\hat{\sigma}_z\hat{\boldsymbol{g}}_R\hat{\rho}_3 + \hat{\boldsymbol{g}}_L\hat{\sigma}_z\hat{\boldsymbol{g}}_R^\dagger\hat{\rho}_3 + \hat{\boldsymbol{g}}_R\hat{\sigma}_z\hat{\boldsymbol{g}}_L^\dagger\hat{\rho}_3
$$
$$
+\hat{\boldsymbol{g}}_R^\dagger\hat{\sigma}_z\hat{\boldsymbol{g}}_L^\dagger\hat{\rho}_3 + \hat{\boldsymbol{g}}_R\hat{\boldsymbol{g}}_L^\dagger\hat{\rho}_3\hat{\sigma}_z + \hat{\boldsymbol{g}}_R^\dagger\hat{\boldsymbol{g}}_L^\dagger\hat{\rho}_3\hat{\sigma}_z)
$$
$$
+G_1(\hat{\sigma}_z\hat{\boldsymbol{g}}_L\hat{\sigma}_z\hat{\boldsymbol{g}}_R\hat{\rho}_3 + \hat{\sigma}_z\hat{\boldsymbol{g}}_L\hat{\sigma}_z\hat{\boldsymbol{g}}_R^\dagger\hat{\rho}_3 + \hat{\boldsymbol{g}}_R\hat{\sigma}_z\hat{\boldsymbol{g}}_L^\dagger\hat{\rho}_3\hat{\sigma}_z + \hat{\boldsymbol{g}}_R^\dagger\hat{\sigma}_z\hat{\boldsymbol{g}}_L^\dagger\hat{\rho}_3\hat{\sigma}_z)
$$
$$
\left.-iG_\varphi(\hat{\sigma}_z\hat{\boldsymbol{g}}_R\hat{\rho}_3 + \hat{\sigma}_z\hat{\boldsymbol{g}}_R^\dagger\hat{\rho}_3 - \hat{\boldsymbol{g}}_R\hat{\rho}_3\hat{\sigma}_z - \hat{\boldsymbol{g}}_R^\dagger\hat{\rho}_3\hat{\sigma}_z)\Big]\right\},
$$
$$
(5.62)
$$

$$
\frac{\mathrm{d}I_s^\nu}{\mathrm{d}T_R} = -\frac{1}{16e^2} \int_{-\infty}^{\infty} \frac{E\mathrm{d}E}{4k_B T^2 \cosh^2\left(\frac{E}{2k_B T}\right)} \operatorname{Tr}\left\{\hat{\rho}_3\hat{\tau}_\nu\Big[G_0(\hat{\boldsymbol{g}}_L\hat{\boldsymbol{g}}_R + \hat{\boldsymbol{g}}_L\hat{\rho}_3\hat{\boldsymbol{g}}_R^\dagger\hat{\rho}_3 + \hat{\boldsymbol{g}}_R\hat{\rho}_3\hat{\boldsymbol{g}}_L^\dagger\hat{\rho}_3\right.
$$
$$
+\hat{\rho}_3\hat{\boldsymbol{g}}_R^\dagger\hat{\boldsymbol{g}}_L^\dagger\hat{\rho}_3) + G_{MR}(\hat{\sigma}_z\hat{\boldsymbol{g}}_L\hat{\boldsymbol{g}}_R + \hat{\sigma}_z\hat{\boldsymbol{g}}_L\hat{\rho}_3\hat{\boldsymbol{g}}_R^\dagger\hat{\rho}_3 + \hat{\boldsymbol{g}}_L\hat{\sigma}_z\hat{\boldsymbol{g}}_R + \hat{\boldsymbol{g}}_L\hat{\sigma}_z\hat{\rho}_3\hat{\boldsymbol{g}}_R^\dagger\hat{\rho}_3 + \hat{\boldsymbol{g}}_R\hat{\sigma}_z\hat{\rho}_3\hat{\boldsymbol{g}}_L^\dagger\hat{\rho}_3
$$
$$
+\hat{\rho}_3\hat{\boldsymbol{g}}_R^\dagger\hat{\sigma}_z\hat{\boldsymbol{g}}_L^\dagger\hat{\rho}_3 + \hat{\boldsymbol{g}}_R\hat{\rho}_3\hat{\boldsymbol{g}}_L^\dagger\hat{\rho}_3\hat{\sigma}_z + \hat{\rho}_3\hat{\boldsymbol{g}}_R^\dagger\hat{\boldsymbol{g}}_L^\dagger\hat{\rho}_3\hat{\sigma}_z)
$$
$$
+G_1(\hat{\sigma}_z\hat{\boldsymbol{g}}_L\hat{\sigma}_z\hat{\boldsymbol{g}}_R + \hat{\sigma}_z\hat{\boldsymbol{g}}_L\hat{\sigma}_z\hat{\rho}_3\hat{\boldsymbol{g}}_R^\dagger\hat{\rho}_3 + \hat{\boldsymbol{g}}_R\hat{\sigma}_z\hat{\rho}_3\hat{\boldsymbol{g}}_L^\dagger\hat{\rho}_3\hat{\sigma}_z + \hat{\rho}_3\hat{\boldsymbol{g}}_R^\dagger\hat{\sigma}_z\hat{\boldsymbol{g}}_L^\dagger\hat{\rho}_3\hat{\sigma}_z)
$$
$$
\left.-iG_\varphi(\hat{\sigma}_z\hat{\boldsymbol{g}}_R + \hat{\sigma}_z\hat{\rho}_3\hat{\boldsymbol{g}}_R^\dagger\hat{\rho}_3 - \hat{\boldsymbol{g}}_R\hat{\sigma}_z - \hat{\rho}_3\hat{\boldsymbol{g}}_R^\dagger\hat{\rho}_3\hat{\sigma}_z)\Big]\right\},
$$
$$
(5.63)
$$

and

$$
\frac{\mathrm{d}I_s^\nu}{\mathrm{d}T_L} = \frac{1}{16e^2} \int_{-\infty}^{\infty} \frac{E\mathrm{d}E}{4k_B T^2 \cosh^2\left(\frac{E}{2k_B T}\right)} \operatorname{Tr}\left\{\hat{\rho}_3\hat{\tau}_\nu\Big[G_0(\hat{\boldsymbol{g}}_L\hat{\rho}_3\hat{\boldsymbol{g}}_R^\dagger\hat{\rho}_3 + \hat{\rho}_3\hat{\boldsymbol{g}}_L^\dagger\hat{\boldsymbol{g}}_R^\dagger\hat{\rho}_3 + \hat{\boldsymbol{g}}_R\hat{\boldsymbol{g}}_L\right.
$$
$$
+\hat{\boldsymbol{g}}_R\hat{\rho}_3\hat{\boldsymbol{g}}_L^\dagger\hat{\rho}_3) + G_{MR}(\hat{\sigma}_z\hat{\boldsymbol{g}}_L\hat{\rho}_3\hat{\boldsymbol{g}}_R^\dagger\hat{\rho}_3 + \hat{\sigma}_z\hat{\rho}_3\hat{\boldsymbol{g}}_L^\dagger\hat{\boldsymbol{g}}_R^\dagger\hat{\rho}_3 + \hat{\boldsymbol{g}}_L\hat{\sigma}_z\hat{\rho}_3\hat{\boldsymbol{g}}_R^\dagger\hat{\rho}_3 + \hat{\rho}_3\hat{\boldsymbol{g}}_L^\dagger\hat{\sigma}_z\hat{\boldsymbol{g}}_R^\dagger\hat{\rho}_3
$$
$$
+\hat{\boldsymbol{g}}_R\hat{\sigma}_z\hat{\boldsymbol{g}}_L + \hat{\boldsymbol{g}}_R\hat{\sigma}_z\hat{\rho}_3\hat{\boldsymbol{g}}_L^\dagger\hat{\rho}_3 + \hat{\boldsymbol{g}}_R\hat{\boldsymbol{g}}_L\hat{\sigma}_z + \hat{\boldsymbol{g}}_R\hat{\rho}_3\hat{\boldsymbol{g}}_L^\dagger\hat{\rho}_3\hat{\sigma}_z)
$$
$$
\left.+G_1(\hat{\sigma}_z\hat{\boldsymbol{g}}_L\hat{\sigma}_z\hat{\rho}_3\hat{\boldsymbol{g}}_R^\dagger\hat{\rho}_3 + \hat{\sigma}_z\hat{\rho}_3\hat{\boldsymbol{g}}_L^\dagger\hat{\sigma}_z\hat{\boldsymbol{g}}_R^\dagger\hat{\rho}_3 + \hat{\boldsymbol{g}}_R\hat{\sigma}_z\hat{\boldsymbol{g}}_L\hat{\sigma}_z + \hat{\boldsymbol{g}}_R\hat{\rho}_3\hat{\sigma}_z\hat{\boldsymbol{g}}_L^\dagger\hat{\rho}_3\hat{\sigma}_z)\Big]\right\}
$$
$$
(5.64)
$$

prior to assuming the right hand side to be a normal metal. When the right hand material is a normal metal, these become

$$
\alpha_\nu^s = T\frac{\mathrm{d}I_s^\nu}{\mathrm{d}T_L} = \frac{N\tau G_q}{8e^2}\int_{-\infty}^{\infty}\frac{E\mathrm{d}E}{4k_BT\cosh^2\left(\frac{E}{2k_BT}\right)}\operatorname{Tr}\left\{(1+\sqrt{1-P^2})\hat{\tau}_\nu(\hat{\boldsymbol{g}}_L+\hat{\boldsymbol{g}}_L^\dagger)\right.
$$

$$
\left.+P[\hat{\tau}_\nu\hat{\sigma}_z(\hat{\boldsymbol{g}}_L+\hat{\boldsymbol{g}}_L^\dagger)+\hat{\sigma}_z\hat{\tau}_\nu(\hat{\boldsymbol{g}}_L+\hat{\boldsymbol{g}}_L^\dagger)]+(1-\sqrt{1-P^2})\hat{\tau}_\nu\hat{\sigma}_z(\hat{\boldsymbol{g}}_L+\hat{\boldsymbol{g}}_L^\dagger)\hat{\sigma}_z\right\}
$$

$$(5.65)$$

and

$$
G_\nu^s = \frac{\mathrm{d}I_s^\nu}{\mathrm{d}V_R} = \frac{N\tau G_q}{8e}\int_{-\infty}^{\infty}\frac{\mathrm{d}E}{4k_BT\cosh^2\left(\frac{E}{2k_BT}\right)}\operatorname{Tr}\left\{\hat{\rho}_3\hat{\tau}_\nu\Big[(1+\sqrt{1-P^2})(\hat{\boldsymbol{g}}_L\right.
$$

$$
+\hat{\rho}_3\hat{\boldsymbol{g}}_L^\dagger\hat{\rho}_3)+P(\hat{\sigma}_z\hat{\boldsymbol{g}}_L+\hat{\boldsymbol{g}}_L\hat{\sigma}_z+\hat{\sigma}_z\hat{\rho}_3\hat{\boldsymbol{g}}_L^\dagger\hat{\rho}_3+\hat{\rho}_3\hat{\boldsymbol{g}}_L^\dagger\hat{\rho}_3\hat{\sigma}_z)
$$

$$
\left.+(1-\sqrt{1-P^2})(\hat{\sigma}_z\hat{\boldsymbol{g}}_L\hat{\sigma}_z+\hat{\rho}_3\hat{\sigma}_z\hat{\boldsymbol{g}}_L^\dagger\hat{\rho}_3\hat{\sigma}_z)\Big]\right\}.
$$

$$(5.66)$$

The thermoelectric spin coefficient in each of the three directions is

$$
\alpha_x^s = \frac{N\tau G_q}{4e^2}\int_{-\infty}^{\infty}\frac{E\mathrm{d}E}{4k_BT\cosh^2\left(\frac{E}{2k_BT}\right)}\operatorname{Tr}\left\{\sqrt{1-P^2}\hat{\sigma}_x(\hat{\boldsymbol{g}}_L+\hat{\boldsymbol{g}}_L^\dagger)\right\}\tag{5.67}
$$

$$
= \frac{N\tau G_q}{2e^2}\int_{-\infty}^{\infty}\frac{E\mathrm{d}E}{4k_BT\cosh^2\left(\frac{E}{2k_BT}\right)}\operatorname{Tr}\left\{\sqrt{1-P^2}\operatorname{Re}\{\hat{\sigma}_x\hat{\boldsymbol{g}}_L\}\right\}\tag{5.68}
$$

$$
\alpha_y^s = \frac{N\tau G_q}{4e^2}\int_{-\infty}^{\infty}\frac{E\mathrm{d}E}{4k_BT\cosh^2\left(\frac{E}{2k_BT}\right)}\operatorname{Tr}\left\{\sqrt{1-P^2}\hat{\sigma}_y(\hat{\boldsymbol{g}}_L+\hat{\boldsymbol{g}}_L^\dagger)\right\}\tag{5.69}
$$

$$
= \frac{N\tau G_q}{2e^2}\int_{-\infty}^{\infty}\frac{E\mathrm{d}E}{4k_BT\cosh^2\left(\frac{E}{2k_BT}\right)}\operatorname{Tr}\left\{\sqrt{1-P^2}\operatorname{Re}\{\hat{\sigma}_y\hat{\boldsymbol{g}}_L\}\right\}\tag{5.70}
$$

$$
\alpha_z^s = \frac{N\tau G_q}{2e^2}\int_{-\infty}^{\infty}\frac{E\mathrm{d}E}{4k_BT\cosh^2\left(\frac{E}{2k_BT}\right)}\operatorname{Tr}\left\{\operatorname{Re}\{\hat{\sigma}_z\hat{\boldsymbol{g}}_L+P\hat{\boldsymbol{g}}_L\}\right\}.\tag{5.71}
$$

$\operatorname{Tr}\{\hat{\boldsymbol{g}}_L\} = 0$ as a consequence of charge conservation. Therefore, the **z**-polarized thermoelectric spin coefficient $\alpha_s^z$, which is does not depend on the polarization strength

of the barrier, becomes proportional to the charge current thermoelectric coefficient $\alpha'$. When the tunneling interface is polarized in the $\boldsymbol{z}$-direction, as is assumed here, the $\boldsymbol{z}$-polarized spin current $I_s^z = \alpha_s^z \Delta T / T$ is proportional to the homogeneously polarized spin current derived previously,

$$I_s = \alpha \frac{\Delta T}{T} = \frac{G_T}{2e} \frac{E(D_L^0 D_R^z + D_L^z D_R^0)}{4k_B T \cosh^2\left(\frac{E}{2k_B T}\right)} \frac{\Delta T}{T}, \tag{5.72}$$

but now with a different prefactor. The difference in prefactor can be attributed to the differing natures of the spin current considered in Chapter 3 and the one considered herein. The direction-dependent spin conductance coefficients are

$$G_x^s = \frac{N\tau G_q}{2e} \int_{-\infty}^{\infty} \frac{\mathrm{d}E}{4k_B T \cosh^2\left(\frac{E}{2k_B T}\right)} \mathrm{Tr}\left\{\sqrt{1-P^2}\,\mathrm{Re}\{\hat{\rho}_3\hat{\sigma}_x\hat{\boldsymbol{g}}_L\}\right\} \tag{5.73}$$

$$G_y^s = \frac{N\tau G_q}{2e} \int_{-\infty}^{\infty} \frac{\mathrm{d}E}{4k_B T \cosh^2\left(\frac{E}{2k_B T}\right)} \mathrm{Tr}\left\{\sqrt{1-P^2}\,\mathrm{Re}\{\hat{\rho}_3\hat{\sigma}_y\hat{\boldsymbol{g}}_L\}\right\} \tag{5.74}$$

$$G_z^s = \frac{N\tau G_q}{2e} \int_{-\infty}^{\infty} \frac{\mathrm{d}E}{4k_B T \cosh^2\left(\frac{E}{2k_B T}\right)} \mathrm{Tr}\left\{\mathrm{Re}\{\hat{\rho}_3\hat{\sigma}_z\hat{\boldsymbol{g}}_L\} + P\,\mathrm{Re}\{\hat{\rho}_3\hat{\boldsymbol{g}}_L\}\right\}. \tag{5.75}$$

Where the charge current thermoelectric coefficients for the case of N/I/X-structures did not necessarily offer new information regarding the thermoelectric currents traveling through the system, these expressions do. The expressions allow for a treatment of thermoelectric effects yielding spin currents also when spin polarization is not necessarily homogeneous along one axis. This is a generalization which enables a broader consideration, and allows us to consider structures we could not envision using the old framework. We now have two frameworks which together enable us to describe a whole range of thermoelectric systems and materials. The primary limitation of the framework derived within this chapter concerns the prerequisite that the materials used abide by the definitions of $\hat{\boldsymbol{h}}_L$ and $\hat{\boldsymbol{h}}_R$. Aside from this the materials considered can have all kinds of properties, and the tunneling interface can have any polarization.

Some of the assumptions made herein prevent the application of spin-dependent biases to these systems. If $\hat{\boldsymbol{h}}_R$ is defined as above, spin-dependent biases can only be applied in the $\boldsymbol{z}$-direction. This would negate the purpose of the whole derivation, which was done in order to describe different spin polarizations. Consequently, we will not perform a derivation for spin-polarized biases here.

The new information attained as a consequence of performing a quasiclassical derivation so far, when a normal metal is assumed on the right, can mainly be found within the

coefficients $G_x^s$, $G_y^s$, $\alpha_x^s$ and $\alpha_y^s$. In the cases where these are non-zero, we are now able to consider spin currents we could not calculate previously, according to

$$I_\nu^s = G_\nu^s \Delta V + \alpha_\nu^s \frac{\Delta T}{T}. \tag{5.76}$$

As the tunneling interface is polarized in the $+\mathbf{z}$-direction, these coefficients in the $\mathbf{x}$- and $\mathbf{y}$-directions equal zero when $P = 1$, as seen from the prefactor $\sqrt{1 - P^2}$. When there is a $100\%$ probability of $\mathbf{z}$-polarized spin tunneling, there is no probability of tunneling of quasiparticles polarized along other axes. Consequently, these tunneling spin currents disappear. Consequently, when $P = 1$, only the $\mathbf{z}$-component of the spin current survives, and only

$$I_z^s = G_z^s \Delta V + \alpha_z^s \frac{\Delta T}{T} \tag{5.77}$$

remains. Comparing $G_z^s$ to $G'$, we can again find the correction term $\text{Tr}\{\text{Re}\{\hat{\rho}_3\hat{\sigma}_z\hat{\boldsymbol{g}}_L\}\}$. From the density of states consideration, we found that a spin-current can only arise as a result of an applied voltage if the interface polarization is $P \neq 0$. Here, however, there might be cases in which spin currents can arise as a result of an applied voltage bias even when no barrier polarization is present.

## 5.4  Heat current

The heat current to be considered is the one arising to the left of the barrier. The heat current must be Taylor expanded to the first order for us to be able to consider the thermoelectric figure of merit, $ZT$. This is due to this property depending on the thermal heat conductance coefficient $G'_Q$. The complete heat conductance coefficients are

$$
\begin{aligned}
G'_Q = T\frac{\mathrm{d}\dot{Q}}{\mathrm{d}T_L} = \frac{1}{4e^2} \int_{-\infty}^{\infty} \frac{E^2 \mathrm{d}E}{4k_B T \cosh^2\left(\frac{E}{2k_B T}\right)} \text{Tr} \Bigg\{ &G_0 \, \text{Re}\Big\{\hat{\boldsymbol{g}}_R\hat{\boldsymbol{g}}_L + \hat{\boldsymbol{g}}_L\hat{\rho}_3\hat{\boldsymbol{g}}_R^\dagger\hat{\rho}_3\Big\} \\
&+ G_{MR} \, \text{Re}\Big\{\hat{\sigma}_z\hat{\boldsymbol{g}}_R\hat{\boldsymbol{g}}_L + \hat{\boldsymbol{g}}_R\hat{\sigma}_z\hat{\boldsymbol{g}}_L + \hat{\rho}_3\hat{\boldsymbol{g}}_L\hat{\rho}_3\hat{\boldsymbol{g}}_R^\dagger\hat{\sigma}_z + \hat{\boldsymbol{g}}_L\hat{\sigma}_z\hat{\rho}_3\hat{\boldsymbol{g}}_R^\dagger\hat{\rho}_3\Big\} \\
&+ G_1 \, \text{Re}\Big\{\hat{\sigma}_z\hat{\boldsymbol{g}}_R\hat{\sigma}_z\hat{\boldsymbol{g}}_L + \hat{\boldsymbol{g}}_L\hat{\sigma}_z\hat{\rho}_3\hat{\boldsymbol{g}}_R^\dagger\hat{\sigma}_z\hat{\rho}_3\Big\} \Bigg\}
\end{aligned} \tag{5.78}
$$

and

$$\frac{\mathrm{d}\dot{Q}}{\mathrm{d}T_R} = -\frac{1}{4e^2} \int_{-\infty}^{\infty} \frac{E^2 \mathrm{d}E}{4k_B T^2 \cosh^2\left(\frac{E}{2k_B T}\right)} \operatorname{Tr}\left\{ G_0 \operatorname{Re}\left\{ \hat{\boldsymbol{g}}_L \hat{\boldsymbol{g}}_R + \hat{\boldsymbol{g}}_L \hat{\rho}_3 \hat{\boldsymbol{g}}_R^\dagger \hat{\rho}_3 \right\} \right.$$
$$\left. + G_{MR} \operatorname{Re}\left\{ \hat{\boldsymbol{g}}_L \hat{\boldsymbol{g}}_R \hat{\sigma}_z + \hat{\boldsymbol{g}}_R \hat{\boldsymbol{g}}_L \hat{\sigma}_z + \hat{\rho}_3 \hat{\boldsymbol{g}}_L \hat{\rho}_3 \hat{\boldsymbol{g}}_R^\dagger \hat{\sigma}_z + \hat{\boldsymbol{g}}_L \hat{\sigma}_z \hat{\rho}_3 \hat{\boldsymbol{g}}_R^\dagger \hat{\rho}_3 \right\} \right.$$
$$\left. + G_1 \operatorname{Re}\left\{ \hat{\sigma}_z \hat{\boldsymbol{g}}_R \hat{\sigma}_z \hat{\boldsymbol{g}}_L + \hat{\boldsymbol{g}}_L \hat{\sigma}_z \hat{\rho}_3 \hat{\boldsymbol{g}}_R^\dagger \hat{\sigma}_z \hat{\rho}_3 \right\} \right\} = -\frac{\mathrm{d}\dot{Q}}{\mathrm{d}T_L}. \tag{5.79}$$

The complete thermoelectric coefficient becomes

$$\frac{\mathrm{d}\dot{Q}}{\mathrm{d}V_R} = \frac{1}{4e} \int_{-\infty}^{\infty} \frac{E \mathrm{d}E}{4k_B T \cosh^2\left(\frac{E}{2k_B T}\right)} \operatorname{Tr}\left\{ G_0 \operatorname{Re}\left\{ \hat{\boldsymbol{g}}_L \hat{\boldsymbol{g}}_R \hat{\rho}_3 + \hat{\boldsymbol{g}}_L \hat{\boldsymbol{g}}_R^\dagger \hat{\rho}_3 \right\} \right.$$
$$\left. + G_{MR} \operatorname{Re}\left\{ \hat{\rho}_3 \hat{\sigma}_z \hat{\boldsymbol{g}}_L \hat{\boldsymbol{g}}_R + \hat{\rho}_3 \hat{\boldsymbol{g}}_L \hat{\sigma}_z \hat{\boldsymbol{g}}_R + \hat{\boldsymbol{g}}_L \hat{\sigma}_z \hat{\boldsymbol{g}}_R^\dagger \hat{\rho}_3 + \hat{\boldsymbol{g}}_L \hat{\boldsymbol{g}}_R^\dagger \hat{\sigma}_z \hat{\rho}_3 \right\} \right.$$
$$\left. + G_1 \operatorname{Re}\left\{ \hat{\sigma}_z \hat{\rho}_3 \hat{\boldsymbol{g}}_L \hat{\sigma}_z \hat{\boldsymbol{g}}_R + \hat{\boldsymbol{g}}_L \hat{\sigma}_z \hat{\boldsymbol{g}}_R^\dagger \hat{\sigma}_z \hat{\rho}_3 \right\} \right\}. \tag{5.80}$$

When the right side is a normal metal, the quasiclassically derived heat conductance coefficient is

$$G_Q' = \frac{1}{2e^2} \int_{-\infty}^{\infty} \frac{E^2 \mathrm{d}E}{4k_B T \cosh^2\left(\frac{E}{2k_B T}\right)} \operatorname{Tr}\left\{ \operatorname{Re}\{ G_0 \hat{\rho}_3 \hat{\boldsymbol{g}}_L + 2 G_{MR} \hat{\sigma}_z \hat{\rho}_3 \hat{\boldsymbol{g}}_L + G_1 \hat{\rho}_3 \hat{\boldsymbol{g}}_L \} \right\}$$

$$\tag{5.81}$$

$$= \frac{G_q N \tau}{e^2} \int_{-\infty}^{\infty} \frac{E^2 \mathrm{d}E}{4k_B T \cosh^2\left(\frac{E}{2k_B T}\right)} \operatorname{Tr}\left\{ \operatorname{Re}\{ \hat{\rho}_3 \hat{\boldsymbol{g}}_L + P \hat{\sigma}_z \hat{\rho}_3 \hat{\boldsymbol{g}}_L \} \right\}. \tag{5.82}$$

The result for the correspondingly derived thermoelectric coefficient is

$$\alpha' = \frac{\mathrm{d}\dot{Q}}{\mathrm{d}V_R} = \frac{N G_q \tau}{e} \int_{-\infty}^{\infty} \frac{E \mathrm{d}E}{4k_B T \cosh^2\left(\frac{E}{2k_B T}\right)} \operatorname{Tr}\left\{ \operatorname{Re}\{ \hat{\boldsymbol{g}}_L + P \hat{\sigma}_z \hat{\boldsymbol{g}}_L \} \right\}, \tag{5.83}$$

which is identical to the thermoelectric coefficient obtained when differentiating the quasiclassical charge current with respect to the temperature. Therefore, the heat and charge current coefficients can be gathered together in a $2 \times 2$ Onsager response matrix in the next section.

A consideration of the spin heat current is not included herein, as the consideration of this parameter does not contribute information which we will use throughout the remainder of this thesis. The coefficients derived from Taylor expanding the spin heat current are not considered on their own, and do not contribute when computing the Seebeck coefficient or thermoelectric figure of merit. Accordingly, such a consideration is disregarded.

## 5.5  Onsager matrix

The first set of results obtained in this section can be grouped together into a $2 \times 2$ Onsager matrix

$$\begin{pmatrix} I_q \\ \dot{Q} \end{pmatrix} = \begin{pmatrix} L_{11} & L_{12} \\ L_{12} & L_{22} \end{pmatrix} \begin{pmatrix} V \\ \Delta T \end{pmatrix} \tag{5.84}$$

when the right-hand-side material is a normal metal with $\hat{\boldsymbol{g}}_R = \hat{\rho}_3$. Spin-dependent biases are not considered. Grouping the expressions together, this becomes

$$\begin{pmatrix} I_q \\ \dot{Q} \end{pmatrix} = \begin{pmatrix} G' & \alpha' \\ \alpha' & G'_Q \end{pmatrix} \begin{pmatrix} V \\ \Delta T/T \end{pmatrix}, \tag{5.85}$$

where the coefficients are

$$\alpha' = \frac{G_q N \tau}{e} \int_{-\infty}^{\infty} \frac{E \mathrm{d}E}{4 k_B T \cosh^2\left(\frac{E}{2k_B T}\right)} \operatorname{Tr}\left\{ \operatorname{Re}\{\hat{\boldsymbol{g}}_L + P\hat{\sigma}_z \hat{\boldsymbol{g}}_L\}\right\} \tag{5.86}$$

$$G' = G_q N \tau \int_{-\infty}^{\infty} \frac{\mathrm{d}E}{4 k_B T \cosh^2\left(\frac{E}{2k_B T}\right)} \operatorname{Tr}\left\{ \operatorname{Re}\{\hat{\rho}_3 \hat{\boldsymbol{g}}_L + P\hat{\rho}_3 \hat{\sigma}_z \hat{\boldsymbol{g}}_L\}\right\} \tag{5.87}$$

$$G'_Q = \frac{G_q N \tau}{e^2} \int_{-\infty}^{\infty} \frac{E^2 \mathrm{d}E}{4 k_B T \cosh^2\left(\frac{E}{2k_B T}\right)} \operatorname{Tr}\left\{ \operatorname{Re}\{\hat{\rho}_3 \hat{\boldsymbol{g}}_L + P\hat{\sigma}_z \hat{\rho}_3 \hat{\boldsymbol{g}}_L\}\right\}. \tag{5.88}$$

This is comparable to the $2 \times 2$ Onsager matrix derived in Refs. [46] and [49]. When the right hand side is a normal metal, using the quasiclassical Green function formalism to

derive the thermoelectric coefficients does not seem to provide new information for the charge and heat current. It does, however, when $\hat{\boldsymbol{g}}_R$ is allowed to remain general. The new information obtainable using this framework which will be employed in the next chapter resides within the direction-dependent thermal spin coefficients, given by

$$\alpha_x^s = \frac{N\tau G_q}{2e^2} \int_{-\infty}^{\infty} \frac{E\,\mathrm{d}E}{4k_B T^2 \cosh^2\left(\frac{E}{2k_B T}\right)} \operatorname{Tr}\left\{\sqrt{1-P^2}\operatorname{Re}\{\hat{\sigma}_x \hat{\boldsymbol{g}}_L\}\right\} \qquad (5.89)$$

$$\alpha_y^s = \frac{N\tau G_q}{2e^2} \int_{-\infty}^{\infty} \frac{E\,\mathrm{d}E}{4k_B T^2 \cosh^2\left(\frac{E}{2k_B T}\right)} \operatorname{Tr}\left\{\sqrt{1-P^2}\operatorname{Re}\{\hat{\sigma}_y \hat{\boldsymbol{g}}_L\}\right\} \qquad (5.90)$$

$$\alpha_z^s = \frac{N\tau G_q}{2e^2} \int_{-\infty}^{\infty} \frac{E\,\mathrm{d}E}{4k_B T^2 \cosh^2\left(\frac{E}{2k_B T}\right)} \operatorname{Tr}\left\{\operatorname{Re}\{\hat{\sigma}_z \hat{\boldsymbol{g}}_L + P\hat{\boldsymbol{g}}_L\}\right\}. \qquad (5.91)$$

The thermoelectric characterization parameters $S$, the Seebeck coefficient, and $ZT$, the thermoelectric figure of merit, are defined in the same manner as in Chapter 3. The Seebeck coefficient is

$$S = -\frac{\alpha'}{G'T}, \qquad (5.92)$$

and the thermoelectric figure of merit is

$$ZT = \left(\frac{G'G_Q'}{(\alpha')^2} - 1\right)^{-1}. \qquad (5.93)$$

We have now presented a complete framework for calculating thermoelectric coefficients in tunneling hybrid structures which reside in the quasiclassical regime. The materials to which these expressions are applied to do not in fact need to be superconducting, but do need to be describable by the Keldysh Green function formalism as well as contain some inherent particle-hole asymmetry. Otherwise, large thermoelectric effects will not be predictable using this procedure. The framework presented is completely general in so far as the materials can be described by the equilibrium matrix

$$\hat{\boldsymbol{h}}_L = \tanh\left(\frac{\beta_L E}{2}\right)\hat{\mathbf{1}} \qquad (5.94)$$

on the left hand side and

$$\hat{\boldsymbol{h}}_R = \begin{pmatrix} \tanh\left(\frac{\beta_L(E+eV_R)}{2}\right)\underline{\mathbf{1}} & 0 \\ 0 & \tanh\left(\frac{\beta_L(E-eV_R)}{2}\right)\underline{\mathbf{1}} \end{pmatrix} \qquad (5.95)$$

on the right, with the chemical potential on the left $\mu_L = 0$ for reference. If these conditions are met, the most general expressions should be applicable to any material system. This allows us to retain information which the albeit simpler methodology for homogeneously polarized asymmetries cannot describe.

# Chapter 6

# Thermoelectric response in hybrids with arbitrary spin-dependent fields

This section will focus on employing the framework for thermoelectric effects derived in Chapter 5. Consequently, we are able to consider hybrid systems which are not necessarily homogeneously spin-polarized. The total system considered is as shown graphically in Figure 4.12, which is repeated below. We consider tunneling currents from the middle of the central nanowire in a superconductor/unknown material/superconductor Josephson junction and into a normal metal electrode. The nanowire of the unknown material is separated from the normal metal electrode by an interface barrier which can have any interface polarization and interface transparency in the tunneling limit. As the unknown material can contain arbitrary spin-dependent fields, tunneling from a conical ferromagnet, a spin-orbit-coupled semiconductor and a normal-metal Josephson junction with spatially varying spin-active interfaces can now be studied. The main focus areas of this section will be the arising heat and charge thermoelectric effects quantified by the thermoelectric coefficient $\alpha'$, the Seebeck coefficient $S$ and the thermoelectric figure of merit $ZT$, as well as the thermal direction-dependent spin currents described by the newly derived thermoelectric spin coefficient $\alpha_s^\nu$.

The results are obtained in the same manner as before. The Usadel equation is solved in the middle of a nanowire squeezed between two superconducting reservoirs. The difference from previous sections is the parameter saved, which now is the $\underline{\gamma}$-matrices instead of the density of states. The quasiclassical framework for randomly polarized thermoelectric effects is then applied to the different structures to be considered in order to quantify the thermoelectric effects arising through tunneling across an interface barrier with changeable polarization. The thermoelectric coefficient $\alpha'$ derived in Chapter 5, which will be considered throughout this chapter, need not always be identical to the
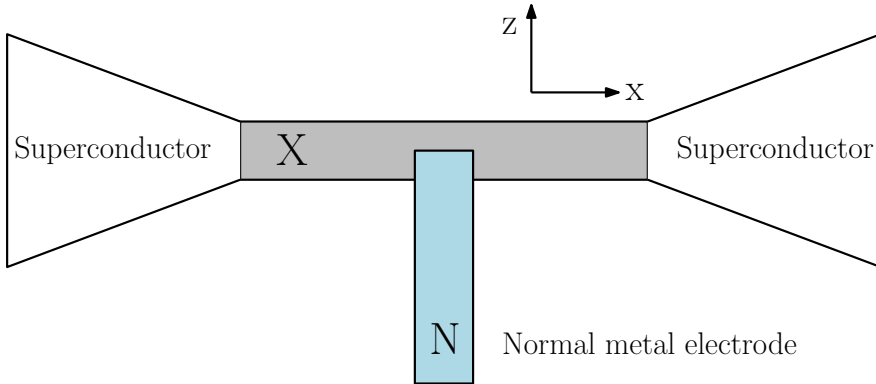
Figure 6.1: Schematic of the experimental setup considered in both sections considering numerical results. There is a tunneling barrier, which can be fully polarized, between the normal metal electrode N and the nanowire X centered between two superconducting reservoirs.

thermoelectric coefficient $\alpha$ discussed in Chapters 3 and 4. Nonetheless, for reasons of simplicity, the notation $\alpha$ will be employed throughout this chapter as well.

The material systems studied are conical ferromagnetism, spin-orbit coupled semiconductor nanowires and superconductor/normal metal/superconductor Josephson junctions with spin-active interfaces. Thermoelectric coefficients connected to spin-orbit coupled semiconductor nanowires will be presented in black and red, conical ferromagnets will be shown in green and yellow and spin-active interfaces in pink and yellow for simplicity in reading. Figures showing the density of states will be presented in blue and green as before.

The goal of the calculations performed herein is to determine and quantify the thermoelectric effects arising in generally polarized spin-split superconducting tunneling junctions. Different hybrid systems are studied in order to maximize the thermoelectric effects arising. In addition to spin-polarization not having to be along only one axis, the main advantage of the material systems considered within this chapter is the absence of the need to apply large magnetic fields of size order $\approx 1$ T for the thermoelectric phenomena to occur. Other means than the Zeeman-splitting of superconductors are utilized to obtain the desired particle-hole asymmetry necessary for achieving large thermoelectric effects.

## 6.1 Absence of Josephson spin supercurrent

Josephson junctions are well known for the charge supercurrent traversing the central layer as a result of a superconducting phase difference. First in this section, we will apply the quasiclassical current expressions defined in Equations 5.6-5.8 to a superconductor/insulator/superconductor (S/I/S) Josephson junction. The expressions for

thermoelectric coefficients are not applied in this case, as the goal is to discern whether a temperature difference applied across the interface barrier is able to generate a spin supercurrent traversing the junction. A thermal spin supercurrent is therefore studied directly, instead of via a thermoelectric coefficient. For this particular study the potential of Josephson tunneling due to a superconducting phase difference is considered, which is neglected throughout the other parts of this thesis. This consideration is performed in order to discern whether a superconducting phase difference, along with a temperature gradient, is capable of generating a spin supercurrent. The case of a barrier fully polarized in the $z$-direction is considered, and only the spin current polarized along this axis should therefore be able to exist. On the right hand side of the interface barrier, this spin current is defined by

$$I_s^z = \frac{N_0 DA}{8} \int_{-\infty}^{\infty} \mathrm{d}E \, \mathrm{Tr} \left\{ \hat{\rho}_3 \hat{\sigma}_z [\check{g}_R (\partial_x \check{g}_R)]^K \right\}. \tag{6.1}$$

Utilizing the complete boundary conditions

$$(\check{g}_R \partial_x \check{g}_R)^K = \frac{1}{4e^2 N_0 DA} [G_0 \check{g}_L + G_{MR}\{\check{\kappa}, \check{g}_L\} + G_1 \check{\kappa} \check{g}_L \check{\kappa} - i G_\phi \check{\kappa}', \check{g}_R]^K, \tag{6.2}$$

the case of $T_L \neq T_R$ can be studied numerically using MATLAB. The Green function matrices are

$$\check{g}_j = \begin{pmatrix} \hat{g}_j^R & \hat{g}_j^K \\ 0 & \hat{g}_j^A \end{pmatrix} \tag{6.3}$$

$$\hat{g}_j^A = -\hat{\rho}_3 \hat{g}_j^{R\dagger} \hat{\rho}_3 \tag{6.4}$$

$$\hat{g}_j^K = \tanh\left(\frac{\beta_j E}{2}\right) (\hat{g}_j^R - \hat{g}_j^A), \tag{6.5}$$

where the superconducting retarded Green function matrix is $\hat{g}_j^R$ is defined as

$$\hat{g}_j^R = \begin{pmatrix} c_j & 0 & 0 & s_j e^{i\theta_j} \\ 0 & c_j & s_j e^{i\theta_j} & 0 \\ 0 & -s_j e^{-i\theta_j} & -c_j & 0 \\ -s_j e^{-i\theta_j} & 0 & 0 & -c_j \end{pmatrix}. \tag{6.6}$$

Here, $\theta_L = 0$, $c_j = \cosh(\Theta_j)$, $\sinh(\Theta_j)$, $\Theta_j = \tanh^{-1}\left(\frac{\Delta_j}{\varepsilon}\right)$ and
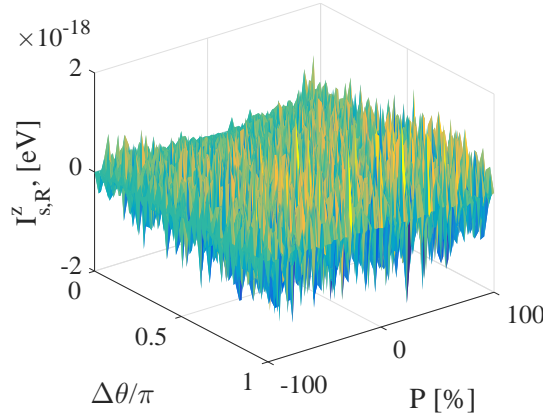
Figure 6.2: $z$-polarized spin supercurrent on the right hand side of the interface in a S/I/S Josephson junction as a function of the polarization and superconducting phase difference. The temperatures and interface parameters used are $T_L = 0.1T_{c,0}$, $T_R = 0.5T_{c,0}$, $\tau = 0.1$ for a tunneling consideration and $G_\varphi = 1.05$ in order to ensure triplet superconductivity.

$$\Delta_j = \Delta_{j,0} \tanh\left(1.74\sqrt{\frac{T_{c0,j}}{T_j} - 1}\right). \qquad (6.7)$$

The two superconductors are assumed identical in all but the phase and temperature. The resulting $z$-polarized spin supercurrent is shown in Figure 6.2. As seen from Figure 6.2, the thermally induced spin supercurrent is numerically equal to zero and accordingly does not exist. This is as could be expected for this situation when considering quasiparticle tunneling, as the coefficient governing the thermal response for spin currents depends on there being a particle-hole asymmetry in the density of states on at least one side of the junction. A temperature gradient over a superconductor/insulator/superconductor Josephson junction can result in a heat current, and a charge supercurrent is generated by the superconducting phase difference, but no spin current is seen to arise. This result is consistent with what one could expect when considering quasiparticle tunneling and the accompanying thermoelectric effects, as no particle-hole asymmetry is present in the S/I/S Josephson junction. The only possibility of an existing spin current would be if the superconducting phase difference, neglected for quasiparticle tunneling, was capable of generating the spin supercurrent. This is, however, not the case. The negative result is included herein for completeness.

## 6.2   Spin-active interfaces

Chapter 4 was devoted to both maximizing the thermoelectric effects arising in Zeeman-split superconducting hybrids, and studying the novel effects which may arise when

more complex structures and materials are employed. The last part of the chapter was focused on determining whether material systems encompassing non-Zeeman split superconductors were capable of generating comparable thermoelectric effects. This was seen to be quite promising, particularly when studying superconductor/normal metal/superconductor (S/N/S) Josephson junctions where the S/N-interfaced are spin-polarized along the **z**-axis. Consequently, the framework presented in Section 5 allowing for the study of thermoelectric effects in materials where spin-polarization can exist along more than only one axis was developed. Within this section, the superconductor/normal metal/superconductor (S/N/S) Josephson junction with spin-active interfaces is once again considered. Now, however, the magnetization direction of the magnetic insulator at the right interface is locked in the $+\boldsymbol{z}$-direction while the left one is not. The left-hand magnetic isolator is allowed to be polarized in varying directions in the $\boldsymbol{yz}$-plane, and the effect of changing this angle on the thermoelectric response of the system is the main focus point of the study. The magnetization matrices for each S/N interface are defined by

$$\widehat{\boldsymbol{M}}_R = \mathrm{diag}(\sigma_z, \sigma_z) \tag{6.8}$$

$$\widehat{\boldsymbol{M}}_L = \cos(\phi)\mathrm{diag}(\sigma_z, \sigma_z) + \sin(\phi)\sin(\alpha)\mathrm{diag}(\sigma_y, \sigma_y^*) + \sin(\phi)\cos(\alpha)\mathrm{diag}(\sigma_x, \sigma_x). \tag{6.9}$$

In order to only vary the magnetization direction in the $\boldsymbol{yz}$-plane we have defined $\alpha = \pi/2$, causing the $\sigma_x$-dependency to disappear. A schematic showing the spin-polarized Josephson junction and highlighting the polarization at the interfaces is shown in Figure 6.3. The thermoelectric effects considered arise due to quasiparticle tunneling from the middle of the normal metal shown in this figure, across a polarized tunneling barrier and into a normal metal electrode. The latter two features are not shown in Figure 6.3, but can be found in Figure 6.1.

The numerical procedure used when obtaining the results presented herein includes solving the Usadel equation, obtaining the $\underline{\gamma}$-matrices in the middle of the normal metal nanowire and calculating the various thermoelectric coefficients using a numerical Riemann sum. The products of these calculations will be presented as three-dimensional MATLAB plots. The coefficients studied are the thermal charge current coefficient $\alpha$, the Seebeck coefficient $S$, the thermoelectric figure of merit $ZT$ and the thermal spin current coefficient $\alpha_s^\nu$. The superscript $\nu$ denotes each of the three spatial directions $\{x, y, z\}$. The thermal spin coefficient in the **z**-direction, $\alpha_s^z$, is expected to be qualitatively identical to the thermal charge coefficient $\alpha$, as $\alpha$ is proportional to the polarization and $\alpha_s^z$ is independent of polarization. Accordingly, when the tunneling barrier is non-polarized and $P = 0$ the thermoelectric coefficient $\alpha$ vanishes along with the Seebeck coefficient $S$ and the thermoelectric figure of merit $ZT$. The thermal spin coefficients in the **x**- and **y**-directions are expected to vary a great deal with the polarization, as they are proportional to $\sqrt{1 - P^2}$. When the spin-dependent tunneling
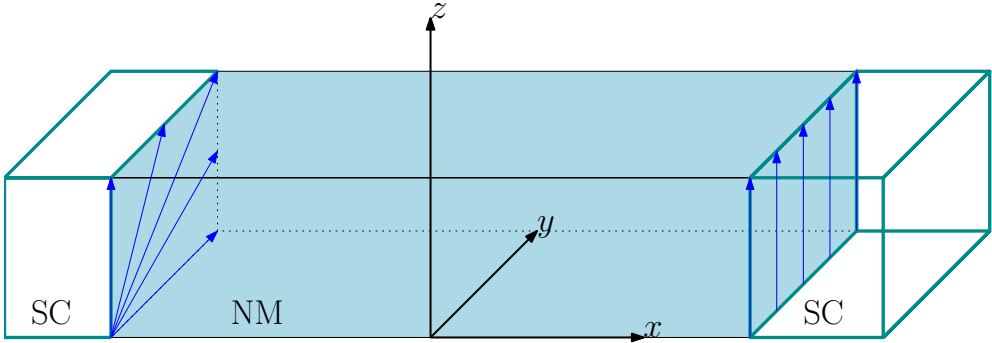
Figure 6.3: Schematic of a superconductor/normal metal/superconductor (S/N/S) Josephson junction with spin-active interfaces. The polarization at the interfaces can be made to vary in the $\boldsymbol{yz}$-plane. $\phi = 0$ represents polarization along the $+\boldsymbol{z}$-axis, when $\phi = \pi/2$ the polarization is along the $+\boldsymbol{y}$-axis and when $\phi = \pi$ the polarization is parallel to the $-\boldsymbol{z}$-axis. The superconductors are in reality very large when compared to the normal metal nanowire.

probability $P$ of the $\mathbf{z}$-polarized interface equals 1, no $\mathbf{x}$- and $\mathbf{y}$- polarized species are able to pass through. Consequently, $\alpha_s^x$ and $\alpha_s^y$ are studied only for the case of a non-polarized barrier with $P = 0$. We expect $\alpha_s^x$ to be close to zero in all cases, as there should be few quasiparticles polarized in the x-direction when the ferromagnetic barrier polarization varies in the $\boldsymbol{yz}$-plane. The more traditional thermoelectric effects, quantified by $\alpha$, $S$ and $ZT$, are presented for the case when the polarization equals $P = 97\%$. This value is chosen as polarizations of that size have been reported for the ferromagnetic insulator GdN at 3 K [68].

The new thermoelectric coefficients are plotted in a non-dimensional manner, as $\frac{\alpha e}{G_\tau \Delta_0}$ where $G_\tau = G_q N \tau$. $G_q$ is the conductance quantum, $N$ the number of tunneling channels and $\tau$ represents interface transparency. The parameter $G_\tau$ governs tunneling from the center of the normal metal nanowire to the normal metal electrode. From the test of charge current expressions in Chapter 5 it would seem that $G_0 = G_q N \tau = \frac{G_\tau}{2}$, at least in the case when $P = 0$. Accordingly, when comparing $\alpha$ herein to the thermoelectric coefficient $\alpha$ from Chapters 3 and 4, one should note that an extra factor of $\frac{1}{2}$ might have to be added to the coefficients. As the same factor is added to all coefficients, this does not make an impact when considering the Seebeck coefficient $S$ and the thermoelectric figure of merit $ZT$, and these will be directly comparable to the results obtained with the $\boldsymbol{z}$-polarized framework. This remains true throughout the remainder of this section.

In contrast to Chapter 4, the angle of the magnetization at the interfaces is here varied instead of $G_\phi$. This is due to ease of experimental consideration, as $G_\phi$ cannot be easily changed in situ. Consequently the thermoelectric parameters are studied in terms of the superconducting phase difference and the angle of magnetization in the $\boldsymbol{yz}$-plane at the S/N interfaces, which both are alterable through for instance external fields and currents. It should be possible to keep these small enough to maintain the low-field

advantage when comparing to thermoelectric effects in Zeeman-split superconducting hybrids. The S/N interfaces are weakly polarized, and the interface polarization within the Josephson junction is again set to $G_{MR} = 0.1$. The normal metal length is $L_N = 15$ nm, $\zeta = 4$, $\xi = 30$ nm and $T = 0.2T_{c,0}$. The different values to be considered for the parameter governing the spin-dependent phase shifts at the magnetic S/N interfaces are $G_\phi = 0.5$, $G_\phi = 1.05$ and $G_\phi = 1.55$.



(a)

(b)

(c)
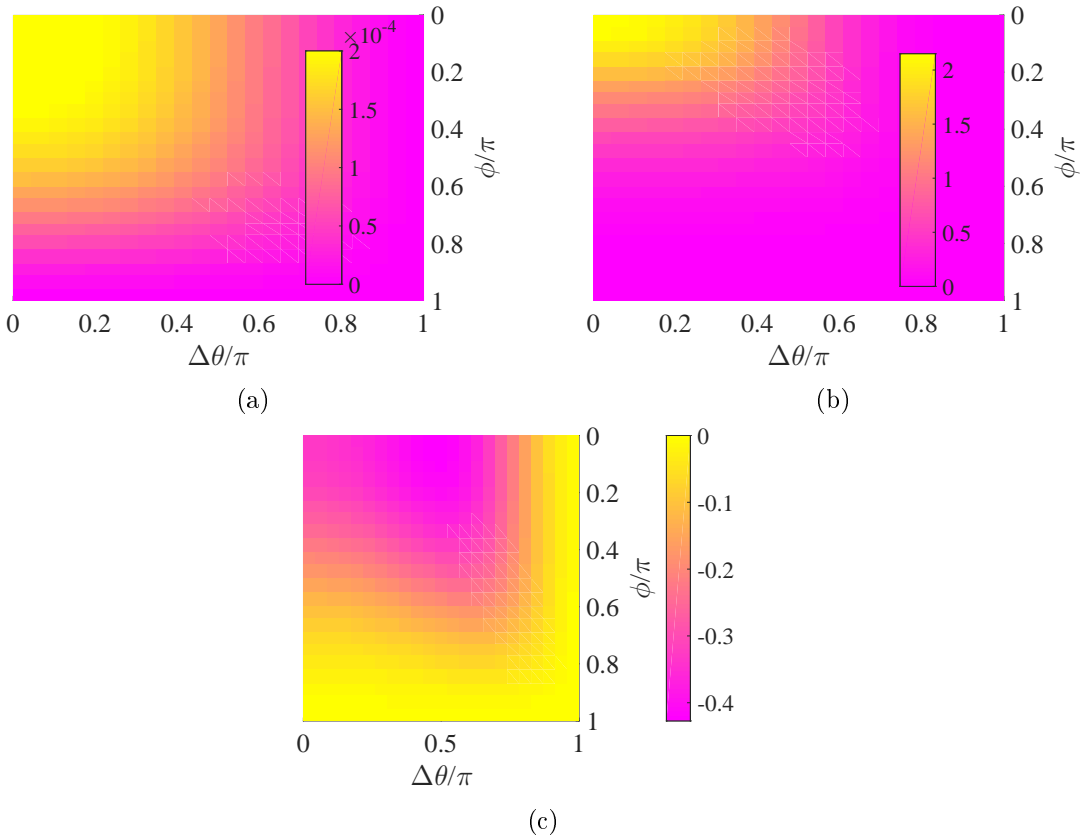
Figure 6.4: (a) Seebeck coefficient $S$, (b) thermoelectric figure of merit $ZT$ and (c) thermoelectric coefficient $\alpha e/(G_\tau \Delta_0)$ for tunneling from $x = L_N/2$ in a S/N/S josephson junction with magnetic interfaces to a normal metal electrode. $T = 0.2T_{c,0}$, $L_N = 15$ nm, $G_{MR} = 0.1$, $G_\phi = 0.5$ and the polarization of the tunneling interface is $P = 97\%$.

Figure 6.4 shows the (a) Seebeck coefficient, (b) thermoelectric figure of merit and (c) thermoelectric coefficient $\alpha$ for a S/N/S Josephson junction with spin-active interfaces, the left-hand one variable in the $\boldsymbol{yz}$-plane. A key parameter in this case is $G_\phi = 0.5$. The thermoelectric effects are seen to be able to match the observations made in Section 4 where both of the spin-active S/N interfaces were polarized along the $\boldsymbol{z}$-axis. Both $ZT \approx 2$ and $S \approx 0.2$ meV are comparable to the N/I/ZS case, and so is $\alpha_{\max} \approx 0.4$. The major advantage to the system considered here concerns the fact that only small applied magnetic fields are necessary to obtaining the effects presented in Figure 6.4.

The thermoelectric coefficient $\alpha$ is here actually quite a lot larger than in the N/I/ZS case, but $G_\tau$ is not directly comparable to the conductance $G_T = G^\uparrow + G^\downarrow$ employed in the framework assuming only homogeneously magnetized systems. In relation to the discussion in Chapter 5 concerning the S/N/S Josephson junction with **z**-polarized spin-active interfaces, the value for the spin-dependent interfacial phase shifts used to obtain the results presented in Figure 6.4, $G_\phi = 0.5$, is smaller than the value providing the maximum thermoelectric effects in the **z**-polarized case.

Figure 6.5 shows the (a)-(b) Seebeck coefficient, (c)-(d) thermoelectric figure of merit and (e)-(f) thermoelectric coefficient versus the interface magnetization angle and super-conducting phase difference for the same S/N/S Josephson junction with spin active interfaces. The difference concerns the spin-dependent phase shifts at the S/N-interfaces, which is $G_\phi = 1.05$ in the left column and $G_\phi = 1.55$ in the column on the right. The Seebeck coefficient, the thermoelectric figure of merit and the thermal charge current coefficient $\alpha$ are seen to decrease with increasing values of $G_\phi$. This can be explained as in Chapter 4, where the features in the densities of states encompassed by the distribution function $C(E) = \left[4k_B T \cosh^2\left(\frac{E}{2k_B T}\right)\right]^{-1}$ are smaller for the largest values of $G_\phi$. This can be seen from Figure 4.15, which shows the difference in spin-dependent density of states for the S/N/S Josephson junction with **z**-polarized interfaces versus the energy and the phase difference for $G_\phi = $ (a) 0.55, (b) 0.8, (c) 1.05 and (d) 1.55. The figures show the case of $\phi = 0$. This is also where the maximum values of $\alpha$, $S$ and $ZT$ are found when $G_\phi = 0.5$, as seen in Figure 6.4.

Interestingly, the largest thermoelectric effects do not occur when both interfaces are **z**-polarized, represented by $\phi = 0$, for all values of $G_\phi$. When $G_\phi = 0$ the maximum values of $\alpha$, $S$ and $ZT$ occur when $\phi = 0$. When $G_\phi = 1.05$ and $G_\phi = 1.55$, however, these parameters seem to be maximized when $\phi = \pi/2$. When this occurs, the left S/N interface is polarized in the **y**-direction. More intuitively, the interface angle $\phi = \pi$ is accompanied by very small thermoelectric effects, as the S/N interfaces will now be polarized in opposite directions.

The thermoelectric effects considered so far do not differ greatly from the ones that could be studied using the framework derived in Chapter 3, apart from the new element of control that is the interface magnetization angle. The most interesting novel effects which can only be studied using the framework presented in Chapter 5 are encompassed by the thermal spin current coefficients $\alpha_s^\nu$, which are presented in Figure 6.6 for the phase-shift parameter $G_\phi = 0.5$. As expected, the thermoelectric coefficient in the **x**-direction is very small. It does, however, exhibit the fascinating property of sign change. This occurs as a result of altering the superconducting phase difference, and not the magnetization angle at the S/N-interfaces. The same behavior of $\alpha_s^x$ can also be found for $G_\phi = 1.05$ and $G_\phi = 1.55$. In spite of this interesting behavior we will neglect the spin current in this direction throughout the rest of this particular consideration as $\alpha_s^x$ is very small, and not useful in real applications.
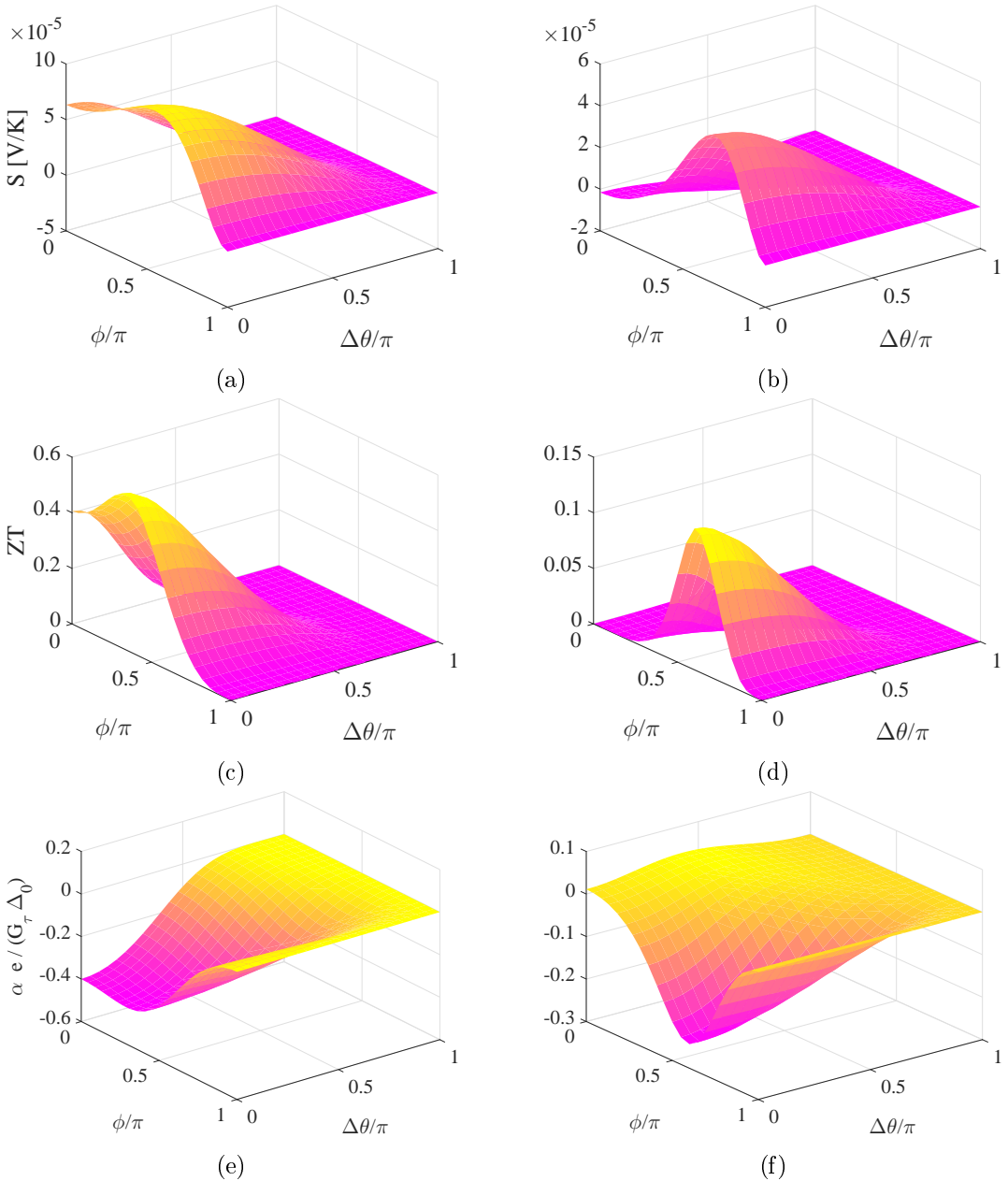
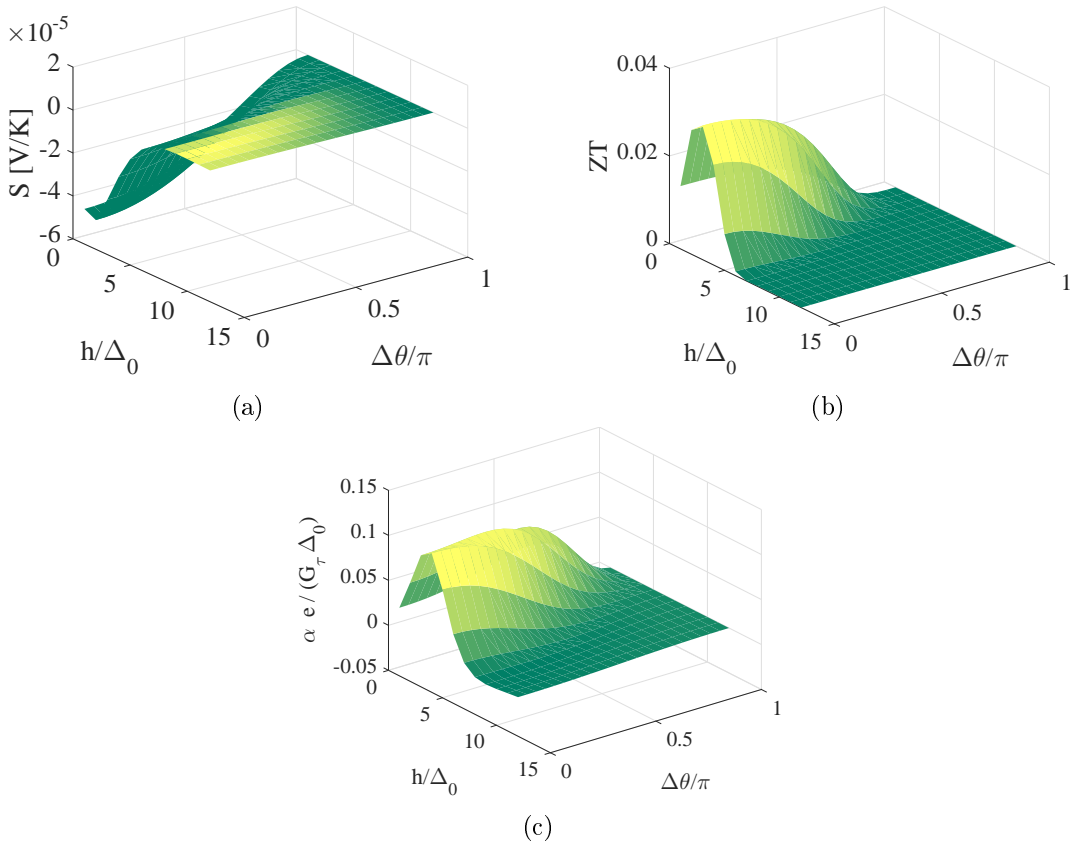Figure 6.5: (a)-(b) Seebeck coefficient $S$, (c)-(d) thermoelectric figure of merit $ZT$ and (e)-(f) thermoelectric coefficient $\alpha$ for tunneling from $x = L_N/2$ in a S/N/S josephson junction with magnetic interfaces to a normal metal electrode. $T = 0.2T_{c,0}$, $L_N = 15$ nm, $G_{MR} = 0.1$ and the polarization is $P = 97\%$. The first column shows $G_\phi = 1.05$ and the second shows $G_\phi = 1.55$.

(a)

(b)



(c)
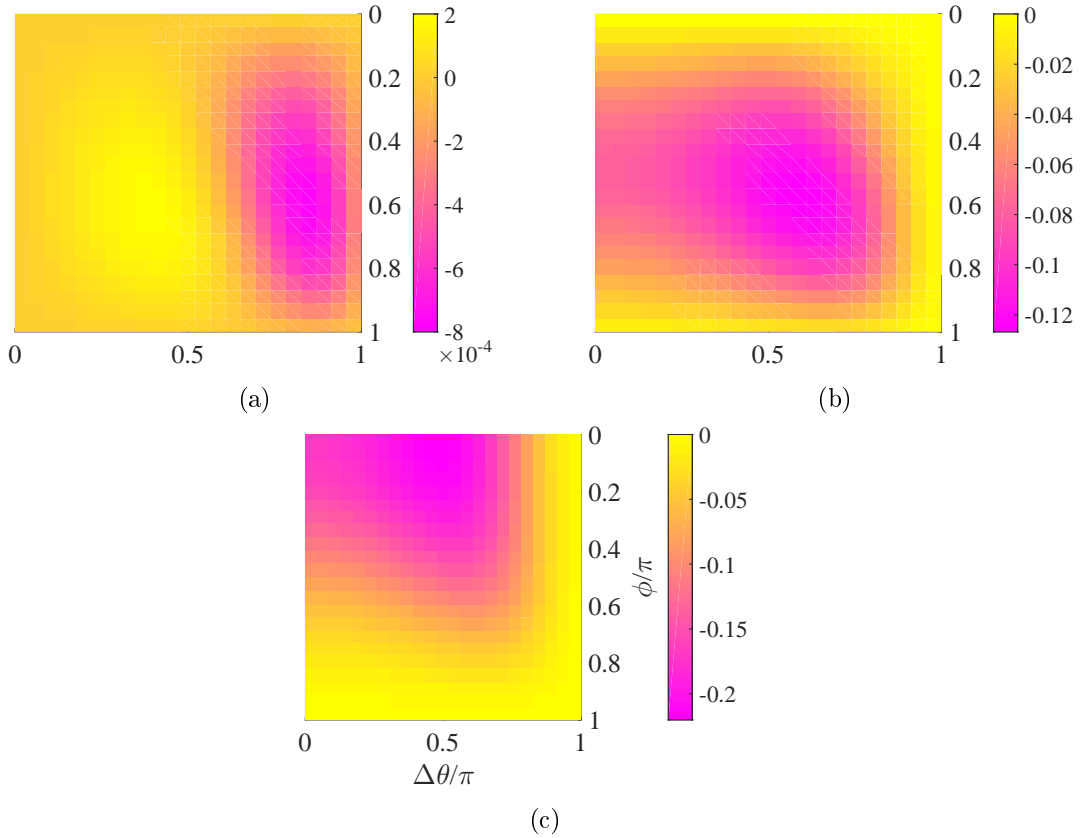
Figure 6.6: Thermoelectric spin-current coefficient $\alpha_s^\nu e^2/(G_\tau \Delta_0)$ in the (a) $\boldsymbol{x}$-direction, (b) $\boldsymbol{y}$-direction and (c) $\boldsymbol{z}$-direction for tunneling from $x = L_N/2$ in a S/N/S josephson junction with spin-active interfaces to a normal metal electrode. $T = 0.2T_{c,0}$, $L_N = 15$ nm, $G_{MR} = 0.1$, $G_\phi = 0.5$ and the polarization is $P = 0$ for maximized spin currents.

The maximum values of the thermal spin currents, $I_s^\nu = \alpha_s^\nu \Delta T/T$, can be found for the expected magnetization angles in the $\boldsymbol{y}$- and $\boldsymbol{z}$-directions. The maximum value for $\alpha_s^y$ is found when the magnetization angle of the left S/N interface is $\phi = \pi/2$ denoting magnetization in the $\boldsymbol{y}$-direction, and $\alpha_s^z$ is maximized when $\phi = 0$. The thermal spin coefficients in the $\boldsymbol{x}$- and $\boldsymbol{y}$-directions disappear when the polarization of the $\boldsymbol{z}$-polarized interface between the center of the normal metal nanowire and the normal metal electrode is $P = 100\%$.

There seems to be a trend for certain parameters were the coefficients always equal zero. Both $\Delta\theta = \pi$ and $\phi = \pi$ seem to consistently result in vanishing thermoelectric effects. For the case of the left side being aligned with $\phi = \pi$ the vanishing thermoelectric effects can be explained from the expressions for the magnetization matrices. When $\phi = \pi$ we see that $\widehat{\boldsymbol{M}}_R = \hat{\sigma}_z$ while $\widehat{\boldsymbol{M}}_L = -\hat{\sigma}_z$. As the interfaces are otherwise equal the spin-splitting inflicted upon the normal metal by each interface cancel each other

out, resulting in the tunneling thermoelectric effects becoming minute and seemingly vanishing.



(a) $\alpha_s^y e^2/(G_\tau \Delta_0)$

(b) $\alpha_s^z e^2/(G_\tau \Delta_0)$

(c) $\alpha_s^y e^2/(G_\tau \Delta_0)$

(d) $\alpha_s^z e^2/(G_\tau \Delta_0)$
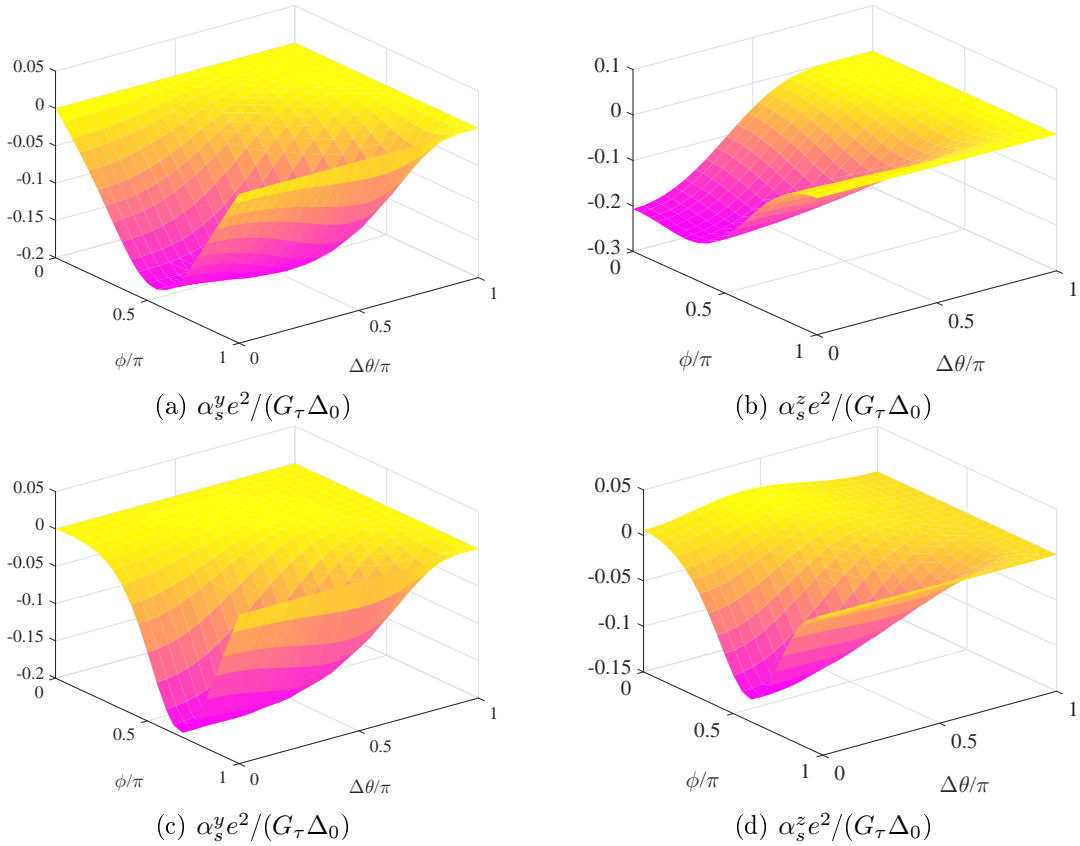
Figure 6.7: Thermoelectric spin-current coefficient $\alpha_s^\nu$ in the (first column) $\boldsymbol{y}$-direction and (second column) $\boldsymbol{z}$-direction for tunneling from $x = L_N/2$ in a S/N/S josephson junction with spin-active interfaces to a normal metal electrode. $T = 0.2T_{c,0}$, $L_N = 15$ nm, $G_{MR} = 0.1$, and the polarization is $P = 0$ for maximized spin currents. The interfacial phase shifts are governed by (a)-(b) $G_\phi = 1.05$ and (c)-(d) $G_\phi = 1.55$.

Figure 6.7 shows the thermal spin coefficients in the **y**- and **z**-directions, $\alpha_s^y$ (left column) and $\alpha_s^z$ (right column), when (a) $G_\phi = 1.05$ and (b) $G_\phi = 1.55$ represent the spin-dependent phase shifts born from scattering at the S/N-interfaces. The thermoelectric spin coefficient in the **z**-direction is seen to qualitatively identical to $\alpha$, only differing by a factor of $1/2P$. The maximum value of $\alpha_s^z$ shifts from $\phi = 0$ to $\phi = \pi/2$ as $G_\phi$ increases, and the maximum value of the coefficient is seen to decrease with increasing $G_\phi$. The thermoelectric spin coefficient in the **y**-direction, however, actually increases with increasing $G_\phi$. Moreover, when $G_\phi = 1.55$, the maximum value of $\alpha_s^y$ is shifted from occurring at the S/N magnetization angle $\phi = \pi/2$, the **y**-axis, to approximately $\phi = 0.6\pi$. Stronger degrees of spin-dependent phase shifts at both interfaces seem to allow for more species polarized in the **y**-direction, allowing for larger thermal spin currents

in this direction to arise. The effect is opposite in the **z**-direction, where larger values of $G_\phi$ results in smaller BCS peaks being encompassed by the distribution function $C(E)$. When the superconducting Cooper pairs within the normal metal nanowire experience large phase shifts, more species become polarized along the **y**-axis than along the **z**-axis. The spin-dependent differences in the density of states in the middle of the normal metal nanowire in the Josephson junction, $D^y(E)$ and $D^z(E)$, evolve with $G_\phi$ and the magnetization angle $\phi$ as expected. This is shown in Figure 6.8. The difference in **z**-polarized density of states, $D^z(E)$, for instance, is larger when $\phi = 0$ and $G_\phi = 0.5$, than when $G_\phi = 1.55$ and $\phi = 0.5\pi$.



(a)                                                      (b)
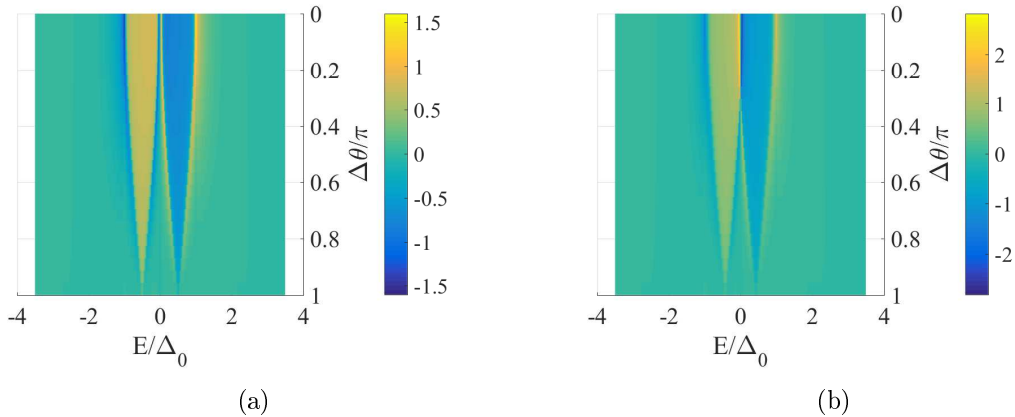
Figure 6.8: (a) $D^y(E)$ and $D^z(E)$ (identical) when $\phi = 0.5\pi$ and (b) $D^y(E)$ when $\phi = 0.6\pi$ in the middle of the normal metal in a S/N/S Josephson junction with spin-active interfaces. $T = 0.2T_{c,0}$, $L_N = 15$ nm, $G_{MR} = 0.1$, $G_\phi = 1.55$ and the polarization is $P = 0$.

As before, we observe that the thermoelectric coefficients vanish when the superconducting phase difference approaches $\pi$. Triplet supercurrents could exist for this phase difference in the structures considered here and accordingly result in thermoelectric effects, but do not seem to do so here. The spin-dependent difference in the density of states in the middle of the normal metal nanowire vanishes as the phase difference approaches $\pi$, and accordingly the thermoelectric spin coefficients practically equal zero when this occurs. This can also be seen from Figure 6.8, where no discernible features are seen when the superconducting phase difference equals $\pi$.

## 6.3   Conical ferromagnet

Spatially varying magnetism in ferromagnetic nanowires was shown in Chapter 4 to result in notable, albeit small, tunneling thermoelectric effects in superconducting hybrids. As this magnetic configuration showed promise but did not quite yield the results we had hoped, the more exotic magnetization texture of conical ferromagnetism was explored. One of the most well-known conical ferromagnets is Holmium [139][140], and

material parameters experimentally verified for this elements are applied herein. The vector describing the direction-dependency of the magnetism in a conical ferromagnet, such as Holmium, can be given by

$$\vec{h}_{Ho} = h_x \hat{x} + h_y \hat{y} + h_z \hat{z} \qquad (6.10)$$

and

$$h_x = h \cos(\phi), \quad h_y = h \sin(\phi) \sin\left(\frac{\theta x}{a}\right), \quad h_z = h \sin(\phi) \cos\left(\frac{\theta x}{a}\right), \qquad (6.11)$$

where $\phi$, $a$ and $\theta$ are material-specific constants. As an analogy to Holmium is considered, these are chosen as $\phi = \frac{4\pi}{9}$, $\theta = \frac{\pi}{6}$ and $a = 0.526$ nm [141][83]. The additional material parameters used for ferromagnetic tunneling in this case are $L_F = 15$ nm for the ferromagnet length, $T = 0.2T_{c,0}$ for temperature, $\zeta = 4$ represents S/F tunneling, $\Gamma = 0.005\Delta_0$ represents inelastic scattering and $\xi = 30$ nm is the superconducting coherence length. The effect of varying the ferromagnetic exchange field $h$ on the thermoelectric effects is considered. As the magnetization in Holmium has been reported to vary drastically, a wide range of magnetic field strengths are included to consider all eventualities. A schematic of the magnetic texture of the conical ferromagnetic nanowire in the S/F/S Josephson junction can be found in Figure 6.9.
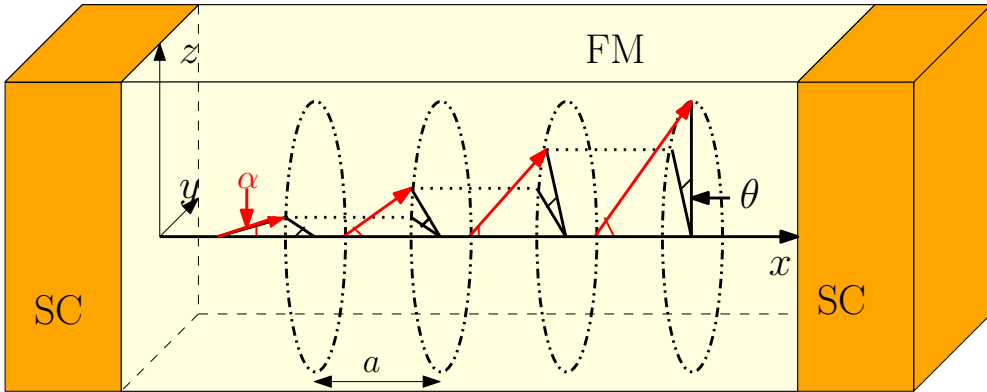


Figure 6.9: Graphical representation of the magnetization structure in a superconductor/ferromagnet/superconductor (S/F/S) Josephson junction with a conical magnetization structure in the ferromagnet.

As the direction of the ferromagnetic exchange field varies greatly in all three spatial directions we are led to expect the possibility of spin currents polarized in more than one direction. We consider the charge current $I = \alpha \Delta T/T$ which depends on the polarization, the thermoelectric parameters $S = -\alpha/(G'T)$ and $ZT = \left(\frac{G'G'_Q}{(\alpha)^2} - 1\right)^{-1}$ and the direction-dependent pure spin currents $I_s^\nu = \alpha_s^\nu \Delta T/T$. The parameters $\alpha$, $G'$ and $G'_Q$ are not exactly equal to $\alpha$, $G$ and $G_Q$ considered in Chapter 3, but seem to differ by only a factor of $1/2$ which is encompassed by the conductance parameter $G_\tau$.

The thermoelectric coefficients depend greatly on the interface polarization governing tunneling from $x = 0.5L_F$ in the conical ferromagnet to a normal-metal electrode as shown in Figure 6.1. If $P = 0$, $\alpha = 0$ along with $S$ and $ZT$. These three parameters are maximized when the barrier is fully polarized and $P = 1$. This is in analogy to what was observed in Chapters 3 and 4. The thermoelectric coefficients governing the thermal spin current according to $I_s = \alpha_s^\nu \Delta T / T$, react to altering $P$ in quite the opposite manner. As we have chosen the polarization of the tunneling interface to be aligned in the $+\mathbf{z}$-direction, the thermal spin currents in the other two directions are maximized when $P = 0$. When $P = 1$, the thermal spin coefficients in the $\mathbf{x}$- and $\mathbf{y}$-directions are $\alpha_s^x = \alpha_s^y = 0$. The spin current in the $\mathbf{z}$-direction on the other hand, which is governed by $\alpha_s^z$, is independent of the polarization in likeness to the $\mathbf{z}$-polarized framework. Moreover, the thermal spin coefficient differs from the charge thermoelectric coefficient by only a factor of $1/2P$.



(a)



(b)



(c)

Figure 6.10: (a) Seebeck coefficient $S$, (b) thermoelectric figure of merit $ZT$ and (c) thermo-electric coefficient $\alpha$ for tunneling from $x = L_F/2$ in a S/F/S josephson junction to a normal metal electrode. The ferromagnetic nanowire has the conical magnetic structure of Holmium. $T = 0.2T_{c,0}$, $L_F = 15$ nm, and the polarization is $P = 97\%$.

Figure 6.10 shows the quasiclassical thermoelectric coefficient $\alpha$, the corresponding See-beck coefficient and the thermoelectric figure of merit for tunneling from $x = L_F/2$ in an superconductor/conical ferromagnet/superconductor Josephson junction to a normal metal electrode at a temperature $T = 0.2T_{c,0}$. The thermoelectric figure of merit and Seebeck coefficient are almost identical in maximum size to the best cases when we considered a ferromagnetic domain wall nanowire in Section 4. These are not very large, even when comparing to realizable bulk thermoelectric materials. What should be noticed here, however, is the size of $\alpha$. This is several orders of magnitude larger than what was to be found in the domain wall case. The coefficients describing the thermal spin currents in the **x**-, **y**- and **z**-directions can be found in Figure 6.11. Here, the existence of pure spin currents which can be generated purely through the application of a temperature gradient is observed in all directions for a non-polarized tunneling interface. For the conical ferromagnet nanowire considered here the largest effects actually occur in the $\boldsymbol{x}$-direction, with $\alpha_s^z$ being smaller than both $\alpha_s^x$ and $\alpha_s^y$. The thermoelectric coefficient in the $\boldsymbol{z}$-direction does however not depend on the polarization at all, and is proportional to $\alpha$.

When the tunneling interface is fully polarized and the polarization $P = 1$, the thermal spin current coefficients in the **x**- and **y**-directions, $\alpha_s^x$ and $\alpha_s^y$, identically equal zero. When $P = 0.97$, however, they do exist to a small degree. As the effects become very small in all three spatial directions this is not shown here. The thermal spin currents depicted in Figure 6.11 are of sizes comparable to what is possible in normal metal/insulator/Zeeman-split superconductor tunneling bilayers, but primarily in the $\boldsymbol{y}$-direction. As the magnetization direction in Holmium varies spatially, the pair-breaking effect of the ferromagnetic exchange field is less pronounced than in the domain wall case. Not as many **z**-polarized quasiparticles exist to tunnel into the normal metal electrode as in the other two directions, but the thermoelectric effects in this direction are still several orders of magnitude greater than in the case of the domain wall ferromagnet.

All the thermoelectric coefficients seem to equal zero when the superconducting phase difference equals $\pi$. It may appear like the same is true for the thermoelectric coefficients $\alpha$ for large values of $h$, but this actually never occurs entirely until $\Delta\theta = \pi$. Even at this point the thermoelectric coefficients do not necessarily identically equal zero but appear to do so in comparison with the large thermoelectric effects arising at other phase differences. This can be understood through considering Figure 6.12.

Figure 6.12a shows the density of states in the middle of the conical ferromagnet nanowire in the S/F/S Josephson junction when the superconducting phase difference is $\Delta\theta = \pi$. At the quasiparticle energy $E = 0$, which represents the Fermi level, there is a peak in the density of states. This indicates triplet superconductivity instead of singlet superconductivity within the ferromagnet. This zero-energy peak is, as one could expect, accompanied by an asymmetry in the density of states $D^\nu(E) = \mathrm{Tr}\,\mathrm{Re}\{\sigma_\nu \boldsymbol{g}^R\}$ where $\nu = \{x, y, z\}$. These are shown in Figure 6.12d for $D^x(E)$, Figure 6.12c for $D^y(E)$ and 6.12b for $D^z(E)$. However, both the zero-energy peak and these asymmetries are

(a) $\alpha_s^x e^2/(G_\tau \Delta_0)$

(b) $\alpha_s^y e^2/(G_\tau \Delta_0)$

(c) $\alpha_s^z e^2/(G_\tau \Delta_0)$
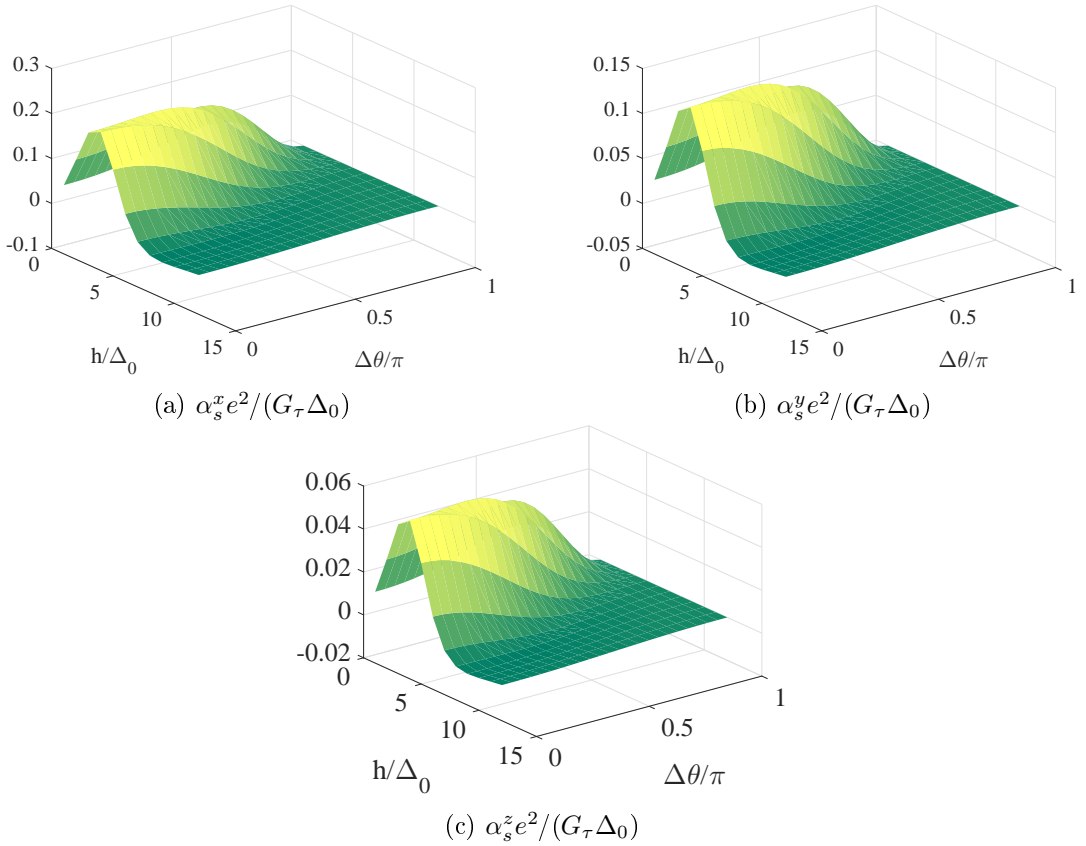
Figure 6.11: Thermoelectric spin-current coefficient $\alpha_s^\nu$ in the (a) $\boldsymbol{x}$-direction, (b) $\boldsymbol{y}$-direction and (c) $\boldsymbol{z}$-direction for tunneling from $x = L_F/2$ in a S/F/S josephson junction to a normal metal electrode. The tunneling polarization is $P = 0$, the ferromagnetic nanowire has the conical magnetic structure of Holmium, $T = 0.2T_{c,0}$ and $L_F = 15$ nm.

minute. Consequently, the resulting bias-induced thermoelectric effects become vanishingly small. At other values for the ferromagnetic exchange field or different material parameters than the ones applied for Holmium this could be different and thermoelectric effects could be observable even at a superconducting phase difference of $\pi$. An interesting feature to notice at the phase difference $\pi$ is the increase in both the zero-energy peak as well as in the asymmetric peaks of $D^\nu(E)$ as the exchange field strength is increased. The triplet Cooper pair peak at zero energy is accompanied by asymmetries in each of the direction-dependent densities of states, and the effect increases with the field. The stronger the field gets at this particular phase difference, the larger the asymmetry becomes. This is in direct contradiction to the response in the density of states to increasing the field at other phase differences. Regardless of the increase with exchange field, however, neither the zero-energy peak nor the asymmetries in the densities of states ever become sufficiently large to generate noticeable thermoelectric effects for the remainder of parameters considered.
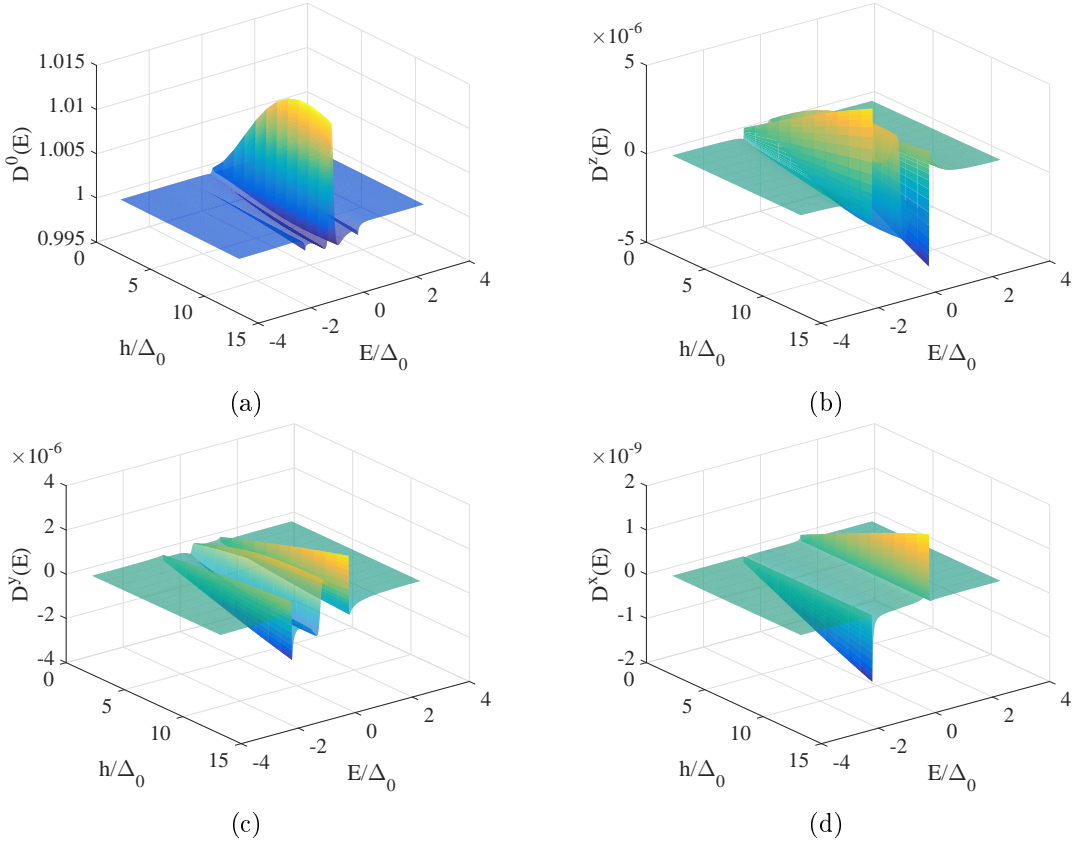
Figure 6.12: (a) $D^0(E)$, (b) $D^z(E)$, (c) $D^y(E)$ and (d) $D^x(E)$ versus the ferromagnetic exchange field $h/\Delta_0$ and the quasiparticle energy $E/\Delta$ at $x = 0.5L_F$ in a superconductor/conical ferromagnet/superconductor Josephson junction for a superconducting phase difference of $\Delta\theta = \pi$. The ferromagnetic nanowire has the conical magnetic structure of Holmium, $T = 0.2T_{c,0}$, $\zeta = 4$, $\Gamma = 0.005\Delta_0$ and $L_F = 15$ nm.

The features in the densities of states crucial to obtaining sizable thermoelectric effects are seen to actually increase with the ferromagnetic exchange field strength when the superconducting phase difference equals $\pi$. Figure 6.13 shows the density of states and direction-dependent spin-dependent difference in the density of states, $D^\nu(E)$, for the superconducting phase difference $\Delta\theta = 0$. The observed trends are here quite different. The largest peaks in the densities of states are situated at much smaller values for the ferromagnetic exchange fields and decrease with increasing field strength. The largest peaks seem to occur around $h = 3\Delta_0$, consistent with the maximum values for $\alpha_s^\nu$, $\alpha$, $S$ and $ZT$. The fact that the difference in **x**-polarized density of states is significantly greater than in the corresponding two directions also provides a reasonable explanation for why the thermoelectric spin coefficient $\alpha_s^x$ is larger than both $\alpha_s^y$ and $\alpha_s^z$. The superconducting peaks in the densities of states are however quite sizable, and spin-polarizations are generated in all three spatial directions through the rotating

(a)



(b)



(c)



(d)
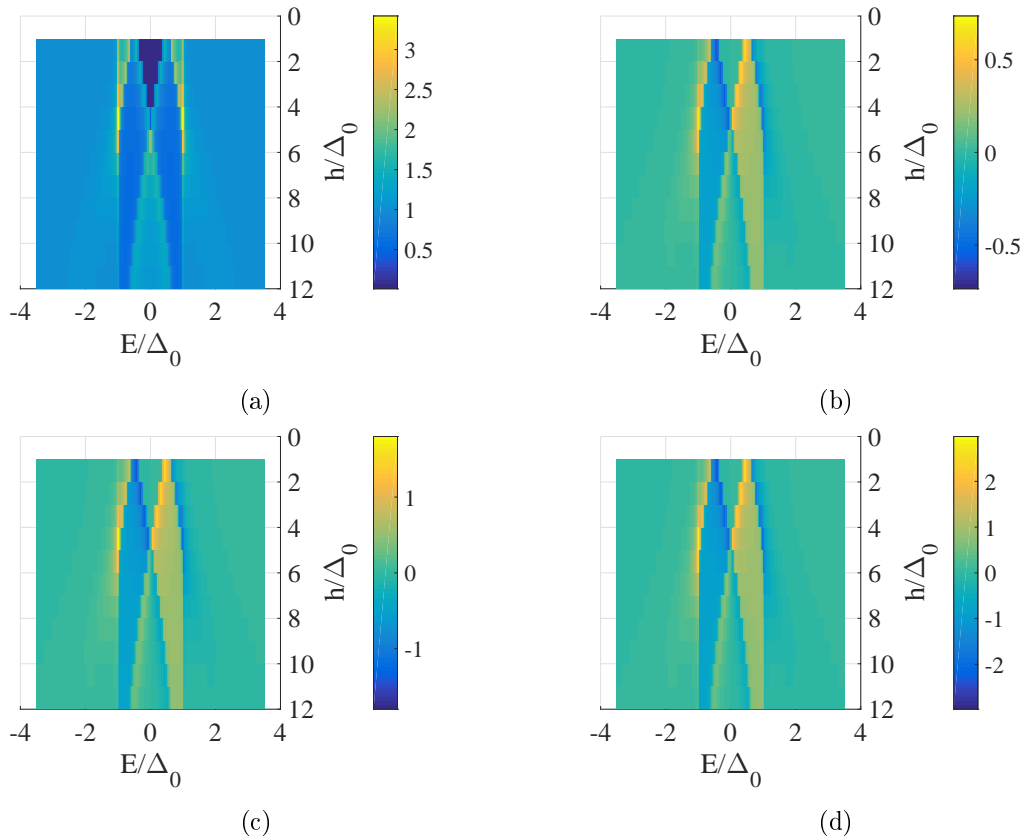
Figure 6.13: (a) $D^0(E)$, (b) $D^z(E)$, (c) $D^y(E)$ and (d) $D^x(E)$ versus the ferromagnetic exchange field $h/\Delta_0$ and the quasiparticle energy $E/\Delta$ at $x = 0.5L_F$ in a superconductor/conical ferromagnet/superconductor Josephson junction for a superconducting phase difference of $\Delta\theta = 0$. The ferromagnetic nanowire has the conical magnetic structure of Holmium, $T = 0.2T_{c,0}$, $\zeta = 4$, $\Gamma = 0.005\Delta_0$ and $L_F = 15$ nm.

magnetism of the conical ferromagnet.

The thermoelectric effects arising due to tunneling from the superconductor/conical ferromagnet/superconductor Josephson junction into a normal-metal electrode are large enough to be noticeable. The thermoelectric figure of merit and Seebeck coefficient are not much larger than what was obtainable for the domain wall case. The pair-breaking effect of the ferromagnetic exchange field could be responsible for this. The thermoelectric charge coefficient $\alpha$ is also somewhat smaller than in the case of the Josephson junctions with spin-active interfaces, but still several orders of magnitude larger than the thermoelectric coefficient in the domain wall Josephson junction. The most notable result within this section concerns the spin thermoelectric coefficients $\alpha_s^x$ and $\alpha_s^y$, which indicate large amounts of **x**- and **y**-polarized quasiparticles tunneling into the normal metal electrode. The sizes of the thermal spin currents which are described

by these coefficients can rival those of the thermal spin currents observed in the case of the normal metal/insulator/Zeeman-split superconductor bilayer when the tunneling barrier is non-polarized.

## 6.4   Spin-orbit coupling

The effect of spin orbit coupling on thermoelectric response has not been previously studied. Josephson junctions with spin-orbit coupled materials as the central layers have been shown to be able to generate long-range triplet supercurrents even when the superconducting phase difference equals $\pi$ [40], but so far thermoelectric effects have not been an area of focus for this class of superconducting hybrids. As particle-hole asymmetries do arise in such junctions, spin-orbit coupled Josephson junctions seem promising as generators of large thermoelectric currents. The uncertainty concerns whether they offer the possibility of thermoelectric effects being present when the superconducting phase difference equals $\pi$. The systems considered in Ref. [40] do generate large zero-energy peaks at $\pi$ phase difference, but this peak is actually not accompanied by a notable spin-dependent particle-hole asymmetry. This section studies tunneling from the middle of the central layer in a superconductor/spin-orbit coupled semiconductor/superconductor Josephson junction into a normal metal electrode. Spin-orbit coupling dynamics are governed by the modified Usadel equation presented in Chapter 2, Equation 2.49. The Keldysh-Usadel tunneling boundary conditions modified to include the spin-orbit field defined in Equations 2.50 and 2.51 are used. The spin-orbit field vector is defined as

$$\boldsymbol{A} = A_x \boldsymbol{x} + A_y \boldsymbol{y} + A_z \boldsymbol{z} \tag{6.12}$$

$$A_x = \beta \sin(\varphi)\sigma_z - \beta \cos(\varphi)\sigma_y, \quad A_y = 0, \quad A_z = 0 \tag{6.13}$$

within this section. Here, $\varphi = 0$ denotes the $-\boldsymbol{y}$-axis, $\varphi = \pi$ the $+\boldsymbol{y}$-axis and $\varphi = \pi/2$ the $+\boldsymbol{z}$-axis. Without a magnetic exchange field applied, the singlet and triplet components of the Green function matrices are not coupled and triplet supercurrents do not arise in the semiconducting nanowire. If no particle-hole asymmetry exists, thermoelectric effects do not arise. Thus, a magnetic field is applied according to

$$\boldsymbol{h} = (0, 0, h). \tag{6.14}$$

The primary goal for utilizing spin-orbit coupled Josephson junctions instead of Zeeman-split superconductors concerns the possibility of applying very weak magnetic fields instead of the 1 T fields. The choice of material for this purpose is crucial. As some semiconducting materials have Lande g-factors much larger than what is common in superconductors, much lower magnetic fields need be applied in order to obtain $h \approx$
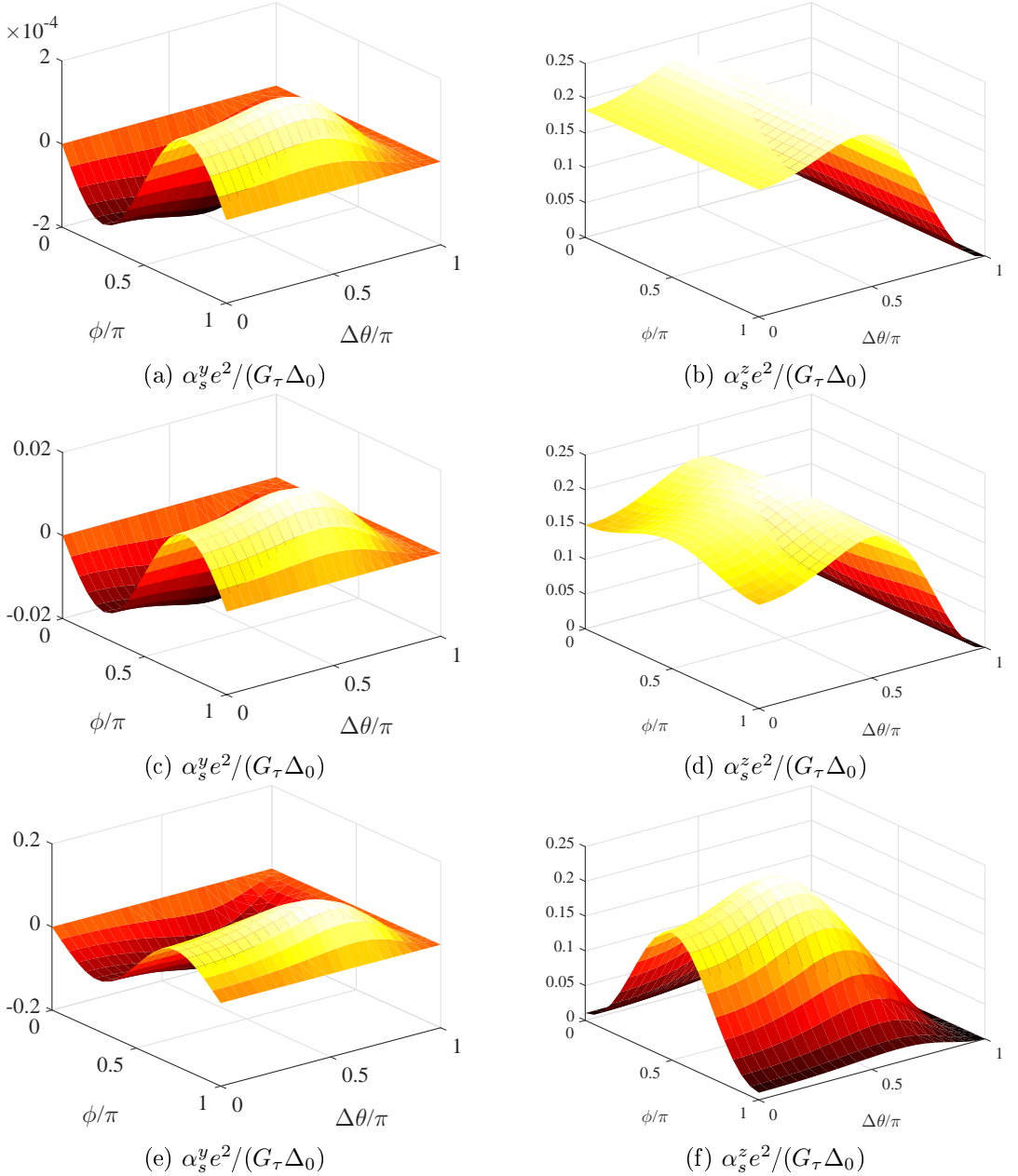
Figure 6.14: $\alpha_s^y$ (first column) and $\alpha_s^z$ (second column) in a superoncudctor/ spin-orbit coupled semiconductor/ superconductor Josephson junction with a semiconductor length of 15 nm, interface transparancy $\zeta = 4$, $\xi = 30$ nm, $T/T_{c,0} = 0.2$, tunneling polarization $P = 0$ and exchange field strength $h = 0.5\Delta_0$. The spin-orbit coupling strength is (a)-(b) $\beta L_{sc} = 0.1$, (c)-(d) $\beta L_{sc} = 1$ and (e)-(f) $\beta L_{sc} = 3$.

$0.5\Delta_0$ within the semiconductor. A more thorough discussion of this can be found in the next section, Section 6.5.

The spin-singlet Cooper pairs leaking from the superconducting reservoir into the spin-orbit couplet semiconductor nanowire interact with the spin-orbit coupling in the semiconducting nanowire. Instead of being in the separate spin up and spin down states, the spin states are now separated in $\pm$-bands. Consequently, the framework assuming homogeneously magnetized systems derived in Chapter 3 cannot be used when studying spin-orbit coupled thermoelectric effects. The quasiclassical framework presented in Chapter 5 is instead employed, as this allows for arbitrary spin-dependent fields.

Transport in the semiconducting nanowire is assumed to be along the $\boldsymbol{x}$-direction, and this is also the direction of the spin-orbit coupling. The angle of the spin-orbit field is therefore varied in the **yz**-plane. For this reason, the spin current in the $\boldsymbol{x}$-direction is expected to be be markedly smaller than the corresponding currents in the $\boldsymbol{y}$- and $\boldsymbol{z}$-directions. This is verified in the numerical results, with $\alpha_s^x \approx 10^{-6}$. This is of little interest when compared to the very large thermoelectric effects arising in the other two directions. Consequently, no results for the thermal spin current coefficient in the **x**-direction are presented herein.

Figure 6.14 shows the thermoelectric spin coefficients in the **x**- and **y**- directions for the exchange field strength $h = 0.5\Delta_0$ and spin-orbit field strengths (a)-(b) $\beta L_{sc} = 0.1$, (c)-(d) $\beta L_{sc} = 1$ and (e)-(d) $\beta L_{sc} = 3$. The thermal spin coefficient in the **z**-direction is very large, where $\alpha_{s,max}^z \approx 0.2$ for all values of the spin orbit field strength. The **y**-directional thermal spin-coefficient, however, is minute for small spin-orbit field strengths and increases radically with increasing values of $\beta$. The values of $\alpha_s^z$ remain rather unchanged. The variation of $\alpha_s^z$ with the direction of the spin-orbit field is non-existent when $\beta = 0.1$, rather small when $\beta = 1$ and large when $\beta = 3$. These trends seem to persist for all the values for the spin orbit field and the magnetic exchange field considered.

The thermal spin coefficient in the **y**-direction is seen to switch sign upon altering the external control parameters which are the spin-orbit field alignment angle $\varphi$ and the superconducting phase difference $\Delta\theta$. Unfortunately, this sign change does not occur upon tuning the superconducting phase difference as was possible in the case of a Zeeman-split Josephson junction. The sign change of $\alpha$ in the superconductor/domain wall ferromagnet/superconductor configuration was not induced by the superconducting phase difference either, but rather by an increase in temperature. In this case, changing the alignment angle of the spin-orbit field in the **yz**-plane switches the sign of of $\alpha_s^y$, and thereby the polarization of the accompanying thermal spin current. This is, however, understandable from what these angles signify. The area within the figures between the angles $\varphi = 0$ and $\varphi = \pi/2$ signifies considering fields aligned in the plane between the $-\boldsymbol{y}$- and $+\boldsymbol{z}$-axes, while the area between $\varphi = \pi/2$ and $\varphi = \pi$ signifies fields aligned in the plane between the $+\boldsymbol{z}$- and the $+\boldsymbol{y}$-axes. It is not all that surprising that the thermoelectric effects arising in these opposite planes are equal, but opposite in sign.

When the spin-orbit field is aligned exactly along the axes $\pm\boldsymbol{y}$ and $\boldsymbol{z}$, the thermal spin current coefficient in the **y**-direction $\alpha_s^y$ equals zero. At these alignment angles no **y**-polarized spin species are allowed to tunnel into the normal metal electrode on account of an applied temperature gradient.

In Figure 6.14, the pure thermal spin current in the **y**-direction is smaller than the one in the **z**-direction, but exhibits a sinusoidal behavior allowing for tuning of the spin current polarization with the largest amplitude we have yet seen in the case where $\beta = 3$. As $\beta$ increases so does $\alpha_s^y$. In contrast to $\alpha_s^z$, the **y**-directional thermal spin coefficients retains the same qualitative shape as the spin-orbit field strength is increased when $h = 0.5\Delta_0$. In the **z**-direction, the quantitative change in $\alpha_s$ is very small and exhibits a slight decrease. Qualitatively, the effect is rather more drastic. This coefficient is not seen to be accompanied by a sign change in the thermal spin current like $\alpha_s^y$ is. The thermal spin coefficient along the **z**-axis is not affected by the spin-orbit field when the field strength $\beta$ is small. Here, the effect from the exchange field $h$ dominates over the impact of the spin-orbit field, and the field angle is irrelevant for the thermoelectric coefficient observed. As the spin-orbit coupling is increased in strength, its impact on the thermal spin current becomes increasingly pronounced. As the exchange field $\boldsymbol{h} = h\boldsymbol{z}$ is imposed in the **z**-direction, the thermoelectric effects arising are large even for low spin-orbit coupling strengths. The **z**-directional thermal spin currents are actually seen to be larger in this case, as the particle-hole asymmetry only exists for **z**-polarized spins when only a magnetic field is applied in this direction. As the strength of spin-orbit coupling increases a growing number of quasiparticles achieve spin states polarized closer to the **y**-axis. Accordingly, $\alpha_s^y$ grows with $\beta$ even as $\alpha_s^z$ decreases. When the spin-orbit coupling is dominant and $\beta L_{sc} = 3$, tuning the direction of the spin-orbit field is able to affect the thermal **z**-polarized spin current greatly. From Figure 6.14f it becomes evident that the maximum value of the thermal **z**-polarized spin current coefficient $\alpha_s^z$ can be found when the spin-orbit field alignment angle $\varphi = \pi/2$. As mentioned above, at this angle the spin-orbit field is aligned in the **z**-direction alongside the magnetic exchange field $\boldsymbol{h}$. From this, it is logical that this angle should be accompanied by the maximum **z**-polarized thermal spin current.

The effect of maximum **z**-polarized thermoelectric effects at the alignment angle $\varphi = \pi/2$ can be discovered also in Figure 6.15. The figure shows the (a)-(b) thermoelectric coefficient, (c)-(d) Seebeck coefficient and (e)-(f) thermoelectric figure of merit for tunneling from the spin-orbit coupled semicondutor nanowire Josephson junction when the spin-orbit coupling is $\beta L_{sc} = 3$. The magnetic exchange field strength is $0.4\Delta_0$ in the left column and $0.5\Delta_0$ in the one to the right. As can be seen, the effect of lowering the magnetic exchange field from $h = 0.5\Delta_0$ to $h = 0.4\Delta_0$ is not large when the Rashba spin-orbit coupling strength is $\beta L_{sc} = 3$. This is also the case when the spin-orbit field is weaker, and $\beta L_{sc} = 0.1$.For this reason, the thermoelectric coefficient, Seebeck coefficient and thermoelectric figure of merit will not be presented herein for these parameter choices. The parameter combination $h = 0.4\Delta_0$ and $\beta L_{sc} = 1$ is accompanied by some rather fascinating effects, and will be discussed in greater detail below. When

(a) $\alpha e/(G_\tau \Delta_0)$

(b) $\alpha e/(G_\tau \Delta_0)$

(c)

(d)

(e)

(f)
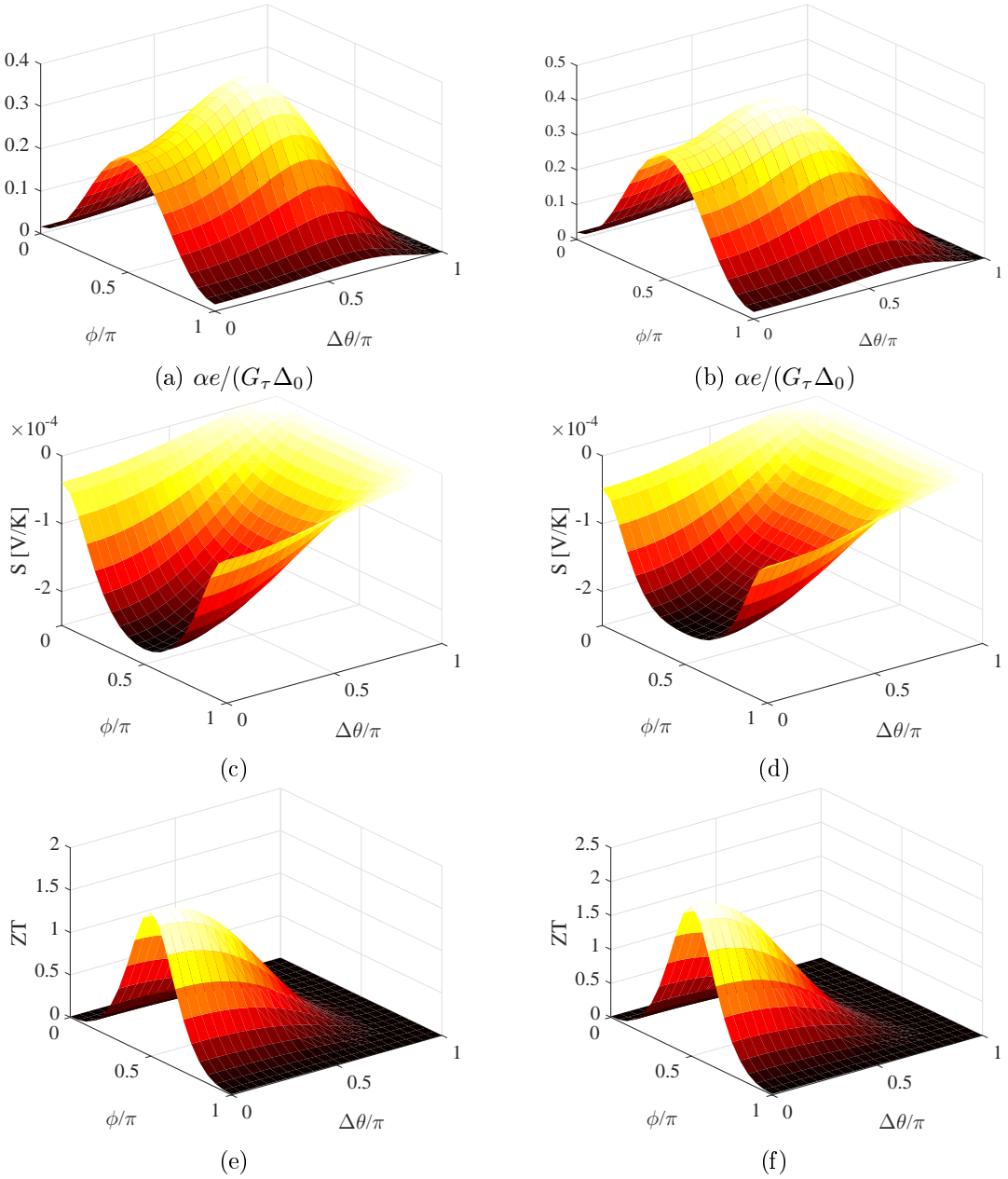
Figure 6.15: (a)-(b) $\alpha e/(G_\tau \Delta_0)$, (c)-(d) $S$ and (e)-(f) $ZT$ in a superoncudctor/ spin-orbit coupled semiconductor/ superconductor Josephson junction with a semiconductor length of 15 nm, interface transparancy $\zeta = 4$, $\xi = 30$ nm, $T/T_{c,0} = 0.2$ and tunneling polarization $P = 97\%$. In the first column $h = 0.4\Delta_0$ and in the second $h = 0.5\Delta_0$. The spin-orbit coupling strength is $\beta L_{sc} = 3$.

studying $\alpha$, $S$ and $ZT$ when $\beta L_{sc} = 3$, however, the trend is very similar to what was observed for the **z**-polarized thermal spin current coefficient $\alpha_s^z$. The expressions for the thermoelectric coefficients rely on traces over products between the retarded Green function matrix and either $\hat{\rho}_3$ or $\hat{\sigma}_z$. Accordingly, only the **z**-polarized quasiparticles are capable of contributing to the tunneling charge thermoelectric effects across the **z**-polarized interface into the normal metal electrode. Hence, the effect is maximized for the largest **z**-aligned magnetic fields at the alignment angle signifying spin-orbit coupling along the **z**-axis, $\varphi = \pi/2$. The Seebeck coefficient, thermoelectric coefficient and thermoelectric figure of merit are seen to become quite large, and rival what was achieved in the normal metal/ Zeeman-split superconductor tunneling bilayer.



(a) $\alpha_s^y e^2/(G_\tau \Delta_0)$                    (b) $\alpha_s^z e^2/(G_\tau \Delta_0)$
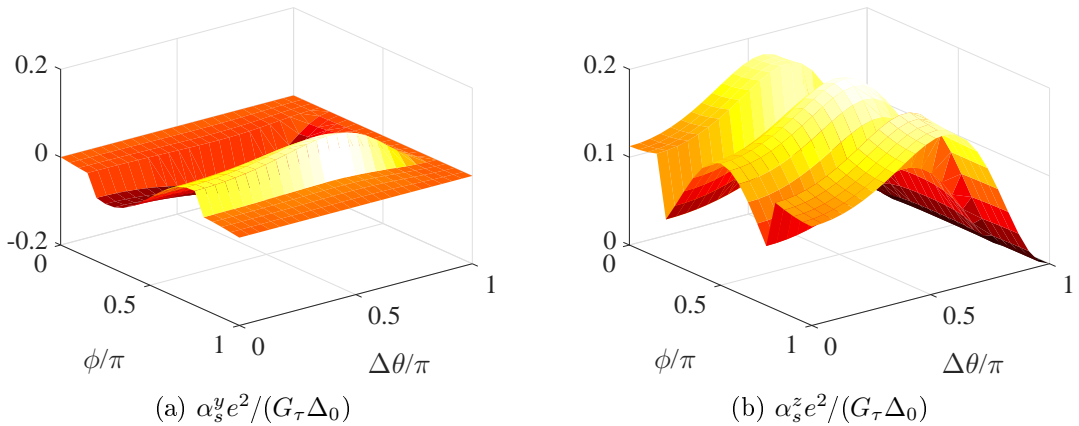
Figure 6.16: (a) $\alpha_s^y$ and (b) $\alpha_s^z$ in a superconductor/ spin-orbit coupled semiconductor/ superconductor Josephson junction with a semiconductor length of 15 nm, interface transparancy $\zeta = 4$, $\xi = 30$ nm, $T/T_{c,0} = 0.2$, tunneling polarization $P = 0$ and exchange field strength $h = 0.4\Delta_0$. The spin-orbit coupling strength is $\beta L_{sc} = 1$.

The thermoelectric spin coefficients are qualitatively identical in the case where $h = 0.3\Delta_0$ to the case where $h = 0.5\Delta_0$. As the maximum values for $\alpha_s^\nu$ are smaller when $h = 0.3\Delta_0$ than when $h = 0.5\Delta_0$, these results do not provide new information and are therefore not included here. This is also true for the charge current thermoelectric parameters $\alpha$ and $ZT$, and these results will not be presented herein either. The Seebeck coefficient $S$ on the other hand attains its maximum values when $h = 0.3\Delta_0$ and $\beta = 0.1$ and $\beta = 3$. As the largest value is only marginally greater than the maximum Seebeck coefficients for the field strengths $h = 0.4\Delta_0$ and $h = 0.5\Delta_0$, and the qualitative behavior of S is identical to the effect in these cases, the results for $S$ when $h = 0.3\Delta_0$ are not included herein either.

Both the qualitative and quantitative behaviors of $\alpha_s^z$ and $\alpha_s^y$ do not change much when tuning the exchange field from $h = 0.5\Delta_0$ to $h = 0.4\Delta_0$ when the spin-orbit coupling equals 0.1 or 3, and these results are therefore not included here. The exception from this trend occurs when $\beta L_{sc} = 1$ and $h = 0.4\Delta_0$. The thermoelectric coefficients governing the creation of pure thermal spin currents arising when $h = 0.4\Delta_0$ and $\beta L_{sc} = 1$ can be
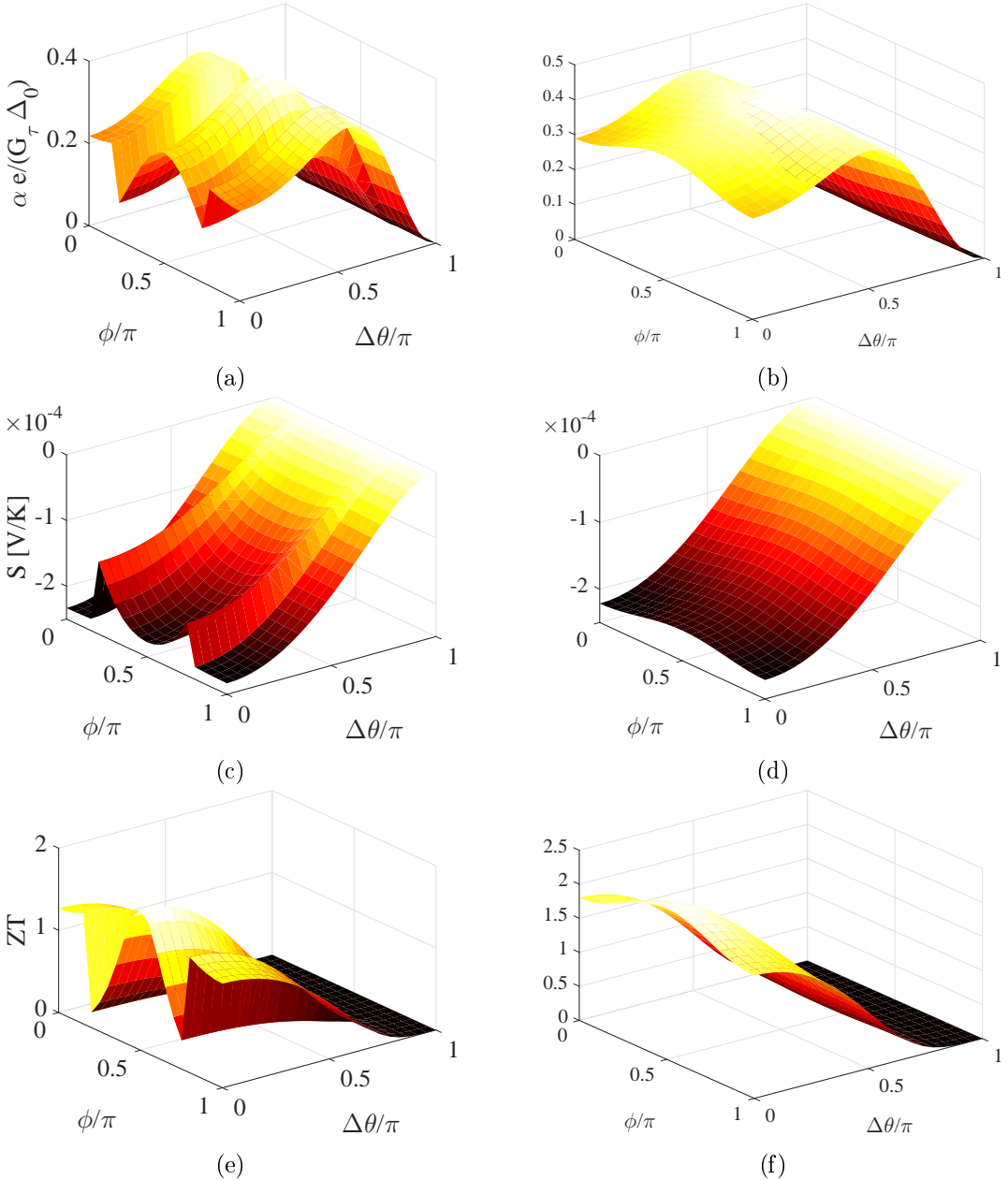
Figure 6.17: (a)-(b) $\alpha$, (c)-(d) $S$ and (e)-(f) $ZT$ in a superconductor/ spin-orbit coupled semi-conductor/ superconductor Josephson junction with a semiconductor length of 15 nm, interface transparancy $\zeta = 4$, $\xi = 30$ nm, $T/T_{c,0} = 0.2$ and tunneling polarization $P = 97\%$. In the first column $h = 0.4\Delta_0$ and in the second $h = 0.5\Delta_0$. The spin-orbit coupling strength is $\beta L_{sc} = 1$.

(a) $\alpha e/(G_\tau \Delta_0)$



(b) ZT



(c) S [V/K]
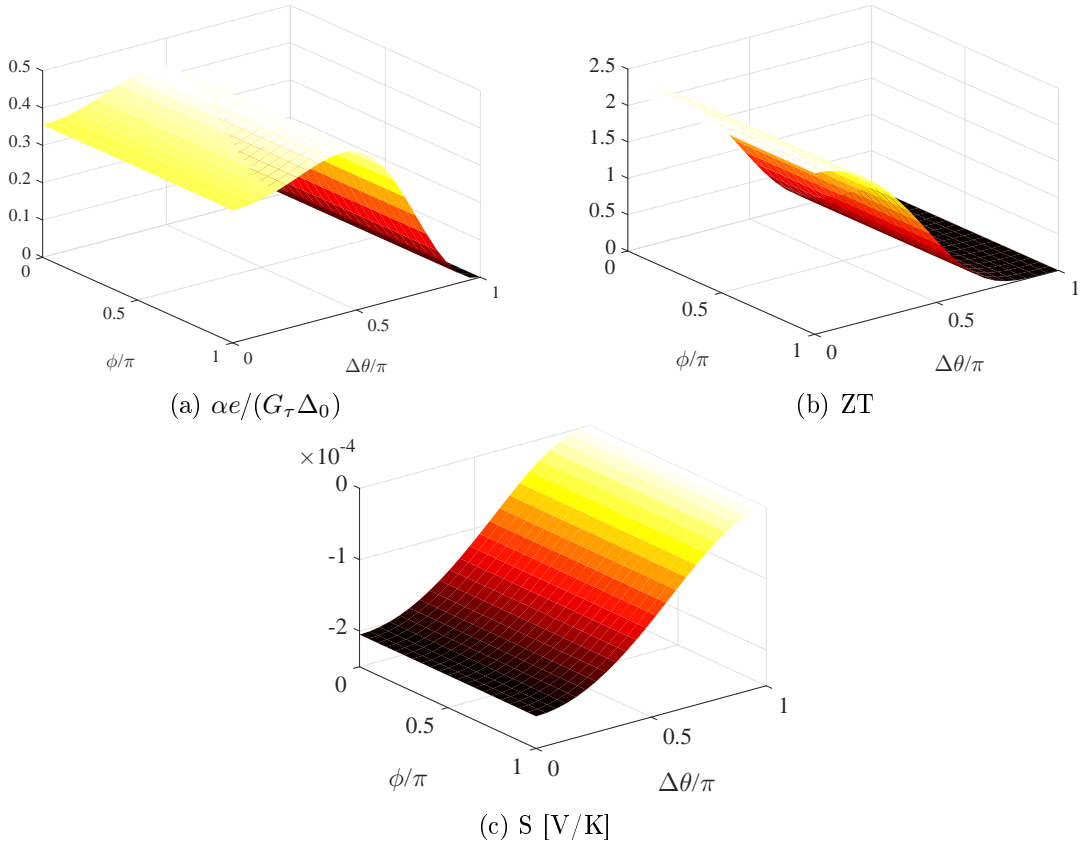
Figure 6.18: (a) $\alpha e/(G_\tau \Delta_0)$, (b) $ZT$ and (c) $S$ in a superconductor/ spin-orbit coupled semi-conductor/ superconductor Josephson junction with a semiconductor length of 15 nm, interface transparancy $\zeta = 4$, $\xi = 30$ nm, $T/T_{c,0} = 0.2$ and tunneling polarization $P = 97\%$. The magnetic exchange field aligned in the **z**-direction is $h = 0.5\Delta_0$. The spin-orbit coupling strength is $\beta L_{sc} = 0.1$.

found in Figure 6.16, where (a) shows $\alpha_s^y$ and (b) shows $\alpha_s^z$. The very abrupt changes in the thermoelectric coefficients seen here persist also when considering the Seebeck coefficient $S$ and the thermoelectric figure of merit $ZT$, as seen in Figures 6.17c and 6.17e.

The (a)-(b) thermoelectric coefficient $\alpha$, (c)-(d) Seebeck coefficient $S$ and (e)-(f) thermoelectric figure of merit $ZT$ are presented in the case of spin-orbit coupling strength $\beta L_s c = 1$ and exchange fields $0.4\Delta_0$ (left column) and $0.5\Delta_0$ (right column) in Figure 6.17. As could be expected from the consideration of conical ferromagnetism and spin-active interfaces, these thermoelectric effects follow the qualitatively identical evolution of the **z**-directed thermal spin current coefficient $\alpha_s^z$ for the same parameters. The previously noted sinusoidal behavior of $\alpha_s^y$ is seen to remain also when $h = 0.4\Delta_0$ and $\beta L_{sc} = 1$, but is decidedly less smooth. There seems, in this case, to be an abrupt dip

in all the thermoelectric effects studied, $\alpha$, $S$, $ZT$ and $\alpha_s^\nu$, for certain alignment angles $\varphi \approx \pm\pi/4$. This abrupt change could be attributed to some flaw in the calculations for these particular values, but why such a fault should be present for the parameters in question is not obvious. The corresponding effects for exchange field $h = 0.5\Delta_0$ and the same spin-orbit coupling does not exhibit the same abrupt behavior. Nor is such behavior present when $h = 0.5\Delta_0$ and $\beta L_{sc} = 0.1$, shown in Figure 6.18. Here, the thermoelectric coefficients are almost constant upon changing the spin-orbit field alignment angle. For this reason, the abrupt behavior of the thermoelectric coefficients upon changing the alignment angle for the particular parameter set of $h = 0.4\Delta_0$ and $\beta L_{sc} = 1$ is somewhat unexpected. The alignment angles causing the dips, at which $S$, $ZT$, $\alpha$ and $\alpha_s^z$ approach zero, seem to be situated about halfway between the $\boldsymbol{z}$-axis and the $\pm\boldsymbol{y}$-axes. For this particular spin-orbit coupling strength and magnetic exchange field, the thermoelectric effects are suppressed when the spin-orbit field is aligned along $\varphi \approx \pm\pi/4$.

When the spin-orbit field is large and $\beta = 3$, the $\boldsymbol{z}$-directional thermoelectric effects quantified by $\alpha$, $S$, $ZT$ and $\alpha_s^z$ approach zero when the spin-orbit field is aligned along the $\pm\boldsymbol{y}$-axis, and $\varphi = \pi$ or $\varphi = 0$. This does not occur for smaller spin-orbit fields, as the magnetic exchange field dominates over the spin-orbit coupling in these cases. The thermoelectric coefficients do not identically equal zero for the angles $\varphi = 0$ and $\varphi = \pi$, but become small, as is logical. More interesting is the fact that the $\boldsymbol{y}$-polarized thermal spin current, quantified by $\alpha_s^y$, equals zero whenever $\varphi = 0$ or $\varphi = \pi$. It would seem that the stark contrast between the $\boldsymbol{z}$-polarization of the exchange field and the $\boldsymbol{y}$-polarized spin orbit field is too large for $\boldsymbol{y}$-polarized species to exist, and tunnel through to the normal metal electrode. Not all $\boldsymbol{z}$-polarized species need lose their polarization direction, and so some thermoelectric effects can arise, but they will be rather small. When the spin-orbit coupling is too weak to have any effect on the spin-polarization of the quasiparticles, the $\boldsymbol{z}$-directional thermoelectric effects do not depend on the spin-orbit field alignment angle at all, and $\alpha_s^y$ is negligibly small. The effect of the $\boldsymbol{z}$-directional coefficients not varying with the spin-orbit alignment angle for weak spin-orbit coupling is particularly clear in for example Figure 6.18, showing $\alpha$, $S$ and $ZT$ for $h = 0.5\Delta_0$ and $\beta L_{sc} = 0.1$.

A common feature throughout the consideration is $\alpha = 0$, $S = 0$, $ZT = 0$ and $\alpha_s^\nu = 0$ when the superconducting phase difference $\Delta\theta = \pi$. At such a superconducting phase difference, singlet superconductivity is suppressed. If nonzero thermoelectric effects were to be observed at a superconducting phase difference $\pi$, this could be attributed to the difference in the spin-dependent density of states not being zero. This could be expected to manifest itself through a zero-energy peak at $\Delta\theta = \pi$, indicating triplet superconducting order. Such a zero-energy peak at $\Delta\theta = \pi$ arising in spin-orbit coupled Josephson junctions was noted in Ref. [40] for pure Rashba spin-orbit coupling. Here, however, our reproduction of this system does not indicate the presence of a spin-dependent difference in the density of states when the superconducting phase difference equals $\pi$. Consequently, the pure triplet peak is not necessarily accompanied
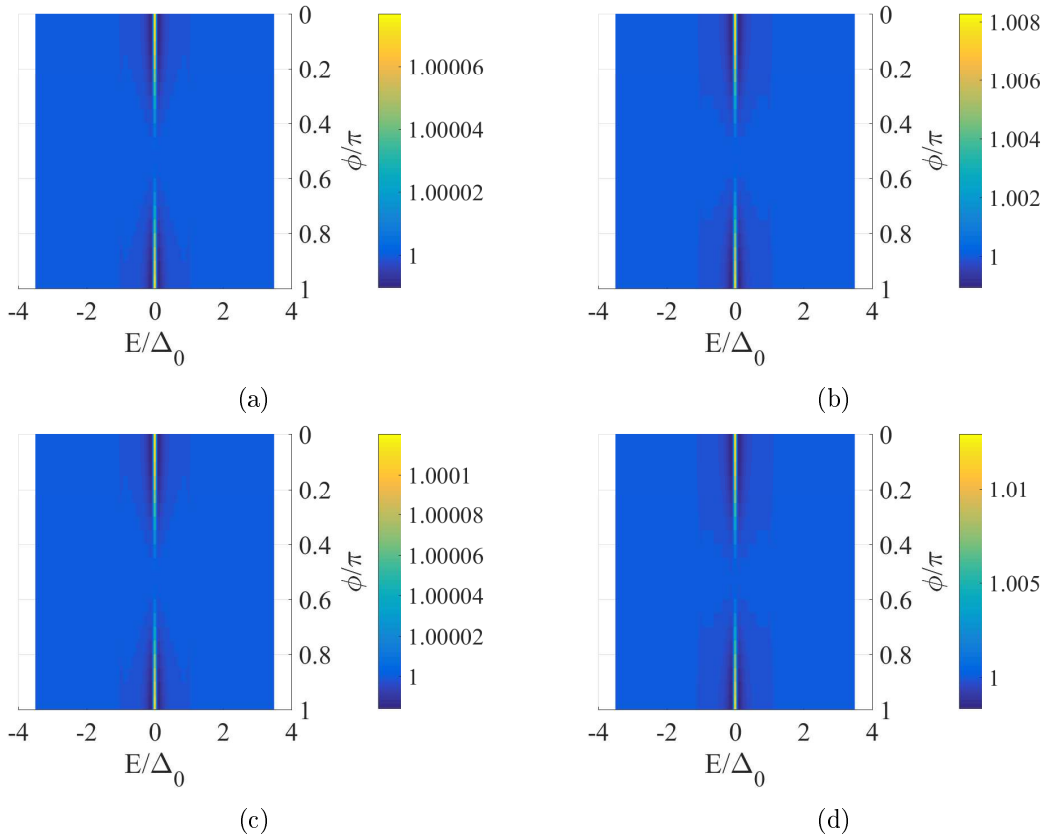
Figure 6.19: Density of states in the middle of the semiconductor nanowire of a superconductor/ spin-orbit coupled semiconductor/ superconductor Josephson junction with $L_{sc} = 15$ nm, $T = 0.2T_{c,0}$, $\Gamma = 0.005\Delta_0$, $\Delta_0 = 1$ meV, $\zeta = 4$ and spin-orbit coupling (first column) $\beta L_{sc} = 0.1$ and (second column) $\beta L_{sc} = 3$. The magnetic exchange field strengths are (a)-(b) $h = 0.4\Delta_0$ and (c)-(d) $0.5\Delta_0$. The density of states varies with quasiparticle energy and the alignment of the spin-orbit field in the **yz**-plane.

by the particle-hole asymmetry necessary to observing thermoelectric effects in these structures.

The densities of states in the middle of the semiconductor nanowire ($x = 0.5L_{sc}$) versus the spin-orbit field alignment angle and quasiparticle energy are shown in Figure 6.19 for the superconducting phase difference $\Delta\theta = \pi$. The exchange field strengths (a)-(b) $h = 0.4\Delta_0$ and (c)-(d) $h = 0.5\Delta_0$ are used. The spin-orbit coupling strengths are $\beta L_{sc} = 0.1$ in the first column and $\beta L_{sc} = 3$ in the second. A zero energy peak does exist for several field angles, but is in all cases very small. The direction-dependent differences in the densities of states in the middle of the nanowire for the same phase difference, $\beta L_{sc} = 3$ and $h = 0.5\Delta_0$, are shown in Figure 6.20, where (a) shows $D^x(E)$, (b) shows $D^y(E)$ and (c) shows $D^z(E)$. In contradiction to what has been observed

for the thermal spin coefficient $\alpha_s^\nu$ so far, the asymmetry in the **x**-direction, $D^x(E)$, is actually the largest when the superconducting phase difference equals $\pi$.



(a)                                                                              (b)



(c)
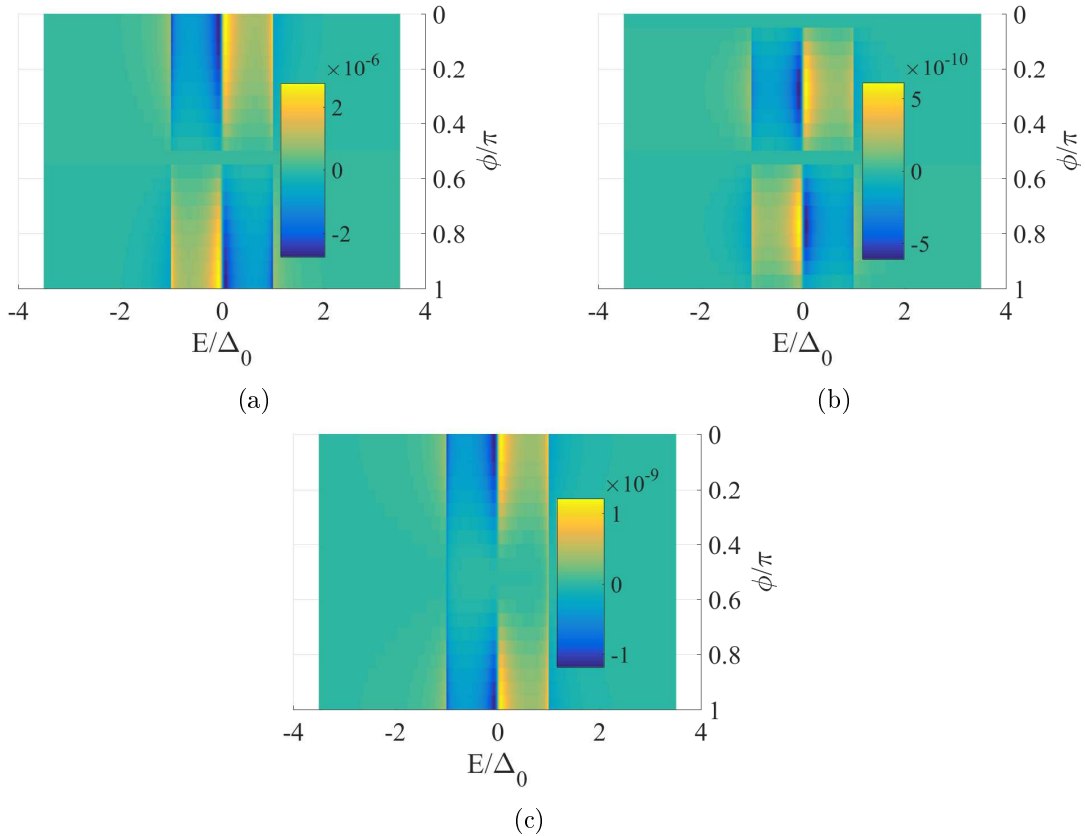
Figure 6.20: (a) $D^x(E)$, (b) $D^y(E)$ and (c) $D^z(E)$ in the middle of the semiconductor nanowire of a superconductor/ spin-orbit coupled semiconductor/ superconductor Josephson junction with $L_{sc} = 15$ nm, $T = 0.2T_{c,0}$, $\Gamma = 0.005\Delta_0$, $\Delta_0 = 1$ meV, $\zeta = 4$, magnetic exchange field strength $h = 0.5\Delta_0$ and spin-orbit coupling $\beta L_{sc} = 3$.

The zero-energy peaks in the densities of states shown in Figure 6.19 are symmetric about the SO field alignment angle $\varphi = 0.5\pi$. This alignment angle signifies spin-orbit coupling along the **z**-axis, parallel to the magnetic exchange field vector, $\boldsymbol{h} = h\boldsymbol{z}$. At this alignment angle, the zero-energy triplet peaks disappear. Instead, the peaks are maximized for alignment angles along the $\pm\boldsymbol{y}$-axis, where $\varphi = \pi$ and $\varphi = 0$ This is somewhat contradictory to the trends seen previously, where thermoelectric effects were suppressed at these angles for large spin-orbit fields. It would however seem that triplet superconductivity is more likely to arise when the spin-orbit field is aligned along these axes when the superconducting phase difference equals $\pi$. For this effect to actually have an impact, however, it would seem that larger magnetic exchange fields would need to be applied. As applying larger fields would negate the purpose of utilizing spin-orbit coupled Josephson junctions instead of merely Zeeman-split superconducting bilayers,

which still exhibit the largest thermoelectric effects, this is not considered herein. Large thermoelectric effects arise in the spin-orbit configuration regardless, and are not needed to be present for all superconducting phase differences. On the contrary, it might be beneficial to be able to switch the thermal charge and spin currents on and off using external means.

In contradiction to what was discovered regarding the pure triplet peak from Ref. [40], the small triplet peaks in Figure 6.19 are seen to be accompanied by tiny spin-dependent asymmetries in the density of states, shown in Figure 6.20. The arising asymmetries are very small, and seem to be maximized for the same field alignment angles as the peaks. The minute sizes of the differences in density of states seen here are not expected to be able to contribute to the thermoelectric coefficients on a large scale. Nonetheless, the coefficients do not necessarily numerically equal zero for this phase difference, but disappear when compared to the large maximum values. The clear trends in the asymmetries in the densities of states along with the fact that the features in especially $D^x(E)$ are not that much smaller than some of the results for the Seebeck coefficient $S$, could indicate that for some variable choices larger asymmetries could arise for the superconducting phase difference $\pi$. Both the strengths of the magnetic exchange field and the spin-orbit field seem important, but Figure 6.20 indicates the alignment angle of the spin-orbit field as a crucial impact factor. Certain parameter choices should exist which would allow for large thermoelectric effects even when the superconducting phase difference equals $\pi$. It is even possible that in some cases the maximum thermoelectric effects arise at this phase difference. This has not been shown so far, however, and the large thermoelectric effects shown herein nonetheless rival those of the normal metal/ insulator/ Zeeman-split superconductor bilayer configuration.

## 6.5  Experimental considerations

The superconducting reservoirs are modeled with a superconducting gap of $\Delta_0 = 1$ meV, and a superconducting coherence length $\xi = 30$ nm. The material choices made for the superconducting reservoirs fit quite well with NbN. This material has a superconducting coherence length close to 30 nm, which we have considered, an energy gap close to 1 meV, and a superconducting critical temperature $T_c = 14$ K. The temperature chosen to consider throughout this section, $T = 0.2T_{c,0}$, becomes $0.2 \cdot 14$ K $= 2.8$ K for the case of NbN. This would also greatly support the choice of GdN as the ferromagnetic insulator between the nanowire X (normal metal with spin-active interfaces, conical ferromagnet or spin-orbit coupled semiconductor) and the normal metal electrode, as we have chosen $P = 97\%$ in our calculations. This has been reported to be the polarization of GdN at 3 K [68]. There is also a strong possibility that these two materials, NbN and GdN, would be compatible to grow together.

Holmium is a spiral conical ferromagnet below $T = 19$ K [142]. Again, the tempera-

ture at which we operate $(0.2T_{c,0})$ is well below this limit for several superconducting materials, for instance NbN. The values considered for the exchange field in the conical ferromagnet are chosen to span a rather large range due to the experimental observations being quite varying. Values for the exchange field in Holmium of $h/\Delta = 1$ [143], $h/\Delta = 3$ [35], $h/\Delta = 15$ [144] and even $h/\Delta = 18$ [145] have been reported. Accordingly, we allow for consideration of the thermoelectric effects over a large range of different ferromagnetic exchange fields in the conical ferromagnet Ho. We realize that this is not a parameter which may be easily altered *in situ*, but the possibility of tuning the superconducting phase difference and the impact this has upon the thermoelectric response of the system should allow for a large enough degree of experimental control.

A major advantage of the thermoelectric effects predicted throughout this section concerns the absence of strong magnetic fields. When Zeeman split superconductors are used, magnetic fields of the order of 1 T need to be applied for the exchange fields within the superconductors to reach $h = 0.5\Delta_0$. This can be attributed to the Lande g-factor within superconducting materials. The Lande g-factor is a central quality for characterizing the response of an electron or hole spin to an applied magnetic field [146], and often takes values close to $g \approx 2$ in superconducting materials such as Al [147]. In semiconducting nanowires containing strong spin-orbit coupling, however, the Lande g-factor can become much larger and take on values of $g \approx 15$ in bulk InAs [146], $g \approx 50$ in bulk InSb [148], $g \approx 9$ in spin-orbit coupled InAs nanowires [149] and even approach $g \approx 70$ in InSb nanowire quantum dots [150]. Using structures containing such materials would reduce the size of the external fields necessary to achieving exchange fields of $h = 0.5\Delta_0$ greatly. Therefore, we have studied superconductor/semiconducting nanowire/superconductor Josephson junctions where the central semiconducting nanowire exhibits strong spin-orbit coupling capable of generating the spin-splitting effect we desire for giant thermoelectric effects to arise.

## 6.6 Summary and discussion

The goal of this section was to study the thermoelectric effects arising in superconducting tunneling hybrids in which the particle-hole symmetry for each spin can be broken along more than one axis. The framework used for the relevant thermoelectric coefficients was presented and derived in Chapter 5. The tunneling junctions considered concern tunneling from the middle of the central layer in a Josephson junction into a normal metal electrode. The tunneling barrier can have any interface transparency and any polarization due the boundary conditions used in the derivation of the framework. The benefit of the tunneling hybrids used herein in contrast to the Zeeman-split hybrids studied in the first part of Chapter 4 is once again the low externally applied magnetic fields required for operation.

The three material systems which underwent extensive scrutiny in this chapter are

Josephson junctions were the central layers are normal metals with spin-active interfaces to the superconductors, conical ferromagnets with the magnetic structure of Holmium and semiconductor nanowires with strong spin-orbit coupling. The common denominator of the Josephson junctions studied herein is the possibility of varying the fields spatially. This provides an additional element of external control in addition to the superconducting phase difference.

The novel effect studied in this chapter is the direction-dependent thermal spin currents governed by $I_s^\nu = \alpha_s^\nu \Delta T / T$. These were derived from the quasiclassical framework in Chapter 5, and are seen to offer a plethora of new effects. The spin polarization of the spin current in the **y**-direction can for instance be switched by altering the alignment of the spin-orbit field in the **yz**-plane, which could potentially be quite useful.

Within this chapter, only Josephson junctions within which the length of the central material is set to 15 nm have been studied for reasons of experimental reproducibility. If smaller central nanowire lengths than 15 nm were to be used, however, the thermoelectric effects calculated for the superconductor/conical ferromagnet/superconductor Josephson junction, the superconductor/spin-orbit coupled semiconductor/superconductor Josephson junction and the S/N/S Josephson junction with spin-active interfaces are expected to increase significantly. Consequently, there is a chance that the thermoelectric effects in structures with critical dimensions approaching the sub-5 nm regime may surpass even those achievable in the Zeeman-split bilayers studied in Chapter 4.

The thermoelectric effects arising are seen to rival those of the normal metal/ insulator/ Zeeman-split bilayer configuration in all the three cases studied. This is very interesting, as even though the configurations presented here are somewhat more complex to fabricate they do not require large magnetic fields to operate. The elements of external control are here many, and include both the temperature and superconducting phase difference in addition to the direction of the magnetic spin active interface in the **yz**-plane, the alignment angle of the spin-orbit field and the exchange field in the spin-orbit couple semiconductor. Other control parameters which are not as easily changed in situ include the spin-dependent scattering at the spin-active interfaces, the strength of the exchange field in the conical ferromagnet, and the strength of the spin-orbit coupling. Once again we can notice the same effect as in Chapter 4, where the thermal charge and spin currents arising can be switched on and off using only the external control parameters such as the field alignment angles and superconducting phase difference.

# Chapter 7

# Conclusions and outlook

We have studied the thermoelectric effects arising in both high-field and low-field superconducting hybrids as a result of Zeeman-splitting, spin-active interfaces, spatially varying magnetization and spin-orbit coupling. Two new frameworks for calculating thermoelectric coefficients, including both the possibility of spin-dependent bias application and arbitrary spin-dependent fields, have been presented. Even though the largest thermoelectric effects are to be found in the case of tunneling between two Zeeman-split superconductors separated by an insulating barrier, the corresponding effects discovered in the low-field hybrids are not far behind. As not all material parameters or spin-splitting configurations have been studied, nor Josephson junctions with sub-5 nm central layer lengths, there is a possibility that the giant high-field thermoelectric effects may even be surpassed.

Even though a vast array of thermoelectric effects have been studied herein, there are many directions left to explore. It would be very interesting to discern whether any low-field superconducting hybrids such as the ones studied in the second part of Chapter 4 and Chapter 6 are able to surpass the thermoelectric effects obtainable in Zeeman-split hybrids. Furthermore, the general quasiclassical framework derived in Chapter 5 could be applied to more complex systems, where normal metal electrodes need not be assumed. This framework could moreover be expanded to include the possibility of spin-dependent biases, as argued for in Chapter 3. If these biases were direction-dependent in the same manner as the spin and spin heat currents this could result in a plethora of new effects. Another possibility offering large potential is the study of thermoelectric effects arising in non-conventional superconducting hybrids [151].

# Bibliography

[1] Kamerlingh Onnes, H. *Leiden Comm.* **120**, **122b**, **124c** (1911).

[2] Bardeen, J., Cooper, L. N., and Schrieffer, J. R. Theory of Superconductivity. *Phys. Rev.* **108**, 1175-1204 (1957).

[3] Meissner, W. and Ochsenfeld, R. Ein neuer Effekt bei Eintritt der Supraleit-fähigkeit. *Die Naturwissenschaften* **21**, 787-788 (1933).

[4] Holm, R. and Meissner, W. Messungen mit Hilfe von flüssigem Helium. XIII *Zeitschrift für Physik* **74**, 715-735 (1932).

[5] Bednorz, J. G. and Müller, K. A. Possible High $T_c$ Superconductivity in the Ba-La-Cu-O System. *Zeit. Phys. B Cond. Matt.* **64**, 189-193 (1986).

[6] Edelman, R. R. and Warach, S. Magnetic Resonance Imaging. *The New England Journal of Medicine* **328**, 708-716 (1993).

[7] Bazley, T. *Japan breaks train speed record with Maglev train* (Al Jazeera, 2015). `http://www.aljazeera.com/news/2015/04/japan-breaks-train-speed-record-maglev-train-150421085448739.html`

[8] Drung, D., *et al.* Highly Sensitive and Easy-to-Use SQUID Sensors. *IEEE Transactions on Applied Superconductivity* **17**, 699-704 (2007).

[9] Makhlin, Y., Schön, G., and Shnirman, A. Josephson-junction qubits with controlled couplings. *Nature* **398**, 305-307 (1999).

[10] Drozdov, A. P., Eremets, M. I., Troyan, I. A., Ksenofontov, V., and Shylin, S. I. Conventional superconductivity at 203 Kelvin at high pressures in the sulfur hydride system. *Nature* **525**, 73-76 (2015).

[11] Moore, G. E. Cramming More Components Onto Integrated Circuits. *Electronics* **38**, 114-117 (1965).

[12] Taur, Y. and Ning, T. H. *Fundamentals of Modern VLSI Devices* (Cambridge University Press, 2nd edition, 2009).

[13] *Introduction to Spintronics and Spin Quantum Computation* (Department of Physics, University of Maryland, 2015). `http://www.physics.umd.edu/rgroups/spin/intro.html`

[14] Datta, S., and Das, B. Electronic analog of the electrooptic modulator. *Appl. Phys. Lett.* **56**, 665-667 (1990).

[15] Chuang, P., *et al.* All-electric all-semiconductor spin field-effect transistors. *Nature Nanotechnology* **10**, 35-39 (2015).

[16] Chumak, A. V., Serga, A. A., and Hillebrands, B. Magnon transistor for all-magnon data processing. *Nature Communications* **5**, 4700 (2014)

[17] Ralph, D. C. and Stiles, M. D. Spin transfer torques. *Journal of Magnetism and Magnetic Materials* **320**, 1190-1216 (2008).

[18] Chiba, T., Bauer, G. E. W., and Takahashi, S. Spin-torque transistor revisited. *Appl. Phys. Lett.* **102**, 192412 (2013).

[19] Bauer, G. E. W., Brataas, A., Tserkovnyak, Y., and van Wees, B. J. Spin-torque transistor. *Appl. Phys. Lett.* **82**, 3928-3930 (2003).

[20] *The Giant Magnetoresistive Head: A giant leap for IBM Research* (IBM Research, 2015). `http://www.research.ibm.com/research/gmr.html`

[21] Linder, J. and Robinson, J. W. A. Superconducting Spintronics. *Nature Physics* **11**, 307–315 (2015).

[22] Yang, H., Yang, S-H., Takahashi, S., Maekawa, S., and Parkin, S. S. P. Extremely long quasiparticle spin lifetimes in superconducting aluminum using MgO tunnel spin injectors. *Nature Materials* **9**, 586-593 (2010).

[23] Quay, C. H. L., Chevallier, D., Bena, C., and Aprili, M. Spin imbalance and spin-charge separation in a mesoscopic superconductor. *Nature Physics* **9**, 84-88 (2013).

[24] Li, B., *et al.* Superconducting spin switch with infinite magnetoresistance induced by an internal exchange field. *Phys. Rev. Lett.* **110**, 097001 (2013).

[25] Zhao, E. and Sauls, J. A. Theory of nonequilibrium spin transport and spin-transfer torque in superconducting-ferromagnetic nanostructures. *Phys. Rev. B* **78**, 174511 (2008).

[26] Ferguson, A. J., Andresen, S. E., Brenner, R., and Clark, R. G. Spin dependent quasiparticle transport in Aluminum single-electron transistors. *Phys. Rev. Lett.* **97**, 086602 (2006).

[27] Cooper, L. N. Bound Electron Pairs in a Degenerate Fermi Gas. *Phys. Rev.* **104**, 1189-1190 (1956).

[28] Eschrig, M., Kopu, J., Cuevas, J. C., and Schön, G. Theory of Half Metal-Superconductor Heterostructures. *Phys. Rev. Lett.* **90**, 137003 (2003).

[29] Eschrig, M. Spin-polarized supercurrents for spintronics: a review of current progress. *Rep. Prog. Phys.* **78**, 104501 (2015).

[30] Bergeret, F. S., Volkov, A. F., and Efetov, K. B. Long-Range Proximity Effects in Superconductor-Ferromagnet Structures. *Phys. Rev. Lett.* **86**, 4096-4099 (2001).

[31] Bergeret, F. S., Volkov, A. F., and Efetov, K. B. Odd triplet superconductivity and related phenomena in superconductor-ferromagnet structures. *Rev. Mod. Phys.* **77**, 1321-1373 (2005).

[32] Keizer, R. S., *et al.* A spin-triplet supercurrent through half-metallic ferromagnet $CrO_2$. *Nature* **439**, 825-827 (2006).

[33] Gomperud, I. and Linder, J. Spin supercurrent and phase-tunable triplet Cooper pairs via magnetic insulators. *Phys. Rev. B* **92**, 035416 (2015).

[34] Moor, A., Volkov, A. F., and Efetov, K. B. Nematic versus ferromagnetic spin filtering of triplet Cooper pairs in superconducting spintronics. *Phys. Rev. B* **92**, 180506(R) (2015).

[35] Di Bernardo, A., *et al.* Signature of magnetic-dependent gapless odd frequency states at superconductor/ferromagnet interfaces. *Nature Communications* **6**, 8053 (2015).

[36] Mironov, S. and Buzdin, A. Triplet proximity effect in superconducting heterostructures with a half-metallic layer. *Phys. Rev. B* **92**, 184506 (2015).

[37] Tedrow, P. M. and Meservey, R. Direct Observation of Spin-State Mixing in Superconductors. *Phys. Rev. Lett.* **27**, 919-921 (1971).

[38] Bergeret, F. S. and Tokatly, I. V. Spin-orbit coupling as a source of long-range triplet proximity effect in superconductor-ferromagnet hybrid structures. *Phys. Rev. B* **89**, 134517 (2014).

[39] Jacobsen, S. H., Ouassou, J. A., and Linder, J. Critical temperature and tunneling spectroscopy of superconductor-ferromagnet hybrids with intrinsic Rashba-Dresselhaus spin-orbit coupling. *Phys. Rev. B* **92**, 024510 (2015).

[40] Jacobsen, S. H. and Linder, J. Giant triplet proximity effect in pi-biased Josephson junctions with spin-orbit coupling. *Phys. Rev. B* **92**, 024501 (2015).

[41] Kuschel, T. and Reiss, G. Spin orbitronics: Charges ride the spin wave. *Nature Nanotechnology* **10**, 22-24 (2015).

[42] Snyder, G. J. and Toberer, E. S. Complex Thermoelectric Materials. *Nature Materials* **7**, 105-114 (2008).

[43] Shakouri, A. Recent Developments in Semiconductor Thermoelectric Physics and Materials. *Annu. Rev. Mat. Res.* **41**, 399-431 (2011).

[44] Abrikosov, A. A. *Fundamentals of the Theory of Metals* (Elsevier Science, 1988).

[45] Bauer, G. E. W., Saitoh, E., and van Wees, B. J. Spin Caloritronics. *Nature Materials* **11**, 391-399 (2012).

[46] Ozaeta, A., Virtanen, P., Bergeret, F. S., and Heikkilä, T. T. Predicted Very Large Thermoelectric Effect in Ferromagnet-Superconductor Junctions in the Presence of a Spin-Splitting Magnetic Field. *Phys. Rev. Lett.* **112**, 057001 (2014).

[47] Krishtop, T., Houzet, M., and Meyer, J. S. Nonequilibrium spin transport in Zeeman-split superconductors. *Phys. Rev. B* **91**, 121407(R) (2015).

[48] Kolenda, S., Wolf, M. J., and Beckmann, D. Observation of Thermoelectric Currents in High-Field Superconductor-Ferromagnet Tunnel Junctions. *Phys. Rev. Lett.* **116**, 097001 (2016).

[49] Linder, J. and Bathen, M. E. Spin caloritronics with superconductors: Enhanced thermoelectric effects, generalized Onsager response-matrix, and thermal spin currents. *Phys. Rev. B* **93**, 224509 (2016).

[50] Kalenkov, M. S., Zaikin, A. D., and Kuzmin, L. S. Theory of a Large Thermoelectric Effect in Superconductors Doped with Magnetic Impurities. *Phys. Rev. Lett.* **109**, 147004 (2012).

[51] Kalenkov, M. S. and Zaikin, A. D. Enhancement of thermoelectric effects in diffusive superconducting bilayers with magnetic interfaces. *Phys. Rev. B* **91**, 064504 (2015).

[52] Machon, P., Eschrig, M., and Belzig, W. Nonlocal thermoelectric effects and nonlocal Onsager relations in a three-terminal proximity-coupled superconductor-ferromagnet device. *Phys. Rev. Lett.* **110**, 047002 (2013).

[53] Martinez-Perez, M. J., Solinas, P., and Giazotto, F. Coherent caloritronics in Josephson-based nanocircuits. *Journal of Low Temperature Physics* **175**, 813-837 (2014).

[54] Strambini, E., Bergeret, F. S., and Giazotto, F. Proximity nanovalve with large phase-tunable thermal conductance. *Appl. Phys. Lett.* **105**, 082601 (2014).

[55] Giazotto, F., Robinson, J. W. A., Moodera, J. S., and Bergeret, F. S. Proposal for a phase-coherent thermoelectric transistor. *Appl. Phys. Lett.* **105**, 062602 (2014).

[56] Muhonen, J. T., Meschke, M., and Pekola, J. P. Micrometre-scale refrigerators. *Rep. Prog. Phys.* **75**, 046501 (2012).

[57] Kawabata, S., Ozaeta, A., Vasenko, A. S., Hekking, F. W. J., and Bergeret, F. S. Efficient electron refrigeration using superconductor/spin-filter devices. *Appl. Phys. Lett.* **103**, 032602 (2013).

[58] Giazotto, F., *et al.* Opportunities for mesoscopics in thermometry and refrigeration: Physics and applications. *Rev. Mod. Phys.* **78**, 217-274 (2006).

[59] Guidry, M. *Gauge Field Theories: An Introduction with Applications* (Wiley, 2004).

[60] Schmidt, K. E. *Unit Conversion* (2015). `http://fermi.la.asu.edu/PHY531/units/`

[61] Mahan, G. *Many-particle Physics* (Plenum, 3rd edition, 2000).

[62] Altland, A. and Simons, B. *Condensed Matter Field Theory* (Cambridge University Press, 2010).

[63] Buschow, K. H. J. *Concise Encyclopedia of Magnetic and Superconducting Materials* (Elsevier Science, 2nd edition, 2005).

[64] Fossheim, K. and Sudbø, A. *Superconductivity: Physics and Applications* (Wiley, 2004).

[65] Linder, J. and Sudbø, A. Josephson effect in thin-film superconductor/ insulator/ superconductor junctions with misaligned in-plane magnetic fields. *Phys. Rev. B* **76**, 064524 (2007).

[66] Dynes, R. C., Narayanamurti, V., and Garno, J. P. Direct Measurement of Quasiparticle-Lifetime Broadening in a Strong-Coupled Superconductor. *Phys. Rev. Lett.* **41**, 1509-1512 (1978).

[67] Meservey, R., Tedrow, P. M., and Fulde, P. Magnetic Field Splitting of the Quasiparticle States in Superconducting Aluminum Films. *Phys. Rev. Lett.* **25**, 1270-1272 (1970).

[68] Pal, A. and Blamire, M. G. Large interfacial exchange fields in a thick superconducting film coupled to a spin-filter tunnel barrier. *Phys. Rev. B* **92**, 180510(R) (2015).

[69] Kittel, C. *Introduction to Solid State Physics* (Wiley, 8th edition, 2005).

[70] Marder, M. P. *Condensed Matter Physics* (Wiley, 2000).

[71] Coey, J. M. D. *Magnetism and Magnetic Materials* (Cambridge University Press, 2009).

[72] Ouassou, J. A. *Full proximity effect in spin-textured superconductor/ferromagnet bilayers.* Specialization Project (Norwegian University of Science and Technology, 2014).

[73] Manchon, A., Koo, H. C., Nitta, J., Frolov, S. M., and Duine, R. A. New perspectives for Rashba spin–orbit coupling. *Nature Materials* **14**, 871-882 (2015).

[74] Winkler, R. *Spin–Orbit Coupling Effects in Two-Dimensional Electron and Hole Systems* (Springer, 2003).

[75] Ouassou, J. A. *Density of States and Critical Temperature in Superconductor/Ferromagnet Structures with Spin-Orbit Coupling.* Diploma Thesis (Norwegian University of Science and Technology, 2015).

[76] Blonder, G. E., Tinkham, M., and Klapwijk, T. M. Transition from metallic to tunneling regimes in superconducting microconstrictions: Excess current, charge imbalance, and supercurrent conversion. *Phys. Rev. B* **25**, 4515-4532 (1982).

[77] Josephson, B. D. Possible new effects in superconductive tunneling. *Phys. Lett.* **1**, 251-253 (1962).

[78] Josephson, B. D. The discovery of tunneling supercurrents. *Rev. Mod. Phys.* **46**, 251-254 (1974).

[79] Golubov, A. A. and Kupriyanov, M. Y. Josephson effect in SNINS and SNIS tunnel structures with finite transparency of the SN boundaries. *Zh. Eksp. Teor. Fiz.* **96**, 1420-1433 (1989).

[80] Belzig, W., Bruder, C., and Schön, G. Local density of states in a dirty normal metal connected to a superconductor. *Phys. Rev. B* **54**, 9443-9448 (1996).

[81] Kastalsky, A., *et al.* Observation of Pair Currents in Superconductor-Semiconductor Contacts. *Phys. Rev. Lett.* **67**, 3026-3029 (1991).

[82] Hammer, J. C., Cuevas, J. C., Bergeret, F. S., and Belzig, W. Density of states and supercurrent in diffusive SNS junctions: Roles of nonideal interfaces and spin-flip scattering. *Phys. Rev. B* **76**, 064514 (2007).

[83] Linder, J., Yokoyama, T., and Sudbø, A. Theory of superconducting and magnetic proximity effect in S/F structures with inhomogeneous magnetization textures and spin-active interfaces. *Phys. Rev. B* **79**, 054523 (2009).

[84] Keldysh, L. V. Diagram technique for nonequilibrium processes. *Soviet Physics JETP* **20**, 1018-1026 (1965).

[85] Larkin, A. I. and Ovchinnikov, Y. N. Nonlinear conductivity of superconductors in the mixed state. *Zh. Eksp. Teor. Fiz.* **68**, 1915-1927 (1975).

[86] Rammer, J. and Smith, H. Quantum field-theoretical methods in transport theory of metals. *Rev. Mod. Phys.* **58**, 323-359 (1986).

[87] Belzig, W., Wilhelm, F. K., Bruder, C., Schön, G., and Zaikin, A. D. Quasiclassical Green's function approach to mesoscopic superconductivity. *Superlattices and Microstructures* **25**, 1251-1288 (1999).

[88] Jauho, A. P. *Introduction to the Keldysh nonequilibrium Green function technique.* Lecture notes (2006). `https://nanohub.org/resources/1877`

[89] Maciejko, J. *An introduction to nonequilibrium many-body theory.* Lecture notes (2007). `http://www.physics.arizona.edu/~stafford/Courses/560A/nonequilibrium.pdf`

[90] Chandrasekhar, V. *An introduction to the quasiclassical theory of superconductivity for diffusive proximity-coupled systems.* (Online, 2008). `http://arxiv.org/pdf/cond-mat/0312507v2.pdf`

[91] Fazio, R. and Lucheroni, C. Local density of states in superconductor-ferromagnetic hybrid systems. *Europhysics Letters* **45**, 707-713 (1999).

[92] Morten, J. P. *Spin and charge transport in dirty superconductors.* Diploma Thesis (Norwegian University of Science and Technology, 2005).

[93] Kuprianov, M. Y. and Lukichev, V. F. Influence of boundary transparency on the critical current of dirty SS'S superconductors. *Zh. Eksp. Teor. Fiz* **94**, 139-149 (1988).

[94] Cottet, A., Huertas-Hernando, D., Belzig, W., and Nazarov, Y. V. Spin-dependent boundary conditions for isotropic superconducting Green's functions. *Phys. Rev. B* **80**, 184511 (2009).

[95] Eschrig, M., Cottet, A., Belzig, W., and Linder, J. General boundary conditions for quasiclassical theory of superconductivity in the diffuse limit: application to strongly spin-polarized systems. *New J. Phys.* **17**, 083037 (2015).

[96] Zhao, E., Löfwander, T., and Sauls, J. A. Phase Modulated Thermal Conductance of Josephson Weak Links. *Phys. Rev. Lett.* **91**, 077003 (2003).

[97] Zhao, E., Löfwander, T., and Sauls, J. A. Nonequilibrium Superconductivity near Spin Active Interfaces. *Phys. Rev. B* **70**, 134510 (2004).

[98] Schopohl, N. Transformation of the Eilenberger equations of superconductivity to a scalar Riccati equation (Online preprint, 1998). `https://arxiv.org/pdf/cond-mat/9804064v1.pdf`

[99] Gomperud, I. R. *Spin- and Charge-Supercurrent and Density of States in Diffusive Spin-Active Josephson Junctions.* Diploma Thesis (Norwegian University of Science and Technology, 2015).

[100] Seebeck, T. J. *Magnetische Polarisation der Metalle und Erze durch Temperatur-Differenz* (Abhandlungen der Königlichen Akademie der Wissenschaften zu Berlin, 1825).

[101] Seebeck, T. J. Ueber die Magnetische Polarisation der Metalle und Erze durch Temperatur-Differenz. *Annalen der Physik* **82**, 133-160 (1826).

[102] Peltier, J. C. A. Nouvelles experiences sur la caloricite des courants electrique. *Ann. Chim. Phys.* **56**, 371-386 (1834).

[103] Ashcroft, N. W. and Mermin, D. N. *Solid State Physics* (Saunders College, 1976).

[104] Mahan, G. D. Figure of merit for thermoelectrics. *J. Appl. Phys.* **65**, 1578-1583 (1989).

[105] Galperin, Y. M., Gurevich, V. L., Kozub, V. I., and Shelankov, A. L. Theory of thermoelectric phenomena in superconductors. *Phys. Rev. B* **65**, 064531 (2002).

[106] Heikkilä, T. T. *The Physics of Nanoelectronics: Transport and Fluctuation Phenomena at Low Temperatures* (Oxford University Press, 2003).

[107] Onsager, L. Reciprocal relations in irreversible processes. I. *Physical Review* **37**, 405-426 (1931).

[108] Proesmans, K., and Van den Broeck, C. Onsager coefficients in periodically driven systems. *Phys. Rev. Lett.* **115**, 090601 (2015).

[109] Kasap, S. *Thermoelectric Effects in Metals: Thermocouples.* (University of Saskatchewan, Online e-Booklet, 2001). `http://www.kasap.usask.ca/samples/Thermoelectric-Seebeck.pdf`

[110] Littman, H. and Davidson, B. Theoretical bound on the thermoelectric figure of merit from irreversible thermodynamics. *J. Appl. Phys.* **32**, 217-219 (1961).

[111] Urech, M., Johansson, J., Poli, N., Korenivski, V., and Haviland, D. B. Enhanced spin accumulation in a superconductor. *J. Appl. Phys.* **99**, 08M513 (2006).

[112] Takahashi, S., Imamura, H., and Maekawa, S. Spin imbalance and magnetoresistance in ferromagnet/ superconductor/ ferromagnet double tunnel junctions. *Phys. Rev. Lett.* **82**, 3911-3914 (1999).

[113] Takahashi, S. and Maekawa, S. Spin injection and detection in magnetic nanostructures. *Phys. Rev. B* **67**, 052409 (2003).

[114] Jin, B. Response of spin-accumulated ferromagnet/ superconductor/ ferromagnet double tunnel junction to applied magnetic field. *Journal of Magnetism and Magnetic Materials* **320**, 603-607 (2008).

[115] Hatami, M., Bauer, G. E. W., Zhang, Q., and Kelly, P. J. Thermal spin-transfer torque in magnetoelectronic devices. *Phys. Rev. Lett.* **99**, 066603 (2007).

[116] Heikkilä, T. T., Hatami, M., and Bauer, G. E. W. Spin heat accumulation and its relaxation in spin valves. *Phys. Rev. B* **81**, 100408(R) (2010).

[117] Vera-Marun, I. J., van Wees, B. J., and Jansen, R. Spin heat accumulation induced by tunneling from a ferromagnet. *Phys. Rev. Lett.* **112**, 056602 (2014).

[118] Dejene, F. K., Flipse, J., Bauer, G. E. W., and van Wees, B. J. Spin heat accumulation and spin-dependent temperatures in nanopillar spin valves. *Nature Physics* **9**, 636-639 (2013).

[119] Kimling, J., *et al.* Spin dependent thermal transport perpendicular to the planes of Co/Cu multilayers. *Phys. Rev. B* **91**, 144405 (2015).

[120] Hao, X., Moodera, J. S., and Meservey, R. Spin-filter effect of ferromagnetic europium sulfide tunnel barriers. *Phys. Rev. B* **42**, 8235-8243 (1990).

[121] Tokuyasu, T., Sauls, J. A., and Rainer, D. Proximity effect of a ferromagnetic insulator in contact with a superconductor. *Phys. Rev. B* **38**, 8823-8833 (1988).

[122] Xiong, Y. M., Stadler, S., Adams, P. W., and Catelani, G. Spin-Resolved Tunneling Studies of the Exchange Field in EuS/Al Bilayers. *Phys. Rev. Lett.* **106**, 247001 (2011).

[123] Giazotto, F., *et al.* Nonequilibrium spin-dependent phenomena in mesoscopic superconductor–normal metal tunnel structures. *Phys. Rev. B* **76**, 184518 (2007).

[124] Dorf, R. C. *CRC Handbook of Engineering Tables* (CRC Press, 2003).

[125] le Sueur, H., Pothier, H., Urbina, C., and Esteve, D. Phase Controlled Superconducting Proximity Effect Probed by Tunneling Spectroscopy. *Phys. Rev. Lett.* **100**, 197002 (2008).

[126] Strambini, E., D'Ambrosio, S., Vischi, F., Bergeret, F. S., Nazarov, Yu. V., Giazotto F. The $\omega$-SQUIPT: phase-engineering of Josephson topological materials. *Online Preprint* (2015). `https://arxiv.org/abs/1603.00338`

[127] Pfeffer, A. H., Duvauchelle, J. E., Courtois, H., Melin, R., Feinberg, D., and Lefloch, F. Subgap structure in the conductance of a three-terminal Josephson junction. *Phys. Rev. B* **90**, 075401 (2014).

[128] McMichael, R. D., and Donahue, M. J. Head to head domain wall structures in thin magnetic strips. *IEEE Transactions on Magnetics* **33**, 4167-4169 (1997).

[129] Kläui, M. Head-to-head domain walls in magnetic nanostructures. *Journal of Physics: Condensed Matter* **20**, 313001 (2008).

[130] Ryazanov, V. V., *et al.* Coupling of Two Superconductors through a Ferromagnet: Evidence for a $\pi$ Junction. *Phys. Rev. Lett.* **86**, 2427-2430 (2001).

[131] Manfrinato, V. R., *et al.* Determining the Resolution Limits of Electron-Beam Lithography: Direct Measurement of the Point-Spread Function. *Nano Letters* **14**, 4406-4412 (2014).

[132] Manfrinato, V. R., *et al.* Resolution limits of electron-beam lithography towards the atomic scale. *Nano Letters* **13**, 1555-1558 (2013).

[133] Mojarad, N., *et al.* Single digit resolution nanopatterning with extreme ultraviolet light for the 2.5 nm technology node and beyond. *Nanoscale* **7**, 4031-4037 (2015).

[134] Tinkham, M. *Introduction to Superconductivity* (Dover, 2nd edition, 2004).

[135] Saira, O.-P., Kemppinen, A., Maisi, V. F., and Pekola, J. P. Vanishing quasiparticle density in a hybrid Al/Cu/Al single-electron transistor. *Phys. Rev. B* **85**, 012504 (2012).

[136] Tedrow, P. M., Tkaczyk, J. E., and Kumar, A. Spin-Polarized Electron Tunneling Study of an Artificially Layered Superconductor with Internal Magnetic Field: EuO-Al. *Phys. Rev. Lett.* **56**, 1746-1749 (1986).

[137] Zhao, E., Löfwander, T., and Sauls, J. A. Heat transport through Josephson point contacts. *Phys. Rev. B* **69**, 134503 (2004).

[138] Linder, J. and Robinson, J. W. A. Strong odd-frequency correlations in fully gapped Zeeman-split superconductors. *Scientific Reports* **5**, 15483 (2015).

[139] Jensen, J. Theory of commensurable magnetic structures in holmium. *Phys. Rev. B* **54**, 4021-4032 (1996).

[140] Pechan, M. J. and Stassis, C. Magnetic structure of Holmium. *J. Appl. Phys.* **55**, 1900-1902 (1984).

[141] Sosnin, I., Cho, H., Petrashov, V. T., and Volkov, A. F. Superconducting Phase Coherent Electron Transport in Proximity Conical Ferromagnets. *Phys. Rev. Lett.* **96**, 157002 (2006).

[142] Chiodi, F., *et al.* Supra-oscillatory critical temperature dependence of Nb-Ho bilayers. *Europhysics Letters* **101**, 37002 (2013).

[143] Gu, Y., Halasz, G. B., Robinson, J. W. A., and Blamire, M. G. Large Superconducting Spin Valve Effect and Ultrasmall Exchange Splitting in Epitaxial Rare Earth Niobium Trilayers. *Phys. Rev. Lett.* **115**, 067201 (2015).

[144] Alidoust, M., Linder, J., Rashedi, G., Yokoyama, T., and Sudbø, A. Spin-polarized Josephson current in S|F|S junctions with inhomogeneous magnetization. *Phys. Rev. B* **81**, 014512 (2010).

[145] Di Bernardo, A., *et al.* Supplemental Material: Intrinsic Paramagnetic Meissner Effect Due to s-Wave Odd-Frequency Superconductivity. *Phys. Rev. X* **5**, 041021 (2015).

[146] Pryor, C. E. and Flatte, M. E. Lande g Factors and Orbital Momentum Quenching in Semiconductor Quantum Dots. *Phys. Rev. Lett.* **96**, 026804 (2006).

[147] Quay, C. H. L., Weideneder, M., Chiffaudel, Y., Strunk, C., and Aprili, M. Quasiparticle spin resonance and coherence in superconducting aluminium. *Nature Communications* **6**, 8660 (2015).

[148] Mourik, V., *et al.* Signatures of Majorana Fermions in Hybrid Superconductor-Semiconductor Nanowire Devices. *Science* **336**, 1003-1007 (2012).

[149] Nadj-Perge, S., Frolov, S. M., Bakkers, E. P. A. M., and Kouwenhoven, L. P. Spin–orbit qubit in a semiconductor nanowire. *Nature* **468**, 1084-1087 (2010).

[150] Nilsson, H. A., *et al.* Giant, level-dependent g factors in InSb nanowire quantum dots. *Nano Letters* **9**, 3151-3156 (2009).

[151] Löfwander, T. and Fogelström, M. Large thermoelectric effects in unconventional superconductors. *Phys. Rev. B* **70**, 024515 (2004).

# Appendices

# Appendix A

# Thermoelectric Onsager matrix for homogeneously magnetized systems

Chapter 3 contains the results of deriving a $4 \times 4$ Onsager matrix describing thermoelectric effects arising in superconducting hybrids spin-split homogeneously along one axis when including the possibility of spin-dependent biases. This appendix contains the essence of the calculations performed in order to obtain this matrix. The calculations are included here instead of in Chapter 3 due to their extensive nature.

## A.1  Charge current

The total charge current when assuming the density of states, temperatures and voltage biases to depend on spin becomes

$$
\begin{aligned}
I = \frac{1}{e} \int_{-\infty}^{\infty} \mathrm{d}E \bigg\{ & \left( G_T F^0 + \frac{G_T P}{2} F^z \right) \left( D_L^0 D_R^0 + \frac{1}{4} D_L^z D_R^z \right) \\
& + \frac{1}{2} \left( \frac{1}{2} G_T F^z + G_T P F^0 \right) \left( D_L^0 D_R^z + D_L^z D_R^0 \right) \bigg\}.
\end{aligned}
\tag{A.1}
$$

The charge current is subsequently Taylor expanded to the first order in each of the eight variables $(V_j^\sigma, T_j^\sigma)$. Differentiating with respect to the first variable and applying the results for $\mathrm{d}F^{0,z}/\mathrm{d}(T, V)_j^\sigma$ derived in Chapter 3 yields

$$\frac{\mathrm{d}I}{\mathrm{d}V_L^\uparrow}(V_L^\uparrow - V_{L,0}^\uparrow) = \frac{1}{e}\int_{-\infty}^\infty \mathrm{d}E\Bigg[\Big(G_T\frac{\mathrm{d}F^0}{\mathrm{d}V_L^\uparrow} + \frac{G_T P}{2}\frac{\mathrm{d}F^z}{\mathrm{d}V_L^\uparrow}\Big)\Big(D_L^0 D_R^0 + \frac{D_L^z D_R^z}{4}\Big)$$
$$+ \frac{1}{2}\Big(\frac{G_T}{2}\frac{\mathrm{d}F^z}{\mathrm{d}V_L^\uparrow} + G_T P\frac{\mathrm{d}F^0}{\mathrm{d}V_L^\uparrow}\Big)\Big(D_L^0 D_R^z + D_L^z D_R^0\Big)\Bigg](V_L^\uparrow - V_{L,0}^\uparrow). \tag{A.2}$$

The terms $\frac{\mathrm{d}F^0}{\mathrm{d}V_L^\uparrow}$ and $\frac{\mathrm{d}F^z}{\mathrm{d}V_L^\uparrow}$ are symmetric functions of E. The same is true of $\Big(D_L^0 D_R^0 + \frac{D_L^z D_R^z}{4}\Big)$. On the other hand, $(D_L^0 D_R^z + D_L^z D_R^0)$ is antisymmetric in E due to $D_j^z(E)$ being antisymmetric and $D_j^0(E)$ symmetric. Integrating

$$\frac{1}{2}\Big(\frac{G_T}{2}\frac{\mathrm{d}F^z}{\mathrm{d}V_L^\uparrow} + G_T P\frac{\mathrm{d}F^0}{\mathrm{d}V_L^\uparrow}\Big)\Big(D_L^0 D_R^z + D_L^z D_R^0\Big) \tag{A.3}$$

with respect to $E$ from $-\infty$ to $\infty$ therefore equals zero. Now,

$$\frac{\mathrm{d}I}{\mathrm{d}V_L^\uparrow}(V_L^\uparrow - V_{L,0}^\uparrow) = \frac{1}{e}\int_{-\infty}^\infty \mathrm{d}E\Bigg[\Big(G_T\frac{\mathrm{d}F^0}{\mathrm{d}V_L^\uparrow} + \frac{G_T P}{2}\frac{\mathrm{d}F^z}{\mathrm{d}V_L^\uparrow}\Big)\Big(D_L^0 D_R^0 + \frac{D_L^z D_R^z}{4}\Big)\Bigg](V_L^\uparrow - V_{L,0}^\uparrow) \tag{A.4}$$

$$= \frac{1}{e}\int_{-\infty}^\infty \mathrm{d}E\Bigg[\Big(\frac{G_T}{2} + \frac{G_T P}{2}\Big)\Big(\frac{e}{4k_B T\cosh^2\big(\frac{E}{2k_B T}\big)}\Big)\Big(D_L^0 D_R^0 + \frac{D_L^z D_R^z}{4}\Big)\Bigg](V_L^\uparrow - V_{L,0}^\uparrow) \tag{A.5}$$

$$= \int_{-\infty}^\infty \mathrm{d}E\Bigg[\frac{G_T}{2}\frac{D_L^0 D_R^0 + \frac{D_L^z D_R^z}{4}}{4k_B T\cosh^2\big(\frac{E}{2k_B T}\big)} + \frac{G_T P}{2}\frac{D_L^0 D_R^0 + \frac{D_L^z D_R^z}{4}}{4k_B T\cosh^2\big(\frac{E}{2k_B T}\big)}\Bigg](V_L^\uparrow - V_{L,0}^\uparrow). \tag{A.6}$$

Similarly, using the same symmetry arguments and expressions for the derivatives of $F^0$ and $F^z$, we can calculate

$$\frac{\mathrm{d}I}{\mathrm{d}V_L^\downarrow}(V_L^\downarrow - V_{L,0}^\downarrow) = \int_{-\infty}^\infty \mathrm{d}E\Bigg[\frac{G_T}{2}\frac{D_L^0 D_R^0 + \frac{D_L^z D_R^z}{4}}{4k_B T\cosh^2\big(\frac{E}{2k_B T}\big)} - \frac{G_T P}{2}\frac{D_L^0 D_R^0 + \frac{D_L^z D_R^z}{4}}{4k_B T\cosh^2\big(\frac{E}{2k_B T}\big)}\Bigg](V_L^\downarrow - V_{L,0}^\downarrow) \tag{A.7}$$

$$\frac{\mathrm{d}I}{\mathrm{d}V_R^\uparrow}(V_R^\uparrow - V_{R,0}^\uparrow) = \int_{-\infty}^\infty \mathrm{d}E\Bigg[-\frac{G_T}{2}\frac{D_L^0 D_R^0 + \frac{D_L^z D_R^z}{4}}{4k_B T\cosh^2\big(\frac{E}{2k_B T}\big)} - \frac{G_T P}{2}\frac{D_L^0 D_R^0 + \frac{D_L^z D_R^z}{4}}{4k_B T\cosh^2\big(\frac{E}{2k_B T}\big)}\Bigg](V_R^\uparrow - V_{R,0}^\uparrow) \tag{A.8}$$

$$\frac{\mathrm{d}I}{\mathrm{d}V_R^\downarrow}(V_R^\downarrow - V_{R,0}^\downarrow) = \int_{-\infty}^\infty \mathrm{d}E\Bigg[-\frac{G_T}{2}\frac{D_L^0 D_R^0 + \frac{D_L^z D_R^z}{4}}{4k_B T\cosh^2\big(\frac{E}{2k_B T}\big)} + \frac{G_T P}{2}\frac{D_L^0 D_R^0 + \frac{D_L^z D_R^z}{4}}{4k_B T\cosh^2\big(\frac{E}{2k_B T}\big)}\Bigg](V_R^\downarrow - V_{R,0}^\downarrow). \tag{A.9}$$

When differentiating with respect to $T_j^\sigma$ it is important to notice the asymmetry of $\frac{\mathrm{d}F^{0,z}}{\mathrm{d}T_j^\sigma}$. The resulting Taylor components of the total charge current are

$$\frac{\mathrm{d}I}{\mathrm{d}T_L^\uparrow}(T_L^\uparrow - T_{L,0}^\uparrow) = \int_{-\infty}^{\infty} \mathrm{d}E\left[\frac{G_T}{4e}\frac{E(D_L^0 D_R^z + D_L^z D_R^0)}{4k_B T^2 \cosh^2\left(\frac{E}{2k_B T}\right)} + \frac{G_T P}{4e}\frac{E(D_L^0 D_R^z + D_L^z D_R^0)}{4k_B T^2 \cosh^2\left(\frac{E}{2k_B T}\right)}\right](T_L^\uparrow - T_{L,0}^\uparrow) \qquad (A.10)$$

$$\frac{\mathrm{d}I}{\mathrm{d}T_L^\downarrow}(T_L^\downarrow - T_{L,0}^\downarrow) = \int_{-\infty}^{\infty} \mathrm{d}E\left[-\frac{G_T}{4e}\frac{E(D_L^0 D_R^z + D_L^z D_R^0)}{4k_B T^2 \cosh^2\left(\frac{E}{2k_B T}\right)} + \frac{G_T P}{4e}\frac{E(D_L^0 D_R^z + D_L^z D_R^0)}{4k_B T^2 \cosh^2\left(\frac{E}{2k_B T}\right)}\right](T_L^\downarrow - T_{L,0}^\downarrow) \quad (A.11)$$

$$\frac{\mathrm{d}I}{\mathrm{d}T_R^\uparrow}(T_R^\uparrow - T_{R,0}^\uparrow) = \int_{-\infty}^{\infty} \mathrm{d}E\left[-\frac{G_T}{4e}\frac{E(D_L^0 D_R^z + D_L^z D_R^0)}{4k_B T^2 \cosh^2\left(\frac{E}{2k_B T}\right)} - \frac{G_T P}{4e}\frac{E(D_L^0 D_R^z + D_L^z D_R^0)}{4k_B T^2 \cosh^2\left(\frac{E}{2k_B T}\right)}\right](T_R^\uparrow - T_{R,0}^\uparrow) \quad (A.12)$$

$$\frac{\mathrm{d}I}{\mathrm{d}T_R^\downarrow}(T_R^\downarrow - T_{R,0}^\downarrow) = \int_{-\infty}^{\infty} \mathrm{d}E\left[\frac{G_T}{4e}\frac{E(D_L^0 D_R^z + D_L^z D_R^0)}{4k_B T^2 \cosh^2\left(\frac{E}{2k_B T}\right)} - \frac{G_T P}{4e}\frac{E(D_L^0 D_R^z + D_L^z D_R^0)}{4k_B T^2 \cosh^2\left(\frac{E}{2k_B T}\right)}\right](T_R^\downarrow - T_{R,0}^\downarrow). \quad (A.13)$$

Defining

$$(V_{j,0}^\sigma, T_{j,0}^\sigma) = (V, T) = (0, T) \qquad (A.14)$$

allows all the factors in front of $(T_{j,0}^\sigma, V_{j,0}^\sigma)$ to disappear and the total charge current to become

$$\begin{aligned}
I = &\frac{G_T}{2}\int_{-\infty}^{\infty}\frac{D_L^0 D_R^0 + \frac{D_L^z D_R^z}{4}}{4k_B T \cosh^2\left(\frac{E}{2k_B T}\right)}\mathrm{d}E[(V_L^\uparrow + V_L^\downarrow) - (V_R^\uparrow + V_R^\downarrow)] \\
&+\frac{G_T P}{4e}\int_{-\infty}^{\infty}\frac{E(D_L^0 D_R^z + D_L^z D_R^0)}{4k_B T \cosh^2\left(\frac{E}{2k_B T}\right)}\mathrm{d}E\frac{[(T_L^\uparrow + T_L^\downarrow) - (T_R^\uparrow + T_R^\downarrow)]}{T} \\
&+\frac{G_T P}{2}\int_{-\infty}^{\infty}\frac{D_L^0 D_R^0 + \frac{D_L^z D_R^z}{4}}{4k_B T \cosh^2\left(\frac{E}{2k_B T}\right)}\mathrm{d}E[(V_L^\uparrow - V_L^\downarrow) - (V_R^\uparrow - V_R^\downarrow)] \\
&+\frac{G_T}{4e}\int_{-\infty}^{\infty}\frac{E(D_L^0 D_R^z + D_L^z D_R^0)}{4k_B T \cosh^2\left(\frac{E}{2k_B T}\right)}\mathrm{d}E\frac{[(T_L^\uparrow - T_L^\downarrow) - (T_R^\uparrow - T_R^\downarrow)]}{T}.
\end{aligned} \qquad (A.15)$$

## A.2 Heat current

The heat current crosses the barrier from the left-hand-side to the right-hand-side electrode. Allowing $T_j^\sigma = T$ and $V_j^\sigma = V = 0$ following the differentiation of $F_j^\sigma$ causes

$$\varepsilon^0 = \frac{E + E}{2} = E \qquad (A.16)$$

$$\varepsilon^z = E - E = 0, \qquad (A.17)$$

and

$$
\begin{aligned}
\dot{Q} = \frac{1}{e^2} \int_{-\infty}^{\infty} E \Bigg\{ &\left( G_T F^0 + \frac{G_T P}{2} F^z \right) \left( D_L^0 D_R^0 + \frac{1}{4} D_L^z D_R^z \right) \\
&+ \frac{1}{2} \left( \frac{1}{2} G_T F^z + G_T P F^0 \right) \left( D_L^0 D_R^z + D_L^z D_R^0 \right) \Bigg\} \mathrm{d}E.
\end{aligned}
$$

(A.18)

One should note the extra asymmetric factor $E$, as this affects which parts of the expressions end up equaling zero. Performing the expansion yields

$$
\frac{\mathrm{d}\dot{Q}}{\mathrm{d}V_L^\uparrow}(V_L^\uparrow - V_{L,0}^\uparrow) = \int_{-\infty}^{\infty} \mathrm{d}E \left[ \frac{G_T}{4e} \frac{E(D_L^0 D_R^z + D_L^z D_R^0)}{4k_B T \cosh^2\left(\frac{E}{2k_B T}\right)} + \frac{G_T P}{4e} \frac{E(D_L^0 D_R^z + D_L^z D_R^0)}{4k_B T \cosh^2\left(\frac{E}{2k_B T}\right)} \right] (V_L^\uparrow - V_{L,0}^\uparrow)
$$

(A.19)

$$
\frac{\mathrm{d}\dot{Q}}{\mathrm{d}V_L^\downarrow}(V_L^\downarrow - V_{L,0}^\downarrow) = \int_{-\infty}^{\infty} \mathrm{d}E \left[ -\frac{G_T}{4e} \frac{E(D_L^0 D_R^z + D_L^z D_R^0)}{4k_B T \cosh^2\left(\frac{E}{2k_B T}\right)} + \frac{G_T P}{4e} \frac{E(D_L^0 D_R^z + D_L^z D_R^0)}{4k_B T \cosh^2\left(\frac{E}{2k_B T}\right)} \right] (V_L^\downarrow - V_{L,0}^\downarrow)
$$

(A.20)

$$
\frac{\mathrm{d}\dot{Q}}{\mathrm{d}V_R^\uparrow}(V_R^\uparrow - V_{R,0}^\uparrow) = \int_{-\infty}^{\infty} \mathrm{d}E \left[ -\frac{G_T}{4e} \frac{E(D_L^0 D_R^z + D_L^z D_R^0)}{4k_B T \cosh^2\left(\frac{E}{2k_B T}\right)} - \frac{G_T P}{4e} \frac{E(D_L^0 D_R^z + D_L^z D_R^0)}{4k_B T \cosh^2\left(\frac{E}{2k_B T}\right)} \right] (V_R^\uparrow - V_{R,0}^\uparrow)
$$

(A.21)

$$
\frac{\mathrm{d}\dot{Q}}{\mathrm{d}V_R^\downarrow}(V_R^\downarrow - V_{R,0}^\downarrow) = \int_{-\infty}^{\infty} \mathrm{d}E \left[ \frac{G_T}{4e} \frac{E(D_L^0 D_R^z + D_L^z D_R^0)}{4k_B T \cosh^2\left(\frac{E}{2k_B T}\right)} - \frac{G_T P}{4e} \frac{E(D_L^0 D_R^z + D_L^z D_R^0)}{4k_B T \cosh^2\left(\frac{E}{2k_B T}\right)} \right] (V_R^\downarrow - V_{R,0}^\downarrow)
$$

(A.22)

and

$$
\frac{\mathrm{d}\dot{Q}}{\mathrm{d}T_L^\uparrow}(T_L^\uparrow - T_{L,0}^\uparrow) = \int_{-\infty}^{\infty} \mathrm{d}E \left[ \frac{G_T}{2e^2} \frac{E^2\left(D_L^0 D_R^0 + \frac{D_L^z D_R^z}{4}\right)}{4k_B T^2 \cosh^2\left(\frac{E}{2k_B T}\right)} + \frac{G_T P}{2e^2} \frac{E^2\left(D_L^0 D_R^0 + \frac{D_L^z D_R^z}{4}\right)}{4k_B T^2 \cosh^2\left(\frac{E}{2k_B T}\right)} \right] (T_L^\uparrow - T_{L,0}^\uparrow)
$$

(A.23)

$$
\frac{\mathrm{d}\dot{Q}}{\mathrm{d}T_L^\downarrow}(T_L^\downarrow - T_{L,0}^\downarrow) = \int_{-\infty}^{\infty} \mathrm{d}E \left[ \frac{G_T}{2e^2} \frac{E^2\left(D_L^0 D_R^0 + \frac{D_L^z D_R^z}{4}\right)}{4k_B T^2 \cosh^2\left(\frac{E}{2k_B T}\right)} - \frac{G_T P}{2e^2} \frac{E^2\left(D_L^0 D_R^0 + \frac{D_L^z D_R^z}{4}\right)}{4k_B T^2 \cosh^2\left(\frac{E}{2k_B T}\right)} \right] (T_L^\downarrow - T_{L,0}^\downarrow)
$$

(A.24)

$$
\frac{\mathrm{d}\dot{Q}}{\mathrm{d}T_R^\uparrow}(T_R^\uparrow - T_{R,0}^\uparrow) = \int_{-\infty}^{\infty} \mathrm{d}E \left[ -\frac{G_T}{2e^2} \frac{E^2\left(D_L^0 D_R^0 + \frac{D_L^z D_R^z}{4}\right)}{4k_B T^2 \cosh^2\left(\frac{E}{2k_B T}\right)} - \frac{G_T P}{2e^2} \frac{E^2\left(D_L^0 D_R^0 + \frac{D_L^z D_R^z}{4}\right)}{4k_B T^2 \cosh^2\left(\frac{E}{2k_B T}\right)} \right] (T_R^\uparrow - T_{R,0}^\uparrow)
$$

(A.25)

$$
\frac{\mathrm{d}\dot{Q}}{\mathrm{d}T_R^\downarrow}(T_R^\downarrow - T_{R,0}^\downarrow) = \int_{-\infty}^{\infty} \mathrm{d}E \left[ -\frac{G_T}{2e^2} \frac{E^2\left(D_L^0 D_R^0 + \frac{D_L^z D_R^z}{4}\right)}{4k_B T^2 \cosh^2\left(\frac{E}{2k_B T}\right)} + \frac{G_T P}{2e^2} \frac{E^2\left(D_L^0 D_R^0 + \frac{D_L^z D_R^z}{4}\right)}{4k_B T^2 \cosh^2\left(\frac{E}{2k_B T}\right)} \right] (T_R^\downarrow - T_{R,0}^\downarrow).
$$

(A.26)

Defining $(V_{j,0}^\sigma, T_{j,0}^\sigma) = (0, T)$ results in the final heat current becoming

$$\dot{Q} = \frac{G_T P}{4e} \int_{-\infty}^{\infty} \frac{E(D_L^0 D_R^z + D_L^z D_R^0)}{4k_B T \cosh^2\left(\frac{E}{2k_B T}\right)} \mathrm{d}E[(V_L^\uparrow + V_L^\downarrow) - (V_R^\uparrow + V_R^\downarrow)]$$

$$+ \frac{G_T}{2e^2} \int_{-\infty}^{\infty} \frac{E^2\left(D_L^0 D_R^0 + \frac{D_L^z D_R^z}{4}\right)}{4k_B T \cosh^2\left(\frac{E}{2k_B T}\right)} \mathrm{d}E \frac{[(T_L^\uparrow + T_L^\downarrow) - (T_R^\uparrow + T_R^\downarrow)]}{T}$$

$$+ \frac{G_T}{4e} \int_{-\infty}^{\infty} \frac{E(D_L^0 D_R^z + D_L^z R_R^0)}{4k_B T \cosh^2\left(\frac{E}{2k_B T}\right)} \mathrm{d}E[(V_L^\uparrow - V_L^\downarrow) - (V_R^\uparrow - V_R^\downarrow)]$$

$$+ \frac{G_T P}{2e^2} \int_{-\infty}^{\infty} \frac{E^2\left(D_L^0 D_R^0 + \frac{D_L^z D_R^z}{4}\right)}{4k_B T \cosh^2\left(\frac{E}{2k_B T}\right)} \mathrm{d}E \frac{[(T_L^\uparrow - T_L^\downarrow) - (T_R^\uparrow - T_R^\downarrow)]}{T}. \tag{A.27}$$

## A.3 Spin current

Performing the differentiations and applying the same assumptions to the spin current yields

$$\frac{\mathrm{d}I_s}{\mathrm{d}V_L^\uparrow}(V_L^\uparrow - V_{L,0}^\uparrow) = \int_{-\infty}^{\infty} \mathrm{d}E \left[ \frac{G_T P}{2} \frac{D_L^0 D_R^0 + \frac{D_L^z D_R^z}{4}}{4k_B T \cosh^2\left(\frac{E}{2k_B T}\right)} + \frac{G_T}{2} \frac{D_L^0 D_R^0 + \frac{D_L^z D_R^z}{4}}{4k_B T \cosh^2\left(\frac{E}{2k_B T}\right)} \right](V_L^\uparrow - V_{L,0}^\uparrow) \tag{A.28}$$

$$\frac{\mathrm{d}I_s}{\mathrm{d}V_L^\downarrow}(V_L^\downarrow - V_{L,0}^\downarrow) = \int_{-\infty}^{\infty} \mathrm{d}E \left[ \frac{G_T P}{2} \frac{D_L^0 D_R^0 + \frac{D_L^z D_R^z}{4}}{4k_B T \cosh^2\left(\frac{E}{2k_B T}\right)} - \frac{G_T}{2} \frac{D_L^0 D_R^0 + \frac{D_L^z D_R^z}{4}}{4k_B T \cosh^2\left(\frac{E}{2k_B T}\right)} \right](V_L^\downarrow - V_{L,0}^\downarrow) \tag{A.29}$$

$$\frac{\mathrm{d}I_s}{\mathrm{d}V_R^\uparrow}(V_R^\uparrow - V_{R,0}^\uparrow) = \int_{-\infty}^{\infty} \mathrm{d}E \left[ -\frac{G_T P}{2} \frac{D_L^0 D_R^0 + \frac{D_L^z D_R^z}{4}}{4k_B T \cosh^2\left(\frac{E}{2k_B T}\right)} - \frac{G_T}{2} \frac{D_L^0 D_R^0 + \frac{D_L^z D_R^z}{4}}{4k_B T \cosh^2\left(\frac{E}{2k_B T}\right)} \right](V_R^\uparrow - V_{R,0}^\uparrow) \tag{A.30}$$

$$\frac{\mathrm{d}I_s}{\mathrm{d}V_R^\downarrow}(V_R^\downarrow - V_{R,0}^\downarrow) = \int_{-\infty}^{\infty} \mathrm{d}E \left[ -\frac{G_T P}{2} \frac{D_L^0 D_R^0 + \frac{D_L^z D_R^z}{4}}{4k_B T \cosh^2\left(\frac{E}{2k_B T}\right)} + \frac{G_T}{2} \frac{D_L^0 D_R^0 + \frac{D_L^z D_R^z}{4}}{4k_B T \cosh^2\left(\frac{E}{2k_B T}\right)} \right](V_R^\downarrow - V_{R,0}^\downarrow) \tag{A.31}$$

and

$$\frac{\mathrm{d}I_s}{\mathrm{d}T_L^\uparrow}(T_L^\uparrow - T_{L,0}^\uparrow) = \int_{-\infty}^{\infty} \mathrm{d}E \left[ \frac{G_T P}{4e} \frac{E(D_L^0 D_R^z + D_L^z D_R^0)}{4k_B T^2 \cosh^2\left(\frac{E}{2k_B T}\right)} + \frac{G_T}{4e} \frac{E(D_L^0 D_R^z + D_L^z D_R^0)}{4k_B T^2 \cosh^2\left(\frac{E}{2k_B T}\right)} \right] (T_L^\uparrow - T_{L,0}^\uparrow) \quad \text{(A.32)}$$

$$\frac{\mathrm{d}I_s}{\mathrm{d}T_L^\downarrow}(T_L^\downarrow - T_{L,0}^\downarrow) = \int_{-\infty}^{\infty} \mathrm{d}E \left[ -\frac{G_T P}{4e} \frac{E(D_L^0 D_R^z + D_L^z D_R^0)}{4k_B T^2 \cosh^2\left(\frac{E}{2k_B T}\right)} + \frac{G_T}{4e} \frac{E(D_L^0 D_R^z + D_L^z D_R^0)}{4k_B T^2 \cosh^2\left(\frac{E}{2k_B T}\right)} \right] (T_L^\downarrow - T_{L,0}^\downarrow) \quad \text{(A.33)}$$

$$\frac{\mathrm{d}I_s}{\mathrm{d}T_R^\uparrow}(T_R^\uparrow - T_{R,0}^\uparrow) = \int_{-\infty}^{\infty} \mathrm{d}E \left[ -\frac{G_T P}{4e} \frac{E(D_L^0 D_R^z + D_L^z D_R^0)}{4k_B T^2 \cosh^2\left(\frac{E}{2k_B T}\right)} - \frac{G_T}{4e} \frac{E(D_L^0 D_R^z + D_L^z D_R^0)}{4k_B T^2 \cosh^2\left(\frac{E}{2k_B T}\right)} \right] (T_R^\uparrow - T_{R,0}^\uparrow) \quad \text{(A.34)}$$

$$\frac{\mathrm{d}I_s}{\mathrm{d}T_R^\downarrow}(T_R^\downarrow - T_{R,0}^\downarrow) = \int_{-\infty}^{\infty} \mathrm{d}E \left[ \frac{G_T P}{4e} \frac{E(D_L^0 D_R^z + D_L^z D_R^0)}{4k_B T^2 \cosh^2\left(\frac{E}{2k_B T}\right)} - \frac{G_T}{4e} \frac{E(D_L^0 D_R^z + D_L^z D_R^0)}{4k_B T^2 \cosh^2\left(\frac{E}{2k_B T}\right)} \right] (T_R^\downarrow - T_{R,0}^\downarrow). \quad \text{(A.35)}$$

Defining $(V_{j,0}^\sigma, T_{j,0}^\sigma) = (0, T)$, the spin current becomes

$$\begin{aligned}
I_s = {} & \frac{G_T P}{2} \int_{-\infty}^{\infty} \frac{D_L^0 D_R^0 + \frac{D_L^z D_R^z}{4}}{4k_B T \cosh^2\left(\frac{E}{2k_B T}\right)} \mathrm{d}E [(V_L^\uparrow + V_L^\downarrow) - (V_R^\uparrow + V_R^\downarrow)] \\
& + \frac{G_T}{4e} \int_{-\infty}^{\infty} \frac{E(D_L^0 D_R^z + D_L^z D_R^0)}{4k_B T \cosh^2\left(\frac{E}{2k_B T}\right)} \mathrm{d}E \frac{[(T_L^\uparrow + T_L^\downarrow) - (T_R^\uparrow + T_R^\downarrow)]}{T} \\
& + \frac{G_T}{2} \int_{-\infty}^{\infty} \frac{D_L^0 D_R^0 + \frac{D_L^z D_R^z}{4}}{4k_B T \cosh^2\left(\frac{E}{2k_B T}\right)} \mathrm{d}E [(V_L^\uparrow - V_L^\downarrow) - (V_R^\uparrow - V_R^\downarrow)] \\
& + \frac{G_T P}{4e} \int_{-\infty}^{\infty} \frac{E(D_L^0 D_R^z + D_L^z D_R^0)}{4k_B T \cosh^2\left(\frac{E}{2k_B T}\right)} \mathrm{d}E \frac{[(T_L^\uparrow - T_L^\downarrow) - (T_R^\uparrow - T_R^\downarrow)]}{T}.
\end{aligned} \quad \text{(A.36)}$$

## A.4  Spin heat current

Now we can differentiate the spin heat current with respect to each of the variables $T_j^\sigma$ and $V_j^\sigma$, followed by allowing $T_{j,0}^\sigma = T$ and $V_{j,0}^\sigma = V = 0$. Once again,

$$\varepsilon^0 = E \quad \text{(A.37)}$$

$$\varepsilon^z = 0, \quad \text{(A.38)}$$

and

$$
\dot{Q}_s = \frac{1}{2e^2} \int_{-\infty}^{\infty} E \Bigg\{ \Big( G_T F^z + 2 G_T P F^z \Big) \Big( D_L^0 D_R^0 + \frac{1}{4} D_L^z D_R^z \Big)
$$
$$
+ \Big( G_T F^0 + \frac{G_T P}{2} F^z \Big) \Big( D_L^0 D_R^z + D_L^z D_R^0 \Big) \Bigg\} dE.
$$

(A.39)

One should again note the extra asymmetric factor $E$, as this affects which parts of the expressions end up equaling zero. Performing the expansion yields

$$
\frac{d\dot{Q}_s}{dV_L^\uparrow} (V_L^\uparrow - V_{L,0}^\uparrow) = \int_{-\infty}^{\infty} dE \left[ \frac{G_T P}{4e} \frac{E(D_L^0 D_R^z + D_L^z D_R^0)}{4 k_B T \cosh^2\left(\frac{E}{2k_B T}\right)} + \frac{G_T}{4e} \frac{E(D_L^0 D_R^z + D_L^z D_R^0)}{4 k_B T \cosh^2\left(\frac{E}{2k_B T}\right)} \right] (V_L^\uparrow - V_{L,0}^\uparrow)
$$

(A.40)

$$
\frac{d\dot{Q}_s}{dV_L^\downarrow} (V_L^\downarrow - V_{L,0}^\downarrow) = \int_{-\infty}^{\infty} dE \left[ - \frac{G_T P}{4e} \frac{E(D_L^0 D_R^z + D_L^z D_R^0)}{4 k_B T \cosh^2\left(\frac{E}{2k_B T}\right)} + \frac{G_T}{4e} \frac{E(D_L^0 D_R^z + D_L^z D_R^0)}{4 k_B T \cosh^2\left(\frac{E}{2k_B T}\right)} \right] (V_L^\downarrow - V_{L,0}^\downarrow)
$$

(A.41)

$$
\frac{d\dot{Q}_s}{dV_R^\uparrow} (V_R^\uparrow - V_{R,0}^\uparrow) = \int_{-\infty}^{\infty} dE \left[ - \frac{G_T P}{4e} \frac{E(D_L^0 D_R^z + D_L^z D_R^0)}{4 k_B T \cosh^2\left(\frac{E}{2k_B T}\right)} - \frac{G_T}{4e} \frac{E(D_L^0 D_R^z + D_L^z D_R^0)}{4 k_B T \cosh^2\left(\frac{E}{2k_B T}\right)} \right] (V_R^\uparrow - V_{R,0}^\uparrow)
$$

(A.42)

$$
\frac{d\dot{Q}_s}{dV_R^\downarrow} (V_R^\downarrow - V_{R,0}^\downarrow) = \int_{-\infty}^{\infty} dE \left[ \frac{G_T P}{4e} \frac{E(D_L^0 D_R^z + D_L^z D_R^0)}{4 k_B T \cosh^2\left(\frac{E}{2k_B T}\right)} - \frac{G_T}{4e} \frac{E(D_L^0 D_R^z + D_L^z D_R^0)}{4 k_B T \cosh^2\left(\frac{E}{2k_B T}\right)} \right] (V_R^\downarrow - V_{R,0}^\downarrow)
$$

(A.43)

and

$$
\frac{d\dot{Q}_s}{dT_L^\uparrow} (T_L^\uparrow - T_{L,0}^\uparrow) = \int_{-\infty}^{\infty} dE \left[ \frac{G_T P}{2e^2} \frac{E^2\left(D_L^0 D_R^0 + \frac{D_L^z D_R^z}{4}\right)}{4 k_B T^2 \cosh^2\left(\frac{E}{2k_B T}\right)} + \frac{G_T}{2e^2} \frac{E^2\left(D_L^0 D_R^0 + \frac{D_L^z D_R^z}{4}\right)}{4 k_B T^2 \cosh^2\left(\frac{E}{2k_B T}\right)} \right] (T_L^\uparrow - T_{L,0}^\uparrow)
$$

(A.44)

$$
\frac{d\dot{Q}_s}{dT_L^\downarrow} (T_L^\downarrow - T_{L,0}^\downarrow) = \int_{-\infty}^{\infty} dE \left[ \frac{G_T P}{2e^2} \frac{E^2\left(D_L^0 D_R^0 + \frac{D_L^z D_R^z}{4}\right)}{4 k_B T^2 \cosh^2\left(\frac{E}{2k_B T}\right)} - \frac{G_T}{2e^2} \frac{E^2\left(D_L^0 D_R^0 + \frac{D_L^z D_R^z}{4}\right)}{4 k_B T^2 \cosh^2\left(\frac{E}{2k_B T}\right)} \right] (T_L^\downarrow - T_{L,0}^\downarrow)
$$

(A.45)

$$
\frac{d\dot{Q}_s}{dT_R^\uparrow} (T_R^\uparrow - T_{R,0}^\uparrow) = \int_{-\infty}^{\infty} dE \left[ - \frac{G_T P}{2e^2} \frac{E^2\left(D_L^0 D_R^0 + \frac{D_L^z D_R^z}{4}\right)}{4 k_B T^2 \cosh^2\left(\frac{E}{2k_B T}\right)} - \frac{G_T}{2e^2} \frac{E^2\left(D_L^0 D_R^0 + \frac{D_L^z D_R^z}{4}\right)}{4 k_B T^2 \cosh^2\left(\frac{E}{2k_B T}\right)} \right] (T_R^\uparrow - T_{R,0}^\uparrow)
$$

(A.46)

$$
\frac{d\dot{Q}_s}{dT_R^\downarrow} (T_R^\downarrow - T_{R,0}^\downarrow) = \int_{-\infty}^{\infty} dE \left[ - \frac{G_T P}{2e^2} \frac{E^2\left(D_L^0 D_R^0 + \frac{D_L^z D_R^z}{4}\right)}{4 k_B T^2 \cosh^2\left(\frac{E}{2k_B T}\right)} + \frac{G_T}{2e^2} \frac{E^2\left(D_L^0 D_R^0 + \frac{D_L^z D_R^z}{4}\right)}{4 k_B T^2 \cosh^2\left(\frac{E}{2k_B T}\right)} \right] (T_R^\downarrow - T_{R,0}^\downarrow).
$$

(A.47)

Upon applying $(V_{j,0}^\sigma, T_{j,0}^\sigma) = (0, T)$, we obtain

$$\dot{Q}_s = \frac{G_T}{4e} \int_{-\infty}^{\infty} \frac{E(D_L^0 D_R^z + D_L^z D_R^0)}{4k_B T \cosh^2\left(\frac{E}{2k_B T}\right)} \mathrm{d}E[(V_L^\uparrow + V_L^\downarrow) - (V_R^\uparrow + V_R^\downarrow)]$$

$$+\frac{G_T P}{2e^2} \int_{-\infty}^{\infty} \frac{E^2\left(D_L^0 D_R^0 + \frac{D_L^z D_R^z}{4}\right)}{4k_B T \cosh^2\left(\frac{E}{2k_B T}\right)} \mathrm{d}E\frac{[(T_L^\uparrow + T_L^\downarrow) - (T_R^\uparrow + T_R^\downarrow)]}{T}$$

$$+\frac{G_T P}{4e} \int_{-\infty}^{\infty} \frac{E(D_L^0 D_R^z + D_L^z R_R^0)}{4k_B T \cosh^2\left(\frac{E}{2k_B T}\right)} \mathrm{d}E[(V_L^\uparrow - V_L^\downarrow) - (V_R^\uparrow - V_R^\downarrow)]$$

$$+\frac{G_T}{2e^2} \int_{-\infty}^{\infty} \frac{E^2\left(D_L^0 D_R^0 + \frac{D_L^z D_R^z}{4}\right)}{4k_B T \cosh^2\left(\frac{E}{2k_B T}\right)} \mathrm{d}E\frac{[(T_L^\uparrow - T_L^\downarrow) - (T_R^\uparrow - T_R^\downarrow)]}{T}$$

(A.48)

for the spin heat current.

# Appendix B

# Quasiclassical approach to thermoelectric effects for arbitrary spin-dependent fields

Deriving the quasiclassical thermoelectric coefficients for tunneling in spin-split superconducting hybrids with general polarization structures is an extensive process. Consequently, the main outline of this derivation can be found here instead of in the main thesis body. What is included here is not the Taylor expansions, but the complete expressions for the commutator terms of all the currents. The Taylor expansions are directly extracted from these.

## B.1    Charge current

The charge current to the right of a fully polarized barrier is

$$
I_q = \frac{1}{16e} \int_{-\infty}^{\infty} \mathrm{d}E \, \mathrm{Tr}\{\hat{\rho}_3 [G_0 \check{g}_L + G_{MR}\{\check{\kappa}, \check{g}_L\} + G_1 \check{\kappa}\check{g}_L\check{\kappa} - iG_\phi \check{\kappa}', \check{g}_R]^K\}, \qquad (B.1)
$$

where the interface parameters are defined by

$$
G_0 = NG_q\tau(1 + \sqrt{1 - P^2}), \qquad G_1 = NG_q\tau(1 - \sqrt{1 - P^2}) \qquad (B.2)
$$

$$
G_{MR} = NG_q\tau P, \qquad\qquad G_\phi = 2G_q\sum_n^N \theta_{nn}. \qquad (B.3)
$$

**First term**

The first commutator term is

$$I_{BC1} = \frac{G_0}{16e} \int_{-\infty}^{\infty} \mathrm{d}E \, \mathrm{Tr}\{\hat{\rho}_3 [\check{\boldsymbol{g}}_L \check{\boldsymbol{g}}_R - \check{\boldsymbol{g}}_R \check{\boldsymbol{g}}_L]^K\}, \tag{B.4}$$

where

$$[\check{\boldsymbol{g}}_L, \check{\boldsymbol{g}}_R]^K = \hat{\boldsymbol{g}}_L^R \hat{\boldsymbol{g}}_R^K + \hat{\boldsymbol{g}}_L^K \hat{\boldsymbol{g}}_R^A - \hat{\boldsymbol{g}}_R^R \hat{\boldsymbol{g}}_L^K - \hat{\boldsymbol{g}}_R^K \hat{\boldsymbol{g}}_L^A. \tag{B.5}$$

Using the relations 5.16 and 5.17 we can consider the first term of the charge current

$$I_{BC1} = \frac{G_0}{16e} \int_{-\infty}^{\infty} \mathrm{d}E \, \mathrm{Tr}\left\{ \hat{\rho}_3 \Big( \hat{\boldsymbol{g}}_L^R (\hat{\boldsymbol{g}}_R^R \hat{\boldsymbol{h}}_R + \hat{\boldsymbol{h}}_R \hat{\rho}_3 \hat{\boldsymbol{g}}_R^{R\dagger} \hat{\rho}_3) - (\hat{\boldsymbol{g}}_L^R \hat{\boldsymbol{h}}_L + \hat{\boldsymbol{h}}_L \hat{\rho}_3 \hat{\boldsymbol{g}}_L^{R\dagger} \hat{\rho}_3) \hat{\rho}_3 \hat{\boldsymbol{g}}_R^{R\dagger} \hat{\rho}_3 \right. $$
$$\left. -\hat{\boldsymbol{g}}_R^R (\hat{\boldsymbol{g}}_L^R \hat{\boldsymbol{h}}_L + \hat{\boldsymbol{h}}_L \hat{\rho}_3 \hat{\boldsymbol{g}}_L^{R\dagger} \hat{\rho}_3) + (\hat{\boldsymbol{g}}_R^R \hat{\boldsymbol{h}}_R + \hat{\boldsymbol{h}}_R \hat{\rho}_3 \hat{\boldsymbol{g}}_R^{R\dagger} \hat{\rho}_3) \hat{\rho}_3 \hat{\boldsymbol{g}}_L^{R\dagger} \hat{\rho}_3 \Big) \right\}, \tag{B.6}$$

or

$$I_{BC1} = \frac{G_0}{16e} \int_{-\infty}^{\infty} \mathrm{d}E \, \mathrm{Tr}\left\{ \hat{\boldsymbol{h}}_R \hat{\rho}_3 \Big( \hat{\boldsymbol{g}}_L \hat{\boldsymbol{g}}_R + \hat{\boldsymbol{g}}_R^\dagger \hat{\boldsymbol{g}}_L^\dagger + \hat{\boldsymbol{g}}_R^\dagger \hat{\boldsymbol{g}}_L + \hat{\boldsymbol{g}}_L^\dagger \hat{\boldsymbol{g}}_R \Big) \right. $$
$$\left. -\hat{\boldsymbol{h}}_L \hat{\rho}_3 \Big( \hat{\boldsymbol{g}}_R \hat{\boldsymbol{g}}_L + \hat{\boldsymbol{g}}_L^\dagger \hat{\boldsymbol{g}}_R^\dagger + \hat{\boldsymbol{g}}_R^\dagger \hat{\boldsymbol{g}}_L + \hat{\boldsymbol{g}}_L^\dagger \hat{\boldsymbol{g}}_R \Big) \right\}. \tag{B.7}$$

Choosing $\hat{\boldsymbol{h}}_L = \tanh\left(\frac{\beta_L E}{2}\right)\hat{\boldsymbol{1}}$, assuming a normal metal electrode on the right by defining $\hat{\boldsymbol{g}}_R = \hat{\boldsymbol{g}}_{\mathrm{NM}} = \hat{\rho}_3$, and using the cyclical property of the trace along with $\hat{\rho}_3\hat{\rho}_3 = \hat{\boldsymbol{1}}$, this simplifies to

$$I_{BC1} = \frac{G_0}{16e} \int_{-\infty}^{\infty} \mathrm{d}E \, \mathrm{Tr}\left\{ \hat{\boldsymbol{h}}_R [\hat{\rho}_3 (\hat{\boldsymbol{g}}_L + \hat{\boldsymbol{g}}_L^\dagger)\hat{\rho}_3 + \hat{\boldsymbol{g}}_L + \hat{\boldsymbol{g}}_L^\dagger] - 2\tanh\left(\frac{\beta_L E}{2}\right)(\hat{\boldsymbol{g}}_L + \hat{\boldsymbol{g}}_L^\dagger) \right\}. \tag{B.8}$$

When the tunneling barrier is non-polarized, and $P = 0$, this term determines the entire charge current as the other three commutator terms disappear.

**Second term**

The second term in the boundary condition equation for the charge current is

$$\text{Tr}\left\{ \hat{\rho}_3 G_{MR} \Big[ \{\check{\boldsymbol{\kappa}}, \check{\boldsymbol{g}}_L\}, \check{\boldsymbol{g}}_R \Big]^K \right\} = G_{MR} \text{Tr}\left\{ \hat{\rho}_3 (\check{\boldsymbol{\kappa}}\check{\boldsymbol{g}}_L\check{\boldsymbol{g}}_R + \check{\boldsymbol{g}}_L\check{\boldsymbol{\kappa}}\check{\boldsymbol{g}}_R - \check{\boldsymbol{g}}_R\check{\boldsymbol{\kappa}}\check{\boldsymbol{g}}_L - \check{\boldsymbol{g}}_R\check{\boldsymbol{g}}_L\check{\boldsymbol{\kappa}})^K \right\},$$
(B.9)

which becomes

$$\text{Tr}\left\{ \hat{\rho}_3 G_{MR} \Big[ \{\check{\boldsymbol{\kappa}}, \check{\boldsymbol{g}}_L\}, \check{\boldsymbol{g}}_R \Big]^K \right\} = G_{MR} \text{Tr}\left\{ \hat{\rho}_3 \Big( \hat{\sigma}_z \hat{\boldsymbol{g}}_L^R \hat{\boldsymbol{g}}_R^K + \hat{\sigma}_z \hat{\boldsymbol{g}}_L^K \hat{\boldsymbol{g}}_R^A + \hat{\boldsymbol{g}}_L^R \hat{\sigma}_z \hat{\boldsymbol{g}}_R^K + \hat{\boldsymbol{g}}_L^K \hat{\sigma}_z \hat{\boldsymbol{g}}_R^A \right.$$
$$\left. - \hat{\boldsymbol{g}}_R^R \hat{\sigma}_z \hat{\boldsymbol{g}}_L^K - \hat{\boldsymbol{g}}_R^K \hat{\sigma}_z \hat{\boldsymbol{g}}_L^A - \hat{\boldsymbol{g}}_R^R \hat{\boldsymbol{g}}_L^K \hat{\sigma}_z - \hat{\boldsymbol{g}}_R^K \hat{\boldsymbol{g}}_L^A \hat{\sigma}_z \Big) \right\}.$$
(B.10)

Now, the general second current term becomes

$$I_{BC2} = \frac{G_{MR}}{16e} \int_{-\infty}^{\infty} \mathrm{d}E \, \text{Tr}\left\{ \hat{\boldsymbol{h}}_R \Big( \hat{\rho}_3\hat{\sigma}_z\hat{\boldsymbol{g}}_L\hat{\boldsymbol{g}}_R + \hat{\rho}_3\hat{\boldsymbol{g}}_R^\dagger\hat{\sigma}_z\hat{\boldsymbol{g}}_L + \hat{\rho}_3\hat{\boldsymbol{g}}_L\hat{\sigma}_z\hat{\boldsymbol{g}}_R + \hat{\rho}_3\hat{\boldsymbol{g}}_R^\dagger\hat{\boldsymbol{g}}_L\hat{\sigma}_z \right.$$
$$+ \hat{\sigma}_z\hat{\rho}_3\hat{\boldsymbol{g}}_L^\dagger\hat{\boldsymbol{g}}_R + \hat{\rho}_3\hat{\boldsymbol{g}}_R^\dagger\hat{\sigma}_z\hat{\boldsymbol{g}}_L^\dagger + \hat{\rho}_3\hat{\boldsymbol{g}}_L^\dagger\hat{\sigma}_z\hat{\boldsymbol{g}}_R + \hat{\rho}_3\hat{\boldsymbol{g}}_R^\dagger\hat{\boldsymbol{g}}_L^\dagger\hat{\sigma}_z \Big)$$
$$- \hat{\boldsymbol{h}}_L \Big( \hat{\rho}_3\hat{\boldsymbol{g}}_R^\dagger\hat{\sigma}_z\hat{\boldsymbol{g}}_L + \hat{\rho}_3\hat{\boldsymbol{g}}_L^\dagger\hat{\boldsymbol{g}}_R^\dagger\hat{\sigma}_z + \hat{\sigma}_z\hat{\rho}_3\hat{\boldsymbol{g}}_R^\dagger\hat{\boldsymbol{g}}_L + \hat{\rho}_3\hat{\boldsymbol{g}}_L^\dagger\hat{\sigma}_z\hat{\boldsymbol{g}}_R^\dagger \right.$$
$$\left. + \hat{\rho}_3\hat{\boldsymbol{g}}_R\hat{\sigma}_z\hat{\boldsymbol{g}}_L + \hat{\rho}_3\hat{\boldsymbol{g}}_L^\dagger\hat{\boldsymbol{g}}_R\hat{\sigma}_z + \hat{\sigma}_z\hat{\rho}_3\hat{\boldsymbol{g}}_R\hat{\boldsymbol{g}}_L + \hat{\rho}_3\hat{\boldsymbol{g}}_L^\dagger\hat{\sigma}_z\hat{\boldsymbol{g}}_R \Big) \right\}.$$
(B.11)

Applying the definitions, we arrive at

$$I_{BC2} = \frac{G_{MR}}{16e} \int_{-\infty}^{\infty} \mathrm{d}E \, \text{Tr}\left\{ \hat{\boldsymbol{h}}_R \Big[ \hat{\sigma}_z(\hat{\boldsymbol{g}}_L + \hat{\boldsymbol{g}}_L^\dagger) + (\hat{\boldsymbol{g}}_L + \hat{\boldsymbol{g}}_L^\dagger)\hat{\sigma}_z + \hat{\rho}_3(\hat{\sigma}_z\hat{\boldsymbol{g}}_L + \hat{\boldsymbol{g}}_L\hat{\sigma}_z + \hat{\boldsymbol{g}}_L^\dagger\hat{\sigma}_z)\hat{\rho}_3 \right.$$
$$\left. + \hat{\sigma}_z\hat{\rho}_3\hat{\boldsymbol{g}}_L^\dagger\hat{\rho}_3 \Big] - 4\tanh\left(\frac{\beta_L E}{2}\right) \Big[ \hat{\sigma}_z(\hat{\boldsymbol{g}}_L + \hat{\boldsymbol{g}}_L^\dagger) \Big] \right\}.$$
(B.12)

**Third term**

The third commutator term is

$$G_1[\check{\boldsymbol{\kappa}}\check{\boldsymbol{g}}_L\check{\boldsymbol{\kappa}}, \check{\boldsymbol{g}}_R]^K, \tag{B.13}$$

where

$$\check{\boldsymbol{\kappa}}\check{\boldsymbol{g}}_L\check{\boldsymbol{\kappa}} = \begin{pmatrix} \hat{\sigma}_z\hat{\boldsymbol{g}}_L^R\hat{\sigma}_z & \hat{\sigma}_z\hat{\boldsymbol{g}}_L^K\hat{\sigma}_z \\ 0 & \hat{\sigma}_z\hat{\boldsymbol{g}}_L^A\hat{\sigma}_z \end{pmatrix}. \tag{B.14}$$

Now,

$$G_1\operatorname{Tr}\left\{\hat{\rho}_3[\check{\boldsymbol{\kappa}}\check{\boldsymbol{g}}_L\check{\boldsymbol{\kappa}}, \check{\boldsymbol{g}}_R]^K\right\} = G_1\operatorname{Tr}\left\{\hat{\rho}_3\Big(\hat{\sigma}_z\hat{\boldsymbol{g}}_L^R\hat{\sigma}_z\hat{\boldsymbol{g}}_R^K + \hat{\sigma}_z\hat{\boldsymbol{g}}_L^K\hat{\sigma}_z\hat{\boldsymbol{g}}_R^A \right.$$
$$\left. -\hat{\boldsymbol{g}}_R^R\hat{\sigma}_z\hat{\boldsymbol{g}}_L^K\hat{\sigma}_z - \hat{\boldsymbol{g}}_R^K\hat{\sigma}_z\hat{\boldsymbol{g}}_L^A\hat{\sigma}_z\Big)\right\}, \tag{B.15}$$

which finally results in

$$I_{BC3} = \frac{G_1}{16e}\int_{-\infty}^{\infty}\mathrm{d}E\operatorname{Tr}\left\{\hat{\boldsymbol{h}}_R\Big(\hat{\rho}_3\hat{\sigma}_z\hat{\boldsymbol{g}}_L\hat{\sigma}_z\hat{\boldsymbol{g}}_R + \hat{\rho}_3\hat{\boldsymbol{g}}_R^\dagger\hat{\sigma}_z\hat{\boldsymbol{g}}_L\hat{\sigma}_z + \hat{\sigma}_z\hat{\rho}_3\hat{\boldsymbol{g}}_L^\dagger\hat{\sigma}_z\hat{\boldsymbol{g}}_R + \hat{\rho}_3\hat{\boldsymbol{g}}_R^\dagger\hat{\sigma}_z\hat{\boldsymbol{g}}_L^\dagger\hat{\sigma}_z\Big)\right.$$
$$\left. -\hat{\boldsymbol{h}}_L\Big(\hat{\sigma}_z\hat{\rho}_3\hat{\boldsymbol{g}}_R^\dagger\hat{\sigma}_z\hat{\boldsymbol{g}}_L + \hat{\rho}_3\hat{\boldsymbol{g}}_L^\dagger\hat{\sigma}_z\hat{\boldsymbol{g}}_R^\dagger\hat{\sigma}_z + \hat{\sigma}_z\hat{\rho}_3\hat{\boldsymbol{g}}_R\hat{\sigma}_z\hat{\boldsymbol{g}}_L + \hat{\rho}_3\hat{\boldsymbol{g}}_L^\dagger\hat{\sigma}_z\hat{\boldsymbol{g}}_R\hat{\sigma}_z\Big)\right\}. \tag{B.16}$$

Assuming a normal metal on the right and using $\hat{\rho}_3\hat{\sigma}_z = \hat{\sigma}_z\hat{\rho}_3$, the third commutator term for the quasiparticle charge current is

$$I_{BC3} = \frac{G_1}{16e}\int_{-\infty}^{\infty}\mathrm{d}E\operatorname{Tr}\left\{\hat{\boldsymbol{h}}_R\Big[\hat{\sigma}_z(\hat{\boldsymbol{g}}_L + \hat{\boldsymbol{g}}_L^\dagger)\hat{\sigma}_z + \hat{\rho}_3\hat{\sigma}_z(\hat{\boldsymbol{g}}_L + \hat{\boldsymbol{g}}_L^\dagger)\hat{\sigma}_z\hat{\rho}_3\Big] \right.$$
$$\left. -2\tanh\Big(\frac{\beta_L E}{2}\Big)\Big[\hat{\boldsymbol{g}}_L + \hat{\boldsymbol{g}}_L^\dagger\Big]\right\}. \tag{B.17}$$

**Fourth term**

The fourth and last term in the boundary condition is

$$-iG_\phi[\check{\boldsymbol{\kappa}}, \check{\boldsymbol{g}}_R]^K. \tag{B.18}$$

We consider

$$\text{Tr}\{\hat{\rho}_3[\check{\boldsymbol{\kappa}}, \check{\boldsymbol{g}}_R]^K\} = \text{Tr}\{\hat{\rho}_3(\hat{\sigma}_z\hat{\boldsymbol{g}}_R^K - \hat{\boldsymbol{g}}_R^K\hat{\sigma}_z)\} \tag{B.19}$$

$$= \text{Tr}\{\hat{\rho}_3\hat{\sigma}_z\hat{\boldsymbol{g}}_R^K - \hat{\rho}_3\hat{\boldsymbol{g}}_R^K\hat{\sigma}_z\} \tag{B.20}$$

$$= \text{Tr}\{\hat{\rho}_3\hat{\sigma}_z\hat{\boldsymbol{g}}_R^K - \hat{\sigma}_z\hat{\rho}_3\hat{\boldsymbol{g}}_R^K\} \tag{B.21}$$

$$= 0 \tag{B.22}$$

as $\hat{\rho}_3\hat{\sigma}_z = \hat{\sigma}_z\hat{\rho}_3$. Consequently, this term does not contribute to the charge current when the tunneling barrier is polarized in the $+\boldsymbol{z}$-direction.

## B.2  Spin current

The spin current to the right of the tunneling barrier is defined by

$$I_s^\nu = \frac{\hbar}{32e^2} \int_{-\infty}^{\infty} \mathrm{d}E \, \text{Tr}\{\hat{\rho}_3\hat{\tau}_\nu[G_0\check{\boldsymbol{g}}_L + G_{MR}\{\check{\boldsymbol{\kappa}}, \check{\boldsymbol{g}}_L\} + G_1\check{\boldsymbol{\kappa}}\check{\boldsymbol{g}}_L\check{\boldsymbol{\kappa}} - iG_\phi\check{\boldsymbol{\kappa}}', \check{\boldsymbol{g}}_R]^K\}. \tag{B.23}$$

**First term**

The first commutator term in the spin current boundary condition is

$$G_0[\check{\boldsymbol{g}}_L, \check{\boldsymbol{g}}_R]^K, \tag{B.24}$$

so the first spin current term is

$$I_s^\nu|_{BC1} = \frac{G_0\hbar}{32e^2} \int_{-\infty}^{\infty} \mathrm{d}E \, \text{Tr}\left\{\hat{\rho}_3\hat{\tau}_\nu\Big[\hat{\boldsymbol{g}}_L\hat{\boldsymbol{g}}_R\hat{\boldsymbol{h}}_R + \hat{\boldsymbol{g}}_L\hat{\boldsymbol{h}}_R\hat{\rho}_3\hat{\boldsymbol{g}}_R^\dagger\hat{\rho}_3 + \hat{\boldsymbol{g}}_R\hat{\boldsymbol{h}}_R\hat{\rho}_3\hat{\boldsymbol{g}}_L^\dagger\hat{\rho}_3 + \hat{\boldsymbol{h}}_R\hat{\rho}_3\hat{\boldsymbol{g}}_R^\dagger\hat{\boldsymbol{g}}_L^\dagger\hat{\rho}_3\right.$$
$$\left. - \Big(\hat{\boldsymbol{g}}_L\hat{\boldsymbol{h}}_L\hat{\rho}_3\hat{\boldsymbol{g}}_R^\dagger\hat{\rho}_3 + \hat{\boldsymbol{h}}_L\hat{\rho}_3\hat{\boldsymbol{g}}_L^\dagger\hat{\boldsymbol{g}}_R^\dagger\hat{\rho}_3 + \hat{\boldsymbol{g}}_R\hat{\boldsymbol{g}}_L\hat{\boldsymbol{h}}_L + \hat{\boldsymbol{g}}_R\hat{\boldsymbol{h}}_L\hat{\rho}_3\hat{\boldsymbol{g}}_L^\dagger\hat{\rho}_3\Big)\Big]\right\}. \tag{B.25}$$

Approximating,

$$I_s^\nu|_{BC1} = \frac{G_0\hbar}{32e^2} \int_{-\infty}^{\infty} \mathrm{d}E \, \text{Tr}\left\{\hat{\rho}_3\hat{\tau}_\nu\Big[\hat{\boldsymbol{g}}_L\hat{\rho}_3\hat{\boldsymbol{h}}_R + \hat{\boldsymbol{g}}_L\hat{\boldsymbol{h}}_R\hat{\rho}_3 + \hat{\rho}_3\hat{\boldsymbol{h}}_R\hat{\rho}_3\hat{\boldsymbol{g}}_L^\dagger\hat{\rho}_3 + \hat{\boldsymbol{h}}_R\hat{\boldsymbol{g}}_L^\dagger\hat{\rho}_3\right.$$
$$\left. - \tanh\left(\frac{\beta_L E}{2}\right)\Big(\hat{\boldsymbol{g}}_L\hat{\rho}_3 + \hat{\rho}_3\hat{\boldsymbol{g}}_L^\dagger + \hat{\rho}_3\hat{\boldsymbol{g}}_L + \hat{\boldsymbol{g}}_L^\dagger\hat{\rho}_3\Big)\Big]\right\}. \tag{B.26}$$

**Second term**

The second term in the boundary condition is

$$G_{MR}[\{\check{\boldsymbol{\kappa}},\check{\boldsymbol{g}}_L\},\check{\boldsymbol{g}}_R]^K, \tag{B.27}$$

so the second spin current term is

$$
\begin{aligned}
I_s^\nu|_{BC2} = \frac{G_{MR}\hbar}{32e^2}\int_{-\infty}^{\infty}\mathrm{d}E\,\mathrm{Tr}\Big\{\hat{\rho}_3\hat{\tau}_\nu\Big[&\hat{\sigma}_z\hat{\boldsymbol{g}}_L\hat{\boldsymbol{g}}_R\hat{\boldsymbol{h}}_R + \hat{\sigma}_z\hat{\boldsymbol{g}}_L\hat{\boldsymbol{h}}_R\hat{\rho}_3\hat{\boldsymbol{g}}_R^\dagger\hat{\rho}_3 + \hat{\boldsymbol{g}}_L\hat{\sigma}_z\hat{\boldsymbol{g}}_R\hat{\boldsymbol{h}}_R \\
&+\hat{\boldsymbol{g}}_L\hat{\sigma}_z\hat{\boldsymbol{h}}_R\hat{\rho}_3\hat{\boldsymbol{g}}_R^\dagger\hat{\rho}_3 + \hat{\boldsymbol{g}}_R\hat{\boldsymbol{h}}_R\hat{\sigma}_z\hat{\rho}_3\hat{\boldsymbol{g}}_L^\dagger\hat{\rho}_3 + \hat{\boldsymbol{h}}_R\hat{\rho}_3\hat{\boldsymbol{g}}_R^\dagger\hat{\sigma}_z\hat{\boldsymbol{g}}_L^\dagger\hat{\rho}_3 + \hat{\boldsymbol{g}}_R\hat{\boldsymbol{h}}_R\hat{\rho}_3\hat{\boldsymbol{g}}_L^\dagger\hat{\rho}_3\hat{\sigma}_z \\
&+\hat{\boldsymbol{h}}_R\hat{\rho}_3\hat{\boldsymbol{g}}_R^\dagger\hat{\boldsymbol{g}}_L^\dagger\hat{\rho}_3\hat{\sigma}_z - \Big(\hat{\sigma}_z\hat{\boldsymbol{g}}_L\hat{\boldsymbol{h}}_L\hat{\rho}_3\hat{\boldsymbol{g}}_R^\dagger\hat{\rho}_3 + \hat{\sigma}_z\hat{\boldsymbol{h}}_L\hat{\rho}_3\hat{\boldsymbol{g}}_L^\dagger\hat{\boldsymbol{g}}_R^\dagger\hat{\rho}_3 + \hat{\boldsymbol{g}}_L\hat{\boldsymbol{h}}_L\hat{\sigma}_z\hat{\rho}_3\hat{\boldsymbol{g}}_R^\dagger\hat{\rho}_3 \\
+\hat{\boldsymbol{h}}_L\hat{\rho}_3\hat{\boldsymbol{g}}_L^\dagger\hat{\sigma}_z\hat{\boldsymbol{g}}_R^\dagger\hat{\rho}_3 &+ \hat{\boldsymbol{g}}_R\hat{\sigma}_z\hat{\boldsymbol{g}}_L\hat{\boldsymbol{h}}_L + \hat{\boldsymbol{g}}_R\hat{\sigma}_z\hat{\boldsymbol{h}}_L\hat{\rho}_3\hat{\boldsymbol{g}}_L^\dagger\hat{\rho}_3 + \hat{\boldsymbol{g}}_R\hat{\boldsymbol{g}}_L\hat{\boldsymbol{h}}_L\hat{\sigma}_z + \hat{\boldsymbol{g}}_R\hat{\boldsymbol{h}}_L\hat{\rho}_3\hat{\boldsymbol{g}}_L^\dagger\hat{\rho}_3\hat{\sigma}_z\Big)\Big]\Big\}.
\end{aligned}
\tag{B.28}
$$

Applying the definitions for $\hat{\boldsymbol{h}}_L$ and $\hat{\boldsymbol{g}}_R$ outlined above leaves us with

$$
\begin{aligned}
I_s^\nu|_{BC2} = \frac{G_{MR}\hbar}{32e^2}\int_{-\infty}^{\infty}\mathrm{d}E\,\mathrm{Tr}\Big\{\hat{\rho}_3\hat{\tau}_\nu\Big[&\hat{\sigma}_z\hat{\boldsymbol{g}}_L\hat{\rho}_3\hat{\boldsymbol{h}}_R + \hat{\sigma}_z\hat{\boldsymbol{g}}_L\hat{\boldsymbol{h}}_R\hat{\rho}_3 + \hat{\boldsymbol{g}}_L\hat{\sigma}_z\hat{\rho}_3\hat{\boldsymbol{h}}_R + \hat{\boldsymbol{g}}_L\hat{\sigma}_z\hat{\boldsymbol{h}}_R\hat{\rho}_3 \\
&+\hat{\rho}_3\hat{\boldsymbol{h}}_R\hat{\sigma}_z\hat{\rho}_3\hat{\boldsymbol{g}}_L^\dagger\hat{\rho}_3 + \hat{\boldsymbol{h}}_R\hat{\sigma}_z\hat{\boldsymbol{g}}_L^\dagger\hat{\rho}_3 + \hat{\rho}_3\hat{\boldsymbol{h}}_R\hat{\rho}_3\hat{\boldsymbol{g}}_L^\dagger\hat{\rho}_3\hat{\sigma}_z + \hat{\boldsymbol{h}}_R\hat{\boldsymbol{g}}_L^\dagger\hat{\rho}_3\hat{\sigma}_z \\
&-\tanh\!\left(\frac{\beta_L E}{2}\right)\Big(\hat{\sigma}_z\hat{\boldsymbol{g}}_L\hat{\rho}_3 + \hat{\sigma}_z\hat{\rho}_3\hat{\boldsymbol{g}}_L^\dagger + \hat{\boldsymbol{g}}_L\hat{\sigma}_z\hat{\rho}_3 + \hat{\rho}_3\hat{\boldsymbol{g}}_L^\dagger\hat{\sigma}_z \\
&\qquad+\hat{\rho}_3\hat{\sigma}_z\hat{\boldsymbol{g}}_L + \hat{\sigma}_z\hat{\boldsymbol{g}}_L^\dagger\hat{\rho}_3 + \hat{\rho}_3\hat{\boldsymbol{g}}_L\hat{\sigma}_z + \hat{\boldsymbol{g}}_L^\dagger\hat{\rho}_3\hat{\sigma}_z\Big)\Big]\Big\}.
\end{aligned}
\tag{B.29}
$$

**Third term**

The third commutator term of the spin current is

$$
\begin{aligned}
I_s^\nu|_{BC3} &= \frac{\hbar G_1}{32e^2}\int_{-\infty}^{\infty}\mathrm{d}E\,\mathrm{Tr}\Big\{\hat{\rho}_3\hat{\tau}_\nu[\check{\boldsymbol{\kappa}}\check{\boldsymbol{g}}_L\check{\boldsymbol{\kappa}},\check{\boldsymbol{g}}_R]^K\Big\} \tag{B.30} \\
&= \frac{\hbar G_1}{32e^2}\int_{-\infty}^{\infty}\mathrm{d}E\,\mathrm{Tr}\Big\{\hat{\rho}_3\hat{\tau}_\nu[\hat{\sigma}_z\hat{\boldsymbol{g}}_L^R\hat{\sigma}_z\hat{\boldsymbol{g}}_R^K + \hat{\sigma}_z\hat{\boldsymbol{g}}_L^K\hat{\sigma}_z\hat{\boldsymbol{g}}_R^A - \hat{\boldsymbol{g}}_R^R\hat{\sigma}_z\hat{\boldsymbol{g}}_L^K\hat{\sigma}_z - \hat{\boldsymbol{g}}_R^K\hat{\sigma}_z\hat{\boldsymbol{g}}_L^A\hat{\sigma}_z]\Big\},
\end{aligned}
\tag{B.31}
$$

which becomes

$$I_s^\nu|_{BC3} = \frac{\hbar G_1}{32e^2} \int_{-\infty}^{\infty} \mathrm{d}E\, \mathrm{Tr}\Bigg\{ \hat{\rho}_3\hat{\tau}_\nu\Big[\hat{\sigma}_z\hat{\boldsymbol{g}}_L\hat{\sigma}_z\hat{\boldsymbol{g}}_R\hat{\boldsymbol{h}}_R + \hat{\sigma}_z\hat{\boldsymbol{g}}_L\hat{\sigma}_z\hat{\boldsymbol{h}}_R\hat{\rho}_3\hat{\boldsymbol{g}}_R^\dagger\hat{\rho}_3$$

$$+\hat{\boldsymbol{g}}_R\hat{\boldsymbol{h}}_R\hat{\sigma}_z\hat{\rho}_3\hat{\boldsymbol{g}}_L^\dagger\hat{\rho}_3\hat{\sigma}_z + \hat{\boldsymbol{h}}_R\hat{\rho}_3\hat{\boldsymbol{g}}_R^\dagger\hat{\sigma}_z\hat{\boldsymbol{g}}_L^\dagger\hat{\rho}_3\hat{\sigma}_z$$

$$-(\hat{\sigma}_z\hat{\boldsymbol{g}}_L\hat{\boldsymbol{h}}_L\hat{\sigma}_z\hat{\rho}_3\hat{\boldsymbol{g}}_R^\dagger\hat{\rho}_3 + \hat{\sigma}_z\hat{\boldsymbol{h}}_L\hat{\rho}_3\hat{\boldsymbol{g}}_L^\dagger\hat{\sigma}_z\hat{\boldsymbol{g}}_R^\dagger\hat{\rho}_3 + \hat{\boldsymbol{g}}_R\hat{\sigma}_z\hat{\boldsymbol{g}}_L\hat{\boldsymbol{h}}_L\hat{\sigma}_z + \hat{\boldsymbol{g}}_R\hat{\sigma}_z\hat{\boldsymbol{h}}_L\hat{\rho}_3\hat{\boldsymbol{g}}_L^\dagger\hat{\rho}_3\hat{\sigma}_z)\Big]\Bigg\}.$$

$$(\text{B.32})$$

When $\hat{\boldsymbol{h}}_L = \tanh\left(\frac{\beta_L E}{2}\right)$ and $\hat{\boldsymbol{g}}_R = \hat{\rho}_3$,

$$I_s^\nu|_{BC3} = \frac{\hbar G_1}{32e^2} \int_{-\infty}^{\infty} \mathrm{d}E\, \mathrm{Tr}\Bigg\{ \hat{\rho}_3\hat{\tau}_\nu\Big[\hat{\sigma}_z\hat{\boldsymbol{g}}_L\hat{\sigma}_z\hat{\rho}_3\hat{\boldsymbol{h}}_R + \hat{\sigma}_z\hat{\boldsymbol{g}}_L\hat{\sigma}_z\hat{\boldsymbol{h}}_R\hat{\rho}_3 + \hat{\rho}_3\hat{\boldsymbol{h}}_R\hat{\sigma}_z\hat{\rho}_3\hat{\boldsymbol{g}}_L^\dagger\hat{\rho}_3\hat{\sigma}_z$$

$$+\hat{\boldsymbol{h}}_R\hat{\sigma}_z\hat{\boldsymbol{g}}_L^\dagger\hat{\rho}_3\hat{\sigma}_z - \tanh\left(\frac{\beta_L E}{2}\right)(\hat{\sigma}_z\hat{\boldsymbol{g}}_L\hat{\sigma}_z\hat{\rho}_3 + \hat{\sigma}_z\hat{\rho}_3\hat{\boldsymbol{g}}_L^\dagger\hat{\sigma}_z + \hat{\rho}_3\hat{\sigma}_z\hat{\boldsymbol{g}}_L\hat{\sigma}_z + \hat{\sigma}_z\hat{\boldsymbol{g}}_L^\dagger\hat{\rho}_3\hat{\sigma}_z)\Big]\Bigg\}.$$

$$(\text{B.33})$$

The **x**-directional component of the third spin current commutator term is

$$I_s^x|_{BC3} = \frac{\hbar G_1}{32e^2} \int_{-\infty}^{\infty} \mathrm{d}E\, \mathrm{Tr}\Bigg\{ \hat{\boldsymbol{h}}_R\Big[\hat{\rho}_3\hat{\sigma}_x\hat{\sigma}_z\hat{\boldsymbol{g}}_L\hat{\sigma}_z\hat{\boldsymbol{g}}_R + \hat{\rho}_3\hat{\boldsymbol{g}}_R^\dagger\hat{\sigma}_x\hat{\sigma}_z\hat{\boldsymbol{g}}_L\hat{\sigma}_z$$

$$+\hat{\sigma}_z\hat{\rho}_3\hat{\boldsymbol{g}}_L^\dagger\hat{\sigma}_z\hat{\sigma}_x\hat{\boldsymbol{g}}_R + \hat{\rho}_3\hat{\boldsymbol{g}}_R^\dagger\hat{\sigma}_z\hat{\boldsymbol{g}}_L^\dagger\hat{\sigma}_z\hat{\sigma}_x\Big] - \tanh\left(\frac{\beta_L E}{2}\right)\Big[\hat{\sigma}_x\hat{\sigma}_z\hat{\boldsymbol{g}}_L\hat{\sigma}_z\hat{\rho}_3\hat{\boldsymbol{g}}_R^\dagger + \hat{\sigma}_z\hat{\rho}_3\hat{\sigma}_x\hat{\boldsymbol{g}}_R\hat{\sigma}_z\hat{\boldsymbol{g}}_L$$

$$+\hat{\sigma}_x\hat{\sigma}_z\hat{\rho}_3\hat{\boldsymbol{g}}_L^\dagger\hat{\sigma}_z\hat{\boldsymbol{g}}_R^\dagger + \hat{\sigma}_z\hat{\sigma}_x\hat{\boldsymbol{g}}_R\hat{\sigma}_z\hat{\rho}_3\hat{\boldsymbol{g}}_L^\dagger\Big]\Bigg\},$$

$$(\text{B.34})$$

becoming

$$I_s^x|_{BC3} = \frac{\hbar G_1}{32e^2} \int_{-\infty}^{\infty} \mathrm{d}E\, \mathrm{Tr}\Bigg\{ \hat{\boldsymbol{h}}_R\Big[\hat{\rho}_3\hat{\sigma}_x\hat{\sigma}_z\hat{\boldsymbol{g}}_L\hat{\sigma}_z\hat{\rho}_3 + \hat{\sigma}_x\hat{\sigma}_z\hat{\boldsymbol{g}}_L\hat{\sigma}_z + \hat{\sigma}_z\hat{\rho}_3\hat{\boldsymbol{g}}_L^\dagger\hat{\sigma}_z\hat{\sigma}_x\hat{\rho}_3 + \hat{\sigma}_z\hat{\boldsymbol{g}}_L^\dagger\hat{\sigma}_z\hat{\sigma}_x\Big]$$

$$+2\tanh\left(\frac{\beta_L E}{2}\right)\Big[\hat{\sigma}_x\hat{\boldsymbol{g}}_L + \hat{\sigma}_x\hat{\boldsymbol{g}}_L^\dagger\Big]\Bigg\}.$$

$$(\text{B.35})$$

In the other two directions, we get

$$
\begin{aligned}
I_s^y|_{BC3} = \frac{\hbar G_1}{32e^2} \int_{-\infty}^{\infty} \mathrm{d}E\, \mathrm{Tr} \bigg\{ \hat{\boldsymbol{h}}_R \Big[ &\hat{\rho}_3 \hat{\sigma}_y \hat{\sigma}_z \hat{\boldsymbol{g}}_L \hat{\sigma}_z \hat{\boldsymbol{g}}_R + \hat{\rho}_3 \hat{\boldsymbol{g}}_R^\dagger \hat{\sigma}_y \hat{\sigma}_z \hat{\boldsymbol{g}}_L \hat{\sigma}_z \\
+ \hat{\sigma}_z \hat{\rho}_3 \hat{\boldsymbol{g}}_L^\dagger \hat{\sigma}_z \hat{\sigma}_y \hat{\boldsymbol{g}}_R + \hat{\rho}_3 \hat{\boldsymbol{g}}_R^\dagger \hat{\sigma}_z \hat{\boldsymbol{g}}_L^\dagger \hat{\sigma}_z \hat{\sigma}_y \Big] - \tanh\!\left(\frac{\beta_L E}{2}\right) &\Big[ \hat{\sigma}_y \hat{\sigma}_z \hat{\boldsymbol{g}}_L \hat{\sigma}_z \hat{\rho}_3 \hat{\boldsymbol{g}}_R^\dagger + \hat{\sigma}_z \hat{\rho}_3 \hat{\sigma}_y \hat{\boldsymbol{g}}_R \hat{\sigma}_z \hat{\boldsymbol{g}}_L \\
&+ \hat{\sigma}_y \hat{\sigma}_z \hat{\rho}_3 \hat{\boldsymbol{g}}_L^\dagger \hat{\sigma}_z \hat{\boldsymbol{g}}_R^\dagger + \hat{\sigma}_z \hat{\sigma}_y \hat{\boldsymbol{g}}_R \hat{\sigma}_z \hat{\rho}_3 \hat{\boldsymbol{g}}_L^\dagger \Big] \bigg\},
\end{aligned}
\tag{B.36}
$$

$$
\begin{aligned}
I_s^y|_{BC3} = \frac{\hbar G_1}{32e^2} \int_{-\infty}^{\infty} \mathrm{d}E\, \mathrm{Tr} \bigg\{ \hat{\boldsymbol{h}}_R \Big[ &\hat{\rho}_3 \hat{\sigma}_y \hat{\sigma}_z \hat{\boldsymbol{g}}_L \hat{\sigma}_z \hat{\rho}_3 + \hat{\sigma}_y \hat{\sigma}_z \hat{\boldsymbol{g}}_L \hat{\sigma}_z + \hat{\sigma}_z \hat{\rho}_3 \hat{\boldsymbol{g}}_L^\dagger \hat{\sigma}_z \hat{\sigma}_y \hat{\rho}_3 + \hat{\sigma}_z \hat{\boldsymbol{g}}_L^\dagger \hat{\sigma}_z \hat{\sigma}_y \Big] \\
&+ 2\tanh\!\left(\frac{\beta_L E}{2}\right) \Big[ \hat{\sigma}_y \hat{\boldsymbol{g}}_L + \hat{\sigma}_y \hat{\boldsymbol{g}}_L^\dagger \Big] \bigg\},
\end{aligned}
\tag{B.37}
$$

$$
\begin{aligned}
I_s^z|_{BC3} = \frac{\hbar G_1}{32e^2} \int_{-\infty}^{\infty} \mathrm{d}E\, \mathrm{Tr} \bigg\{ \hat{\boldsymbol{h}}_R \Big[ &\hat{\rho}_3 \hat{\boldsymbol{g}}_L \hat{\sigma}_z \hat{\boldsymbol{g}}_R + \hat{\rho}_3 \hat{\boldsymbol{g}}_R^\dagger \hat{\boldsymbol{g}}_L \hat{\sigma}_z + \hat{\sigma}_z \hat{\rho}_3 \hat{\boldsymbol{g}}_L^\dagger \hat{\boldsymbol{g}}_R + \hat{\rho}_3 \hat{\boldsymbol{g}}_R^\dagger \hat{\sigma}_z \hat{\boldsymbol{g}}_L^\dagger \Big] \\
&- \tanh\!\left(\frac{\beta_L E}{2}\right) \Big[ \hat{\sigma}_z \hat{\rho}_3 \hat{\boldsymbol{g}}_R^\dagger \hat{\boldsymbol{g}}_L + \hat{\rho}_3 \hat{\boldsymbol{g}}_R \hat{\sigma}_z \hat{\boldsymbol{g}}_L + \hat{\boldsymbol{g}}_L^\dagger \hat{\sigma}_z \hat{\boldsymbol{g}}_R^\dagger \hat{\rho}_3 + \hat{\sigma}_z \hat{\rho}_3 \hat{\boldsymbol{g}}_L^\dagger \hat{\boldsymbol{g}}_R \Big] \bigg\},
\end{aligned}
\tag{B.38}
$$

and

$$
\begin{aligned}
I_s^z|_{BC3} = \frac{\hbar G_1}{32e^2} \int_{-\infty}^{\infty} \mathrm{d}E\, \mathrm{Tr} \bigg\{ \hat{\boldsymbol{h}}_R \Big[ &\hat{\rho}_3 \hat{\boldsymbol{g}}_L \hat{\sigma}_z \hat{\rho}_3 + \hat{\boldsymbol{g}}_L \hat{\sigma}_z + \hat{\sigma}_z \hat{\rho}_3 \hat{\boldsymbol{g}}_L^\dagger \hat{\rho}_3 + \hat{\sigma}_z \hat{\boldsymbol{g}}_L^\dagger \Big] \\
&- 2\tanh\!\left(\frac{\beta_L E}{2}\right) \Big[ \hat{\sigma}_z \hat{\boldsymbol{g}}_L + \hat{\boldsymbol{g}}_L^\dagger \hat{\sigma}_z \Big] \bigg\}.
\end{aligned}
\tag{B.39}
$$

**Fourth term**

The fourth spin current commutator term is

$$
-\left[iG_\phi \check{\boldsymbol{\kappa}}, \check{\boldsymbol{g}}_R\right]^K = -iG_\phi (\hat{\sigma}_z \hat{\boldsymbol{g}}_R^K - \hat{\boldsymbol{g}}_R^K \hat{\sigma}_z),
\tag{B.40}
$$

so

$$I_{s,R}^{\nu}|_{BC4} = -iG_\varphi \frac{\hbar}{32e^2} \int_{-\infty}^{\infty} dE \, \mathrm{Tr}\{\hat{\rho}_3 \hat{\tau}_\nu [\check{\boldsymbol{\kappa}}, \check{\boldsymbol{g}}_R]^K\} \tag{B.41}$$

$$= -iG_\varphi \frac{\hbar}{32e^2} \int_{-\infty}^{\infty} dE \, \mathrm{Tr}\{\hat{\rho}_3 \hat{\tau}_\nu (\hat{\sigma}_z \hat{g}_R^K - \hat{g}_R^K \hat{\sigma}_z)\} \tag{B.42}$$

$$= -iG_\varphi \frac{\hbar}{32e^2} \int_{-\infty}^{\infty} dE \, \mathrm{Tr} \left\{ \hat{\rho}_3 \hat{\tau}_\nu \left( \hat{\sigma}_z \hat{g}_R^R \hat{h}_R + \hat{\sigma}_z \hat{h}_R \hat{\rho}_3 \hat{g}_R^{R\dagger} \hat{\rho}_3 - \hat{g}_R^R \hat{h}_R \hat{\sigma}_z - \hat{h}_R \hat{\rho}_3 \hat{g}_R^{R\dagger} \hat{\rho}_3 \hat{\sigma}_z \right) \right\}. \tag{B.43}$$

Applying the simplification $\hat{\boldsymbol{g}}_R = \hat{\rho}_3$, this becomes

$$I_{s,R}^{\nu}|_{BC4} = -iG_\varphi \frac{\hbar}{32e^2} \int_{-\infty}^{\infty} dE \, \mathrm{Tr} \left\{ \hat{\rho}_3 \hat{\tau}_\nu \left( \hat{\sigma}_z \hat{\rho}_3 \hat{h}_R + \hat{\sigma}_z \hat{h}_R \hat{\rho}_3 - \hat{\rho}_3 \hat{h}_R \hat{\sigma}_z - \hat{h}_R \hat{\rho}_3 \hat{\sigma}_z \right) \right\}. \tag{B.44}$$

The general components of the spin current vector are

$$I_{s,R}^{x}|_{BC4} = -iG_\varphi \frac{\hbar}{32e^2} \int_{-\infty}^{\infty} dE \, \mathrm{Tr}\{\hat{\rho}_3 \hat{\sigma}_x [\check{\boldsymbol{\kappa}}, \check{\boldsymbol{g}}_R]^K\} \tag{B.45}$$

$$= -iG_\varphi \frac{\hbar}{16e^2} \int_{-\infty}^{\infty} dE \, \mathrm{Tr}\{\hat{\rho}_3 \hat{\sigma}_x \hat{\sigma}_z \hat{g}_R^R \hat{h}_R + \hat{\sigma}_x \hat{\sigma}_z \hat{h}_R \hat{\rho}_3 \hat{g}_R^{R\dagger}\} \tag{B.46}$$

$$I_{s,R}^{y}|_{BC4} = -iG_\varphi \frac{\hbar}{32e^2} \int_{-\infty}^{\infty} dE \, \mathrm{Tr}\{\hat{\rho}_3 \hat{\sigma}_y [\check{\boldsymbol{\kappa}}, \check{\boldsymbol{g}}_R]^K\} \tag{B.47}$$

$$= -iG_\varphi \frac{\hbar}{16e^2} \int_{-\infty}^{\infty} dE \, \mathrm{Tr}\{\hat{\rho}_3 \hat{\sigma}_y \hat{\sigma}_z \hat{g}_R^R \hat{h}_R + \hat{\sigma}_y \hat{\sigma}_z \hat{h}_R \hat{\rho}_3 \hat{g}_R^{R\dagger}\} \tag{B.48}$$

$$I_{s,R}^{z}|_{BC4} = -iG_\varphi \frac{\hbar}{32e^2} \int_{-\infty}^{\infty} dE \, \mathrm{Tr}\{\hat{\rho}_3 \hat{\sigma}_z [\check{\boldsymbol{\kappa}}, \check{\boldsymbol{g}}_R]^K\} \tag{B.49}$$

$$= -iG_\varphi \frac{\hbar}{32e^2} \int_{-\infty}^{\infty} dE \, \mathrm{Tr}\{\hat{\rho}_3 \hat{g}_R^R \hat{h}_R + \hat{h}_R \hat{\rho}_3 \hat{g}_R^{R\dagger} - \hat{\rho}_3 \hat{g}_R^R \hat{h}_R - \hat{h}_R \hat{\rho}_3 \hat{g}_R^{R\dagger}\} = 0, \tag{B.50}$$

leaving the end result when the right side is occupied by a normal metal to be

$$I_{s,R}^{x}|_{BC4} = -iG_\varphi \frac{\hbar}{16e^2} \int_{-\infty}^{\infty} dE 2 \, \mathrm{Tr}\{\hat{\sigma}_x \hat{\sigma}_z \hat{h}_R\} = 0 \tag{B.51}$$

$$I_{s,R}^{y}|_{BC4} = -iG_\varphi \frac{\hbar}{16e^2} \int_{-\infty}^{\infty} dE \, \mathrm{Tr}\{\hat{\sigma}_y \hat{\sigma}_z \hat{h}_R\} = 0 \tag{B.52}$$

$$I_{s,R}^{z}|_{BC4} = 0. \tag{B.53}$$

## B.3    Heat current

When $\mu_L = 0$, the heat current to the left of the barrier is defined by

$$
\dot{Q}_L = -\frac{1}{16e^2} \int_{-\infty}^{\infty} \mathrm{d}E\, E\, \mathrm{Tr}\left\{ [G_0 \check{\boldsymbol{g}}_R + G_{MR}\{\check{\boldsymbol{\kappa}}, \check{\boldsymbol{g}}_R\} + G_1 \check{\boldsymbol{\kappa}}\check{\boldsymbol{g}}_R\check{\boldsymbol{\kappa}} - iG_{\phi}\check{\boldsymbol{\kappa}}', \check{\boldsymbol{g}}_L]^K \right\}. \quad \text{(B.54)}
$$

The heat current commutator terms are

$$
\dot{Q}|_{BC1} = -\frac{G_0 \hbar}{16e^2} \int_{-\infty}^{\infty} \mathrm{d}E\, E\, \mathrm{Tr}\left\{ \hat{\boldsymbol{g}}_R \hat{\boldsymbol{g}}_L \hat{\boldsymbol{h}}_L + \hat{\boldsymbol{g}}_R \hat{\boldsymbol{h}}_L \hat{\rho}_3 \hat{\boldsymbol{g}}_L^{\dagger} \hat{\rho}_3 + \hat{\boldsymbol{g}}_L \hat{\boldsymbol{h}}_L \hat{\rho}_3 \hat{\boldsymbol{g}}_R^{\dagger} \hat{\rho}_3 + \hat{\boldsymbol{h}}_L \hat{\rho}_3 \hat{\boldsymbol{g}}_L^{\dagger} \hat{\boldsymbol{g}}_R^{\dagger} \hat{\rho}_3 \right.
$$
$$
\left. - \left( \hat{\boldsymbol{g}}_R \hat{\boldsymbol{h}}_R \hat{\rho}_3 \hat{\boldsymbol{g}}_L^{\dagger} \hat{\rho}_3 + \hat{\boldsymbol{h}}_R \hat{\rho}_3 \hat{\boldsymbol{g}}_R^{\dagger} \hat{\boldsymbol{g}}_L^{\dagger} \hat{\rho}_3 + \hat{\boldsymbol{g}}_L \hat{\boldsymbol{g}}_R \hat{\boldsymbol{h}}_R + \hat{\boldsymbol{g}}_L \hat{\boldsymbol{h}}_R \hat{\rho}_3 \hat{\boldsymbol{g}}_R^{\dagger} \hat{\rho}_3 \right) \right\}, 
$$
$$
\text{(B.55)}
$$

$$
\dot{Q}|_{BC2} = -\frac{G_{MR}\hbar}{16e^2} \int_{-\infty}^{\infty} \mathrm{d}E\, E\, \mathrm{Tr}\left\{ \hat{\sigma}_z \hat{\boldsymbol{g}}_R \hat{\boldsymbol{g}}_L \hat{\boldsymbol{h}}_L + \hat{\sigma}_z \hat{\boldsymbol{g}}_R \hat{\boldsymbol{h}}_L \hat{\rho}_3 \hat{\boldsymbol{g}}_L^{\dagger} \hat{\rho}_3 + \hat{\boldsymbol{g}}_R \hat{\sigma}_z \hat{\boldsymbol{g}}_L \hat{\boldsymbol{h}}_L \right.
$$
$$
+ \hat{\boldsymbol{g}}_R \hat{\sigma}_z \hat{\boldsymbol{h}}_L \hat{\rho}_3 \hat{\boldsymbol{g}}_L^{\dagger} \hat{\rho}_3 + \hat{\boldsymbol{g}}_L \hat{\boldsymbol{h}}_L \hat{\sigma}_z \hat{\rho}_3 \hat{\boldsymbol{g}}_R^{\dagger} \hat{\rho}_3 + \hat{\boldsymbol{h}}_L \hat{\rho}_3 \hat{\boldsymbol{g}}_L^{\dagger} \hat{\sigma}_z \hat{\boldsymbol{g}}_R^{\dagger} \hat{\rho}_3 + \hat{\boldsymbol{g}}_L \hat{\boldsymbol{h}}_L \hat{\rho}_3 \hat{\boldsymbol{g}}_R^{\dagger} \hat{\rho}_3 \hat{\sigma}_z
$$
$$
+ \hat{\boldsymbol{h}}_L \hat{\rho}_3 \hat{\boldsymbol{g}}_L^{\dagger} \hat{\boldsymbol{g}}_R^{\dagger} \hat{\rho}_3 \hat{\sigma}_z - \left( \hat{\sigma}_z \hat{\boldsymbol{g}}_R \hat{\boldsymbol{h}}_R \hat{\rho}_3 \hat{\boldsymbol{g}}_L^{\dagger} \hat{\rho}_3 + \hat{\sigma}_z \hat{\boldsymbol{h}}_R \hat{\rho}_3 \hat{\boldsymbol{g}}_R^{\dagger} \hat{\boldsymbol{g}}_L^{\dagger} \hat{\rho}_3 + \hat{\boldsymbol{g}}_R \hat{\boldsymbol{h}}_R \hat{\sigma}_z \hat{\rho}_3 \hat{\boldsymbol{g}}_L^{\dagger} \hat{\rho}_3 \right.
$$
$$
\left. \left. + \hat{\boldsymbol{h}}_R \hat{\rho}_3 \hat{\boldsymbol{g}}_R^{\dagger} \hat{\sigma}_z \hat{\boldsymbol{g}}_L^{\dagger} \hat{\rho}_3 + \hat{\boldsymbol{g}}_L \hat{\sigma}_z \hat{\boldsymbol{g}}_R \hat{\boldsymbol{h}}_R + \hat{\boldsymbol{g}}_L \hat{\sigma}_z \hat{\boldsymbol{h}}_R \hat{\rho}_3 \hat{\boldsymbol{g}}_R^{\dagger} \hat{\rho}_3 + \hat{\boldsymbol{g}}_L \hat{\boldsymbol{g}}_R \hat{\boldsymbol{h}}_R \hat{\sigma}_z + \hat{\boldsymbol{g}}_L \hat{\boldsymbol{h}}_R \hat{\rho}_3 \hat{\boldsymbol{g}}_R^{\dagger} \hat{\rho}_3 \hat{\sigma}_z \right) \right\},
$$
$$
\text{(B.56)}
$$

$$
\dot{Q}|_{BC3} = -\frac{G_1 \hbar}{16e^2} \int_{-\infty}^{\infty} \mathrm{d}E\, E\, \mathrm{Tr}\left\{ \hat{\sigma}_z \hat{\boldsymbol{g}}_R \hat{\sigma}_z \hat{\boldsymbol{g}}_L \hat{\boldsymbol{h}}_L + \hat{\sigma}_z \hat{\boldsymbol{g}}_R \hat{\sigma}_z \hat{\boldsymbol{h}}_L \hat{\rho}_3 \hat{\boldsymbol{g}}_L^{\dagger} \hat{\rho}_3 + \hat{\boldsymbol{g}}_L \hat{\boldsymbol{h}}_L \hat{\sigma}_z \hat{\rho}_3 \hat{\boldsymbol{g}}_R^{\dagger} \hat{\rho}_3 \hat{\sigma}_z \right.
$$
$$
+ \hat{\boldsymbol{h}}_L \hat{\rho}_3 \hat{\boldsymbol{g}}_L^{\dagger} \hat{\sigma}_z \hat{\boldsymbol{g}}_R^{\dagger} \hat{\rho}_3 \hat{\sigma}_z - ( \hat{\sigma}_z \hat{\boldsymbol{g}}_R \hat{\boldsymbol{h}}_R \hat{\sigma}_z \hat{\rho}_3 \hat{\boldsymbol{g}}_L^{\dagger} \hat{\rho}_3 + \hat{\sigma}_z \hat{\boldsymbol{h}}_R \hat{\rho}_3 \hat{\boldsymbol{g}}_R^{\dagger} \hat{\sigma}_z \hat{\boldsymbol{g}}_L^{\dagger} \hat{\rho}_3
$$
$$
\left. + \hat{\boldsymbol{g}}_L \hat{\sigma}_z \hat{\boldsymbol{g}}_R \hat{\boldsymbol{h}}_R \hat{\sigma}_z + \hat{\boldsymbol{g}}_L \hat{\sigma}_z \hat{\boldsymbol{h}}_R \hat{\rho}_3 \hat{\boldsymbol{g}}_R^{\dagger} \hat{\rho}_3 \hat{\sigma}_z ) \right\},
$$
$$
\text{(B.57)}
$$

and

$$
\dot{Q}|_{BC4} = iG_{\varphi} \frac{\hbar}{16e^2} \int_{-\infty}^{\infty} \mathrm{d}E\, E\, \mathrm{Tr}\left\{ \hat{\sigma}_z \hat{\boldsymbol{g}}_L \hat{\boldsymbol{h}}_L + \hat{\sigma}_z \hat{\boldsymbol{h}}_L \hat{\rho}_3 \hat{\boldsymbol{g}}_L^{\dagger} \hat{\rho}_3 - \hat{\boldsymbol{g}}_L \hat{\boldsymbol{h}}_L \hat{\sigma}_z - \hat{\boldsymbol{h}}_L \hat{\rho}_3 \hat{\boldsymbol{g}}_L^{\dagger} \hat{\rho}_3 \hat{\sigma}_z \right\} = 0.
$$
$$
\text{(B.58)}
$$

# Appendix C

# Fundamentals of the numerical procedure

MATLAB was employed to perform several crucial tasks throughout the course of this work. Every numerical consideration made has depended upon MATLAB. In this chapter, we will outline the methodology and highlight the essential MATLAB functions used for the completion of this task. Due to the different nature of the MATLAB programs, this chapter is split into three individual part. These will be presented in the same order as was employed for the rest of the thesis. First we will highlight the procedures used when calculating thermoelectric coefficients using the framework for homogeneously magnetized materials in the case when analytical expressions for the densities of states are readily attainable. Secondly, we will embark upon the process of describing how to quantify the thermoelectric effects when the densities of states are not known. This is the case when more complex structures than bulk materials are used. The procedure involves solving the Usadel equation for the different material systems followed by a numerical integration process based on a Riemann sum. The exact expressions being summed over differ depending on whether the formalism for homogeneous or arbitrary polarization is used.

## C.1 Analytical thermoelectric coefficients

The thermoelectric coefficients derived in Chapter 4 depend on the temperature, the quasiparticle energy in relation to the Fermi energy, and the spin-dependent densities of states for the material systems on each side of the junction. For this reason, in order to quantify thermoelectric effects in such structures the temperature must be defined and the densities of states be known. When these are obtainable purely through analytical expressions, the procedure to procuring the thermoelectric coefficients is fairly

straightforward. Throughout this thesis, only the densities of states for normal metals, superconductors, Zeeman-split superconductors and Josephson junctions of regular and Zeeman-split superconductors with $L_N \ll \xi$ have been definable analytically. Therefore, the self-consistent solution for the superconducting gap $\Delta$ defined in equation 2.9 must be implemented for all the Zeeman-split superconductors considered. We have achieved this by using the MATLAB function *fsolve* along with the initial guess of $\Delta(h_S, T) = \Delta_0$ when $h_S/\Delta_0 = 0$ and $T/T_{c,0} = 0.01$. When one side of the junction is occupied by non-split conventional superconductors the gap depends only on temperature as in equation 2.8.

First, we consider the bilayers (N/I/ZS, S/I/ZS, and ZS/I/ZS). The material-specific parameters to be defined are $\Gamma$ and the polarization $P$, along with starting and stopping energies and step lengths for temperature and exchange field. As temperature and applied exchange field are the easiest parameters to vary externally when considering a potential experiment, these are the ones we mainly consider. Defining vectors for these parameters, the thermoelectric coefficients $\alpha$, $G$ and $G_Q$ can now be computed using the MATLAB function *integral(function,xstart,xend)*. We define the thermoelectric coefficients to depend on energy using function handles, and integrate from $E_{\text{start}} = -3.5\Delta_0$ to $E_{\text{end}} = 3.5\Delta_0$. The Seebeck coefficient $S = -P\alpha/(GT)$ and thermoelectric figure of merit $ZT = (\frac{G_Q G}{(P\alpha)^2} - 1)^{-1}$ are calculated from $\alpha$, $G$ and $G_Q$, and the resulting three-dimensional MATLAB *surf plots* can be found in Chapter 4. For the more complex structures containing at least one Josephson junction, the superconducting phase difference becomes the main parameter to vary as this is manageable *in situ*. When only one Josephson junction is present we choose a value for the temperature $T/T_{c,0}$, and alter the spin-splitting field $h_S/\Delta_0$ and the superconducting phase difference $\Delta\theta$. When both sides are occupied by a Josephson junction we define the temperature and field, and vary both $\Delta\theta_L$ and $\Delta\theta_R$.

## C.2   Solving the Usadel equation

There are no analytical expressions sufficiently describing the density of states when more complex structures are being considered. Therefore we need to solve the Riccati-parametrized Usadel equation (Eq. 2.49) for $\underline{\gamma}$ and $\underline{\tilde{\gamma}}$ in order to determine $D^0(E)$ and $D^z(E)$, or $\hat{g}^R$. Depending on which formalism is applicable, either the densities of states or the Green functions are subsequently integrated to obtain the thermoelectric coefficients. This, again, depends on the spin polarization and electronic structure of the material system under consideration.

The Riccati-parametrized Usadel equation is a $2 \times 2$ matrix equation. As it is accompanied by different boundary conditions depending on interface transparency and polarization, this constitutes a boundary value problem. As such, we chose to solve the equation using the MATLAB function *bvp4c*. The Usadel equation was defined

within a separate function yielding results for each of the $\underline{\gamma}$-matrix components, and the same was done for the boundary conditions. Depending on which materials were used (superconductors, normal metals, ferromagnets and spin-orbit coupled semiconducting nanowires) these take on different forms, as outlined throughout this thesis. Additionally, an initial guess function had to be supplied to the boundary value problem solver. A zero-vector was supplied as a first guess, and the solution from the last iteration was subsequently fed to the solver. In all cases where the Usadel equation has had to be solved, an S/X/S Josephson junction has been point of interest. In most of the cases the Kuprianov-Lukichev tunneling boundary conditions (2.37) have been employed, such as for all S/F/S structures along with the spin-orbit coupled semiconductor nanowire. The only case in which different boundary conditions were employed was when spin-active interfaces were being considered, and Cottet's boundary conditions for weakly polarized interfaces (2.38) were used.

Solving the Usadel equation yielded a specific value for each $\underline{\gamma}$-matrix component for each energy and superconducting phase difference supplied to the program. This solution value was then saved as either $D^0(E, \Delta\theta)$ and $D^z(E, \Delta\theta)$-matrices in the case of homogeneously polarized spin-split structures, or as $\underline{\gamma}_{ij}(E, \Delta\theta)$ and $\underline{\tilde{\gamma}}_{ij}(E, \Delta\theta)$-matrices when the quasiclassical regime was employed. These were subsequently translated into the retarded Green function matrices which constitute the main body of the matrix thermoelectric coefficients. In all cases, the Usadel equation was solved in the middle of the nanowire X, at $x = 0.5L_X$. Quasiparticle transport across a tunneling barrier from the middle of the Josephson junction S/X/S to the normal metal electrode N is therefore always assumed to occur at this point. This is of course a rather dramatic simplification, but as we have observed the density of states to be quite robust in these structures when moving away from the center of the nanowire, it should not cause too much of a deviation from a fairly realistic case.

Solving the Usadel equation can be very time consuming, depending on the step length employed, number of phase differences considered, complexity of the materials used and interface parameters chosen. Adding spin-orbit coupling, for instance, enhances the complexity of the problem significantly. Therefore, the task of solving the Usadel equation has been performed by the cluster computer system Kongull at NTNU. This was done in order to ensure an energy step length of $\Delta E = 10^{-3}$, which was necessary when integrating the densities of states and $\gamma$-matrices numerically in energy. Moreover, this allowed us to consider a larger number of phase differences, exchange fields in the case of Zeeman-split superconductors, magnetization strengths in the case of ferromagnets, spin-orbit coupling strengths and interface polarizations for spin-active interfaces.

## C.3 Numerical approach for therm. el. coefficients

Once the Usadel equation was solved for the superconductor/ conical ferromagnet/ superconductor Josephson junction, the superconductor/ spin-orbit coupled semiconductor/ superconductor Josephson junction and the superconductor/ normal metal with spin-active interfaces/ superconductor Josephson junction, numerical integration had to be performed in order to quantify the thermoelectric effects. First, the saved matrices for $\underline{\gamma}$ and $\underline{\tilde{\gamma}}$, or $D^0$ and $D^z$, versus the energy and the superconducting phase difference were loaded. In all cases, between 12 and 24 matrices with dimensions $24 \times 7000$ or $24 \times 3500$ were loaded for each specific system, where the different matrices differed in only one property. Next, the necessary helping matrices where defined along with the polarization of the tunneling interface, $P\epsilon[0,1]$. Finally, the Riemann sum over the energy could be performed to approximate the numerical integral. The step length of $dE = 10^{-3}$ was used in order for the Riemann sum to approximate the real integral to a satisfactory degree. Once the thermoelectric coefficients were calculated, $ZT$ and $S$ could be determined. In the case of the formalism for structures with arbitrary spin-dependent fields, the direction-dependent thermal spin coefficient $\alpha_s^\nu$ is included in addition to the formerly mentioned $\alpha$, $G$ and $G_Q$.

# Appendix D

# Article published in Physical Review B 93, 224509 (2016)

# Spin caloritronics with superconductors: Enhanced thermoelectric effects, generalized Onsager response-matrix, and thermal spin currents

Jacob Linder and Marianne Etzelmüller Bathen

*Department of Physics, NTNU, Norwegian University of Science and Technology, N-7491 Trondheim, Norway*

It has recently been proposed and experimentally demonstrated that it is possible to generate large thermoelectric effects in ferromagnet/superconductor structures due to a spin-dependent particle-hole asymmetry. Here, we show theoretically that quasiparticle tunneling between two spin-split superconductors enhances the thermoelectric response manyfold compared to when only one such superconductor is used, generating Seebeck coefficients ($S > 1$ mV/K) and figures of merit ($ZT \simeq 40$) far exceeding the best bulk thermoelectric materials, and it also becomes more resilient toward inelastic-scattering processes. We present a generalized Onsager response-matrix that takes into account spin-dependent voltage and temperature gradients. Moreover, we show that thermally induced spin currents created in such junctions, even in the absence of a polarized tunneling barrier, also become largest in the case in which spin-dependent particle-hole asymmetry exists on both sides of the barrier. We determine how these thermal spin-currents can be tuned both in magnitude and sign by several parameters, including the external field, the temperature, and the superconducting phase difference.

## I. INTRODUCTION

Merging the phenomena of superconductivity and magnetism by creating hybrid structures of materials with these properties is known to give rise to interesting quantum effects [1]. In particular, the field of superconducting spintronics [2] has in recent years gained increasing attention due to the intriguing prospect of procuring spin transport with little or no dissipation of energy. In addition to coupling the charge and spin degrees of freedom in such systems, it has been shown in recent developments that adding heat transport to the picture yields surprising new effects [3–10]. A main motivation for the study of thermoelectricity is that unused waste heat could be utilized as electric currents, and it is desirable to make this conversion process as efficient as possible.

It was theoretically proposed in Ref. [3] that by lifting the spin degeneracy of the density of states in superconductors (e.g., by proximity to magnetic materials), very large thermoelectric effects could be achieved. Reference [4] showed that an electron-hole asymmetry induced by magnetic impurities in superconductors could lead to sizable thermoelectric currents. Subsequent works demonstrated how it was possible to achieve even higher thermoelectric figures of merit $ZT$ and Seebeck coefficients $S$ by making use of the large accumulation of quasiparticle states at energies near the gap edge ($E \simeq \Delta_0$) in superconductors [5,6]. Large thermophases induced in magnetic Josephson junctions have also been studied [10]. The usage of superconducting elements in low-temperature thermometry and refrigeration has been studied extensively in the past [11], but it is only quite recently that the incorporation of magnetic elements into such structures has sparked considerable interest.

The strong coupling of spin, heat, and charge transport in superconducting structures allows us to envision a number of interesting cryogenic thermoelectric devices exceeding the performance of their nonsuperconducting counterparts, such as highly sensitive thermal sensors. A recent preprint [12] reported experimental observation of the large thermoelectric currents predicted in [5] by utilizing a

normal metal/ferromagnetic barrier/superconductor junction (Cu/Fe/Al). Upon application of strong in-plane magnetic fields $B \sim 1$ T, Seebeck coefficients $|S|$ up to 0.1 mV/K were measured. The key to achieving this effect is to create a spin-dependent particle-hole asymmetry in the superconductor (Al) by applying an in-plane field. Due to the magnetic barrier (Fe), tunneling of one spin species is favored compared to the other, thus effectively probing the energy asymmetry for each spin $\sigma$. This scenario raises a tantalizing question: what happens if a spin-dependent particle-hole asymmetry exists not only on one side of the magnetic barrier, but on both sides? One might expect that creating such an asymmetry in all regions of the system would strongly enhance thermoelectric effects even beyond what has been predicted so far for bilayer structures.

In this work, we confirm this hypothesis and show that quasiparticle tunneling between two spin-split superconductors not only increases the thermoelectric response of the system manyfold, but importantly it also displays a robustness toward inelastic scattering in the system. The latter aspect is of particular importance with regard to material choice and possible use of thermoelectric effects in cryogenic devices. For instance, Al is known to have a weak inelastic-scattering rate (modeled by, e.g., a Dynes [13] parameter $\Gamma$), but it also has a very low critical temperature $T_c = 1.2$ K. By achieving large thermoelectric effects even at considerable inelastic scattering $\Gamma$, it becomes possible to use superconductors with much higher critical temperatures such as NbN featuring $T_c = 14$ K. Our results, therefore, provide a way in which robust spin caloritronics with superconductors can be achieved above the sub-Kelvin regime, featuring figures of merit up to $ZT \simeq 40$ and Seebeck coefficients $S > 1$ mV/K, which far exceed even the best thermoelectric bulk materials, such as $CsBi_4Te_8$ and $Bi_2Te_3$, that have $ZT \simeq 2$ at room temperature [14].

Previous works [3,5] have considered how voltage and temperature gradients induce thermoelectric effects in superconducting junctions where spin degeneracy is lifted. Here, we present a generalized Onsager response-matrix that takes into account the possibility of having spin-dependent voltages and temperature biases. The latter scenarios can

be realized through tunneling between ferromagnetic and nonmagnetic materials, as predicted in Refs. [15–17]. In Ref. [18], spin-dependent heat conductance was observed in F/N/F spin-valve nanopillars. This was assumed to arise due to spin heat accumulation, and a difference in the effective spin temperature of up to 350 mK was reported. The same effect was also observed in Ref. [19] more recently, but the authors in that case were more reluctant to conclude that the observation did in fact prove the existence of spin heat accumulation.

Hybrid structures with spin-split superconductors admit thermally induced spin currents without requiring any polarized barrier, as noted in Ref. [5], but this phenomenon has not yet been studied in detail. We demonstrate that these spin currents are in fact the largest precisely in the case in which a spin-dependent particle-hole asymmetry exists on both sides of the barrier. Moreover, we determine how these thermal spin currents can be tuned, both in magnitude and sign, by several parameters, including the external field, temperature, and the superconducting phase difference when incorporating Josephson junctions into the geometry.

## II. THEORY

The system under consideration is shown in Fig. 1(a) and consists of two spin-split superconductors separated by a magnetic barrier with an in-plane magnetic field applied. Possible material choices could be Al/Fe/Al, along the lines of Ref. [12], but NbN/GdN/NbN might be more beneficial due to the strong polarization of GdN [20] and high $T_c$ of NbN. An additional advantage of using a more strongly polarized ferromagnetic barrier is that it can by itself induce an exchange field into both of the superconductors [21], necessitating lower externally applied fields. If desirable, one can substitute one of the superconducting electrodes with a thin normal metal in proximity to a superconducting film, in which case the normal metal mimics a spin-split superconductor in the presence of an in-plane field $B$. When the Coulomb blockade and the supercurrent response are suppressed, quasiparticle tunneling dominates the transport across the junction [22]. We seek to establish a spin-dependent particle-hole asymmetry throughout the system, which is accomplished by using not just a single spin-split superconductor, as in, e.g., [5,6,12], but two. In this way, both electrodes $S_L$ and $S_R$ outlined in Fig. 1(a) host a large particle-hole asymmetry for spin $\sigma$. Because of this, a crucial effect comes into play: since now the asymmetry exists

on both sides of the junction, an additional term appears in the thermoelectric currents, as we will show below. We will also demonstrate that large thermoelectric effects are retained in the proposed setup even in the presence of substantial inelastic scattering.

An important point that should be emphasized is the role of the phonon contribution to the thermal conductance, which is known to be important for semiconducting thermoelectric materials. In contrast, in metals the heat transfer by electrons strongly dominates over the phonon contribution at low temperatures. However, in the superconducting state, the electron contribution decreases with temperature due to the exponential decrease in the carrier density, while the phonon contribution increases due to suppression of the phonon-electron scattering. Therefore, a model neglecting phonon heat transfer in the superconducting bulk becomes less applicable as $T \to 0$. For specific superconducting materials, the model applicability requires a detailed comparison of electron and phonon thermal conductivities.

The charge and heat tunneling currents carried by spin species $\sigma$ read [23,24]

$$I_{\text{heat}}^{\sigma} = \frac{G_{\sigma}}{e^2} \int_{-\infty}^{\infty} dE(E - \mu_L) \mathcal{D}_L^{\sigma}(E - \mu_L) \mathcal{D}_R^{\sigma}(E) F(E),$$

$$I_{\text{charge}}^{\sigma} = \frac{G_{\sigma}}{e} \int_{-\infty}^{\infty} dE \mathcal{D}_L^{\sigma}(E - \mu_L) \mathcal{D}_R^{\sigma}(E) F(E), \quad (1)$$

where $I_{\text{heat}}^{\sigma}$ is the heat current flowing out of the left electrode. Here, the quasiparticle energy $E$ is measured relative to the Fermi level in the right superconductor, $\mu_L$ is the Fermi level in the left region ($\mu_R = 0$ for reference), $\mathcal{D}_j^{\sigma}$ is the density of states for spin $\sigma$ in region $j$, $f_j(E)$ is the distribution function in region $j$, and $F = f_L(E - \mu_L) - f_R(E)$. The superconducting regions are assumed to have a small thickness ($t \sim 10$–20 nm) as in the experiment of Ref. [12], so that an externally applied field splits the density of states according to

$$\mathcal{D}^{\sigma} = \left| \text{Re} \left\{ \frac{E + \sigma h_S + i\Gamma}{\sqrt{(E + \sigma h_S + i\Gamma)^2 - \Delta^2}} \right\} \right|, \quad (2)$$

with $h_S$ being the induced Zeeman field in S, and $\Delta = \Delta(h_S, T)$ is the superconducting gap. Its dependence on $h_S$ and $T$ is shown in Fig. 1(b), featuring a first-order phase transition at $(h/\Delta_0, T/T_{c,0}) = (0.52, 0.53)$, where $\Delta_0$ and $T_{c,0}$ are the bulk superconducting gap and the critical temperature in the absence of the field, respectively. Interfacial spin-flip scattering would likely reduce the net barrier polarization effect due to the randomization of spin.

## III. RESULTS

### A. Thermoelectric figure of merit and Seebeck coefficient

In the presence of a voltage difference $V$ or temperature gradient $\Delta T$ across the bilayer, the Onsager matrix equation [25] describing the linear response for the total charge $I = I_{\text{charge}}^{\uparrow} + I_{\text{charge}}^{\downarrow}$ and heat current $\dot{Q} = I_{\text{heat}}^{\uparrow} + I_{\text{heat}}^{\downarrow}$ flowing through the interface reads

$$\begin{pmatrix} I \\ \dot{Q} \end{pmatrix} = \begin{pmatrix} L_{11} & L_{12} \\ L_{12} & L_{22} \end{pmatrix} \begin{pmatrix} V \\ \Delta T/T \end{pmatrix}, \quad (3)$$



FIG. 1. Left panel: quasiparticle tunneling between two thin superconductors (SCs) $S_L$ and $S_R$ separated by a magnetic barrier (MB). A spin-dependent particle-hole asymmetry is induced via an external in-plane magnetic field. Right panel: self-consistent solution of the order parameter in a spin-split superconductor as a function of exchange field $h_S$ and temperature $T$.
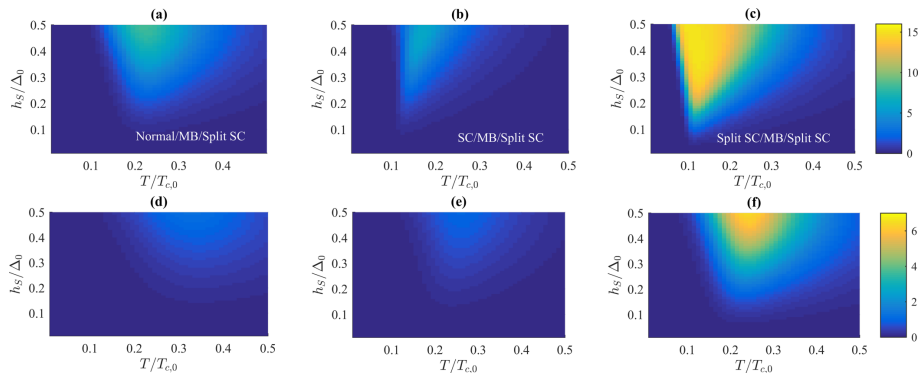
FIG. 2. Figure of merit $ZT$ in the $h_S$-$T$ plane for a barrier polarization $P = 97\%$. In the top row, $\Gamma/\Delta_0 = 10^{-3}$, while in the bottom row the inelastic scattering is substantial, $\Gamma/\Delta_0 = 0.05$. Three bilayer setups separated by a magnetic barrier (MB) are compared: (a) and (d) normal metal/MB/spin-split superconductor, (b) and (e) superconductor/MB/spin-split superconductor, (c) and (f) spin-split superconductor/MB/spin-split superconductor. As seen, the thermoelectric response is dramatically enhanced in the last case.

where we have used the fact that $L_{21} = L_{12}$ due to symmetry (as can also be proven analytically). We defined here $\Delta T/2T = (T_L - T_R)/(T_L + T_R)$. To identify the Onsager coefficients $L_{ij}$, one performs an expansion of Eq. (1) to lowest order in applied voltage $V$ and temperature gradient $\Delta T$, which after some algebra yields the result

$$L_{11} = G_T \int_{-\infty}^{\infty} dE \left(\mathcal{D}_L^0 \mathcal{D}_R^0 + \mathcal{D}_L^z \mathcal{D}_R^z/4\right) C(E),$$

$$L_{22} = \frac{G_T}{e^2} \int_{-\infty}^{\infty} dE \left(\mathcal{D}_L^0 \mathcal{D}_R^0 + \mathcal{D}_L^z \mathcal{D}_R^z/4\right) E^2 C(E), \quad (4)$$

$$L_{12} = \frac{G_T P}{2e} \int_{-\infty}^{\infty} dE \left(\mathcal{D}_L^0 \mathcal{D}_R^z + \mathcal{D}_L^z \mathcal{D}_R^0\right) E C(E),$$

with $C(E) = [4k_B T \cosh^2(\beta E/2)]^{-1}$. We have defined here

$$\mathcal{D}_j^0 = (\mathcal{D}_j^\uparrow + \mathcal{D}_j^\downarrow)/2, \quad \mathcal{D}_j^z = \mathcal{D}_j^\uparrow - \mathcal{D}_j^\downarrow \quad (5)$$

for side $j \in \{L, R\}$. In previous proposals, a spin-dependent particle-hole asymmetry existed only in $S_R$, while a metal [5] or a superconductor with a tunable gap [6] was used instead of $S_L$. However, in the present case the asymmetry of the structure is maximized in the sense that it exists on both sides of the interface, and, importantly, it generates additional terms in the Onsager coefficients, as shown in Eq. (4). For instance, the coefficient $L_{12}$ responsible for inducing heat flow due to a voltage gradient (and also an electric current due to a temperature gradient) now couples the antisymmetric (in $E$) component $\mathcal{D}^z$ on the left side of the magnetic barrier to the symmetric component $\mathcal{D}^0$ of the right side and vice versa. This strongly modifies the thermoelectric response of the system. Of particular interest are the Seebeck coefficient $\mathcal{S}$ (the voltage induced due to a temperature difference after opening the circuit) and the dimensionless figure of merit $ZT$ (which quantifies the ability of the system to produce thermoelectric

power efficiently) [26]:

$$\mathcal{S} = -\frac{L_{12}}{L_{11} T}, \quad ZT = \left(\frac{L_{11} L_{22}}{L_{12}^2} - 1\right)^{-1}. \quad (6)$$

We now proceed to show that due to the additional spin splitting in $S_L$ ($\mathcal{D}_L^z \neq 0$), the thermoelectric effects are enhanced manifold compared to when a metal or conventional superconductor is used, and that they remain large even in the presence of substantial inelastic scattering $\Gamma$.

In Figs. 2(a)–2(c), we have plotted the thermoelectric figure of merit $ZT$ obtained as a function of temperature $T/T_{c,0}$ and exchange field $h_S/\Delta_0$ upon using a magnetic barrier with polarization $P = 0.97$ (as suitable for, e.g., GdN [27]) and with inelastic scattering $\Gamma/\Delta_0 = 10^{-3}$. Extraordinarily large figures of merit $ZT > 15$ are obtained when the quasiparticle tunneling occurs between two spin-split superconductors, as shown in Fig. 2(c). In comparison, the best thermoelectric materials at room temperature ($CsBi_4Te_8$ and $Bi_2Te_3$) reach $ZT \simeq 2$. When only one spin-split superconductor is used [5,6], the thermoelectric response is much smaller, as seen in Figs. 2(a) and 2(b). For smaller polarization values $P$, the figure of merit $ZT$ is suppressed for every type of hybrid structure but still remains largest for tunneling between two spin-split superconductors. The precise dependence on the barrier polarization is shown in Fig. 3(a). As $P$ increases, $ZT$ becomes colossal and reaches almost 40 in magnitude. Since the exchange splitting of the density of states in the superconductors is tunable via an external field, it should be possible to exert well-defined control over the thermoelectric response of the system.

To demonstrate the robustness of the results toward inelastic scattering, we plot in Figs. 2(d)–2(f) the figure of merit $ZT$ for a 50-times-larger inelastic scattering rate $\Gamma/\Delta_0 = 0.05$. This amounts to quite heavy suppression of the BCS coherence peaks in the density of states, and it smoothes out the
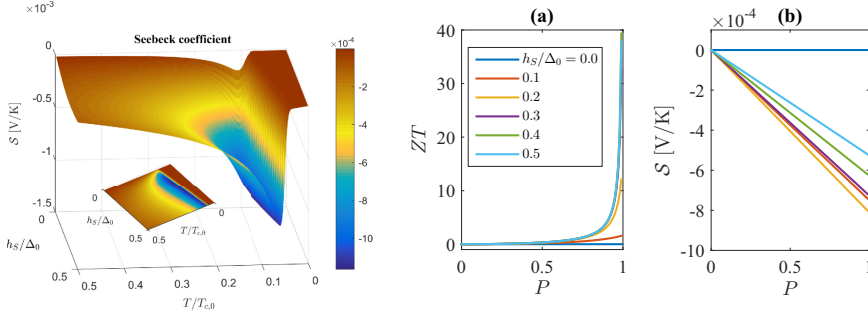
FIG. 3. Left panel: Seebeck coefficient $\mathcal{S}$ for quasiparticle tunneling between two spin-split superconductors separated by a magnetic barrier. We set $P = 97\%$ and $\Gamma/\Delta_0 = 10^{-3}$. The inset shows a bird's-eye view of the same plot. Right panels: (a) The figure of merit and (b) the Seebeck coefficient for the same setup as a function of the barrier polarization $P$. We have set $T/T_{c,0} = 0.15$ and $\Gamma/\Delta_0 = 10^{-3}$. Close to $P = 1$, figures of merit $ZT \simeq 40$ are obtained.

spectral features greatly. In spite of this, it is seen that in the case of quasiparticle tunneling between two spin-split superconductors, a figure of merit close to $ZT > 5$ is retained [Fig. 2(f)], whereas in the other cases $ZT$ is close to an order of magnitude smaller. Another measure of the efficiency of thermoelectric effects is the Seebeck coefficient $\mathcal{S}$, and we plot its behavior in Fig. 3 for the setup shown in Fig. 1(a). Magnitudes of $|\mathcal{S}| > 1$ mV/K are attainable, which is an order of magnitude larger than in the experiment of Ref. [12], where only one spin-split superconductor was used. It should be noted that a rather weak polarization $P \simeq 0.1$ was utilized in Ref. [12], and for larger polarizations $\mathcal{S}$ could theoretically reach the order of 1 mV/K in such a setup as well by fine-tuning the parameters.

### B. Generalized Onsager response-matrix

In addition to applying a voltage or temperature bias, it is also experimentally feasible to create a spin-dependent voltage and temperature bias, $V_s$ and $\Delta T_s$, respectively. Tunneling between ferromagnetic materials and nonmagnetic conductors has been predicted to result in spin-dependent effective temperatures and voltages, and recent experimental results support these claims [18]. This would allow for the application of spin-dependent biases through the addition of ferromagnetic layers to one of the electrodes, and heating these to different temperatures. In the presence of spin-dependent gradients, the Onsager response-matrix is generalized to

$$
\begin{pmatrix} I \\ \dot{Q} \\ I_s \\ \dot{Q}_s \end{pmatrix} = \begin{pmatrix} G & P\alpha & PG & \alpha \\ P\alpha & G_Q & \alpha & PG_Q \\ PG & \alpha & G & P\alpha \\ \alpha & PG_Q & P\alpha & G_Q \end{pmatrix} \begin{pmatrix} V \\ \Delta T/T \\ V_s/2 \\ \Delta T_s/(2T) \end{pmatrix}. \quad (7)
$$

Above, we have defined the spin current $I_s = I_{\text{charge}}^\uparrow - I_{\text{charge}}^\downarrow$ and spin heat current $\dot{Q}_s = I_{\text{heat}}^\uparrow - I_{\text{heat}}^\downarrow$. The applied voltage and temperature biases in the spin-dependent case are

given by

$$
V = \sum_\sigma \left( V_L^\sigma - V_R^\sigma \right)/2, \ V_s = \sum_\sigma \sigma \left( V_L^\sigma - V_R^\sigma \right),
$$
$$
\Delta T = \sum_\sigma \left( T_L^\sigma - T_R^\sigma \right)/2, \ \Delta T_s = \sum_\sigma \sigma \left( T_L^\sigma - T_R^\sigma \right), \quad (8)
$$

and $T = \sum_\sigma (T_R^\sigma + T_L^\sigma)/4$. To simplify the expressions, spin-dependent biases were assumed to exist only on the left-hand side of the barrier. Consequently, we have defined $T_R^\uparrow =$
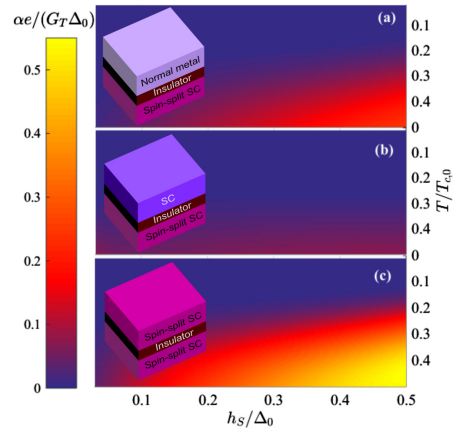


FIG. 4. Plot of the normalized thermoelectric response coefficient $(\alpha e)/(G_T \Delta_0)$ that governs the thermally induced spin current for bilayer junctions without any polarizing barrier: (a) normal metal/insulator/spin-split SC, (b) SC/insulator/spin-split SC, and (c) spin-split SC/insulator/spin-split SC.
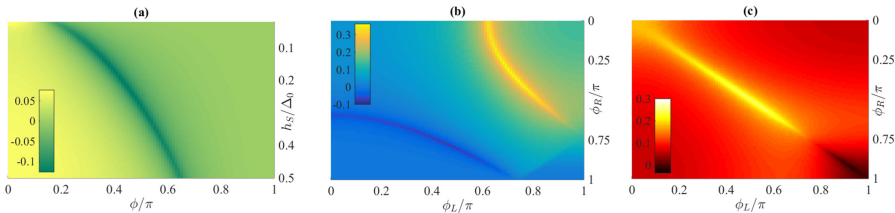
FIG. 5. Plot of the normalized thermoelectric response coefficient $(\alpha e)/(G_T \Delta_0)$ that governs the thermally induced spin current for three types of structures. (a) Tunneling between a superconducting electrode and the normal part of a spin-split SC/normal/spin-split SC junction. We have set $T/T_{c,0} = 0.5$. The sign of $\alpha$ can be changed, inverting the direction of the spin current flow, by tuning $h_S$ or the superconducting phase difference $\phi$. (b) Tunneling between the normal parts of a SC/N/SC and a spin-split SC/N/spin-split SC junction, with $T/T_{c,0} = 0.4$ and $h_S/\Delta_0 = 0.4$. Two arcs with opposite signs cross the $\phi_L$-$\phi_R$ parameter space, where $\phi_L$ is the phase difference between the SCs and $\phi_R$ is the phase difference between the spin-split SCs. (c) Tunneling between the normal parts of two spin-split SC/N/spin-split SC junctions, having set $T/T_{c,0} = 0.4$ and $h_S/\Delta_0 = 0.2$. The normal layers are all assumed to be short compared to the penetration depth of the superconducting correlations, so that they become fully proximitized. We acknowledge the challenge in experimentally realizing tunneling between the weak links of two Josephson junctions, as in (b) and (c), but we nevertheless include these results to demonstrate the interesting behavior of the thermal spin current in this scenario.

$T_R^\downarrow = T_R$ and $V_R^\uparrow = V_R^\downarrow = 0$ for reference. The thermoelectric coefficients in Eq. (7) read $G = L_{11}$, $G_Q = L_{22}$, and

$$\alpha = \frac{G_T}{2e} \int_{-\infty}^{\infty} dE \left( \mathcal{D}_L^0 \mathcal{D}_R^z + \mathcal{D}_L^z \mathcal{D}_R^0 \right) EC(E). \quad (9)$$

This reveals some interesting cross-couplings between spin and heat flow that exist due to the spin-dependent particle-hole asymmetry induced in the superconductors by an exchange field. For instance, one can obtain a heat current $\dot{Q}$ by applying a spin-dependent voltage $V_s$. The response-matrix presented above is general, as it allows for arbitrary voltage, and temperature differences for each spin.

### C. Thermally induced spin currents

Equation (7) shows that even in the absence of any barrier polarization in the junction ($P = 0$), a spin current $I_s$ can be induced via a temperature gradient $\Delta T$ without any accompanying charge flow, according to $I_s = \alpha \Delta T / T$. This fact was also noted in Ref. [5]. We emphasize that this thermal spin current will also flow in the bulk of the superconductor since it is carried by spin-polarized quasiparticles. Up to now, this phenomenon has not been studied in detail, and we therefore determine in what follows how this spin current can be controlled both in magnitude and in sign by using hybrid structures with spin-split superconductors. The quantity of interest is thus the thermoelectric coefficient $\alpha$ in Eq. (9), and in what follows we compute it numerically for several types of hybrid structures, setting $\Gamma/\Delta_0 = 0.005$.

We start by comparing in Fig. 4 the thermal spin current for the same structures as in Fig. 2 (normal/spin-split SC, SC/spin-split SC, and spin-split SC/spin-split SC), but now with the absence of any polarizing barrier ($P = 0$). The resulting $\alpha$ is by far the largest in case (c), demonstrating again the advantage in creating a spin-dependent particle-hole asymmetry on both sides of the interface. By incorporating a

Josephson junction in the geometry, the superconducting phase difference becomes an additional external control parameter that can be used to adjust the thermal spin current, similarly to the setup of Ref. [6]. We find that not only the magnitude of $\alpha$, and in turn $I_s$, but also its sign can be changed. This is shown in Fig. 5, where we plot the normalized thermoelectric coefficient $(\alpha e)/(G_T \Delta_0)$ for various types of hybrid structures incorporating spin-split superconductors. Varying the precise values of $h_S$ and $T$ produces qualitatively similar plots in all cases, and thus we show only one representative plot for each type of system in Fig. 5. The thermal spin current responds to a change in the superconducting phase difference $\phi$ since the proximity-induced minigap $\Delta_g$ in the normal metal region depends on it via $\Delta_g = \Delta(h,T)\cos(\phi/2)$, where $\Delta(h,T)$ is the gap in the bulk superconductors of the Josephson contact. Figure 5 demonstrates that the thermal spin current demonstrates a rich variety of qualitative behavior, depending on the type of structure that is used.

### IV. CONCLUDING REMARKS

The above results thus show that spin-dependent thermoelectric effects in superconductors are increased when a spin-dependent particle-hole asymmetry exists in both adjacent layers to a magnetic tunneling barrier. Coupling spin and heat transport is the foundation for spin caloritronics [28], which suggests that highly sensitive thermoelectric elements can be tailored by using superconductors, leading to efficiencies far exceeding what is possible in nonsuperconducting materials. An interesting future direction could be to explore the role of unconventional superconducting pairing symmetries combined with magnetic elements with regard to thermoelectric effects [29], such as $d$-wave pairing of high-$T_c$ cuprates or $p$-wave pairing in uranium-based ferromagnetic superconductors. The study of Josephson junction geometries is also of interest: by combining such a setup with one spin-split superconductor so that a proximity-induced super-

conducting gap can be tuned, the figure of merit can under ideal circumstances become comparable [6] to the present case with tunneling between two spin-split superconductors. Moreover, the existence of strong odd-frequency triplet pairing in spin-split superconductors was recently highlighted [30], and it suggests that other systems in which odd-frequency superconducting pairing is present and renders the electronic density of states spin-dependent, such as junctions with magnetic spin valves [31,32], spin-active interfaces [8,33–36], inhomogeneous magnetization [37,38], or spin-orbit coupling

[39–42], could host large thermoelectric effects as well. We leave these prospects for forthcoming studies.

[1] M. Eschrig, Spin-polarized supercurrents for spintronics: A review of current progress, Rep. Prog. Phys. **78**, 104501 (2015).

[2] J. Linder and J. W. A. Robinson, Superconducting spintronics, Nat. Phys. **11**, 307 (2015).

[3] P. Machon, M. Eschrig, and W. Belzig, Nonlocal Thermoelectric Effects and Nonlocal Onsager Relations in a Three-Terminal Proximity-Coupled Superconductor-Ferromagnet Device, Phys. Rev. Lett. **110**, 047002 (2013).

[4] M. S. Kalenkov, A. D. Zaikin, and L. S. Kuzmin, Theory of a Large Thermoelectric Effect in Superconductors Doped with Magnetic Impurities, Phys. Rev. Lett. **109**, 147004 (2012).

[5] A. Ozaeta, P. Virtanen, F. S. Bergeret, and T. T. Heikkilä, Predicted Very Large Thermoelectric Effect in Ferromagnet-Superconductor Junctions in the Presence of a Spin-Splitting Magnetic Field, Phys. Rev. Lett. **112**, 057001 (2014).

[6] F. Giazotto, J. W. A. Robinson, J. S. Moodera, and F. S. Bergeret, Proposal for a phase-coherent thermoelectric transistor, Appl. Phys. Lett. **105**, 062602 (2014).

[7] M. S. Kalenkov and A. D. Zaikin, Enhancement of thermoelectric effect in diffusive superconducting bilayers with magnetic interfaces, Phys. Rev. B **91**, 064504 (2015).

[8] P. Machon, M. Eschrig, and Belzig, Giant thermoelectric effects in a proximity-coupled superconductor-ferromagnet device, New J. Phys. **16**, 073002 (2014).

[9] S. Kawabata et al., Efficient electron refrigeration using superconductor/spin-filter devices, Appl. Phys. Lett. **103**, 032602 (2013).

[10] F. Giazotto, T. T. Heikkilä, and F. S. Bergeret, Very Large Thermophase in Ferromagnetic Josephson Junctions, Phys. Rev. Lett. **114**, 067001 (2015).

[11] F. Giazotto, T. Heikkilä, A. Luukanen, A. M. Savin, and J. P. Pekola, Opportunities for mesoscopics in thermometry and refrigeration: Physics and applications, Rev. Mod. Phys. **78**, 217 (2006).

[12] S. Kolenda, M. J. Wolf, and D. Beckmann, Observation of Thermoelectric Currents in High-Field Superconductor-Ferromagnet Tunnel Junctions, Phys. Rev. Lett. **116**, 097001 (2016).

[13] R. C. Dynes, V. Narayanamurti, and J. P. Garno, Direct Measurement of Quasiparticle-Lifetime Broadening in a Strong-Coupled Superconductor, Phys. Rev. Lett. **41**, 1509 (1978).

[14] G. J. Snyder and E. S. Toberer, Complex thermoelectric materials, Nat. Mater. **7**, 105 (2008).

[15] M. Hatami, G. E. W. Bauer, Q. Zhang, and P. J. Kelly, Thermal Spin-Transfer Torque in Magnetoelectronic Devices, Phys. Rev. Lett. **99**, 066603 (2007).

[16] I. J. Vera-Marun, B. J. van Wees, and R. Jansen, Spin Heat Accumulation Induced by Tunneling from a Ferromagnet, Phys. Rev. Lett. **112**, 056602 (2014).

[17] T. T. Heikkilä, M. Hatami, and G. E. W. Bauer, Spin heat accumulation and its relaxation in spin valves, Phys. Rev. B **81**, 100408(R) (2010).

[18] F. K. Dejene, J. Flipse, G. E. W. Bauer, and B. J. van Wees, Spin heat accumulation and spin-dependent temperatures in nanopillar spin valves, Nat. Phys. **9**, 636 (2013).

[19] J. Kimling, R. B. Wilson, K. Rott, J. Kimling, G. Reiss, and D. G. Cahill, Spin-dependent thermal transport perpendicular to the planes of Co/Cu multilayers, Phys. Rev. B **91**, 144405 (2015).

[20] A. Pal, K. Senapati, Z. Barber, and M. Blamire, Pure second harmonic current-phase relation in spin-filter Josephson junctions, Nat. Commun. **5**, 3340 (2014).

[21] T. S. Santos, J. S. Moodera, K. V. Raman, E. Negusse, J. Holroyd, J. Dvorak, M. Liberati, Y. U. Idzerda, and E. Arenholz, Determining Exchange Splitting in a Magnetic Semiconductor by Spin-Filter Tunneling, Phys. Rev. Lett. **101**, 147201 (2008).

[22] R. Meservey and P. M. Tedrow, Spin-polarized electron tunneling, Phys. Rep. **238**, 173 (1994).

[23] T. Heikkilä, The Physics of Nanoelectronics: Transport and Fluctuation Phenomena at Low Temperatures (Oxford University Press, Oxford, 2013).

[24] G. Mahan, Many-particle Physics, 3rd ed. (Plenum, New York, 1990).

[25] L. Onsager, Reciprocal relations in irreversible processes. I, Phys. Rev. **37**, 405 (1931); Reciprocal relations in irreversible processes. II, **38**, 2265 (1931).

[26] H. Littman and B. Davidson, Theoretical bound on the thermoelectric figure of merit from irreversible thermodynamics, J. Appl. Phys. **32**, 217 (1961).

[27] A. Pal and M. Blamire, Large interfacial exchange fields in a thick superconducting film coupled to a spin-filter tunnel barrier, Phys. Rev. B **92**, 180510(R) (2015).

[28] G. E. W. Bauer, E. Saitoh, and B. J. van Wees, Spin caloritronics, Nat. Mater. **11**, 391 (2012).

[29] T. Löfwander and M. Fogelström, Large thermoelectric effects in unconventional superconductors, Phys. Rev. B **70**, 024515 (2004).

[30] J. Linder and J. W. A. Robinson, Strong odd-frequency correlations in fully gapped Zeeman-split superconductors, Sci. Rep. **5**, 15483 (2015).

[31] K. Halterman, P. H. Barsic, and O. T. Valls, Odd Triplet Pairing in Clean Superconductor/Ferromagnet Heterostructures, Phys. Rev. Lett. **99**, 127002 (2007).

[32] T. Yu. Karminskaya, A. A. Golubov, and M. Yu. Kupriyanov, Anomalous proximity effect in spin-valve superconductor/ferromagnetic metal/ferromagnetic metal structures, Phys. Rev. B **84**, 064531 (2011).

[33] Y. Asano, Y. Sawa, Y. Tanaka, and A. A. Golubov, Odd-frequency pairs and Josephson current through a strong ferromagnet, Phys. Rev. B **76**, 224525 (2007).

[34] I. Gomperud, and J. Linder, Spin supercurrent and phase-tunable triplet Cooper pairs via magnetic insulators, Phys. Rev. B **92**, 035416 (2015).

[35] C. Triola, E. Rossi, and A. V. Balatsky, Effect of a spin-active interface on proximity-induced superconductivity in topological insulators, Phys. Rev. B **89**, 165309 (2014).

[36] D. Terrade, P. Gentile, M. Cuoco, and D. Manske, Proximity effects in a spin-triplet superconductor ferromagnet heterostructure with a spin-active interface, Phys. Rev. B **88**, 054516 (2013).

[37] A. Cottet, Inducing Odd-Frequency Triplet Superconducting Correlations in a Normal Metal, Phys. Rev. Lett. **107**, 177001 (2011).

[38] A. Di *et al.* Bernardo , Signature of magnetic-dependent gapless odd frequency states at superconductor/ferromagnet interfaces, Nat. Commun. **6**, 8053 (2015).

[39] S. H. Jacobsen, J. A. Ouassou, and J. Linder, Critical temperature and tunneling spectroscopy of superconductor-ferromagnet hybrids with intrinsic Rashba-Dresselhaus spin-orbit coupling, Phys. Rev. B **92**, 024510 (2015).

[40] S. H. Jacobsen and J. Linder, Giant triplet proximity effect in $\pi$-biased Josephson junctions with spin-orbit coupling, Phys. Rev. B **92**, 024501 (2015).

[41] J. Arjoranta and T. Heikkilä, Intrinsic spin-orbit interaction in diffusive normal wire Josephson weak links: Supercurrent and density of states, Phys. Rev. B **93**, 024522 (2016).

[42] P. Gentile, M. Cuoco, A. Romano, C. Noce, D. Manske, and P. M. R. Brydon, Spin-Orbital Coupling in a Triplet Superconductor-Ferromagnet Junction, Phys. Rev. Lett. **111**, 097003 (2013).

# List of Figures